POLITECNICO DI MILANO

Department of Civil and Environmental Engineering

Doctoral School in Structural, Earthquake and Geotechnical Engineering

Multilayer Precast Façade Panel: Structural Optimization for Energy Retrofitting

Supervisor

Prof. Marco di Prisco

PhD Candidate

Isabella Giorgia Colombo

Co-supervisor

Dr. Matteo Colombo

January 2015

Isabella Giorgia Colombo

Multilayer Precast Façade Panel: Structural Optimization for Energy Retrofitting

e-mail:
isabellagiorgia.colombo@polimi.it

Multilayer Precast Façade Panel: Structural Optimization for Energy Retrofitting

A Thesis

presented to

the Academic Faculty

by

Isabella Giorgia Colombo

In Partial Fulfillment

of the Requirements for the Degree

Doctor of Philosophy

in

Structural, Earthquake and Geotechnical Engineering

January 2015

page intentionally left blank

Doctoral School in Structural, Earthquake and Geotechnical Engineering

Department of Civil and Environmental Engineering

POLITECNICO DI MILANO

XXVII cycle

Faculty Members

Prof. Roberto Paolucci (Co-ordinator)

Prof. Raffaele Ardito

Prof. Fabio Biondini

Prof. Gabriella Bolzon

Prof. Claudia Comi

Prof. Alberto Corigliano

Prof. Dario Coronelli

Prof. Claudio di Prisco

Prof. Marco di Prisco

Prof. Roberto Felicetti

Prof. Liberato Ferrara

Prof. Attilio Frangi

Prof. Elsa Garavaglia

Prof. Cristina Jommi

Prof. Pier Giorgio Malerba

Prof. Stefano Mariani

Prof. Roberto Paolucci

Prof. Umberto Perego

Prof. Federico Perotti

Prof. Lorenza Petrini

Prof. Luigi Zanzi

page intentionally left blank

To Maurizio

page intentionally left blank

Abstract

In Europe residential and commercial buildings are responsible of about 40% of the total energy consumption and the 70% of this energy is used for heating. To reduce this consumption, Standards introduce limits to guarantee the energy saving in new buildings, but also the energy retrofitting of existing buildings has to be considered, because of their large impact on the phenomenon.

In this perspective a multi-layer prefabricated façade sandwich panel characterized by an internal EPS layer and by two external layers of Textile Reinforced Concrete (TRC) is proposed. Just the insulating material is used to transfer the shear between the external TRC layers. The maximum size of the panel is 1.50 x 3.30 m^2; the panel height is properly chosen in order to fix it to the frame concrete beams by means of four punctual connectors placed near to the four corners.

The main advantages of the solution if compared with the thermal coating (EIFS system) are: the lower impact on occupant life (no scaffoldings required), the possibility to obtain the desired finishing in terms of surface roughness, color, pattern (including the reproduction of the original façade), the increase in impact resistance (low floors), the higher quality of finishing and the higher durability. The latter aspect is particularly important, especially considering an expected building life of at least 30 years. Aesthetic and durability aspects are directly related to the use of a high strength fine-grained concrete in TRC.

The main goal of the work is to provide the mechanical characterization of this panel. The research is developed at material, cross-section and full-structure level.

Material level includes the investigation performed on Textile Reinforced Concrete specimens in order to assess their behaviour in tension, considering both standard and extreme conditions (residual strength after exposure to freezing and thawing cycles).

At lab-scale level, failure modes of the sandwich solution have been investigated. In particular, small (550x150 mm^2) and big (1200x300 mm^2) sandwich beams, characterized by the stratigraphy described above, were tested according to a four point load scheme. Both geometries were tested in standard conditions, and small beams were also tested after the exposure to freezing and thawing cycles. Furthermore, the behaviour of the sandwich solution when loaded with a concentrated load is investigated.

Concerning full-scale level, tests were developed considering a real panel simply supported on four points and loaded initially with a distributed load, in order to asses the Serviceability Limit State behaviour, and then with concrete blocks up to failure, in order to determine the maximum load brought at Ultimate Limit State.

In parallel, analytical and numerical analysis have been performed and the adopted models have been validated with respect to the collected experimental results.

Acknowledgements

Think different.

— Steve Jobs

The research, whose results are presented in this thesis, has been carried out at Politecnico di Milano, Department of Civil and Environmental Engineering, in the Lecco campus (Polo Territoriale di Lecco). The work was developed in the framework of a European Project (EASEE - Envelope Approach to improve Sustainability and Energy efficiency in Existing multi-storey multi-owner residential buildings), that financially supported the research activities and allowed the production of the real scale panel.

I would like to thank all my colleagues, friends and family who made the development of this thesis possible, supporting me during these three years, encouraging me and giving me good advices.

A special thank goes to my supervisor, professor Marco di Prisco, not only for his precious guidance and his crucial help in solving problems, but especially for being an example of dedication and passion in everything he does.

With gratitude I thank Dr. Matteo Colombo, the researcher who followed me step by step in this work, the person without whom this thesis would not have been developed, not only a scientific mentor, but also a good friend.

An important support was given to me also by my colleagues and dear friends Dr. Giulio Zani and Dr. Paolo Martinelli; with them I have been working every day side by side for four years, sharing scientific results, life events and emotions. The collaboration with my friend and ex-colleague Dr. Anna Magri played a key role, especially in the beginning phase of this thesis.

Thanks also to Marco Rampini and Farhang Pouyaei for their valuable advises during the writing of the thesis.

For his precious help in the specimen preparation and the test execution, I thank the technician and friend Andrea Stefanoni. For all the burocratic issues and the friendship, I thank Laura Losapio, always helpful and smiling.

The EASEE project allowed me to establish interactions with researchers from the ABC Department of Politecnico di Milano and people from the enterprises. The Small and Medium Enterprises involved in the design and production of the façade panels have been Halfen (Italian division) for the assessment of the anchoring, STAM (Italy) for the design of the mould and Magnetti Building (Italy) for the production of the full scale panel. In particuar, I gratefully thank Eng. Francesco Sonzogni (Magnetti), Eng. Claudio Failla (Magnetti), and Eng. Stefano Ellero (STAM); without them the test on a real scale panel would not have been possible. The collaboration with them was a great opportunity to face with their know-how and to take into account the process of product industrialization. Thanks to all the members of the EASEE consortium, coming from all over Europe, for the precious discussions which took place during international meetings; this has been a great opportunity of professional and personal growth.

I would like to acknowledge all the friends that I met during this experience, in particular Dr. Alessio Caverzan, Dr. Pamela Bonalumi, Dr. Giada Colasante, Dr. Massimiliano Cremonesi, Dr. Mara Pagani, Dr. Andrea Galli, Dr. Patrick Bamonte, Nicola Cefis, Eleonora Lai and Charlotte Tavecchio.

Friends and family have been essential to me; thanks especially to my parents and my husband Maurizio, for being every day my support, my motivation, the people who, more than everyone, believe in me and in my capabilities.

Contents

page intentionally left blank

List of Figures

List of Tables

1

Introduction

In 2010 in Europe residential and commercial buildings were responsible of about 40% of the total energy consumption and the 70% of this energy was used for heating [ODYSSEE_MURE (2012)]. To reduce this consumption, Standards introduce limits to guarantee the energy saving in new buildings, but also the energy retrofitting of existing buildings has to be considered because of their large impact on the phenomenon.

The European project *EASEE* - Envelope Approach to improve Sustainability and Energy Efficiency in existing multi-storey multi-owner residential buildings [EASEE (2016)] - acts in this perspective. One of the main project objectives is the design of a technological solution representing a valid and more durable alternative to the Exterior Insulation and Finishing System (EIFS), which is usually used for the energy retrofitting of existing buildings and typically consists of an insulation panel made of polystyrene foam, secured to the exterior wall surface with an adhesive or mechanical anchoring, on which a water-resistant base coating (reinforced with fibreglass mesh) and a finishing coating are applied. Targets of the project are multi-storey multi-owner residential buildings, dated before 1975,

characterized by reinforced concrete frame structures and cavity brick walls. Two departments of Politecnico di Milano (Department of Architecture, Built environment and Construction engineering - ABC - and Department of Civil and Environmental Engineering - DICA) are involved in the project, together with other research institutes and small and medium enterprises coming from all over Europe.

The solution proposed by the consortium, shown in Figure 1.1, consists in a multi-layer prefabricated façade sandwich panel characterized by an internal insulation layer, made of expanded polystyrene (EPS), and by two external layers in Textile Reinforced Concrete (TRC). TRC is a composite cement-based material that allows designers to obtain thin and lightweight panels thanks to the high load brought in tension.

The maximum size of the panel is 1.50 x 3.30 m^2. The panel height is properly chosen in order to fix it to the frame concrete beams by means of four punctual connectors placed near to the four corners on the short edges: the two upper connectors are aimed to resist only the wind pressure acting on the panel, while the two connectors placed at the bottom are loaded both by wind pressure and self weight of the panel.

The polystyrene layer is chosen to be 100 mm thick in order to guarantee a proper thermal insulation, significantly reducing heat losses of the building. Considering e.g. a typical existing wall made of external plaster, brick masonry 120 mm thick, air cavity, brick masonry 80 mm thick and internal plaster, its thermal transmittance U is estimated to be 1.16 W/m^2K; the addition of an EPS layer 100 mm thick leads to a significant reduction of the thermal transmittance down to 0.26 W/m^2K. This value is lower than the one specified for external walls by the Italian standards currently in force.

In order to correct the out of plumb of the existing façade, an air cavity is left between the panel and the wall. The thickness of this cavity is related to the

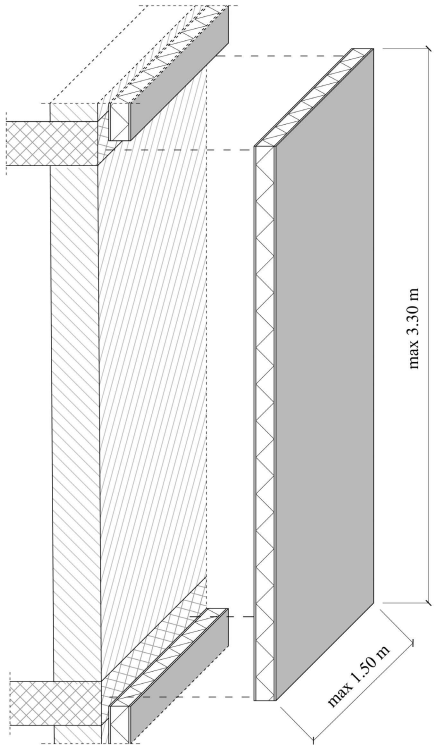

Figure 1.1: Sandwich panel solution proposed for the energy retrofitting of existing buildings.

extent of the out of plumb.

In order to prevent the thermal bridges caused by connectors, the insulating material is used to transfer the shear between the two external TRC layers; in the panel just few connecting devices, active only in extreme conditions (e.g. fire), are provided to prevent the detachment between the two TRC layers.

The main advantages of the solution if compared with the thermal coating (EIFS system) are:

- the lower impact on occupant life (no scaffoldings required);

- the possibility to obtain the desired finishing in terms of surface roughness, color, pattern (including the reproduction of the original façade);
- the increase in impact resistance (low floors);
- the higher quality of finishing;
- the higher durability.

The latter aspect is particularly important, especially considering a residual expected building life of at least 30 years. Aesthetic and durability aspects are directly related to the use of a high strength fine-grained concrete in TRC.

The proposed panel is also characterized by all the advantages related to pre-casting in terms of quality control and fast mounting. The use of TRC allows to keep the weight of the panel under 70 kg/m^2; that means building site safety during panel handling and low building mass rise, particularly important in seismic areas.

An innovative in-pressure casting technique is adopted to avoid the use of glue and to prevent the debonding between the layers thanks to the good bond obtained during the production.

Within the project, ABC department is in charge of studying the panel thermal behaviour and the process of assessment of existing building using 3D laser scanning, while DICA department is responsible of the investigation and optimization of the panel mechanical behaviour.

1.1 Levels of investigation

The mechanical characterization of the panel is carried out operating at three levels: material, lab-scale and full-structure level.

Material level includes the investigation performed on Textile Reinforced Concrete specimens in order to assess their behaviour in tension, considering both standard and extreme conditions (residual strength after exposure to freezing and thawing cycles).

At lab-scale level failure modes of the sandwich solution have been investigated. In particular, small (550x150 mm^2) and big (1200x300 mm^2) sandwich beams, characterized by the stratigraphy described above, were tested according to a four point load scheme. Both geometries were tested in standard conditions, while small beams were also tested after the exposure to freezing and thawing cycles. Furthermore, the behaviour of the sandwich solution when loaded with a concentrated load is investigated.

Concerning full-scale level, tests were developed considering a real panel simply supported on four points and loaded initially with a distributed load, in order to asses the Serviceability Limit State behaviour, and then with concrete blocks up to failure, in order to determine the maximum load brought at Ultimate Limit State.

In parallel, analytical and numerical analysis have been developed and the models proposed have been validated with respect to the collected experimental results.

The research has been financially supported by the EASEE project (Grant Agreement No.: 285540; starting date: March 1st, 2012; duration: 48 months). The production and testing of the full-scale panel has been possible thanks to the cooperation with Stam (society of mechanical engineering), that designed the formwork for the in-pressure casting, and Magnetti Building (precast industry), that cast the panel and took part in the tests.

1.2 Outline of the thesis

The thesis is organized in nine chapters.

In the introduction the engineering problem is described; then, the main objectives of the research and the levels at which it has been developed are highlighted.

In Chapter 2 an overview of sandwich structures is provided, focusing in particular on cladding sandwich panels, including those characterized by traditional reinforced concrete and Textile Reinforced Concrete faces. An analytical model proposed in literature and its development are also included.

Chapter 3 concerns the state-of-the-art of Textile Reinforced Concrete: the tensile behaviour of the composite material, the fields of application and durability aspects are here addressed.

Chapters 4, 5, 6 and 7 are inherent with the experimental campaign developed at material, lab-scale and full-scale level. Chapter 4 is devoted to the investigation of TRC tensile behaviour in standard conditions and after the exposure to freezing-thawing cycles. Chapter 5 collects experimental results obtained testing the sandwich solution according to four point load and concentrated load test set-ups. Chapter 6 presents the results of four point load tests performed on sandwich beams previously treated with freezing-thawing cycles. Chapter 7 includes the behaviour of a real scale panel both at Serviceability and Ultimate Limit State.

In Chapter 8 the non-linear behaviour of the sandwich solution is predicted through an analytical solution and a finite element model.

In the last chapter concluding remarks and further developments are drawn.

2

State-of-the-art of sandwich structures

2.1 Principle of sandwich structures

The success of sandwich structures is related to their higher bending stiffness and lower maximum face stresses if compared to mono-layer structures, although the presence of the core implies an increment in weight that, for some applications, can even double. As an example, Vinson (2005) compares a mono-layer construction and a sandwich structure, as those shown in Figure 2.1. Considering a ratio of face thickness to core depth equal to 1/20, the sandwich structure results in a bending stiffness 300 times higher and in maximum stresses 30 times lower than the mono-layer element.

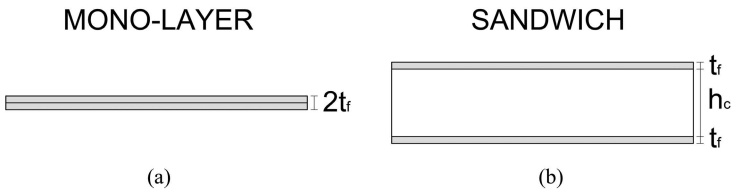

Figure 2.1: Mono-layer (a) and sandwich (b) structure.

2.2 Main type of sandwich construction

Structural sandwiches are usually characterized by two faces (often identical in material, fibre orientation and thickness), which primarily resist the in-plane and bending loads, and by an inner core, that resists transverse shear loads. In special cases the faces can differ one from the other; possible reasons are: that one is the primary load-carrying, that the outer face has to withstand elevated temperature or a corrosive environment, etc. [Vinson (1999)]

In a sandwich structure the two faces are relatively thin and characterized by a high strength, while the core is relatively thick, light and characterized by an adequate stiffness in the direction normal to the faces. The faces may be steel, aluminium, wood, fibre-reinforced plastic or concrete; the core may be in cork, balsa wood, rubber, solid plastic material (polyethylene), rigid foam material (polyurethane, polystyrene, phenolic foam), mineral wool slabs, foam honeycombs, metal, paper. [Davies (2001)]

Four main types of core can be identified (Figure 2.2):

1. foam or solid core (relatively cheap, can be made of balsa, wood or foam/plastic materials with various densities and shear moduli);
2. honeycomb core (widely used since II World War; the most common are the hexagonally-shaped cell and the square cell structures);
3. web core;
4. corrugated or truss core.

In the case of web and truss core, a portion of the in-plane and bending loads is carried by the core.

As underlined by Davies (2001), in composite panels the positive properties of the individual materials can be combined and the negative properties eliminated.

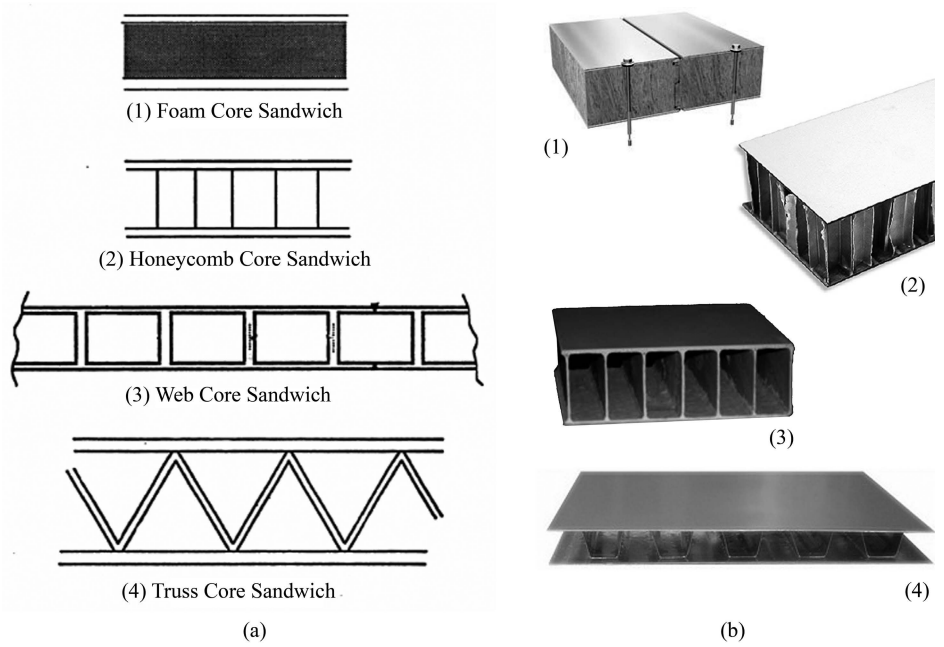

Figure 2.2: Main types of core [Vinson (1999)] (a) and commercial examples of each sandwich panel ("Ruukki" wall and ceiling panel, "CelComponents" honeycomb panel, web panel and "B-MEK CO." truss panel) (b).

The author provides two meaningful examples: the use of thermal insulating plastic foam or mineral wool is possible only if these core materials are protected against moisture by means of diffusion-proof facings; the strength and stiffness of thin-walled metal claddings can be exploited only if they are stiffened against buckling due to compression by the presence of the core.

2.3 Brief historical overview

Since 1940s sandwich constructions have been used primarily in the aircraft industry and later in missile and spacecraft structures [Vinson (1999)].

Although the sandwich principle was used earlier in less spectacular applica-

tions, the first major construction in which sandwich panels were used is quoted to be the World War II Mosquito aircraft [Davies (2001)], built in England by means of plywood sandwich panels [Vinson (1999)]. In the same decade, in the USA, fuselages were designed and fabricated using reinforced plastic faces and low density core, e.g. Wright Patterson Air Force Base used fibreglass-reinforced polyester faces with both a glass-fabric honeycomb and a balsa core, while Hexcel Corporation began the production of honeycomb core for sandwich structures, becoming one of the most important firm in the sandwich construction field (even today this company produces over the 50% of the world's honeycomb core materials) [Vinson (2005)].

Starting from 1960s, the sandwich solution was applied in other fields, such as buildings, refrigerated storages and automotive and shipbuilding industries; in the same years a worldwide boom in prefabricated building elements took place, favouring the diffusion of sandwich products [Davies (2001)].

2.4 Cladding sandwich panels in buildings

Davies (2001) constitutes a reference for cladding wall and roof sandwich panels applied in buildings. In particular, the book focuses on panels characterized by both the inner and the outer faces formed of flat or profiled metal (steel or aluminium) sheets that act compositely with a relatively low strength core, which has suitable insulating and stiffening properties (Figure 2.3). The bond between the components can be obtained through a line foaming process, the use of adhesives or mechanical fastenings.

Davies' choice of this particular sandwich solution is related to the favourable combination of the positive properties of metal facings (load-bearing capacity, protection of the insulation against mechanical damage, weather protection and vapour barrier) with the complementary positive core properties (thermal and

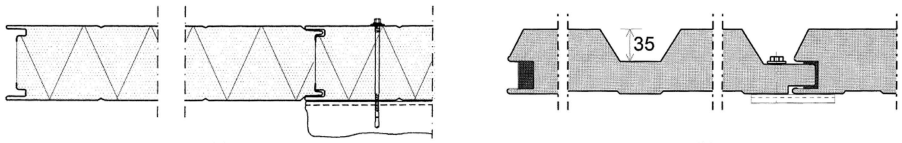

Figure 2.3: Wall sandwich panels with flat (a) and profiled (b) metal sheets [Davies (2001)].

acoustic insulation and corrosion protection).

According to Davies (2001), these panels result characterized by:

- high load-bearing capacity at low weight;
- excellent and durable thermal insulation;
- absolute water and vapour barrier;
- excellent airtightness;
- surface finished facings providing resistance to weather and aggressive environments;
- capacity for rapid erection without lifting equipment; easier installation in hostile weather conditions;
- easy repair or replacement in case of damage;
- economical mass production to pre-cut lengths of components of uniform high quality;
- long life at low maintenance cost;
- behaviour in fire of panels with mineral wool cores.

However, Davies (2001) identifies also some less favourable properties:

- behaviour in fire of elements with rigid plastic foam cores;
- deformation when one side is exposed to heat, e.g. strong sunlight;
- creep under sustained load of elements with rigid foam cores;
- low thermal capacity;
- although sandwich elements give good sound insulation compared with alternative wall and roof construction of similar weight, the insulation level achieved is characteristic of lightweight construction.

Other possible boards to be used in faces are: timber-based boards, wood-based chipboard, plywood, gypsum boards, gypsum boards reinforced with fibres, cement-based boards and plastic boards.

While in aerospace and automotive applications other considerations may prevail over costs, in building industry the performance to cost ratio is one of the main parameter to be considered in order to make the product competitive on the market. However, all requirements concerning safety, serviceability, durability and aesthetic have to be satisfied. [Davies (2001)]

According to Davies (2001), these sandwich solutions are designed in such a way that they act as a composite load-bearing unit for the expected working life (Figure 2.4(a,b,c)). The adhesive bond between the faces and the core is supposed to carry a shear stress equal to the shear stresses in the core.

Aims of the core material and its adhesive bond are: to prevent the upper face slipping (Figure 2.4(d)), that happens when the adhesive is characterized by poor bond; to prevent the shear failure or a reduced shear action (Figure 2.4(e)), that occurs when the core is characterized by insufficient shear strength or stiffness; to avoid the local buckling of the upper compressed face (Figure 2.4(f)), mainly dependent on the core stiffness.

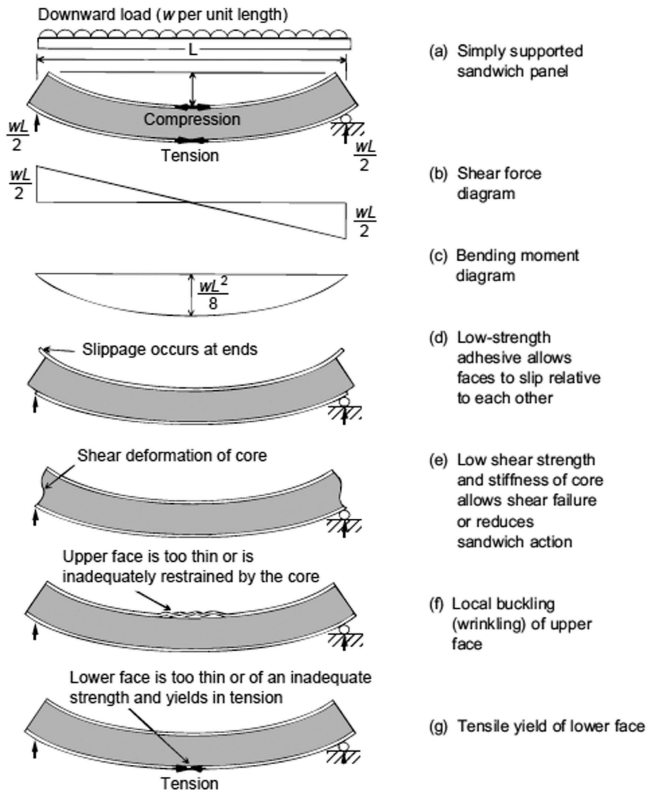

Figure 2.4: Composite behaviour of the panel (a,b,c) and possible modes of failure (d,e,f,g) [Davies (2001)].

The last mode of failure shown in Figure 2.4, see subfigure (g), is due to the tensile failure of the lower face. This failure mode is the less probable between those presented for this kind of panel.

2.5 Traditional R/C cladding sandwich panels

In building industry, also pre-cast R/C cladding sandwich panels are largely used worldwide, especially in Europe and North America, as structural and insulating

wall in multi-unit residential, commercial and warehouse building [Einea et al. (1991)]. These panels are generally made of two external reinforced concrete layers connected through the insulation layer by means of various type of shear connectors (e.g. concrete webs, metal connectors, plastic connectors or a combination of them).

The main difference comparing them with those presented in Subsection 2.4 is that they are not designed in order to behave as composite panel, exploiting the adhesive bond. Another important difference is related to the higher order of weight of the panels.

Depending on the strength and stiffness of the shear connectors used, a sandwich behaves as fully-composite, partially-composite or non-composite panel (Figure 2.5) [Salmon et al. (1997)]. In the first case, the connectors are able to transfer the shear forces between the two external layers, hence both of them carry the applied load acting as a compact section. When the connectors transfer a minimal part of the shear force from one external layer to the other, the system is considered non-composite: the amount of load carried by each layer, and hence the stress distribution, depends on the stiffness of the layer itself. As underlined by Einea et al. (1991), in many non-composite panels the load is carried by just one concrete layer, that is considered as the structural one, while the other layer does not contribute to the strength of the panel and is used mainly for aesthetic purposes, to enhance the panel durability and to encase the insulating material. Partially-composite panels lie in between these two extremes [Metelli et al. (2011)].

The thickness of each concrete layer depends on its structural function, the concrete cover required, the anchorage of the connectors and the finishing; however, in conventional sandwich panels, it is never smaller than 50 mm [Einea et al. (1991)].

Some studies concerning the bending behaviour of sandwich panels were devel-

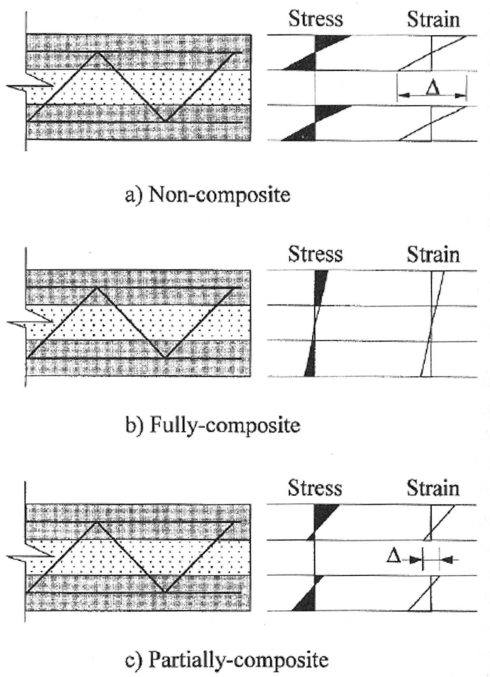

Figure 2.5: Non-composite (a), fully-composite (b) and partially-composite (c) panel [Salmon et al. (1997)].

oped [Gara et al. (2012)], paying particular attention to the relationship between the shear connectors used and the obtained composite action [Benayoune et al. (2008), Naito et al. (2011)].

However, the high costs of full-scale testing, the difficulty in fabricating small-scale panels and the reluctance of the producers in sharing the information with their competitors lead to a lack of information on the mechanical performances of the pre-cast concrete sandwich panels [Benayoune et al. (2008)].

The main advantage of a sandwich solution, that is the integration between the thermal insulation and the wall structural element, has to be added to all the advantages related to prefabrication, such as quality control and fast mounting. The main disadvantages are related to the insufficient architectural design range,

the clumsy appearance and the corrosion damages that, according to Hegger and Horstmann (2009), induce a decreasing in the acceptance of this technology for façade.

Moreover, the insulation efficiency of the sandwich panel depends on the thermal resistance of the insulation material, generally polystyrene or polyurethane, and this efficiency can be considerably reduced by the thermal bridges caused by the presence of the shear connectors, that can be significant especially in the fully-composite solution.

2.6 From R/C to TRC cladding sandwich panels

In order to exploit the advantages of a prefabricated sandwich solution while solving corrosion problems, improving the design possibility and obtaining the desired finishing, Hegger and Horstmann (2009) proposed sandwich panels with both the concrete layers made of Textile Reinforced Concrete (TRC) (Figure 2.6) and pointed out the good mechanical behaviour of this solution.

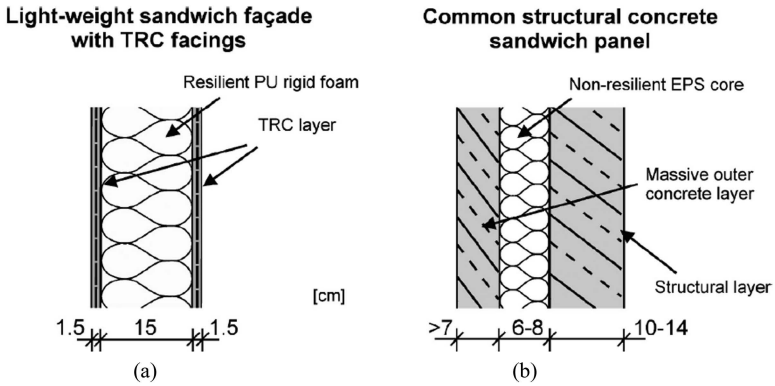

Figure 2.6: Comparison between light-weight TRC sandwich panels (a) and traditional R/C sandwich panels (b) [Hegger and Horstmann (2009)].

Hegger and Horstmann (2009) investigated TRC sandwich beams in which the shear stresses are transferred just through adhesive bond; however, in the real scale panels, they introduced connecting devices in order to guarantee a durable connection between the TRC layers and a proper sandwich action. Besides, in the wall elements they proposed the inner profiled layer as structural and the dead load of the outer thin concrete layer is transferred to it by the foam and the pin connectors.

The results of tests performed by Hegger and Horstmann (2009) on TRC sandwich beams are shown in Figure 2.7 in terms of bending moment vs. displacement curves. The specimens are characterized by different core material (PU = polyurethane; XPS = extruded polystyrene) and densities and by different adhesive bond (obtained by gluing or by pressing a notched core into a fresh concrete layer).

Panel	Core	Interface	Span L_s (m)	Failure Load F_u (kN/m)	Deflection w (mm)
P1	PU 32	Notched	1.9	27.6	43.0
P2	PU 32	Glued	1.9	18.1	29.2
P3	PU 200	Notched	1.9	151.2[1)]	28.0
P4	PU 40	Notched	4.9	23.2	99.8
P5	PU 50	Notched	1.9	49.0	32.0
P6	XPS 32	Notched	1.9	58.0	40.0

[1)] tensile failure of fabrics 1 (5 layers) in lower facing.

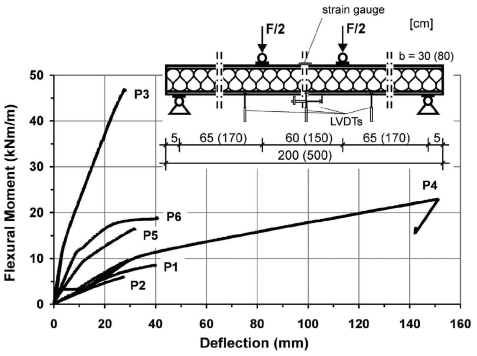

Figure 2.7: Results of tests performed on TRC sandwich beam specimens [Hegger and Horstmann (2009)].

An investigation concerning the influence of shear connectors on the behaviour of these TRC sandwich panels can be found in Shams et al. (2014b); in particular, carbon fabric shear grids and glass fibre reinforced polymer pin connectors are taken into account and tensile, shear and bending behaviours are investigated.

This thesis, as anticipated in the Introduction, concerns a multi-layer prefabricated façade sandwich characterized by an internal insulation layer made of expanded polystyrene foam (EPS, 100 mm thick) and by two external layers of Textile Reinforced Concrete (TRC, 10 mm thick). This sandwich solution is adopted in the external façade panel proposed for energy retrofitting of existing buildings in the framework of a more extensive research project [EASEE (2016)]; the maximum dimension of this panel is 1.5 x 3.3 m^2. The real panel is supposed to be placed on an existing wall by means of four punctual connectors placed near to the four corners of the panel on the short edges: the two upper connectors are aimed to resist only the wind pressure acting on the panel, while the two connectors placed at the bottom are loaded both by wind pressure and self weight of the panel. In order to prevent the thermal bridges caused by connectors, the insulating material is used to transfer the shear between the two external TRC layers; hence, in a full-scale panel designed with this technology, just few connecting devices, active only in extreme conditions (e.g. fire), must be provided to prevent the detachment between the two TRC layers.

This approach, that consists in transferring the shear by means of the core material, is commonly adopted for building sandwich panels characterized by metallic or polymeric external skins, as seen in Subsection 2.4; an example of an experimental investigation performed on such kind of panel can be found in [Sharaf et al. (2010)].

Nevertheless, Ferrara et al. (2008), Colombo et al. (2008), di Prisco et al. (2012), di Prisco and Zani (2012) and Müller et al. (2012) proposed cement based sandwich elements in which advanced cementitious composites are used for the external layers and the connection between the layers is obtained only through the bond between the insulating material and the cementitious layer without any connector.

In Figure 2.8 the roof sandwich panel proposed by di Prisco et al. (2012) is

shown together with some experimental results. This panel is characterized by an upper layer in High Performance Fibre Reinforced Concrete 20 mm thick, a polystyrene layer 64 mm thick and a lower Textile Reinforced Concrete layer 6 mm thick. In the figure also a picture of the panel edge is plotted.

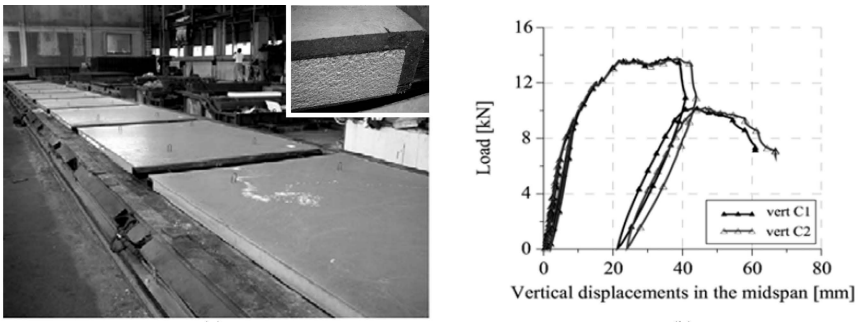

Figure 2.8: Sandwich panel production with a zoom on the panel edge (a) and load vs. vertical displacement curves at midspan (b) [di Prisco et al. (2012)].

2.7 Analytical models

2.7.1 Plane Section approach

The simplest analytical model that can be applied to a sandwich beam is the plane section model.

It is based on the assumption that the section remains plane and, hence, there is a linear strain distribution over the cross section ($\vartheta_{core} = \vartheta_{face}$, Figure 2.9); the shear deformations (γ_{xz}, considering x as the longitudinal axis and z the vertical one) of both the faces and of the core are assumed to be negligible. The elastic stress distribution over the cross-section is reported in Figure 2.9.

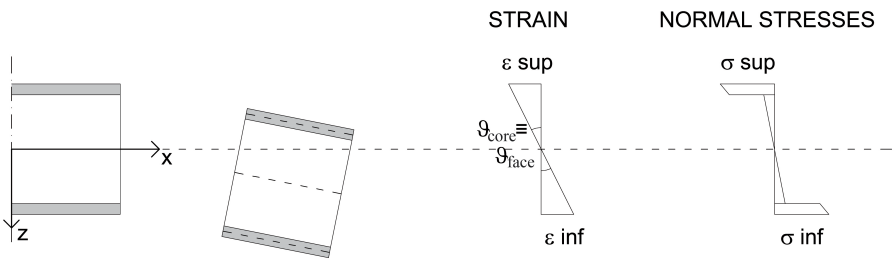

Figure 2.9: Strain and stress distribution according to the plane section approach.

2.7.2 Stamm and Witte Theory

As the shear deformation of the core generally plays a key role in the global behaviour of a sandwich panel, the plane section approach is not suitable in order to predict the real response.

In their book, Stamm and Witte (1974) propose an analytical model for sandwich beams, that takes into account the shear deformation of the core. Two variations of that model are described: the first concerns sandwich beams characterized by thin faces, while the second is related to sandwich beams with thick outer layers, whose bending stiffness can not be neglected. The analytical solution of the first case was previously found by Plantema (1966).

The bending and shear stress distribution over the cross-section is shown in Figure 2.10 for both the situations.

Sandwich beams with thin faces

The analytical model in the case of thin faces is based on the following assumptions:

- the material of the faces is linear elastic; the core is homogeneous and it also obeys the Hooke's Law;

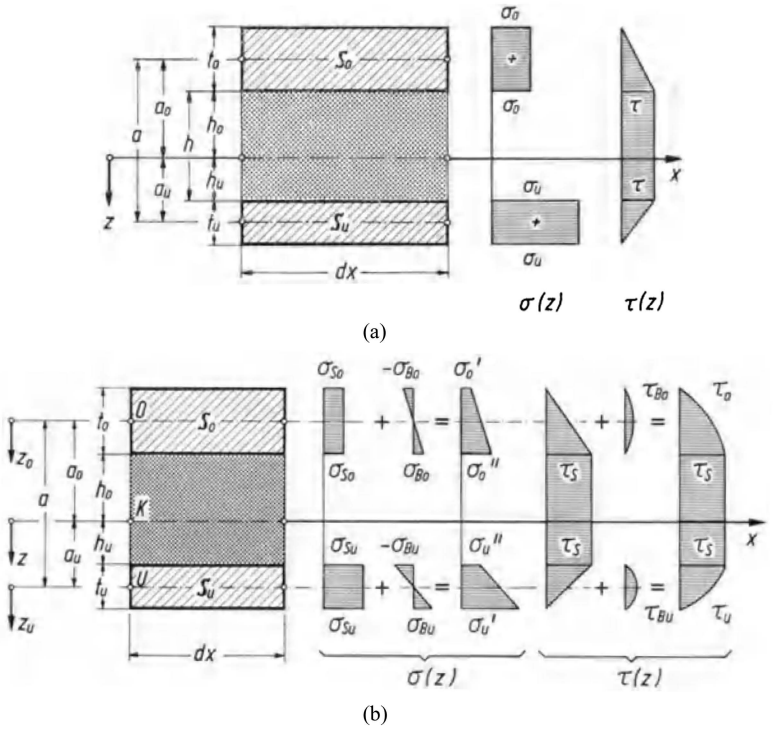

Figure 2.10: Distribution of normal and shear stresses in a sandwich beam characterized by thin (a) or thick (b) faces [Stamm and Witte (1974)].

- the faces are planar, parallel to each other and so thin that their own bending stiffness can be neglected. So, in the outer layers, a membrane stress state is assumed, with the normal stresses taken constant over the face thickness (Figure 2.10(a));

- the shear stiffness of the outer layers is large, hence their shear deformations γ_{xz}^{face} can be neglected; the cross sections of the outer layers thus remain planar and perpendicular to the axis even after the deformation (Bernoulli hypothesis);

- the core is soft if compared with the outer faces, hence σ_x^{core} can be taken

equal to zero, while τ_{xz}^{core} is constant (Figure 2.10(a));

- due to the shear deformation of the core, the total cross section of the sandwich beam is not flat, but it deforms to a broken line (as shown in Figure 2.11);
- the sandwich panel is calculated as a one-dimension structure, e.g. a beam;
- both a transverse and a longitudinal load are supposed to act on the sandwich beam, hence the second order effects are taken into account;
- small displacements and deformations are considered.

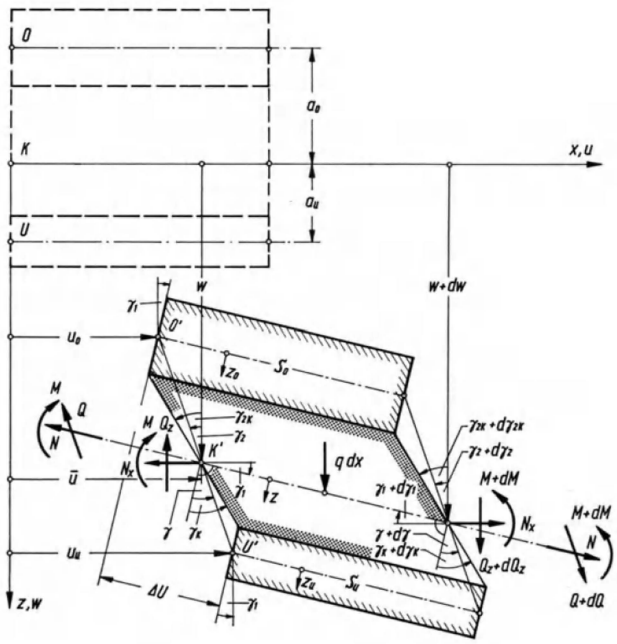

Figure 2.11: Sandwich beam element in deformed configuration [Stamm and Witte (1974)].

The axial stiffness of the faces results:

$$D_o = E_o b t_o \tag{2.1}$$

$$D_u = E_u b t_u \tag{2.2}$$

respectively for the upper (o) and the lower (u) outer layer, considering the elastic moduli (E_o and E_u), the thickness of each face (t_o and t_u) and the depth of the sandwich beam (b). Hence, the global axial stiffness of the faces results:

$$D = D_o + D_u \tag{2.3}$$

Considering a_o and a_u as defined in Figure 2.11, the sandwich bending stiffness B_S results:

$$B_S = D_o a_o^2 + D_u a_u^2 \tag{2.4}$$

The shear stiffness of the core is equal to:

$$A = G\frac{ba^2}{h} \tag{2.5}$$

considering G the shear modulus of the core, b the depth of the beam, a as defined in Figure 2.10 and h the height of the core.

Finally, if there is no normal force acting on the beam (N=0, first order theory), the differential equations governing the problem for a generic load q result:

$$\begin{cases} w^{IV} = +\frac{q}{B_S} - \frac{q^{II}}{A} \\ \gamma^I = -\frac{q}{A} \end{cases} \tag{2.6}$$

where w and γ represent respectively the vertical displacement and the rotation, as illustrated in Figure 2.11.

Sandwich beams with thick faces

If the sandwich is characterized by thick faces, their bending stiffness is not negligible if compared to the one of the whole sandwich beam. Hence, the previous model, whose solution is due to Plantema (1966), is implemented by Stamm and Witte (1974) superimposing the local bending state of each external layer to the membrane state of stress of these outer layers due to sandwich global behaviour. The distribution of stresses here considered is plotted in Figure 2.10(b).

If there is no normal force acting on the beam (N=0, first order theory), the differential equations governing the problem for a generic load q result:

$$\begin{cases} -\frac{B_u+B_o}{A} w^{VI} + \frac{B}{B_S} w^{IV} = +\frac{q}{B_S} - \frac{q^{II}}{A} \\ -\frac{B_u+B_o}{A} \gamma^{IV} + \frac{B}{B_S} \gamma^{II} = -\frac{q^I}{A} \end{cases} \tag{2.7}$$

considering:

$$B_o = E_o \frac{bt_o^3}{12} \tag{2.8}$$

$$B_u = E_u \frac{bt_u^3}{12} \tag{2.9}$$

and

$$B = B_S + B_o + B_u \tag{2.10}$$

Solving the differential equations for a simply supported beam loaded with a concentrated load placed at a distance e from the support (Figure 2.12), Stamm and Witte (1974) found the following equations for vertical displacements and

rotations at point $x = e$:

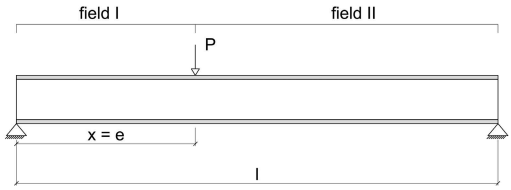

Figure 2.12: Simply supported sandwich beam loaded with a concentrated load.

$$w_1 = \frac{Pl^3}{B}\left[\frac{1}{6}(1-\varepsilon)\xi(2\varepsilon-\varepsilon^2-\xi^2)+\frac{1}{\alpha\lambda^2}(1-\varepsilon)\xi-\frac{1}{\alpha\lambda^3}\frac{sinh[\lambda(1-\varepsilon)]}{sinh\lambda}sinh(\lambda\xi)\right] \tag{2.11}$$

$$w_2 = \frac{Pl^3}{B}\left[\frac{1}{6}(1-\xi)\varepsilon(2\xi-\xi^2-\varepsilon^2)+\frac{1}{\alpha\lambda^2}(1-\xi)\varepsilon-\frac{1}{\alpha\lambda^3}\frac{sinh(\lambda\varepsilon)}{sinh\lambda}sinh[\lambda(1-\xi)]\right] \tag{2.12}$$

$$\gamma_1 = \frac{Pl^2}{B}\beta\left[1-\varepsilon-\frac{sinh[\lambda(1-\varepsilon)]}{sinh\lambda}cosh(\lambda\xi)\right] \tag{2.13}$$

$$\gamma_2 = \frac{Pl^2}{B}\beta\left[-\varepsilon+\frac{sinh(\lambda\varepsilon)}{sinh\lambda}cosh[\lambda(1-\xi)]\right] \tag{2.14}$$

considering:

$$\xi = \frac{x}{l} = \frac{e}{l} = \varepsilon \tag{2.15}$$

$$\alpha = \frac{B_o + B_u}{B_S} \tag{2.16}$$

$$\beta = \frac{B_S}{Al^2} \tag{2.17}$$

$$\lambda = \sqrt{\frac{1+\alpha}{\alpha\beta}} \tag{2.18}$$

Index 1 refers to field I in Figure 2.12, while index 2 refers to field II.

The following moment can be also computed:

$$M_{S1} = Pl\frac{1}{1+\alpha}\left[(1-\varepsilon)\xi - \frac{sinh[\lambda(1-\varepsilon)]}{\lambda sinh\lambda}sinh(\lambda\xi)\right] \tag{2.19}$$

$$M_{S2} = Pl\frac{1}{1+\alpha}\left[(1-\xi)\varepsilon - \frac{sinh(\lambda\varepsilon)]}{\lambda sinh\lambda}sinh\lambda(1-\xi)\right] \tag{2.20}$$

$$M_{u,o1} = Pl\frac{\alpha_{u,o}}{1+\alpha}\left[(1-\varepsilon)\xi + \frac{sinh[\lambda(1-\varepsilon)]}{\alpha\lambda sinh\lambda}sinh(\lambda\xi)\right] \tag{2.21}$$

$$M_{u,o2} = Pl\frac{\alpha_{u,o}}{1+\alpha}\left[(1-\xi)\varepsilon + \frac{sinh(\lambda\varepsilon)]}{\alpha\lambda sinh\lambda}sinh\lambda(1-\xi)\right] \tag{2.22}$$

considering:

$$\alpha_o = \frac{B_o}{B_S} \tag{2.23}$$

$$\alpha_u = \frac{B_u}{B_S} \tag{2.24}$$

Indexes u, o refer respectively to the lower and the upper face, while index S refers to the sandwich action due to the interaction between the two faces.

2.7.3 Stamm and Witte Theory implemented by Shams et al. (2014a)

Shams et al. (2014a) implemented the Stamm and Witte analytical model in order to account the non-linear behaviour of the materials.

As the equations in Stamm and Witte (1974) are solved for constant bending and axial stiffness, to avoid solving the differential equations with a stiffness function, Shams et al. (2014a) propose constant average stiffness values for the full length of the beam.

Firstly, the beam is divided into a finite number of elements with equal length and an axial and a bending stiffness are assigned to each element, depending if the section is cracked or un-cracked. Then, overall stiffness EI and EA (originally called $B_{o,u}$ and $D_{o,u}$) are computed for the beam combining the partial stiffness.

Two ways to compute the overall stiffness are proposed by the authors:

- weighting the beam stiffness basing on the deflection (model A);
- weighting the beam stiffness basing on the internal forces (model B).

Once computed the load-dependant axial and bending stiffness for each element, separately for the upper and the lower faces, model A weights them considering the vertical displacement w_i computed for the i-th element and uses the average values as a constant over the beam length (Figure 2.13(a)):

$$EI_A = \frac{\sum_{i=1}^{n} EI_i \cdot w_i}{\sum_{i=1}^{n} w_i} \tag{2.25}$$

$$EA_A = \frac{\sum_{i=1}^{n} EA_i \cdot w_i}{\sum_{i=1}^{n} w_i} \tag{2.26}$$

On the other hand, model B weights EI and EA computed for each element according to the average bending moment acting on the same element (Figure 2.13(b)):

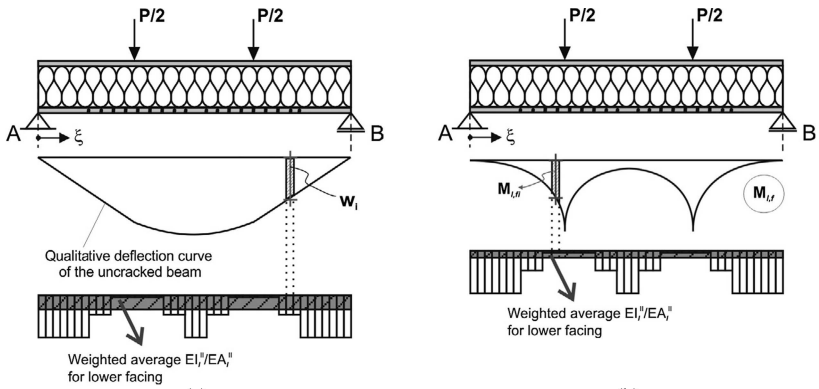

Figure 2.13: Beam stiffness weighting basing on the displacement (a) or on the bending moment (b) [Shams et al. (2014a)].

$$EI_B = \frac{\sum_{i=1}^{n} EI_i \cdot M_i}{\sum_{i=1}^{n} M_i} \tag{2.27}$$

$$EA_B = \frac{\sum_{i=1}^{n} EA_i \cdot M_i}{\sum_{i=1}^{n} M_i} \tag{2.28}$$

Investigating several Textile Reinforced Concrete sandwich panels (characterized by different reinforcement and slenderness), Shams et al. (2014a) found that model A accurately assesses the load-deflection behaviour taking into account the cracking of the concrete faces.

The analytical results are strongly affected by the shear stiffness of the core; the model used for deriving this stiffness is described in Hegger et al. (2011).

3

State-of-the-art of TRC

Textile Reinforced Concrete (TRC) is a composite cement-based material reinforced with Alkali Resistant (AR) glass, carbon or aramid fabrics. The combination of fabrics and fine-grained concrete, which in fact resembles more a mortar than a concrete, allows architects and engineers to design thin and lightweight structures characterized by a high load-bearing capacity in tension.

In the present work, AR-glass reinforcement is used because of its good performance to cost ratio. A picture of a TRC specimen reinforced with four layer of AR-glass fabric is shown in Figure 3.1. Each fabric is obtained by weaving filament yarns. One yarn consists of several hundreds up to thousands single filaments (see Figure 3.1 "AR-glass yarn").

AR-glass is able to resist the corrosive alkaline solution in the concrete thanks to its content of zircon (more than 15%). However, this reinforcement is not completely immune to degradation, hence the application of a proper coating is useful in order to guarantee the desired durability [Gries et al. (2006)].

The filament diameter ranges between 9 and 27 μm. The fineness of a yarn depends on the number of filaments, the average filament diameter and the fibre

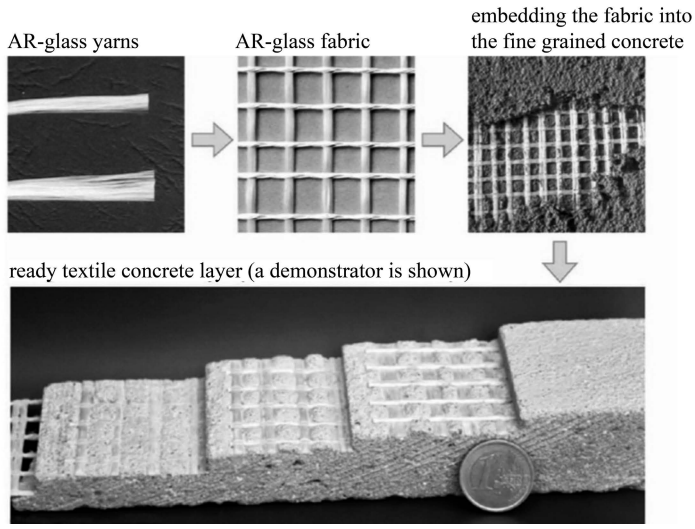

Figure 3.1: Textile Reinforced Concrete sample [Curbach and Sheerer (2011)].

density; this fineness is expressed in terms of Tex (gram per 1 km). Depending on the fineness, the mechanical properties of AR-glass yarn vary up to a tensile strength of 1400 MPa and up to an elongation equal to 2%. The modulus of elasticity is equal to 70-80 GPa. [Gries et al. (2006)]

Three main textile fabrics are applied in concrete as reinforcement [Gries et al. (2006)]:

- scrims, that are textile fabrics produced by superimposing thread systems, with or without fixing the crossing points;
- warp knits; the only difference with scrims is that the weft threads are inserted according to the mesh pattern (Figure 3.2(a));
- woven fabrics, that are fabrics manufactured by shedding two rectangular crossing thread systems, warp and weft. Different weaving patterns can be followed; a common woven fabric is the leno weave (Figure 3.2(b)).

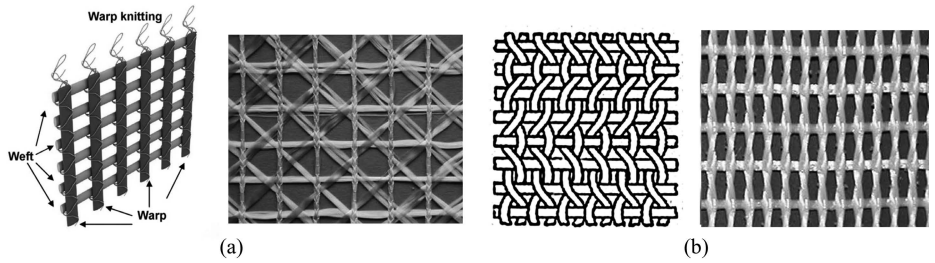

Figure 3.2: Warp knitting fabric [sketch by de Andrade Silva et al. (2011) and picture by Gries et al. (2006)] (a) and leno weave fabric [sketch by Peled (2013)](b).

The main advantages of Textile Reinforced Concrete are related to its durability and strength performance, since no cover against corrosion is required, while it is also possible to align fibres along the load direction. In particular, thanks to the bi-dimensionality of the fabrics, a bi-axial load can be supported easily by such a reinforced structure. Both new structures and existing buildings constitute the fields of application of this composite material [Curbach and Sheerer (2011), Horstmann et al. (2008), Hegger and Voss (2008)].

During the last ten years, the scientific community's growing interest in the technology has been demonstrated by the establishment of several research projects, the majority in Germany, Israel and the USA. In the last few years a research project focusing on TRC was also set up at the Politecnico di Milano, in Italy.

3.1 Tensile behaviour of TRC

As a composite material, the strength and ductility of TRC depend not only on those of its components, but also on the bond between reinforcement and matrix. Analysis of this bond is thus one of the main topics in TRC studies, because it affects both the peak load and the ultimate strain of the composite material due

to the brittleness of the AR glass reinforcement.

In the case of TRC, bond behaviour is quite different to that observed in steel reinforcement due to the inhomogeneity of the fibre cross-section.

The bond between steel bar and matrix in R/C is governed by several mechanisms, including adhesion, which is lost after the first slippage of the steel, friction, and the most efficient contribution of mechanical bonding in the form of bar ribs.

Textile reinforcement, on the other hand, is composed of thousands of filaments, only the most external of which are in contact with the matrix. In addition, only a part of the filaments is anchored in the cement paste and thus the inner filaments can slip easily within the roving. The bond may also be influenced by fabric coating. In Yarn-Matrix-Bond theory [Banholzer (2004)], developed from an experimental investigation into filament pull-out, the roving is schematized as a cylindrical structure comprised of concentric rings, each one composed of several filaments (Figure 3.3(a)). The roving failure mechanism is initiated by the failure of the outer filament ring, followed by that of each adjacent layer until reaching the core filaments at the ultimate collapse. The telescopic behaviour of the yarn during a pull-out test is shown in Figure 3.3(b).

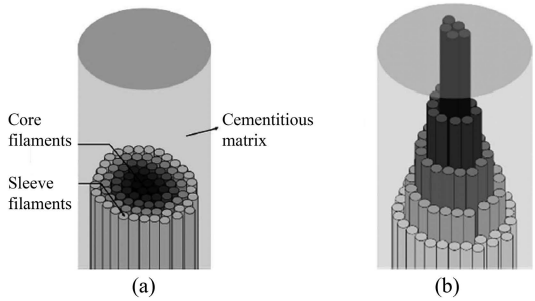

Figure 3.3: Idealization of a yarn embedded in a matrix (a) and telescopic failure of the yarn itself (b) [Cohen and Peled (2010)].

The bond in TRC can be affected by many factors, such as curing conditions and pressure applied after laminate casting [Mobasher et al. (2006)], fabrication technique [Peled et al. (2006)], fibre type and treatment of fibre surface [Peled et al. (2008)].

In particular, according to Mobasher et al. (2006), an increase of bond at matrix/fabric interface is observed when the matrix is fully hydrated and when a pressure is applied on the specimen after casting in order to facilitate matrix penetration in the fabric openings. Such increase in bonding may enhance the composite strength, but leads to the fabric failure prior to pull-out, thus reducing the composite ductility.

The pultrusion process used instead of the hand lay-up technique for the specimen production can enhance the bond properties, especially in the case of polyvinylalcohol (PVA) and polypropylene (PP) fabrics (Peled et al. (2006)).

The penetration of the matrix in between the filaments constituting each yarn is an essential requirement for a good bond. According to Peled et al. (2008), the more compact and dense is the bundle, the lower is the average bond strength, while a better penetrability results in an improved bond strength, as more filaments are in direct contact with the hydration products of the cement matrix (Figure 3.4(a)). The same results are confirmed by the pull-out load vs. slip curves shown in Figure 3.4(b).

Peled et al. (2008) also found out that the bond between PP fibres and cement matrix can be improved by treating the surface of the bundles through a proper detergent in order to help the fibre-matrix affinity.

Other researchers studied the bond phenomenon performing pull-out tests and developing several models [e.g. Butler et al. (2011), Soranakom and Mobasher (2009), Sueki et al. (2007), Zastrau et al. (2003)].

The typical non-linear tensile stress versus strain curve of Textile Reinforced Concrete is shown in Figure 3.5. As proposed by Hegger et al. (2004), this curve

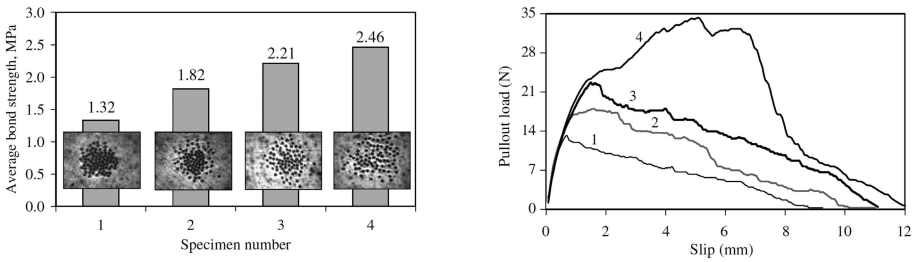

Figure 3.4: Average bond strength of four PP specimens whose cross-section is observed through optical microscope (a) and pull-out load vs. slip response of these PP specimens (b) [Peled et al. (2008)].

can be divided into three sections:

- a first linear branch (I, Figure 3.5), in which the material is un-cracked and the slope reflects the elastic modulus of the concrete. The contribution to stiffness offered by the reinforcement is negligible according to Ohno (1994);

- a non-linear response stage (II, Figure 3.5). Once the tensile strength of the matrix is reached, the whole force is transferred through the crack to the fabric (IIa). Thanks to the bond between textile and concrete, the reinforcement redistributes the load until the tensile strength of the matrix is reached in another section of the specimen, thus creating a new crack. Repetition of this process results in the formation of a multi-crack pattern along the specimen, the distance and width of which are strictly related to fabric geometry and to the bond between reinforcement and concrete. In Figure 3.5, multi-cracking occurs in the branch defined by a fairly constant load, with an increase in the total equivalent strain taking place due to multiple crack formation. Increasing the deformation, only the contribution of the fabric (IIb) is noticeable, with no further cracks appearing and the fabric strained upwards. Figure 3.5 also presents a comparison of the

behaviour of the fabric with that of TRC; the difference between the two curves is due to the tension stiffening effect;

- a final stage (III, Figure 3.5), defined by the failure of the AR-glass fabric when the textile reaches ultimate strain. The occurrence of this event depends on a series of parameters such as nature of fibre, fabric geometry, reinforcement ratio and bond phenomena. TRC reinforced with AR-glass fabrics does not experience the final plateau indicated by the dashed line, since the reinforcement is characterized by brittle failure without any plastic deformation.

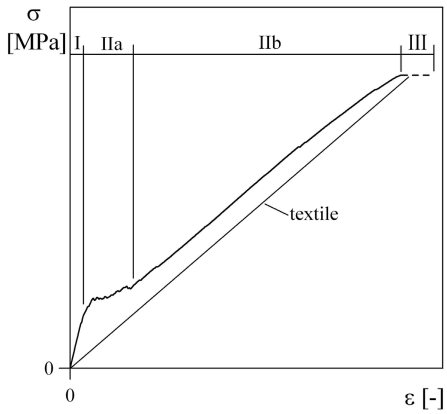

Figure 3.5: Tensile behaviour of Textile Reinforced Concrete, typical tensile stress vs. strain curve [after Hegger et al. (2004)].

3.2 Fields of application

TRC capabilities can be expressed both in the retrofitting of existing structures and in the design of new structural elements. All the examples collected in this Section refer to TRC reinforced with AR-glass fabrics, as this kind of reinforcement is the most diffuse thanks to its good performance/cost ratio.

Concerning existing buildings, the application of a thin layer of the composite on existing structures to improve their performances is one of the most promising use of Textile Reinforced Concrete. Mechtcherine (2013) underlines that repair layers have not only a strengthening, but also a protective function, as the fine crack pattern that characterizes TRC is beneficial for the protection of the concrete substrate; the protective function can be the main purpose of the repair measure. Possible applications in the framework of structural retrofitting are: R/C beams (Figure 3.6 (a)), columns (Figure 3.6 (b)), roof structures (Figure 3.6 (c)) and coupling beams.

The coupling beams represent a key element in braced structures when subjected to seismic actions, therefore their strengthening is crucial for the behaviour of buildings in seismic areas. To demonstrate the effectiveness of the TRC application on a real structure, a R/C coupling beam specimen was realized (1:2 scale size, Figure 3.7(a)) and tested at the Politecnico di Milano laboratories in the framework of the RELUIS project (REte dei Laboratori Universitari di Ingegneria Sismica) [Muhaxheri (2014)]. Both un-strengthened and retrofitted solutions were tested with monotonic and cyclic load. The coupling beam was 450 mm long, 300 mm high and 100 mm wide and was reinforced with $\phi 8$ longitudinal steel bars and $\phi 6$ stirrups 100 mm spaced. As visible in Figure 3.7(b) the strengthening with the used TRC implies, in the case of monotonic load, an increase of about 78% in terms of maximum peak load, enhancing slightly also the ductility.

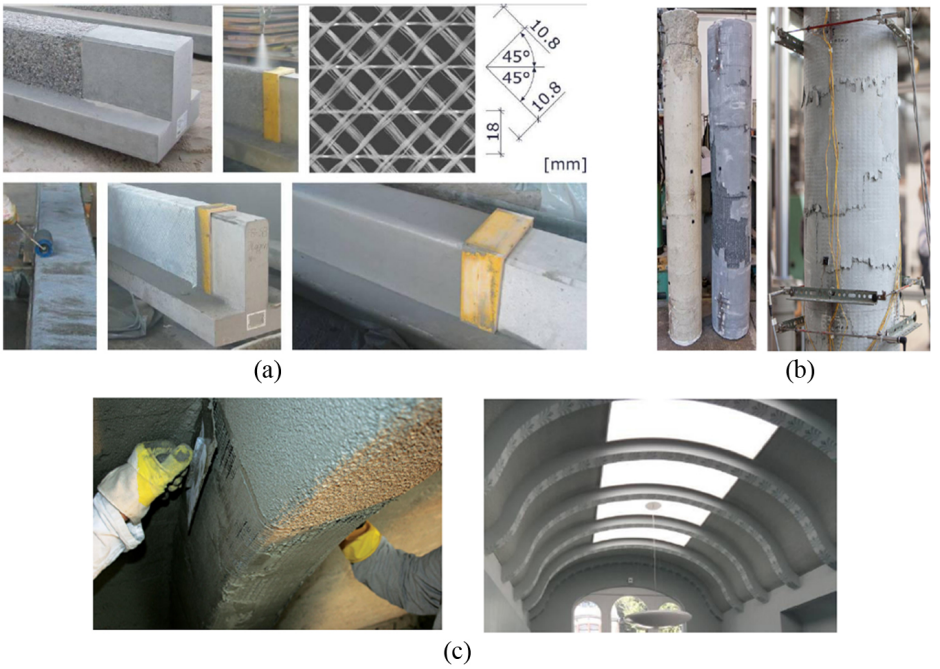

Figure 3.6: TRC used to retrofit a R/C beam (a), a R/C column (b) and a roof structure (c) [Curbach and Sheerer (2011)] .

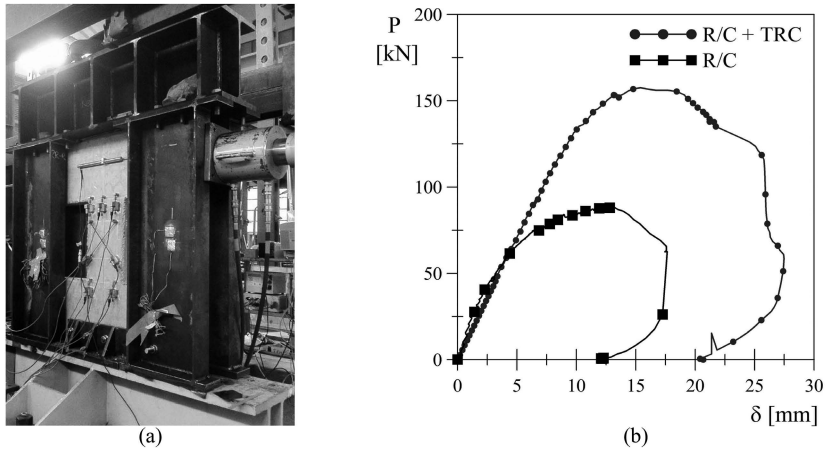

Figure 3.7: R/C coupling beam duting test (a) and load vs. stroke curves for unstrengthened and retrofitted coupling beam (b) [after Muhaxheri (2014)] .

The structures on which TRC is applied could be undamaged or damaged (e.g. because of an earthquake). An example of a pre-cracked R/C element retrofitted with TRC is shown in Figure 3.8. In order to obtain a good bond between the concrete and the applied TRC layer, the concrete surface has to be treated, e.g. through sandblast, or even better through water-pressure cleaning.

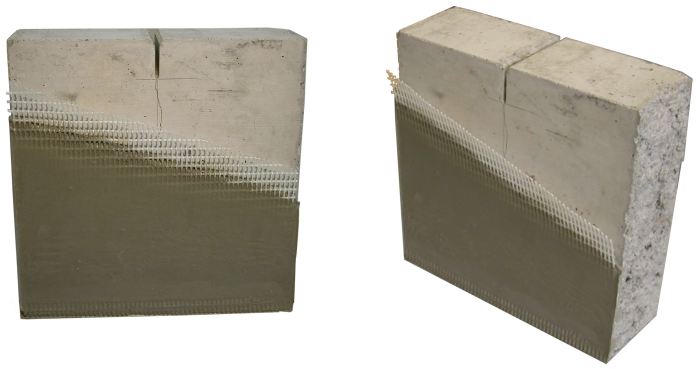

Figure 3.8: R/C element retrofitted with TRC.

To analyse the contribution of the retrofitting material in the post-crack behaviour, an innovative test technique was developed at Politecnico di Milano. This method, known as DEWS (Double Edge Wedge Splitting), was applied by Magri (2012) to investigate the effectiveness of two retrofitting materials, TRC and UHPFRC (Ultra High Performance Fiber Reinforced Concrete), when applied to 300x300x100 mm R/C plates (Figure 3.8), characterized by three different levels of damage: undamaged structure, element damaged at Serviceability Limit State and element damaged at Ultimate Limit State (crack opening w equal to 0, 0.3 and 3 mm respectively). Just 6 mm or 20 mm respectively of TRC or UHPFRC were applied to the existing structure. The DEWS technique is illustrated in Figure 3.9 together with the compression vectors developed in the specimen during the test.

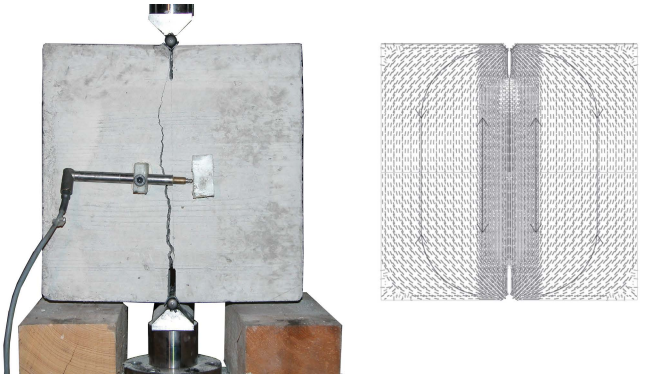

Figure 3.9: DEWS test on a R/C element [after Magri (2012)].

The main advantage of the DEWS technique is the possibility to create a pure tensile stress distribution along the ligament of the notched specimen, without any crosswise compressive stress, by applying a compressive load, thus avoiding the typical problems of direct tensile tests, e.g. gluing of steel plates on the specimen edges to distribute the stresses. This advantage characterizes also other indirect tensile tests, such as bending and Brazilian test, but the DEWS technique allows to minimize the structural effect and to compare the strengthened specimens with the un-strengthened one not only in terms of load, but also in terms of ductility. In particular, the ductility depends both on the retrofitting material deformation and on its delamination. When stresses are transferred from the support to the retrofitting layer, the latter could deform over the detachment length.

As can be seen in Figure 3.10, the effectiveness of the TRC retrofitting layer both in terms of peak load and ductility is visible in all the damage situations considered. In undamaged situations and at SLS the TRC solution proposed is even better than the UHPFRC one, even considering that TRC solution is 70% lighter and about 50% less expensive than UHPFRC. Due to the small thickness, delamination risk is strongly reduced with respect to UHPFRC and therefore no special devices are often required to fix the retrofitting layer to the support.

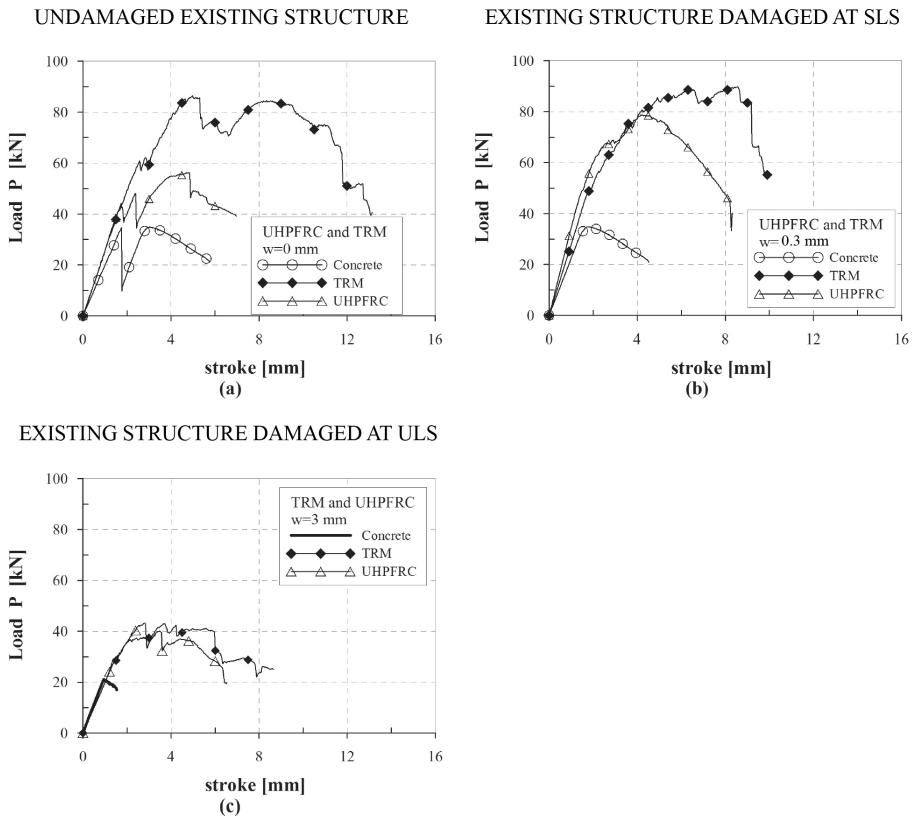

Figure 3.10: Results of DEWS test on R/C elements retrofitted with TRC and UHPFRC for different original crack openings ($w = 0, 0.3, 3mm$) [after Magri (2012)].

Concerning new structural elements, TRC can be used in the production of façade panels (Figure 3.11(a)), roof elements (Figure 3.11(b)), grid structures (Figure 3.11(c)), precast multi-layered roof and wall panels (Figure 3.12) and tunnel linings (Figure 3.13).

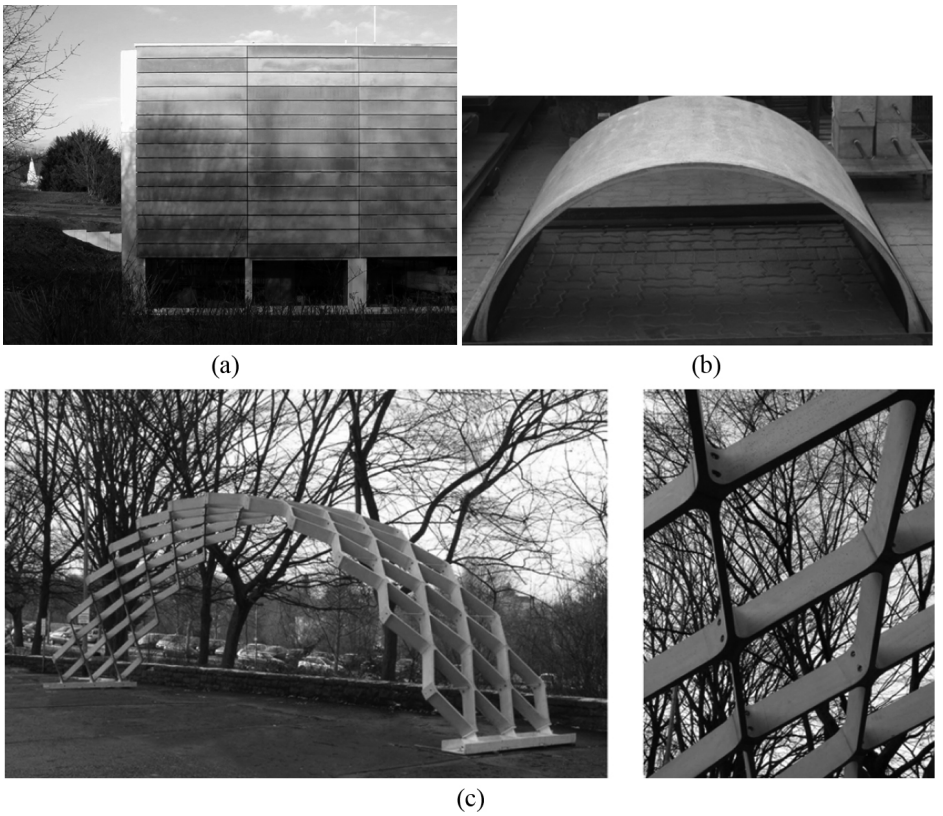

Figure 3.11: Façade TRC elements applied on the Institute of Structural Concrete at RWTH Aachen University, Germany (a), TRC barrel shell roof element (b) and TRC grid structure (c) [Hegger and Voss (2008)].

Figure 3.11(a) shows the first application of TRC in a ventilated building façade. This application was realized in 2002 on a building of the Institute of Structural Concrete in RWTH Aachen University. Each panel, 2385 *mm* long,

325 mm wide and 25 mm thick, is characterized by a weight of 57.5 kg/m^2 and is fixed to the reinforced concrete substructure through four anchorage points. The design is performed so that the elements remain un-cracked under service loads.

The barrel shell roof element shown in Figure 3.11(b) clearly points out the easiness of realizing complex geometries (such as curved shapes) by using Textile Reinforced Concrete. The prototype segment shown in the picture is characterized by length of 1.5 m.

The rhomboid grid structure, whose pictures are presented in Figure 3.11(c), is a prototype realized at RWTH Aachen University. Each rhomboid modulus has outer dimensions of 1000 x 600 x 160 mm; the thickness of the walls is equal to 25 mm and the weight is about 23 kg. The design was performed considering a supported glass roofing. The arch obtained assembling the rhomboid elements has a span of 10 m, an hight of the vault of 3 m and a width of 1.8 m.

Figure 3.12: Assembly of modular prototype TRC sandwich building [Hegger and Horstmann (2009)].

An entire modular prototype building was also assembled at RWTH Aachen University by using sandwich panels both for wall (1 x 2.82 m) and roof (1 x 4.73 m) elements (Figure 3.12). The sandwich cross-section is characterized by two

external layer in TRC 15 mm thick an by an internal insulation layer 150 mm thick.

Multi-layer roof sandwich elements made of UHPFRC, polystirene and TRC (25+80+6 mm) were studied at Politecnico di Milano [di Prisco and Zani (2012), Zani (2013)].

An example of a tunnel lining in which a layer of TRC is used is shown in Figure 3.13 . The multilayer element, investigated in the framework of the European A.C.C.I.D.E.N.T Project (Advanced Cementitious Composite In DEsign and coNstruction of safe Tunnel), is made of Steel Fiber Reinforced Concrete (SFRC) and High Performance Fiber Reinforced Concrete (HPFRC); one AR-glass fabric is embedded at the interface to enhance the performance during exceptional loads [di Prisco et al. (2013)].

Another interesting application, presented by Curbach and Sheerer (2011), is represented by TRC pedestrian bridges. An example is the 17 m long foot and bicycle bridge realized in Kempten in 2007 by joining 18 TRC u-shaped modular shell elements 30 mm thick. When all the segments were cast and aligned (Figure 3.14(a)), they were longitudinally pre-stressed; then the bridge was transported to its location and placed (Figure 3.14(b)).

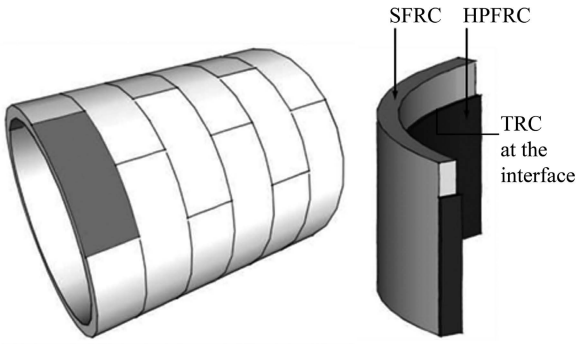

(a)

(b)

Figure 3.13: Multilayer tunnel lining: sketch of the geometry and stratigraphy (a) and prototype exposed to the MadeExpo exhibition (b) [di Prisco et al. (2013)].

(a)

(b)

Figure 3.14: U-shaped TRC pre-fabricated elements (a) and assembled bridge placed in Kempten (b) [Curbach and Sheerer (2011)].

3.3 Durability of TRC

As TRC is a structural material, its durability has to be proved in order to guarantee the maintenance of the mechanical response during the expected life time of the construction.

A number of researchers have developed durability models to quantify strength loss in textile reinforced composites resulting from AR-glass degradation problems and weathering conditions (humidity and temperature) [Orlowsky and Raupach (2008), Purnell and Beddows (2005)]. The durability model proposed by Orlowsky and Raupach (2008) allows to predict the strength loss over the life time of a TRC component stored outside in a certain clime. In the application proposed by the authors, a loss of about 37% is estimated for a TRC element stored in Aachen for 50 years. As underlined by the researchers, the higher the temperature and the water content, the higher the loss of strength. In fact, in the early summer, when it rains more frequently and the temperature are higher than in winter, the gradient of strength loss is steepest. Hence, the porosity of the matrix plays a key role in the durability of TRC.

Other researchers have focused on the effect of matrix composition (hydration kinetics and alkalinity) on TRC durability [Butler et al. (2010)], observing that an alkali reduced matrix exhibits strong performance even if exposed to accelerated ageing. The decrease in toughness with increasing alkalinity depends mainly on the formation of solid phases in the fabric-matrix interface, rather than on deterioration of the AR glass fabric.

When the TRC layer is exposed to an external environment, it can be subjected to freezing-thawing attack and its durability can be reduced. Some codes like ASTM International C666/C 666M - 03 "Standard Test Method for Resistance of Concrete to Rapid Freezing and Thawing" present methods to evaluate the freezing-thawing durability, but the main aim of these standards is to com-

pare different concrete mixes and not to quantify the expected service life due to material performance. In fact, as underlined by Neville (1996), it is difficult to define a correlation between the number of cycles performed in the lab and the service life of actual concrete because it is difficult to determine the number of cycles to which an element is exposed to, especially considering a south-facing exposure. *However, the ability of concrete to withstand a considerable number of laboratory freezing and thawing cycles (say 150) is a probable indication of its high degree of durability under service conditions* [Neville (1996)].

According to Neville (1996), freezing-thawing damage in concrete occurs when the dilating pressure due to freezing of water in the capillary pores exceeds the tensile strength of the material. It was found that gel pore water does not freeze above -20 ℃, hence only macroscopic water sucked up by capillary pores can freeze in standard service conditions [Setzer (1997)]. The expansion due to freezing causes an increase in volume of water of about 9% and the consequent expulsion of excess water; the pressure depends on the resistance to flow, related mainly on the permeability of the hardened cement paste (the higher the permeability the lower the pressure). An increasing of the total moisture content due to the diffusion of water during thawing caused by osmotic pressure magnifies the phenomenon. The repetition of freezing-thawing cycles leads to the development of pressure and its consequences.

The resistance of concrete to freezing-thawing phenomenon depends on the degree of saturation, the pore system of the hardened cement paste (distance to the nearest unfilled void), the permeability and the water to cement ratio.

If the concrete degree of saturation is below a certain threshold, the material is highly resistant to frost (dry concrete is totally unaffected). The critical saturation of concrete depends on the size of the body, its homogeneity and the rate of freezing. If excess water can be expelled into cavities closed enough to the pores in which ice is being formed, the material is characterized by no critical

saturation value. For conventional concrete, the use of a proper amount of an Air Entrained Agent (AEA) is essential because the air bubbles created in the paste can cut the water paths and provide additional space for the escape of excess water, preventing the development of the dilating pressure [Lomboy and Wang (2009)].

Low permeability and low water/binder ratio are other two fundamental properties that characterize a concrete with a high freezing-thawing resistance. High Strength Concrete (HSC), typically characterized by a water to binder ratio lower than 0.30 and by a very low permeability, is considerably less vulnerable to the freezing-thawing attack than conventional concrete [Sun et al. (1999) and Marzouk and Jiang (1994), respectively considering up to 500 and 700 cycles], even without using AEA [Lomboy and Wang (2009), Figure 3.15 (a)]. This is due to the fact that, on one side, a limited amount of water can penetrate into the concrete and, on the other side, the pores in HSC are very fine and the pore water is difficult to freeze. The reduced vulnerability of High Strength Concrete with respect to conventional concrete is also clearly visible in Figure 3.16, in which specimens cast without using AEA and treated with 300 cycles are shown: subfigure (a) refers to conventional concrete specimens (w/b = 0.55), while subfigure (b) refers to HSC specimens (w/b = 0.25).

It is still not clear if the use of AEA is necessary in the case of HSC to make it freezing-thawing resistant [Aitcin (2003)]: concerning this topic controversial results were obtained, as summarized by Wang et al. (2009), who found the reasons in the deficiency of standard test methods and in the differences in the mixing and curing methods adopted. However, experience has proven that the criteria adopted to classify a conventional concrete as freezing-thawing resistant (e.g. those proposed by Canadian Standard CSA A23.1) are too severe in the case of HSC [Aitcin (2003)]. In fact, using a proper mixture for HSC, it is possible to guarantee a very limited strength loss even without using AEA, as demonstrated

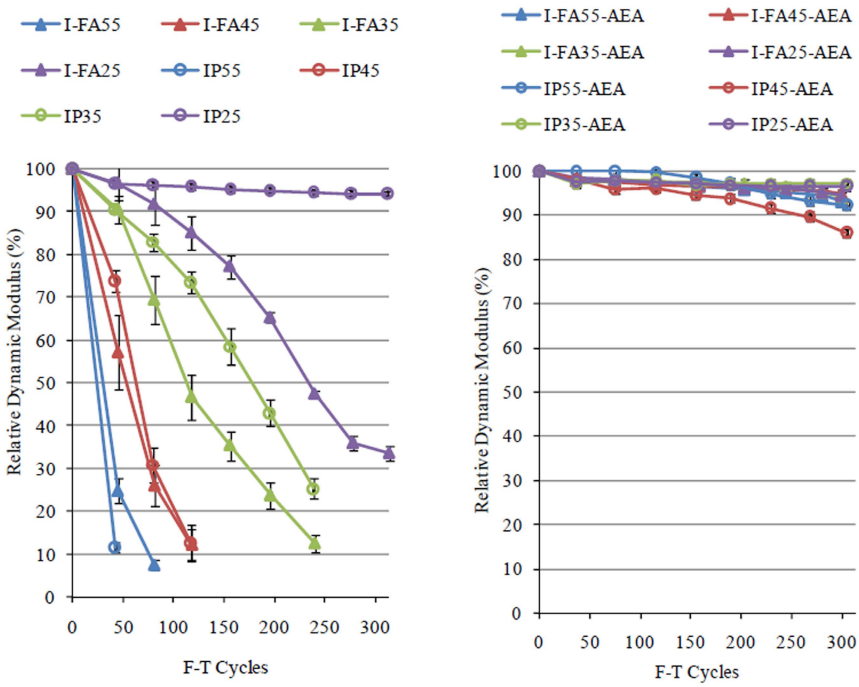

Figure 3.15: Relative Dynamic Modulus of concrete without (a) and with (b) AEA subjected to freezing-thwing cycles [Lomboy and Wang (2009)]. I-FA and IP refer to different mix design; for each mix, different water/binder ratio are considered (0.25, 0.35, 0.45 and 0.55).

Figure 3.16: Conventional concrete (a) and High Strength Concrete (b) specimens after the exposure to 300 cycles [Wang et al. (2009)].

by specimens IP25 in Figure 3.15 (a).

The combined action of load and freezing and thawing considerably reduces the number of cycles up to failure both for conventional and high strength concrete (Figure 3.17): the lower the grade of concrete, the lower the number of cycles sustained [Sun et al. (1999)].

Concerning cement based composites, few investigations of freezing-thawing behaviour can be found for fibre reinforced concrete [Graybeal and Tanesi (2007), Cavdar (2014), Sun et al. (1999)] (Figure 3.18), while no information are available on the mechanical performances of TRC in such condition. As already discussed, freezing and thawing can affect the cement paste and therefore the bond between fabric and mortar, that is the main mechanism governing the tensile behaviour of TRC.

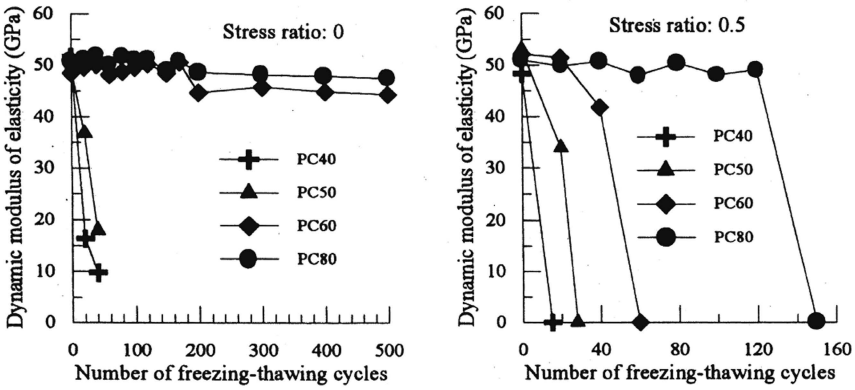

Figure 3.17: Loss of dynamic modulus of elasticity of Portland Cement concrete under the double action of load and freeze-thaw cycles - no stress (a) and stress ratio =0.5 (b). Strength grades: C40, C50, C60 and C80. [Sun et al. (1999)]

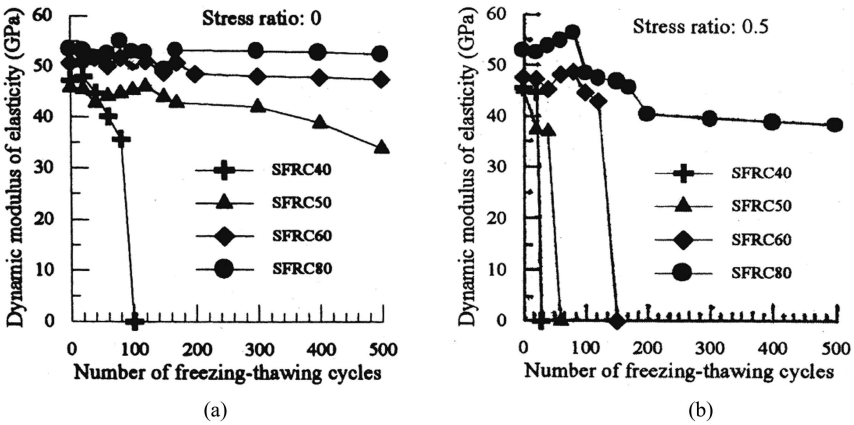

Figure 3.18: Loss of dynamic modulus of elasticity of Steel Fibre Reinforced Concrete under the double action of load and freeze-thaw cycles - no stress (a) and stress ratio =0.5 (b). Strength grades: C40, C50, C60 and C80. [Sun et al. (1999)]

4

TRC tensile behaviour

4.1 Tensile behaviour in standard conditions

This section presents the main results of an extended experimental campaign finalized at optimizing the tensile behaviour of Textile Reinforced Concrete and tries to answer to some very important questions raised by TRC users:

1. How do fabric geometry, position and reinforcement ratio affect the tensile behaviour of the composite?

2. Does composite curing method affect the final tensile behaviour of TRC?

3. Does strain rate play a key role in the definition of ductility and strength in uniaxial tensile behaviour?

4. TRC experiences a multicrack pattern and even global hardening response in some cases: is this size-effect dependent?

4.1.1 Materials

TRC specimens tested during the experimental investigation were created by reinforcing a high strength concrete with different layers of Alkali-Resistant glass fabric. Three types of fabric (named F1, F2 and F3) were used as reinforcement. The material properties are described below.

Matrix

A high strength concrete, characterized by a water to binder ratio of 0.19 and a maximum grain size of 600 μm, was used to cast the TRC specimens. The matrix mix design is summarized in Table 4.1.

Table 4.1: Mix design $w/(c+s) = 0.19$

Component	Content
Cement I 52.5	600 kg/m^3
Quarzite sand 0-600 μm	957 kg/m^3
Water	209 l/m^3
Superplasticizer	44*-56** kg/m^3
Slag	500 kg/m^3

* Specimens reinforced with fabric F1
** Specimens reinforced with fabric F2-F3-DS

The chemical composition, particle size and other characteristics of the slag are summarized in Table 4.2. The raw material comes entirely from the recovery of the iron furnaces silica-glass waste.

The maximum aggregate size and superplasticizer addition were designed to allow the matrix to flow through the mesh of the fabric; a high flowing capability should guarantee a good bond between fabric and concrete. Two superplasticizer contents were considered: 44 kg/m^3, used in case of reinforcement F1, and 56 kg/m^3, used in the case of reinforcements F2 and F3 in order to improve concrete

Table 4.2: Chemical composition, grain size and other characteristics of the slag

Chemical analysis	
Oxides	Content
SiO_2	39.00%
Al_2O_3	11.00%
Fe_2O_3	0.70%
TiO_2	0.55%
CaO	37.50%
MgO	8.30%
K_2O	0.30%
Na_2O	0.20%
MnO	0.80%
C	0.20%
S	1.00%
Mineralogy	Amorphous (glass)
Grain size	12 μm
Moisture	$< 0.1\%$
pH	7

workability, since dry sand (DS) was included in the recipe involving the latter two fabric types. A low relative humidity was obtained by keeping this sand in an oven for half an hour before manufacturing the specimens.

Following the European Standard for cement testing (UNI EN 196 - part 1, 2005), bending and compressive tests were carried out on prismatic specimens in order to quantify the mechanical properties of the matrix; Tables 4.3 and 4.4 display the bending tensile strength (f_{ctf}), tensile strength (f_{ctm}) and cubic compressive strength (f_{cc}) for both mix designs.

Tensile strength was deduced from the bending tensile strength via the formula proposed in the *fib* Model Code 2010:

$$f_{ctm} = A_{fl} \cdot f_{ctf} \tag{4.1}$$

Table 4.3: Bending, tensile and compressive strength - specimens reinforced with fabric F1 (superplasticizer 44 kg/m^3)

Specimen	*Batch*	$f_{ctf}[MPa]$	$f_{ctm}[MPa]$	$f_{cc}[MPa]$	
N1	1	14.98	6.63	114.81	103.6
N2	1	16.97	7.51	106.38	126.68
N3	1	17.86	7.9	107.03	107.63
N4	2	19.51	8.63	99.74	108.53
N5	2	19.15	8.47	114.33	113.05
N6	2	20.72	9.17	114.71	121.11
Average		18.2	8.05	111.46	
STD		2.05	0.91	7.54	
STD%		11.25	11.25	6.76	

Table 4.4: Bending, tensile and compressive strength - specimens reinforced with fabrics F2 and F3 (superplasticizer 56 kg/m^3, DS)

Specimen	*Batch*	$f_{ctf}[MPa]$	$f_{ctm}[MPa]$	$f_{cc}[MPa]$	
N1	4	13.82	6.1	98.69	114.29
N2	4	17.45	7.7	103.23	107.47
N3	5	11.76	5.2	94.9	92.38
N4	5	12.32	5.45	97.92	80.34
N5	5	13.58	6	94.22	94.86
N6	6	13.65	6.03	103.26	95.79
N7	6	12.72	5.63	92.39	93.01
N8	6	13.62	6.02	97.43	100.55
Average		13.62	6.02	97.54	
STD		1.72	0.76	7.54	
STD %		12.62	12.62	7.73	

with:

$$A_{fl} = \frac{\alpha_{fl} \cdot h_b^{0.7}}{1 + \alpha_{fl} \cdot h_b^{0.7}} \tag{4.2}$$

where h_b is the beam depth, equal to 40 mm, and α_{fl} is a coefficient that decreases with increasing concrete brittleness. This coefficient was considered here to be equal to 0.06 as suggested for normal strength concrete ($A_{fl} = 0.44$); however, for high strength concrete such as the one used in the present study, its value is expected to be lower.

The tensile strength f_{ctm} of batch 6 as deduced from the bending test (Table 4.4) was compared with the strength value obtained by testing, in direct tension, 400 x 70 x 6 mm plain concrete specimens cast in the same batch; these specimens had the same sizes as the tested TRC samples. Through indirect measurement, the average value, obtained as discussed before ($\alpha_{fl} = 0.06$), was found to be equal to 6.02 MPa. In contrast, direct measurement resulted in a value of 4.77 MPa, albeit with greater scatter (22%). These results justify the necessity of employing a lower value of α_{fl}, as suggested in the *fib* Model Code 2010; a value of α_{fl} equal to 0.04 should provide a reliable prediction of tensile strength ($A_{fl} = 0.35$).

According to Model Code 1990 and Müller et al. (2008) a value of A_{fl} equal to 0.30 can be computed, taking into account the characteristic length of the considered concrete.

Table 4.4 reveals that the inclusion of dry sand resulted in a decrease in material strength of about 25% for tension and 12% for compression. This is probably related to the lower water to binder ratio, not all the cement is hydrated, and to the higher air voids content.

Fabric

Three different fabrics (F1, F2 and F3) were used to reinforce the TRC specimens (Figure 4.1). The geometrical and mechanical properties of each fabric are summarized in Table 4.5. The choice of these three fabrics was made after performing several investigations aimed at optimizing performance in terms of the ductility of the composite material, the bond between matrix and fabric, and internal filament slip. The variables considered in the preliminary study were fabric geometry (warp and weft spacing and their cross-section), fabric weaving and fabric coating, with the ultimate aim being to achieve maximum TRC strength and ductility.

The best results were obtained using tight warp and weft spacing, the leno weave fabrication technique and a coated (rather than uncoated) fabric.

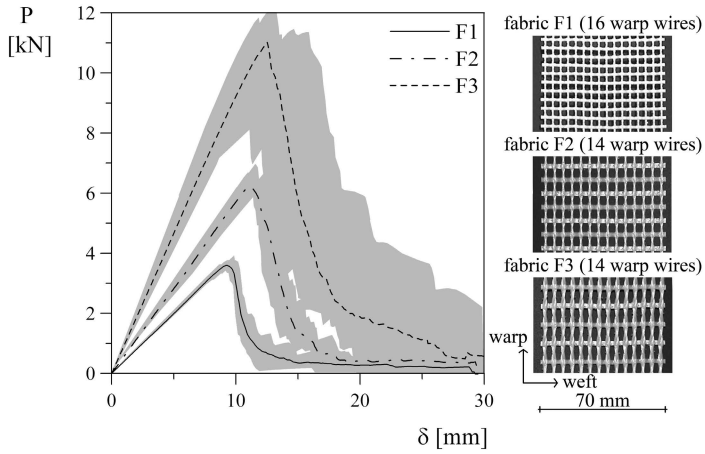

Figure 4.1: Uniaxial tension test results: load vs. displacement average curves for fabrics F1, F2 and F3.

For each kind of reinforcement considered, ten uniaxial tensile tests were performed in order to characterize fabric tensile behaviour. These tensile tests were

Table 4.5: Geometrical and mechanical characteristics of fabrics

	$F1$	$F2$	$F3$
Material	AR-glass	AR-glass	AR-glass
Coating	SBR* water resin	SBR* water resin	SBR* water resin
Fabrication technique	Leno weave	Leno weave	Leno weave
Warp wire spacing $[mm]$	4.4	4.9	4.9
Weft wire spacing $[mm]$	5	7.1	10.1
Warp $[Tex^{**}]$	2 x 320	2 x 640	2 x 1200
Weft $[Tex^{**}]$	640	1200	1200
Warp filament diameter $[\mu m]$	14	14	19
Weft filament diameter $[\mu m]$	14	19	19
Max. tensile load on 70 mm $[kN]^{***}$	3.67	6.58	11.02

* SBR=Styrene-Butadiene Rubber
** 1 Tex = 1g/km
*** Average value of 10 tensile tests

carried out using an INSTRON 5867 electromechanical press with a maximum load capacity of 30 kN. Specimens 400 mm x 70 mm in size were clamped to the machine, with five layers of adhesive paper tape applied to the upper and lower ends of each sample to prevent slip between clamps and fabric. The pressure applied to the pneumatic clamps was equal to 5.8 MPa for fabric F1 and 8.5 MPa for fabric F3. The tests were displacement-controlled by imposing a constant stroke rate of 100 mm/min. Load-displacement curves are shown in Figure 4.1.

Nominal stress was calculated by dividing the maximum tensile load by the nominal area of warp roving (considering the amount of warp roving in each fabric). The nominal stresses for each fabric were respectively equal to 896 MPa for F1, 918 MPa for F2 and 820 MPa for F3. The huge scattering observed in Figure 4.1, with reference to fabric F3, is mainly dependent on the relatively reduced clamping pressure when compared to the peak load measured. A possible sliding could affect the peak strain and therefore can be regarded as the main responsible for the quite high dispersion in the softening regime.

According to Curbach and Jesse (1999) the tensile strength of a filament with diameter 13.5 μm (used in 310 and 620 tex yarn) is about 2300 MPa, whereas

the strength of the corresponding yarn is about 1400 MPa, representing a loss of about 40%. In contrast, the loss in strength realized when using a filament with diameter 16.0 μm (used in 1100 tex yarn) is about 70%, from 2100 MPa to 600 MPa. Possible reasons for this, according to Curbach and Jesse, are the non-uniform distribution of the load between the filaments inside the yarn and the presence of defects. In the present study, a loss in strength of about 55-60% was computed both for 14 μm diameter filaments of fabrics F1 and F2, and for 19 μm filaments of fabric F3, with respect to the filament strength obtained by linear interpolation from the results of Curbach and Jesse (14 μm: 2260 MPa and 19 μm: 1912 MPa). For the lower filament diameter, the strength loss was higher than that observed by Curbach and Jesse. This could be due to a structural effect in fabric manufacture during which filaments are weaved and twisted, thus leading to possible damage.

4.1.2 Specimens preparation and test set-up

Specimen preparation

The method of manufacture employed to produce the specimens was the hand lay-up technique (Figure 4.2(a)), which is characterized by the exertion of a negligible pressure during production. A proper formwork with a transparent bottom plate was used in order to check by visible inspection the penetration of the matrix into the fabric mesh. A number of overlapping steel rails were used as separation layers in-between the different textile layers (Figure 4.2(b)). A suitable amount of concrete was spread onto the formwork bottom plate and smoothed with a roller to remove any air bubbles, with the reinforcement positioned tight and fixed at the edge. This procedure was then repeated to create a multilayer specimen.

The specimens used in the experimental investigation were reinforced according to three different procedures, as shown in Figure 4.3:

- one single fabric between two concrete layers;
- two fabrics (in direct contact with each other) between concrete;
- two single fabric layers divided by a 2 *mm*-thick layer of concrete.

In all cases the warp was parallel to the long side of the specimen.

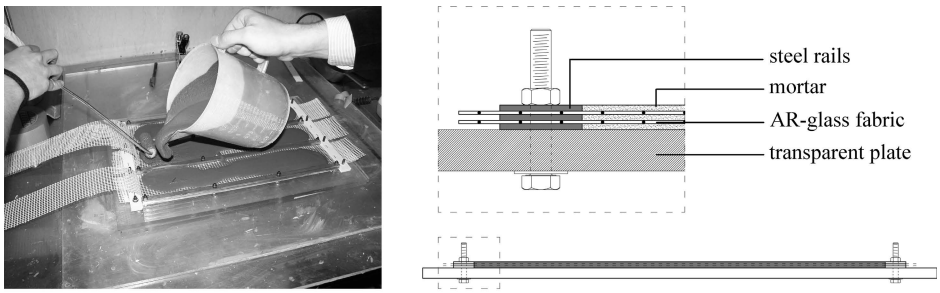

Figure 4.2: Specimen preparation (a) and section of the specimen in the formwork (b).

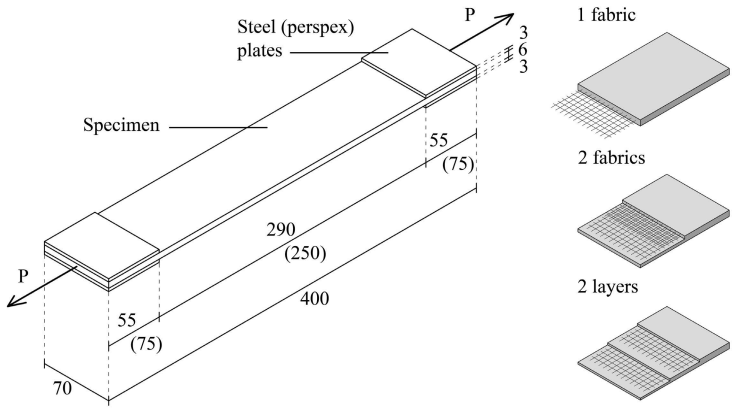

Figure 4.3: Specimen geometry and reinforcement layout (measurements in mm; measurements in brackets refer to perspex plate solution).

The obtained specimens were 400 *mm* long, 70 *mm* wide and 6 *mm* thick

(Figure 4.3), with at least three nominally identical specimens manufactured for each test. After one day in a climate chamber at 98% RH, specimens were demoulded and cured in a wet environment (RH $>$ 98%) for 28 days until being tested. Keeping the specimens in this wet environment ensured the avoidance of any loss in planarity arising from non-uniform shrinkage.

Test set-up

TRC specimens were tested using the same electromechanical press employed for the fabric tensile tests (Figure 4.4). A pressure ranging between 3.9 and 5.6 MPa was applied to clamp the specimen edges, while 3 mm thick plates were glued to the surface of the specimen at the grips to better distribute the clamping pressure and thus minimize damage associated with local crushing; 75 x 70 mm perspex plates were used with F1, and 55 x 70 mm steel plates were used with F2 and F3 (Figure 4.3). To prevent torsional and bending moments caused by misalignment of the constraints, spherical joints were placed at the ends. Spherical joints were always used for F1 specimens because the peak load never surpassed 8 kN. For higher peak loads the specimens could use only backlashes of the clamping devices, thus preventing precise detection of first cracking strength.

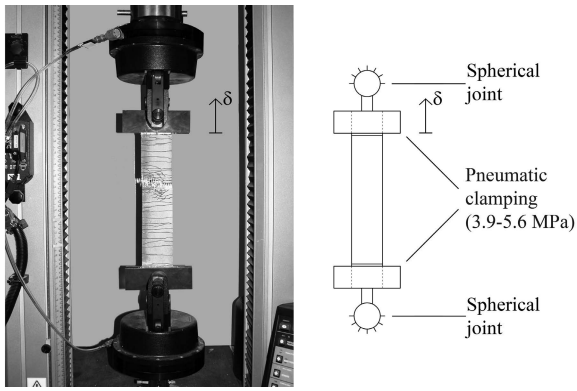

Figure 4.4: Tensile test set-up.

The tests were displacement-controlled by imposing a constant stroke rate of 0.02 mm/sec.

In terms of clamping, according to Hartig et al. (2012), this type of set-up involving glued steel plates can be classified as "rigid load application": concrete cracking is prevented within the supported range, while the main transfer mechanism between specimen and clamping device is adhesive tension and shear. On the contrary, in terms of displacements allowed at the ends, it might be classified as a rotating end uniaxial tension apparatus.

4.1.3 Main experimental results

In this section the main experimental results achieved in this experimental campaign are collected. A complete discussion concerning this results can be found in Colombo et al. (2013).

Influence of fabric position, reinforcement ratio and geometry

In order to understand the influence of fabric position and reinforcement ratio on the TRC tensile behaviour, different fabric types (F1, F2 and F3) are combined according to the different configurations shown in Figure 4.3. The tested solutions are:

- F1 - 1 fabric; F1 - 2 fabrics; F1 - 2 layers;
- F2 - 1 fabric; F2 - 2 fabrics; F2 - 2 layers;
- F3 - 1 fabric.

The achieved geometric reinforcement ratios (A_f/A_c, where A_f is the equivalent section area of reinforcement and A_c is the specimen cross-section) are collected in Table 4.6. The equivalent section area of reinforcement (A_f) was computed in terms of the Tex of each single roving, the number (n) of rovings

across specimen width (16 for F1 and 14 for both F2 and F3) and the AR-glass density (ρ):

$$A_f = \frac{n \cdot Tex}{\rho} \tag{4.3}$$

Table 4.6: Nominal reinforcement ratio for specimens reinforced with fabrics F1, F2 and F3

Fabric	1 *fabric*	2 *fabrics*	2 *layers*
F1	0.97%	1.94%	1.94%
F2	1.71%	3.42%	3.42%
F3	3.20%	-	-

The results of tensile tests on these specimens are shown in Figures 4.5, 4.6 and 4.7 by means of nominal stress (σ) vs. normalized displacement (δ/l) curves. Nominal stress was obtained by dividing the load by specimen cross-section, whereas normalized displacement was calculated as the applied stroke displacement (δ) divided by the initial distance between clamping edges. It is worth noting that each average curve in every graph is interrupted when the first of the three nominally identical specimens reaches the ultimate normalized displacement; as a result, the peak of the average curve differs from the average peak value. For each configuration the average curve of 3 nominally identical tests is shown together with a shadowed area representing result scatter, while typical cracking patterns are displayed to the right.

In the case of the F1 - 1 fabric test (Figure 4.5), the second and third branches typical of TRC multi-cracking behaviour (Figure 3.5) are absent. Analysis of the cracking pattern reveals that just few cracks appeared in the specimens; this is likely the result of a release of energy at the onset of cracking that was too large to allow stress redistribution between concrete and reinforcement, thus causing the failure of the composite itself. This situation is similar to that occurring in

an R/C section characterized by minimum reinforcement endowed by negligible ductility.

In the F1 - 2 fabrics scenario, bond failure prevented the onset of stage IIb (Figure 3.5) despite the increase in total reinforcement, resulting in progressive sliding of the fabric as highlighted by the longer IIa branch.

For F1 - 2 layers, typical TRC behaviour was achieved, with a very dense cracking pattern exhibited.

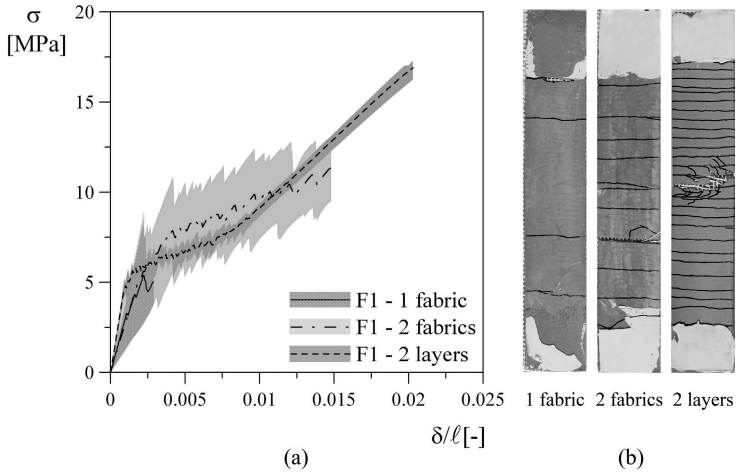

Figure 4.5: TRC reinforced with fabric F1. Nominal stress vs. normalized displacement curves in uniaxial tension (a) and specimen cracking pattern (b).

The same behaviour is evident in Figure 4.6 for both F2 - 2 fabrics and F2 - 2 layers. The solutions have the same reinforcement ratio and experience a similar cracking pattern and ultimate strain. However, the use of 2 layers resulted in a higher tensile strength due to the better bond guaranteed by the concrete layer between the two fabrics. When two fabrics are in contact, the area of the matrix-fabric interface decreases and sliding takes place. Bonding thus has a significant effect on the composite material, determining both its strength and ductility.

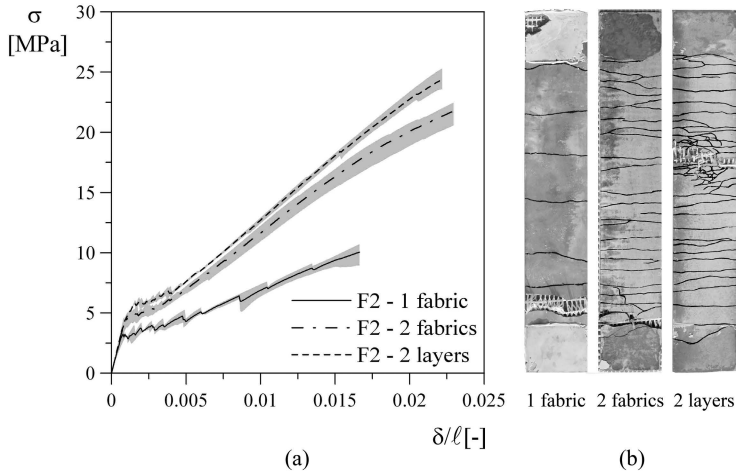

Figure 4.6: TRC reinforced with fabric F2. Nominal stress vs. normalized displacement curves in uniaxial tension (a) and specimen cracking pattern (b).

As with every composite material, the load-bearing capacity is strictly connected to the bond behaviour of the reinforcing material, with strong and weak bonds associated with brittle to ductile behaviour, respectively.

According to several research investigations, the easiest way to highlight bond failure is via computation of the peak load of the AR-glass fabric, with and without the matrix. This method reflects the extremely fine matrix used which prevents any significant contribution from aggregate interlocking after cracking, as well as the lack of any random fibre contribution due to the presence of the fabric as the only reinforcement. In the present study, an Effectiveness Factor (EF) was determined by dividing F1 - 2 fabrics peak load by twice the peak load experimentally calculated by stretching only fabric F1. If EF is less than 1 (as in this case), a bond weakness is immediately highlighted, whereas values of EF larger than unity indicate the occurrence of a positive interaction with the matrix which exerts a tension stiffening effect. The computed average EF factors for each fabric type and configuration are shown in Table 4.7.

Table 4.7: Average Effectiveness Factor for each fabric type and configuration

Fabric	1 *fabric*	2 *fabrics*	2 *layers*
F1	1.00	0.91	1.07
F2	0.76	0.83	0.81
F3	0.68	-	-

The 2 layers configuration generally resulted in a higher TRC strength than the 2 fabrics configuration. This likely reflects the fact that, despite having the same reinforcement ratio, the former has a larger contact surface area between matrix and reinforcement. The change from 2 fabrics to 2 layers led to an increase in TRC tensile strength from 13.52 MPa to 17.88 MPa for fabric F1, and from 22.37 MPa to 24.42 MPa for fabric F2. Crack distance decreased with increasing reinforcement ratio until cracking appeared at each weft roving, maximizing the mechanical performance of the composite (Figures 4.5(b) and 4.6(b)). The ultimate strains reached in the 2 fabrics and 2 layers configurations were comparable, and both greater than 2%. When typical TRC behaviour was achieved, all tests exhibited good repeatability, with a peak load scattering (maximum distance from the average value) always less than 2% .

Fabric F3, characterized by a cross-sectional area equal to 94% of that represented by two F2 fabrics, was also analyzed. A comparison between the results achieved using two layers of fabric F2 and those using one central layer of fabric F3 is presented in Figure 4.7(a). As can be seen from this figure, a multicracking phase occurred after the first linear branch in both cases. However, the first cracking strength for fabric F2 was higher than that for fabric F3; this difference is comparable to inter-batch variation in concrete tensile strength and is accompanied by a further decrease in EF to 0.68 (Table 4.7). This EF decrease also affected the stiffness of the last branch, in which no further cracking occurred. The peak strength reached was equal to 25 MPa for F2 and 15 MPa for F3,

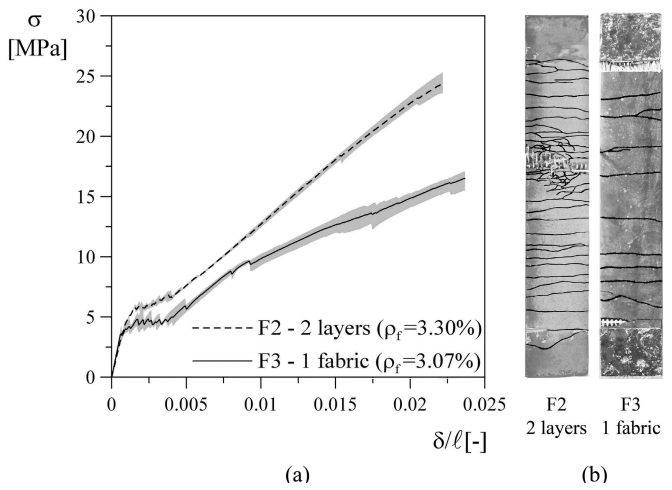

Figure 4.7: Comparison between TRC reinforced with fabric F2 - 2 layers and fabric F3 - 1 fabric (similar ρ_f). Nominal stress vs. normalized displacement curves in uniaxial tension (a) and specimen cracking pattern (b).

while the ultimate strain was greater than 2%. The cracking pattern observed in F3 samples was characterized by a larger distance between cracks (about every 30 mm, Figure 4.7(b)). The bond area in contact with the cementitious matrix was significantly larger in the case of 2 layers, resulting in the roving being better anchored to the matrix.

In order to investigate the influence of fabric weft on the TRC behaviour, fabrics with the same warp and weft cross-section, warp spacing, but different weft spacing were investigated, with four weft spacings in fabric F3 considered: 10, 20, 30 and 50 mm. Three nominally identical tests were performed on as many specimens reinforced with each of these fabric-spacing types. The obtained results in terms of nominal stress versus normalized displacement are reported in Figure 4.8(a).

The lowest first cracking strength was observed in specimens containing fabric with the smallest weft spacing (about 3 MPa), because of the reduced effective

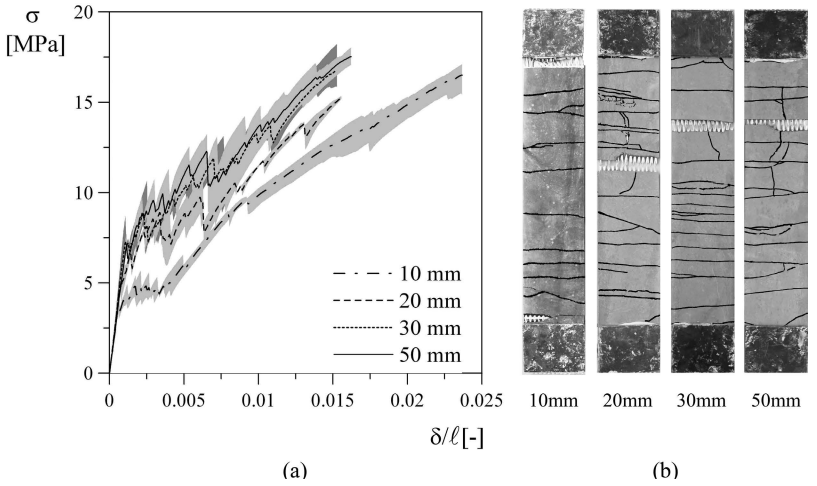

Figure 4.8: Influence of fabric geometry (different weft spacing) for specimens reinforced with F3 - 1 fabric: nominal stress vs. normalized displacement curves in uniaxial tension (a) and specimen cracking pattern (b).

tension stiffening induced along the warp. In terms of bond effectiveness the weft can play a double role: on one hand it can act as a direct anchorage to warp sliding, while on the other hand it may represent a defect in the matrix cross-section that could favour both warp delamination and/or crack propagation in the weft direction. In fabrics with small weft spacing, the weft defect action prevailed over the contribution of weft as direct anchor. In contrast, when weft spacing was wider the tension stiffening action prevailed, with first cracking strength reaching values of around 7 MPa. In the case of 30 mm and 50 mm weft spacing, the stiffness of the multicracking branch was higher because the process of longitudinal delamination was prevented by the presence of a longer bond length. In terms of ductility, specimens with 10 mm weft spacing were characterized by larger ultimate strain because longitudinal crack propagation, caused by the dense presence of weft-derived defects, allowed the roving to stretch and expand. Analysis of Figure 4.8(b), which shows the different cracking pat-

terns, reveals that cracks also appeared between the weft rovings in the 30 mm weft spacing specimens. Significantly, the peak load was roughly the same for all weft spacing configurations: weft spacing variation thus affects only tension stiffening and not the value of the Effectiveness Factor (EF).

Influence of curing method

A variety of curing methods were investigated in order to analyze the influence of different shrinkage conditions on the bonding mechanism. Specimens 400 x 70 x 6 mm^3 in size and reinforced with F3 - 1 fabric (reinforcement ratio equal to 3.07%) were cured using one of three methods: water or air for 28 days, and 6 days in air at 60 ℃. The latter scenario corresponds to a curing time of 28 days when the *fib* Model Code 2010 strength-time curve valid for concrete is assumed. The obtained results in terms of stress versus nominal displacement curves are shown in Figure 4.9.

Specimens cured in water exhibited the lowest first cracking strength and a final branch with the lowest stiffness. One possible reason for this is that the water penetration between roving and matrix makes telescopic failure easier, damages the fabric and reduces the bond strength.

The samples cured in free air exhibited the best performance in terms of first cracking strength, ultimate tensile strength and cracking pattern (Figure 4.9(b)); this phenomenon can be explained by the more significant shrinkage produced using this method, which improves the bond between matrix and fabric. As a matter of fact, looking at the matrix interface sleeve in which the glass roving is embedded, when the concrete is subjected to a contraction due to shrinkage, a normal stress takes place and consequently friction increases. The first cracking strength obtained in this case is comparable with the value of tensile strength f_{ctm} deduced by bending tests (around 6 MPa - Table 4.4).

The average curve for specimens cured at 60 ℃ for 6 days falls between those

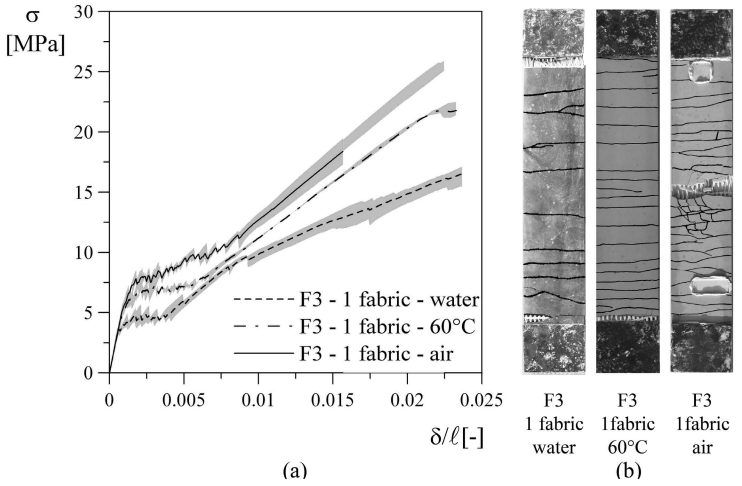

Figure 4.9: Influence of curing conditions on F3 - 1 fabric specimens: nominal stress vs. normalized displacement curves in uniaxial tension (a) and specimen cracking pattern (b).

of the two other methods. This intermediate behaviour reflects the shrinkage compensation obtained via oven curing and the slow initial hydration of slag [Neville (1996)].

Strain-rate effect

The mechanical behaviour of cement-based materials is known to be widely dependent on strain rate. Although several experiments have been performed on concretes and fibre-reinforced cementitious composites (looking at impact problems at different strain rates), relatively few have considered the creep effect in TRC [e.g. de Andrade Silva et al. (2011)]. The displacement rate commonly adopted by TRC researchers - and also used in all the other tests presented in this chapter - is equal to $2 \cdot 10^{-2} \quad mm/s$.

In order to understand the influence of strain rate on TRC behaviour in static and quasi-static regimes, different displacement rates, corresponding to different

strain rates, were considered. In particular, in addition to the usual stroke rate, two other displacement rates were analyzed (two orders of magnitude higher and lower, respectively):

- $2 \quad mm/s \quad (0.69 \cdot 10^{-2} \quad s^{-1})$;
- $2 \cdot 10^{-2} \quad mm/s \quad (0.69 \cdot 10^{-4} \quad s^{1})$;
- $2 \cdot 10^{-4} \quad mm/s \quad (0.69 \cdot 10^{-6} \quad s^{-1})$.

The strain rates (in brackets) were obtained by dividing the displacement rate by the average gauge length of the specimens (e.g. 290 mm).

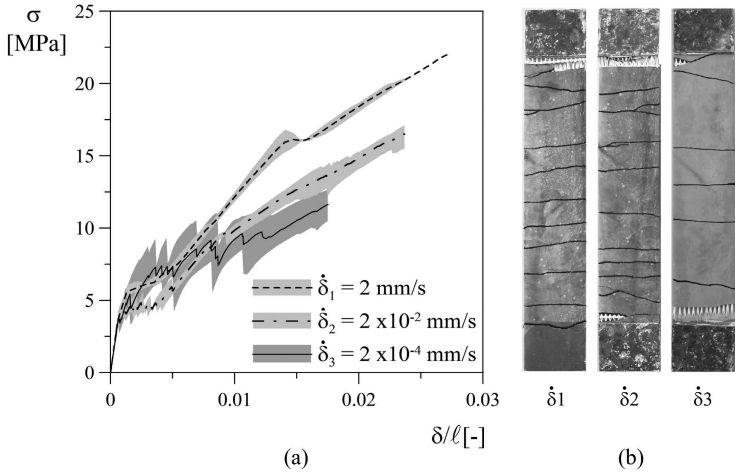

Figure 4.10: Influence of test displacement rate for F3 - 1 fabric specimens. Nominal stress vs. normalized displacement curves in uniaxial tension (a) and specimen cracking pattern (b).

For each displacement rate, three specimens reinforced with F3 - 1 fabric were tested; the obtained results are shown in Figure 4.10 in terms of average stress versus normalised displacement curves and representative specimen crack patterns for each displacement rate.

At the higher displacement rate (2 mm/s), typical TRC behaviour was observed, i.e. characterized by 3 branches. The first of these corresponded to linear-elastic behaviour, and was followed by the formation of multiple cracking after the occurrence of first cracking at around 6.4 MPa; during the final stage, after a low stress increase, the cracks widened until specimen failure. In all specimens, but especially in numbers 2 and 3, a change in stiffness at about 16 MPa of nominal stress was observed. Significantly, the final slopes of all the strain rates investigated were almost identical.

Typical TRC behaviour was also observed at the intermediate displacement rate ($2 \cdot 10^{-2}$ mm/s), the speed most commonly employed in TRC tensile tests. In this case the second phase started at a lower stress value (about 4 MPa), while the peak stress reached was lower in comparison to that seen at the higher displacement rate (about 17 MPa and 22.4 MPa, respectively).

For the lowest displacement rate considered ($2 \cdot 10^{-4}$ mm/s) the 3 branches could not be clearly identified, with only a multicracking phase up to failure observed after an initial linear-elastic phase. At this displacement rate, a reduction in bond strength between matrix and fabric was observed after the occurrence of first cracking (at 3.7 to 5.1 MPa), followed by sliding. The strength reached in this last test was close to 13 MPa.

Looking at the results, a loss in strength and ductility with decreasing displacement rate is apparent. In addition, a coarser specimen cracking pattern was exhibited with the decrease from 10^{-2} to 10^{-6} s^{-1}, while a strength reduction of around 23.5% was observed after the displacement rate was decreased from 10^{-2} to 10^{-4} s^{-1} and from 10^{4} to 10^{-6} s^{-1}.

The significant role played by strain rate in the tensile behaviour of TRC could be due to creep effect related to both the glass material employed and the interface bond strength. Further research is thus required to better understand the role of each mechanism.

Size effect

In order to appreciate the role of the size effect in uniaxial tension hardening derived from the multicracking phenomenon controlled by bond effectiveness, three different specimen lengths were investigated: 290, 150 and 75 mm. All specimens were reinforced with F3 - 1 fabric (reinforcement ratio equal to 3.07%), with the results presented in Figure 4.11. Figure 4.11(a) shows that all the average curves obtained for the different lengths overlap for displacement values lower than 0.2 mm. This likely reflects the fact that the displacement measured by the mechanical press is expressed as the sum of two components: specimen elongation and specimen sliding in the clamps. In fact, in the first linear-elastic branch the contribution of sliding predominates, so the curves appear to overlap. However, closer analysis of the stress vs. normalised displacement curves obtained by dividing relative displacement by free length reveals variation in specimen initial stiffness (Figure 4.11(b)). As a result, although the initial slope of the nominal stress versus normalized displacement curves should represent the elastic modulus of the concrete, which was the same for all specimens, the results are altered due to specimen sliding between the clamps. With reference to post-cracking behaviour, the curves reveal tension stiffening to be controlled by specimen length: the longer the specimen, the smaller the ductility. A finer cracking pattern (Figure 4.11(c)) was observed in shorter specimens, correlating with the previous results.

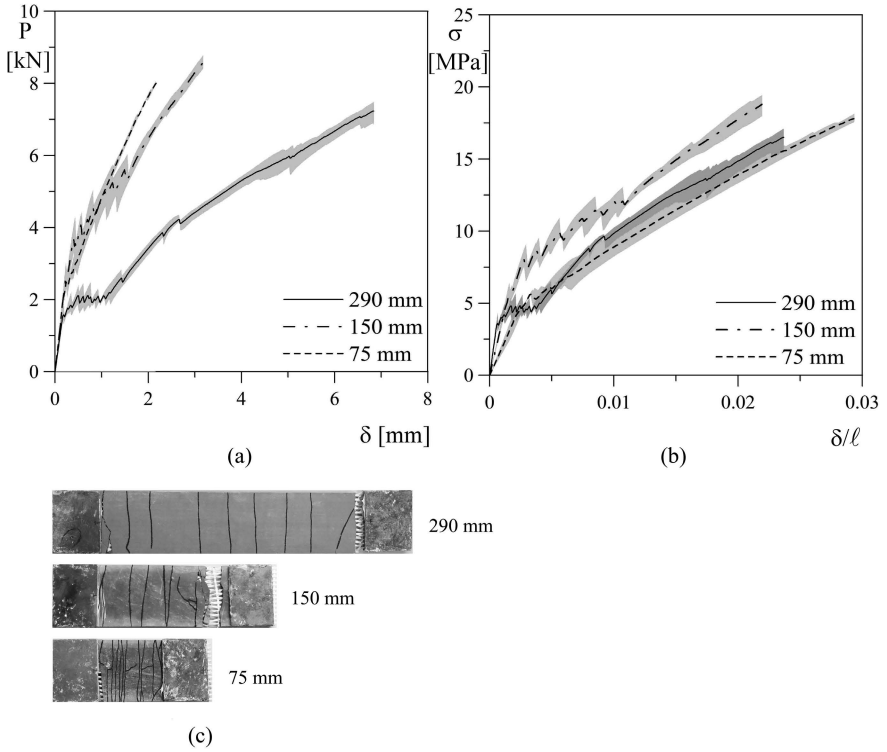

Figure 4.11: Influence of specimen size for F3 - 1 fabric reinforcement: load vs. displacement curves in uniaxial tension (a), nominal stress vs. normalized displacement curves in uniaxial tension (b), and specimen cracking pattern (c).

4.2 Tensile behaviour after freezing-thawing cycles

Considering the results presented in the previous section, the "F3 - 1 fabric" solution cured in air is selected to be used in the sandwich façade panel as the use of just one fabric makes the casting operation easier and the curing in air does not affect the thermal and mechanical properties of the insulation material.

In order to study the durability of this solution, its residual tensile behaviour when subjected to freezing-thawing cycles is investigated through a proper experimental campaign.

In the following paragraphs the materials involved in the casting phase, the specimen preparation (including thermal treatment), the adopted test procedure and the experimental results are presented.

4.2.1 Materials

Cementitious matrix

The matrix used to cast the TRC specimens is the same described in Table 4.1, considering an amount of superplasticizer equal to 56 kg/m^3. Hence, the mechanical characteristics of the mortar are those presented in Table 4.4.

AR-glass fabric

Fabric "F3" (presented in Table 4.5 and Figure 4.1) is used as reinforcement for the TRC specimens subjected to freeze-thaw attack.

4.2.2 Specimen preparation and test procedure

Specimens

The specimens used in the experimental investigation were 400 mm long, 70 mm wide (b) and 6 mm thick (t) and were reinforced with 1 layer of fabric F3 placed in the middle of the TRC thickness. The nominal reinforcement ratio (A_{fabric}/bt) was equal to 3.2%.

The same hand lay-up technique explained above was employed to produce the specimens. In all the specimens produced the warp was taken parallel to the long side. The specimens remained one day in the mould within a wet environment (>95% RH) and then were cured in air for 28 days before carrying out the thermal treatments. The air condition was that of an office with temperature ranging between 18 and 22 ℃ during winter and between 22 and 27 ℃ during summer; the related relative humidity ranges were respectively 40-60% and 50-80%. Table 4.8 summarizes all the dates related to the specimen history (the specimen identification is explained in the following).

Even if all the surfaces of the specimens were in contact with air during curing, the shrinkage of the mortar caused a loss of planarity in some specimens. This fact may be due to the unequal shrinkage behaviour of the side initially in contact with the mould with respect to the opposite side [Mechtcherine and Leboldt (2011)] and to the deformability of the fabric, that causes during casting a small eccentricity of the fabric inside the specimen, thus precluding the perfect symmetry of the specimen itself. The consequent lack of planarity of the specimens was computed by measuring the out of plane distance between the two ends of each specimen and the mid-section.

After the 28 days in air, the specimens were cut and reduced to a length of 375 mm in order to prevent the water absorption by the portion of the fabric overhanging the specimen. Then, the specimens were thermally treated by dif-

Table 4.8: Specimen history: dates of casting, pre-cracking, beginning and end of cycles and performing of the test

Spec.	*Casting*	*Pre cracking*	*Beginning of cycles*	*End of cycles*	*Tension test*
U0	30/06/2011	-	-	-	17/01/2012
U25	18/07/2011	-	23/09/2011	28/09/2011	16/01/2012
U50	18/07/2011	-	23/09/2011	04/10/2011	16/01/2012
U75	18/07/2011	-	23/09/2011	10/10/2011	16/01/2012
U100	20/07/2011	-	23/09/2011	15/10/2011	17/01/2012
U150	17/04/2012	-	23/10/2012	24/11/2012	20/12/2012
U500	17/04/2012	-	28/06/2012	05/12/2012	20/12/2012
C0	20/03/2013	21/05/2012	-	-	06/05/2013
C25	12/04/2012	21/05/2012	16/07/2012	21/07/2012	27/07/2012
C50	10/04/2012	21/05/2012	27/09/2012	08/10/2012	26/10/2012
C75	10/04/2012	21/05/2012	28/06/2012	14/07/2012	16/07/2012
C100	10/04/2012	21/05/2012	28/06/2012	21/07/2012	27/07/2012
C150	12/04/2012	21/05/2012	30/07/2012	30/08/2012	24/09/2012
C500	12/04/2012	21/05/2012	28/06/2012	05/12/2012	20/12/2012

ferent numbers of freezing-thawing cycles according to procedure A of ASTM International C666/C 666M - 03 "Standard Test Method for Resistance of Concrete to Rapid Freezing and Thawing". The range of temperature varies between +4 ℃ and -18 ℃ with both cooling and heating rate equal to 11 ℃/h and a 30 minutes rest phase both at +4 ℃ and at -18 ℃ (Figure 4.12). Each specimen was completely immersed in water, icing and de-icing during thermal cycles. Different scenarios were considered and in particular 25, 50, 75, 100, 150 and 500 cycles were taken into account. Figure 4.13 shows the distribution of the specimens in the climatic chamber both in section and plan view. In order to take into account the effect of freezing and thawing when the material, even at the Serviceability Limit State, is working in cracked condition, some specimens were pre-cracked before the thermal cycles. In particular, 3 un-cracked and 3 pre-cracked nominally identical specimens were adopted for each cycle number

considered.

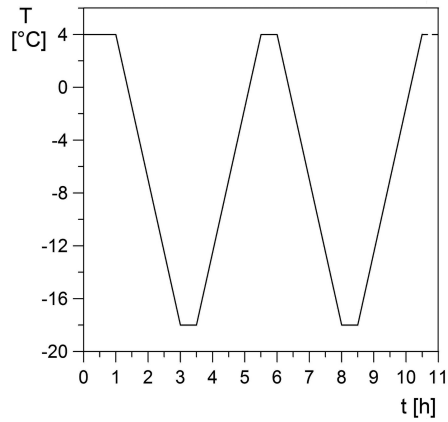

Figure 4.12: Freezing-thawing cycles: temperature-time curve.

In the case of high cycle number, a surface damage was experienced by some specimen. In the case of un-cracked specimens, after 150 cycles a loss of some mortar from the lateral surface was observed, while after 500 cycles a light deterioration of the upper surface is visible. Considering pre-cracked specimens, the phenomenon is more evident: a damage of the upper surface was experienced starting from 75 cycles and grew with the increasing number of cycles (Figure 4.14). This deterioration caused a loss of specimen mass, that has to be regarded when the mass variation due to the cycle exposure is analysed. It is worth noting that the surface damage concerns only the upper surface, that was not in contact with the formwork, while the lower surface is always in perfect conditions. This fact has to be considered when the production process of a structural product is designed.

Once exposed to thermal cycles, each specimen was tested in uniaxial tension according to the experimental set-up shown in Figure 4.4. The same test set-up was used to pre-crack the specimens. Three specimens, not thermally damaged,

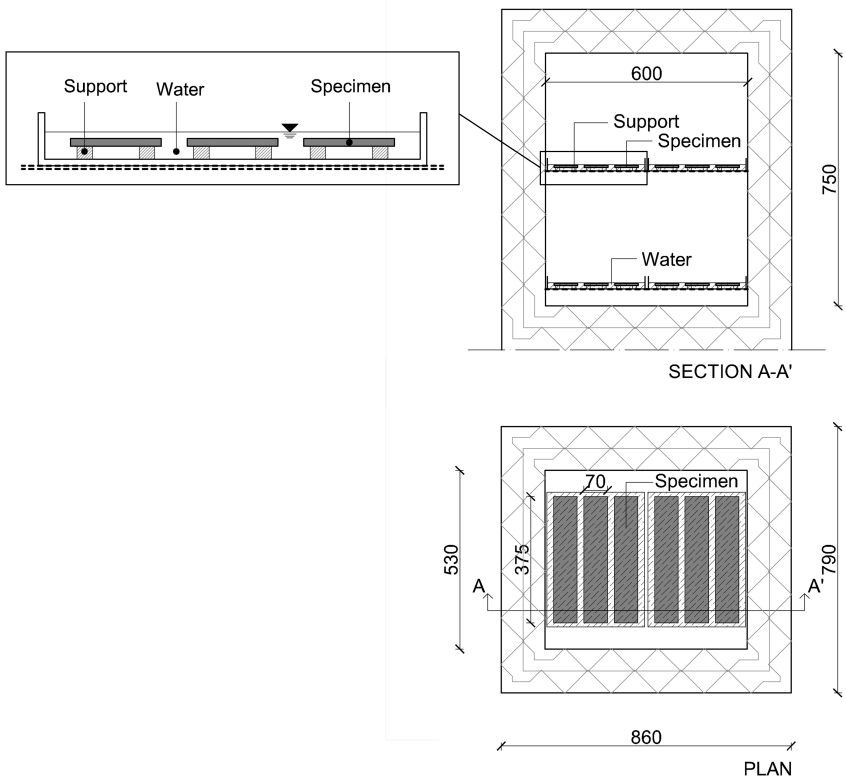

Figure 4.13: Freezing-thawing cycles - specimen distribution in the climatic chamber: section and plan.

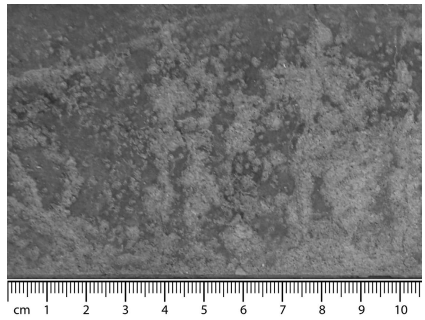

Figure 4.14: Damage of the mortar surface in pre-cracked 500 cycles specimen.

were used to compare the mechanical properties.

Each specimen is identified trough the following notation: a letter, that specifies if the specimen was un-cracked (U) or pre-cracked (C) when thermally treated; a number, that stands for the number of cycles the specimen was exposed and another number that denotes the nominally identical specimens (e.g. U500_2 stands for un-cracked specimen treated trough 500 cycles, specimen number 2).

Test set-up and test procedure

The uniaxial tensile test, carried out using the electromechanical press, is shown in Figure 4.4. A pressure equal to 5.1 MPa was applied to clamp the specimen edges according to a rigid clamping scheme for which 55 x 70 x 3 mm^3 steel plates were glued on each face of the specimen at the ends in order to better distribute the clamping pressure and thus minimizing the damage associated with the local crushing of concrete. As explained above, for these specimens the maximum load is too high for the spherical joints, hence just backlashes of the clamping devices prevent torsional and bending moments caused by an eventual misalignment of the constrains. The tests were displacement-controlled by imposing a constant stroke (δ in Figure 4.4) rate equal to 0.02 mm/s.

The pre-cracking phase was carried out using the same test set-up explained above, but using a soft clamping system (Figure 4.15(a)): in this system, the plates adopted to minimize the local crushing of concrete were not glued, but only supported by the clamping pressure applied by the press; a thin rubber interlayer is placed between the specimen and each steel plate to prevent local stress concentration caused by the uneven concrete surface. In this case, as explained by Hartig et al. (2012), the load is transferred basing on the Coulomb friction and cracks can occur in the supported parts of the specimen. As slip occurred between specimen and clamping devices, larger displacement were recorded if compared with the rigid clamping case, so the stiffness of the initial elastic branch is smaller.

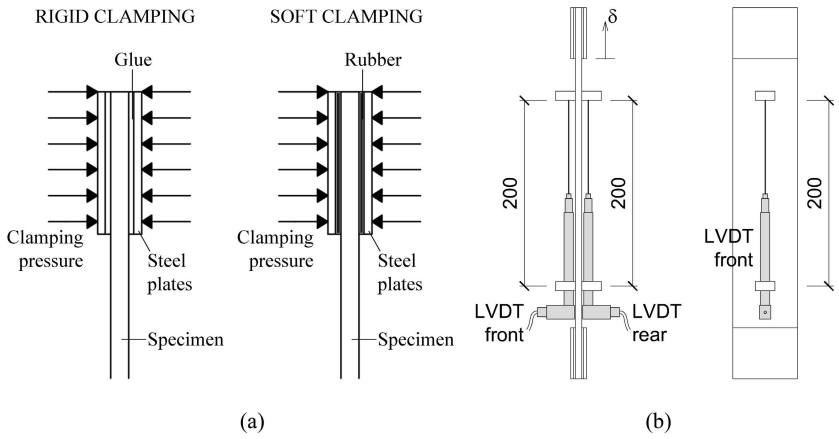

Figure 4.15: Difference between rigid and soft clamping system (a) and LVDT placement on the specimen in the case C0 (b) - measures in mm.

Figure 4.16 describes the test procedure adopted for un-cracked (Figure 4.16(a)) and cracked (Figure 4.16(b)) specimens. In particular, in the case of un-cracked situation, the specimens were exposed to thermal cycles and then tested in direct tension up to failure with rigid clamping. On the contrary, in the case of cracked situation, the specimens were pre-cracked in uniaxial tension with the soft clamping scheme up to a load corresponding to 1.2 times the first cracking load of the specimen itself. Once pre-cracked, each specimen was exposed to thermal cycles and then tested in uniaxial tension up to failure with a rigid clamping. In the same figure 4.16(b) two displacement references are introduced: in particular, δ refers to the displacement starting from the pristine condition, while δ_1 is measured starting from the end of the pre-cracking phase.

Figure 4.17 shows the nominal stress ($\sigma = P/A$; P = load, A = original cross-section area) versus displacement (δ) curves obtained during the pre-cracking operation for all the specimens. Each curve represents the average of 3 nominally identical tests. It is worth noting that each average curve in the graph and in all

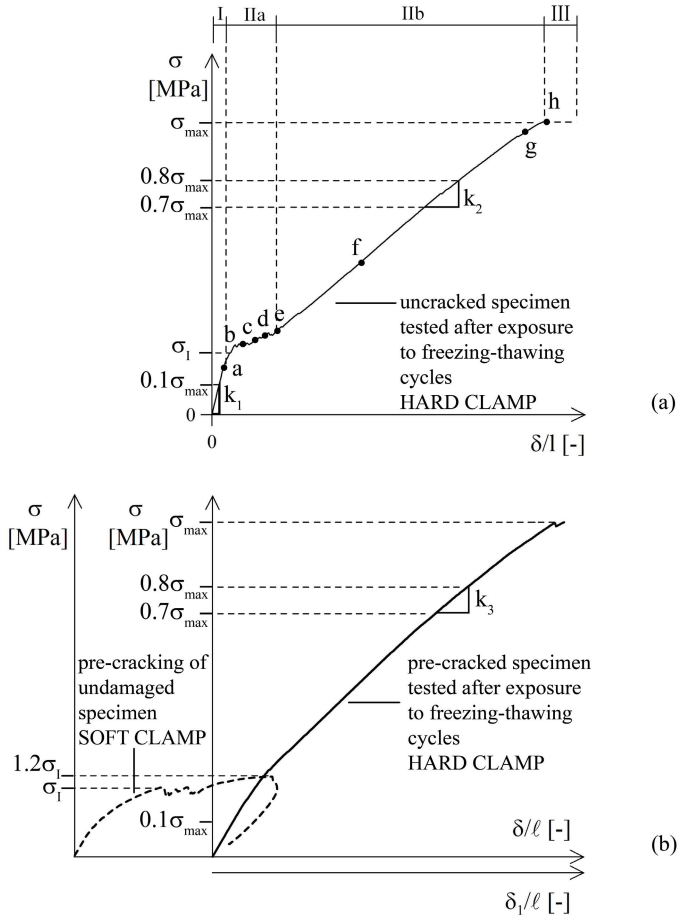

Figure 4.16: Test procedure for a) un-cracked (U) and b) pre-cracked (C) specimen.

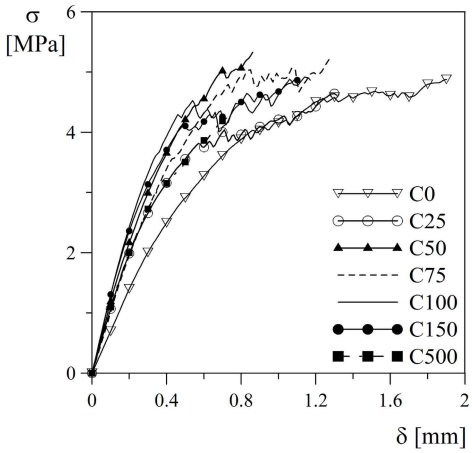

Figure 4.17: Pre-cracking - Nominal stress vs. displacement average curves in uniaxial tension.

the further graphs is interrupted when the first of the three nominally identical specimens reaches the ultimate displacement; as a result, the peak of the average curve differs from the average peak value. It is worth to remind that all the pre-cracking operations were performed before the thermal cycles and, therefore, all the curves presented in Figure 4.17 refers to the not thermally damaged material. The number of cycles displayed in the legend just refers to the cycles the specimen was exposed, after this pre-cracking phase. The scattering of the results is due to the soft clamping system that enhances the slip of the specimen in the clamped zone.

4.2.3 Experimental results

The results of the experimental campaign are reported in this paragraph in terms of nominal stress (σ) versus normalized displacement (δ/l) curves. The stress is obtained by dividing the load by the initial area of the specimen cross section; the normalized displacement was evaluated as the ratio between the displacement

(δ, Figure 4.4) and the specimen initial free length (l).

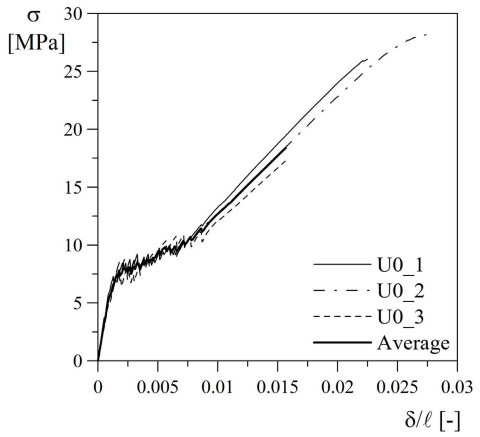

Figure 4.18: Un-cracked 0 cycles specimens - Nominal stress vs. normalized displacement curves in uniaxial tension.

Figure 4.18 shows the results of the uniaxial tensile tests performed on material not exposed to any thermal cycle (0 cycles, un-cracked). These results are considered as a reference in the following in order to evaluate the effect of freezing and thawing on the material behaviour when un-cracked condition is considered. In these results the three phases that typically characterize the non linear response of Textile Reinforced Concrete can be observed. The first cracking was reached when the tensile strength of the matrix was exceeded and then multi-cracking strain hardening behaviour occurred. A final branch, in which no further cracks develop, takes place: its extension depends on the reinforcement ratio, the fabric geometry and its coating and it stops with fabric failure. The pictures in Figure 4.19 show a typical sequence of crack pattern during a test; the spalling phenomenon, that is observable just in the very final phase of the test (points g and h), can be due to the small thickness of the specimen with respect to the reinforcing fabric adopted. The only exception to the described behaviour is test U0_3: during this test a transverse crack occurred in the thickness of

the specimen within the clamped area, thus causing a slip of the fabric inside the specimen leading to an earlier failure (Figure 4.18). The same results are summarized in Table 4.9 together with those of all the other tests performed on un-cracked material after the exposure to thermal cycles. The table shows, for each specimen, the following parameters:

- a number, that identifies the batch;
- the geometrical sizes (thickness t and width b) used to determine the area (A) of each specimen cross-section;
- the percentage variation of the mass after the exposure to the thermal cycles ($\Delta m/m_i$; Δm = difference between the final and the initial mass, m_i = initial mass);
- the maximum load reached (P_{max}) together with the corresponding elongation recorded by the machine (δ_u);
- the maximum nominal stress (σ_{max}) together with the corresponding normalized displacement (δ_u/l);
- the first cracking stress (σ_I), obtained dividing the load corresponding to the first cracking by the initial area of the specimen cross section (this first cracking load was detected as the point in which the curve deviate more than 2% from the initial stiffness);

- the effectiveness factor (EF), calculated as the ratio between the maximum load reached (P_{max}) and the average peak load experimentally measured by stretching only the fabric (Table 4.5 and Figure 4.1, fabric F3).

Table 4.9: Test results - un-cracked (U) specimens

Spec.	*Batch*	t $[mm]$	b $[mm]$	$\Delta m/m_i$ [%]	P_{max} $[kN]$	δ_u $[mm]$	σ_{max} $[MPa]$	δ_u/l [%]	σ_I $[MPa]$	EF $[-]$
U0_1	1	6	70.5	-	11.01	6.47	26.04	2.25	7.31	1
U0_2	1	6.1	70.5	-	12.13	7.91	28.21	2.75	5.85	1.1
U0_3	1	6.4	70.7	-	7.81*	4.48*	17.56*	2.32*	5.14	0.71*
Av.	-	6.2	70.6	-	11.57	7.19	27.13	2.5	6.1	1.05
U25_1	2	6.2	70.4	0.26	12.04	7.36	27.58	2.92	6.88	1.09
U25_2	2	5.9	70.3	0.11	11.68	6.48	28.17	2.44	8.91	1.06
U25_3	2	6	71	0.07	11.96	7.27	28.09	2.78	9.24	1.09
Av.	-		70.6	0.15	11.9	7.04	27.94	2.71	8.34	1.08
U50_1	2	6	70.1	0.37	11.34	7.44	26.81	2.82	6.71	1.03
U50_2	2	6	71.8	0.43	10.82	7.13	25.1	2.63	8.43	0.98
U50_3	2	6	70.2	0.34	10.91	6.4	25.9	2.48	4.76	0.99
Av.	-	6	70.7	0.38	11.02	7	25.95	2.64	6.63	1
U75_1	2	6.2	71	0.85	11.93	7.31	27.11	2.8	8.44	1.08
U75_2	2	6.2	70.1	0.79	10.98	6.2	25.27	2.37	7.46	1
U75_3	2	6.3	70.2	0.82	12.13	6.71	27.42	2.57	7.22	1.1
Av.	-	6.2	70.4	0.82	11.68	6.74	26.6	2.58	7.71	1.06
U100_1	5	6.1	70.5	1.45	10.69	6.54	24.85	2.48	10.81	0.97
U100_2	5	6.1	70.3	1.35	10.63	6.25	24.78	2.39	9.64	0.96
U100_3	5	6.5	69.9	1.52	10.43	6.08	22.95	2.31	8.55	0.95
Av.	-	6.2	70.2	1.44	10.58	6.29	24.2	2.39	9.67	0.96
U150_1	6	6.4	70.2	2.98	10.55	6.61	23.47	2.41	4.58	0.96
U150_2	6	6.6	70.7	3.67	11.07	7.38	23.72	2.69	3.77	1
U150_3	6	6.3	70.4	3.13	9.96	6.39	22.46	2.33	3.68	0.9
Av.	-	6.4	70.4	3.26	10.53	6.79	23.22	2.48	4.01	0.95
U500_1	6	6	70.2	3.11	8.61	5.56	20.43	2.02	3.88	0.78
U500_2	6	6	70.5	3.47	9.27	6.15	21.92	2.24	3.14	0.84
U500_3	6	5.8	70.9	3.4	9.68	6.25	23.53	2.27	6.24	0.88
Av.	-	5.9	70.5	3.33	9.19	5.99	21.96	2.18	4.42	0.83

* rejected values due to test problem (during multi-cracking phase a crack forms in the clamping area, where steel plates are glued on the specimen; in the third phase, when load is carried by the fabric, this crack localizes and there is no load transfer from steel plates to the specimen)

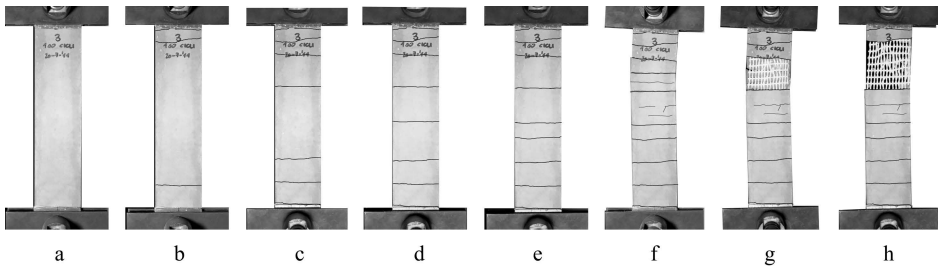

Figure 4.19: Typical sequence of crack pattern during a test (each point is indicatively identified in the σ-δ/l curve of Figure 4.16(a), specimen U100_3 is taken as an example).

Three not-treated specimens were also tested following the "pre-cracked" test procedure with a soft clamping in the starting phase up to a certain level of load (1.2 times the first cracking load) and with a rigid clamping up to failure (Figure 4.20, 4.21 and 4.22, $(\sigma - \delta/l)$ curves). The obtained average curve is considered as reference for all the pre-cracked specimens tested after the exposure to freezing and thawing.

Comparing these results with the curves collected in Figure 4.18, it is clear that the slip of the specimen inside the clamping region affects not only the first cracking strength (about 30% less than hard clamping), but also the peak strength, even if less (15%) also due to the fact that the last phase of the two testing modalities involves the same rigid clamping condition.

To better understand the magnitude of the slipping phenomenon, particularly in the soft clamping case, the zero cycles specimens were instrumented with two LVDT displacement transducers, one on the front and one on the rear side, during the tests (Figure 4.15(b)). The gauge length astride the centre of each specimen (l_{LVDT}) was equal to 200 mm. Just in one pre-cracking phase (C0_3) the LVDT measures are not available because of a technical problem on the data acquisition system (Figure 4.22(a)). The comparison between the nominal strain ($\varepsilon = \delta_{LVDT}/l_{LVDT}$, average between the front and the rear value), obtained from

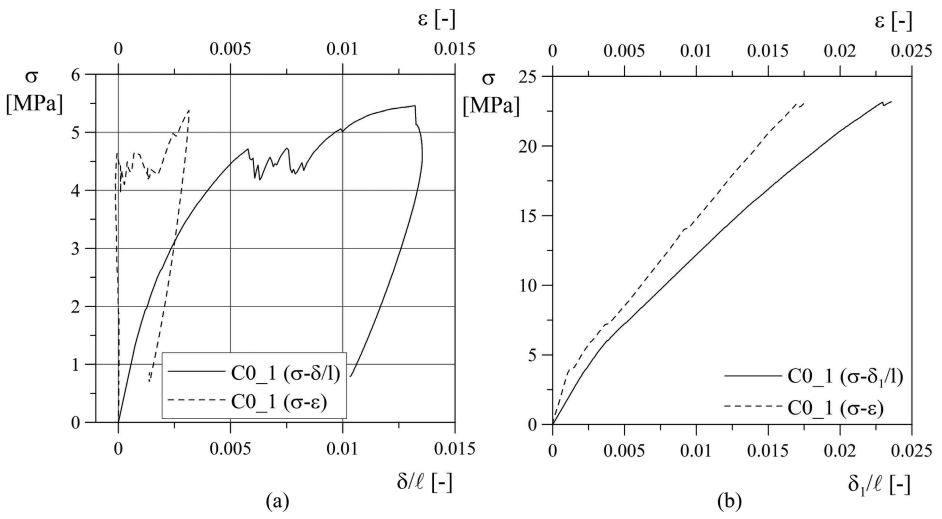

Figure 4.20: C0_1 (pre-cracked 0 cycles specimen 1) - Nominal stress vs. normalized displacement curves in uniaxial tension: pre-cracking phase (a) and test on freezing-thawing pre-cracked specimen (b).

the LVDT measures (δ_{LVDT}), and the normalized displacement (δ/l) is proposed in Figures 4.20, 4.21 and 4.22. Subfigures (a) refer to the soft-clamping phase, while subfigures (b) refer to rigid-clamping phase. It is worth noting that the difference between the solid and dashed curves is due to the specimen sliding inside the clamping system. It is quite obvious to observe how soft clamping is characterized by a larger sliding and a difference between the two measurement (ε and δ/l) larger than 220% is available at the end of the pre-cracking branch for soft-clamp, while a difference of about 25-30% can be measured at failure for rigid-clamp.

The results of the uniaxial tensile tests on the material exposed to several freezing-thawing cycles are presented in Figures 4.23 - 4.28 respectively for 25, 50, 75, 100, 150 and 500 cycles. Subfigures (a) refer to the un-cracked situation,

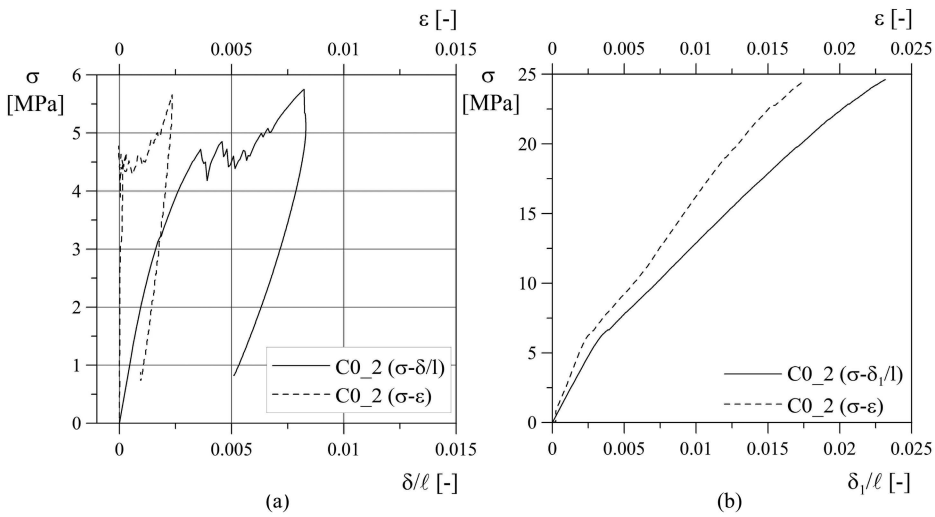

Figure 4.21: C0_2 (pre-cracked 0 cycles specimen 2) - Nominal stress vs. normalized displacement curves in uniaxial tension: pre-cracking phase (a) and test on freezing-thawing pre-cracked specimen (b).

while subfigures (b) consider specimens pre-cracked before the thermal treatment. For each case, the 3 curves corresponding to 3 nominally identical tests are reported together with the average curve. It is worth noting that the material response is characterized by a good repeatability even increasing the number of cycles. Nevertheless, a slightly larger scattering is available when testing the material exposed to freezing and thawing in cracked condition, even if for the peak load a maximum distance from the average value always smaller than 10% was registered. The same results are summarized in tables 4.9 and 4.10 respectively for un-cracked and cracked condition.

A comparison between the average curves obtained for all the cycle numbers considered is reported in Figures 4.29 and 4.30 respectively for un-cracked and cracked situation. In the same figures also a typical crack pattern observed at the failure is presented for each situation. It is possible to observe that the multi-

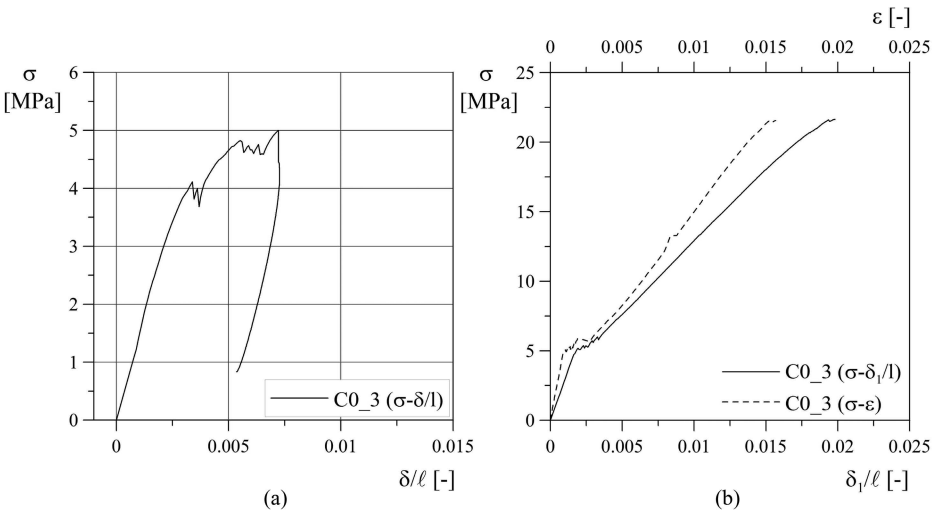

Figure 4.22: C0_3 (pre-cracked 0 cycles specimen 3) - Nominal stress vs. normalized displacement curves in uniaxial tension: pre-cracking phase (a) and test on freezing-thawing pre-cracked specimen (b). C0_3 (σ-ε) is not available because of a technical problem on the data acquisition system.

cracking pattern is denser in the case of pre-cracked specimens, if compared with un-cracked specimens.

A general look at the average curve comparison suggests that freezing and thawing has a negligible effect on the ultimate strength of the composite both in un-cracked and cracked condition, while a higher sensitivity to this environmental condition seems to characterize the first cracking strength of the matrix. In the case of 150 and 500 cycles of Figure 4.30(a), the behaviour is comparable with the 0 cycles situation. This evidence may be related to a self-healing phenomenon and a late hydration of pre-cracked specimens.

In Figure 4.31 two pictures of specimens treated with freezing-thawing cycles and then tested in tension are shown. It is possible to notice that, next to a crack developed in correspondence with a weft yarn, another crack forms and, on

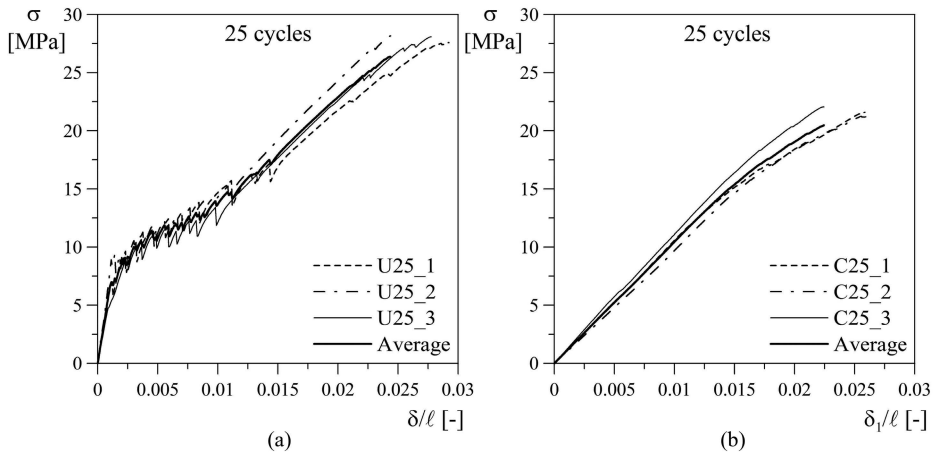

Figure 4.23: 25 cycles - Nominal stress vs. normalized displacement curves in uniaxial tension: un-cracked (a) and pre-cracked (b) specimens.

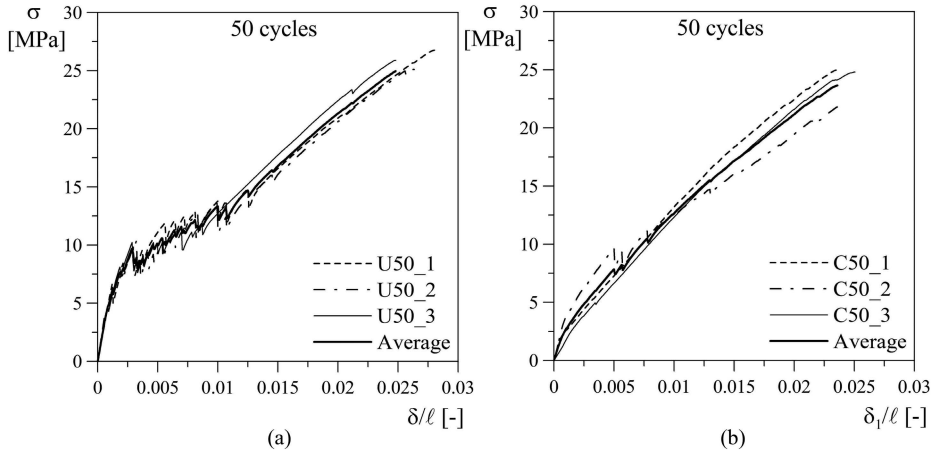

Figure 4.24: 50 cycles - Nominal stress vs. normalized displacement curves in uniaxial tension: un-cracked (a) and pre-cracked (b) specimens.

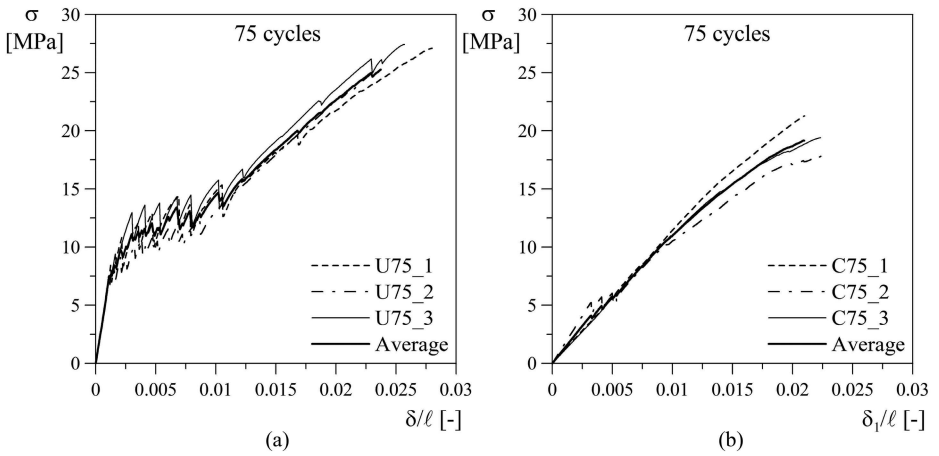

Figure 4.25: 75 cycles - Nominal stress vs. normalized displacement curves in uniaxial tension: un-cracked (a) and pre-cracked (b) specimens.

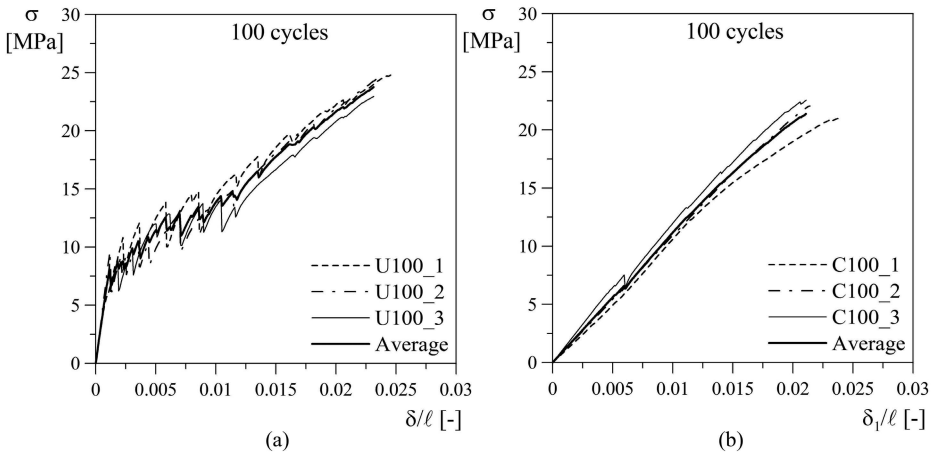

Figure 4.26: 100 cycles - Nominal stress vs. normalized displacement curves in uniaxial tension: un-cracked (a) and pre-cracked (b) specimens.

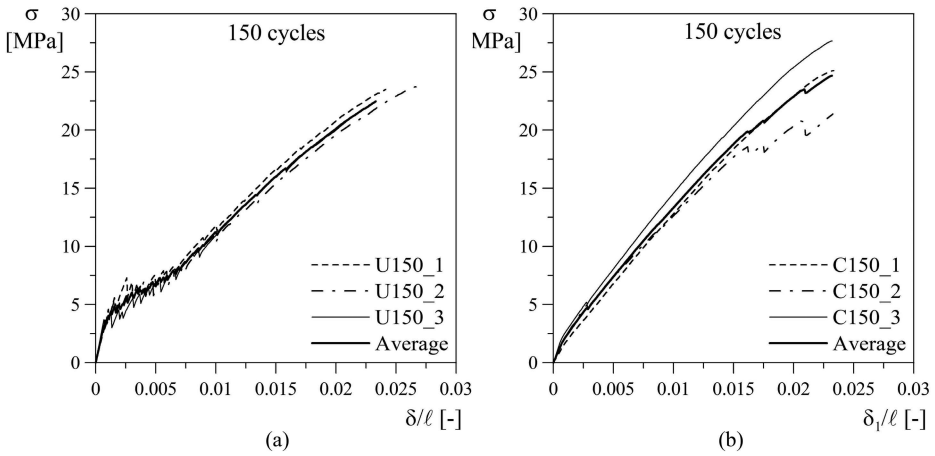

Figure 4.27: 150 cycles - Nominal stress vs. normalized displacement curves in uniaxial tension: un-cracked (a) and pre-cracked (b) specimens.

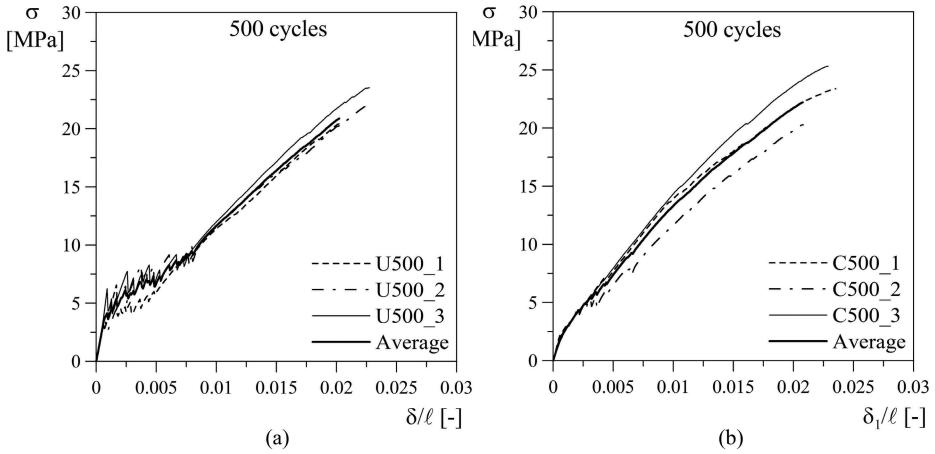

Figure 4.28: 500 cycles - Nominal stress vs. normalized displacement curves in uniaxial tension: un-cracked (a) and pre-cracked (b) specimens.

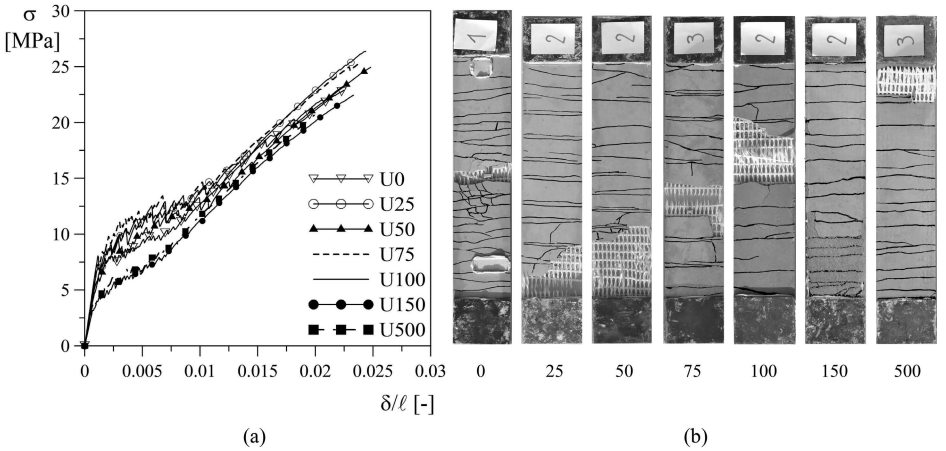

Figure 4.29: Average nominal stress vs. normalized displacement curves after different number of cycles and corresponding crack patterns - un-cracked specimens.

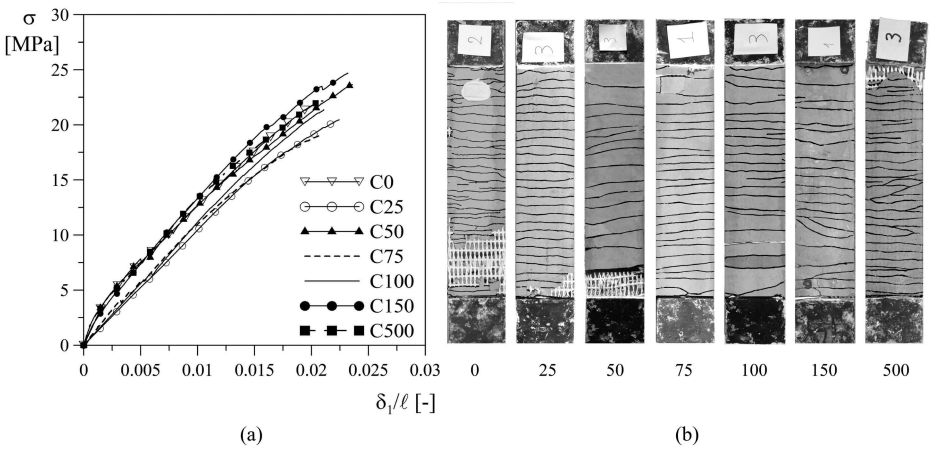

Figure 4.30: Average nominal stress vs. normalized displacement curves after different number of cycles and corresponding crack patterns - pre-cracked specimens.

Table 4.10: Test results - pre-cracked (C) specimens

Spec.	*Ba–tch*	t $[mm]$	b $[mm]$	$\Delta m/m_i$ [%]	P_{max} $[kN]$	δ_u $[mm]$	σ_{max} $[MPa]$	δ_u/l [%]	σ_I^* $[MPa]$	EF $[-]$
C0_1	7	6.4	70.0	-	10.39	6.26	23.19	2.36	4.72	0.94
C0_2	7	6.1	70.7	-	10.62	6.26	24.62	2.32	4.72	0.96
C0_3	7	6	70.3	-	9.13	5.3	21.65	1.98	4.11	0.83
Average	-	6.2	70.3	-	10.05	5.94	23.15	2.22	4.52	0.91
C25_1	3	6.2	70.1	5.64	9.38	7.21	21.59	2.58	3.82	0.85
C25_2	3	6.4	71.5	5.48	9.75	7.26	21.3	2.62	4.07	0.88
C25_3	3	5.9	70.2	4.77	9.13	6.17	22.05	2.24	4.19	0.83
Average	-		70.6	5.29	9.42	6.88	21.64	2.48	4.03	0.85
C50_1	4	6.2	70.2	5.08	10.72	6.52	25.06	2.27	5.03	0.97
C50_2	4	6.2	70.9	5.98	9.46	6.52	21.8	2.36	4.79	0.86
C50_3	4	6.6	69.8	5.56	11.08	6.81	24.8	2.5	5.81	1.01
Average	-		70.3	5.54	10.41	6.62	23.89	2.41	5.21	0.95
C75_1	4	6.2	70.9	5.53	9.35	5.75	21.27	2.1	3.61	0.85
C75_2	4	6.4	70.3	4.91	8.05	6.17	17.88	2.25	4.73	0.73
C75_3	4	6.5	70.6	4.94	8.9	6.2	19.39	2.23	3.87	0.81
Average	-	6.4	70.6	5.13	8.77	6.04	19.52	2.19	4.07	0.8
C100_1	4	5.9	69.9	7.9	8.66	6.51	21	2.39	3.53	0.79
C100_2	4	6.1	71.6	4.91	9.63	5.86	22.05	2.14	4.87	0.87
C100_3	4	5.9	70.7	4.83	9.4	5.82	22.55	2.11	4.66	0.85
Average	-	6	70.7	5.88	9.23	6.07	21.86	2.21	4.35	0.84
C150_1	3	5.9	69.9	1.99	10.36	6.41	25.11	2.33	4.29	0.94
C150_2	3	5.9	70.8	0.27	8.92	6.37	21.36	2.32	4.35	0.81
C150_3	3	5.4	70.6	0.16	10.55	6.33	27.67	2.32	4.31	0.96
Average	-	5.7	70.4	0.8	9.94	6.37	24.71	2.32	4.36	0.9
C500_1	3	5.9	70	4.73	9.65	6.51	23.38	2.35	4.39	0.88
C500_2	3	6.1	71.4	3.87	8.83	5.72	20.28	2.08	3.55	0.8
C500_3	3	5.5	70.5	3.37	9.82	6.24	25.31	2.29	3.04	0.89
Average	-	5.8	70.6	3.99	9.43	6.16	22.99	2.24	3.66	0.86

* values obtained in the pre-cracking phase (soft clamp) before thermal cycles

the edge, a H crack propagation can be observed: this behaviour characterizes many un-cracked specimens. The development of the longitudinal crack at the middle of the specimen thickness may cause a detachment of the mortar cover and an exposure of the fabric. It is worth noting that this detachment happens

at a stress level close to the maximum tensile strength (σ_{max}) and, therefore, at Serviceability Limit State ($\sigma_{SLS} \leq 0.4\sigma_{max}$) delamination never occurs.

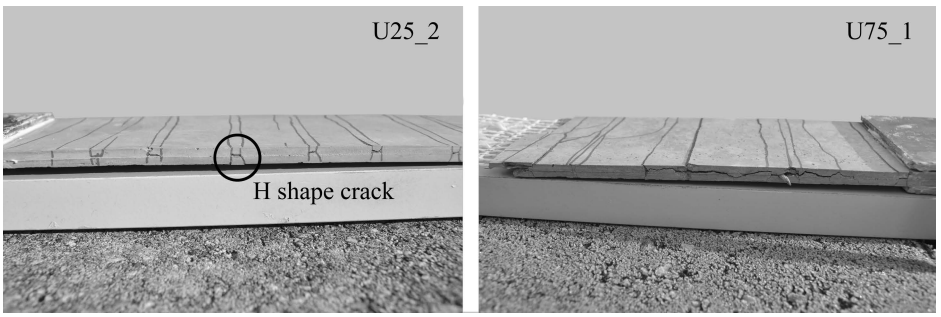

Figure 4.31: Specimens after tensile test.

To investigate the influence of thermal cycles on the material response, the variation with cycle number of the main parameters that characterize the material response is shown in Figure 4.32. In all the graphs, each marker represents the value assumed by the considered parameter for each specimen, normalized by the average value registered in the zero cycles case. The solid line connects the average value computed for the different number of cycles in case of un-cracked specimens, while the dashed line refers to pre-cracked condition.

Figure 4.32(a) shows the trend of the maximum nominal stress registered for the different number of cycles considered. The negligible effect of the freezing-thawing cycles on the ultimate strength is here confirmed. For un-cracked specimens, a slight decrease in the maximum stress with the increasing number of cycles is visible; however, even if 500 cycles are performed, the 80% of the initial maximum nominal stress is still reached by the material. For pre-cracked specimens, the strength variation ranges between 0.8 and 1.2 without a clear trend. It is worth noting that the peak strength of each test has been normalized with respect to the peak strength obtained with the same clamping modalities at zero cycles and, therefore, pre-cracked specimens adopt a normalizing value

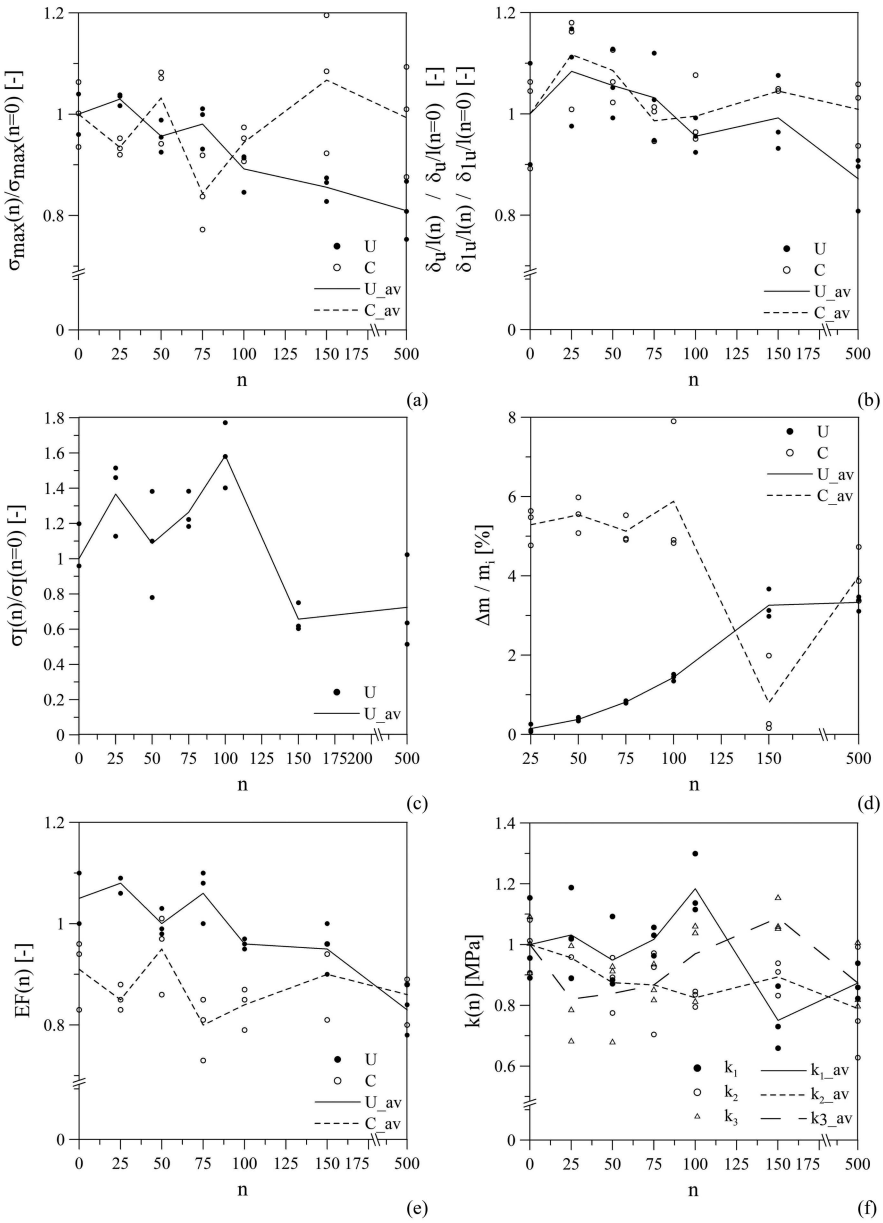

Figure 4.32: Test results: (a) peak strength vs. number of cycles, (b) peak normalized displacement vs. number of cycles, (c) first cracking strength vs. number of cycles, (d) mass variation vs. number of cycles, (e) EF vs. number of cycles and (f) specimen stiffness vs. number of cycles.

that is 15% lower than the un-cracked one (0 cycles lines in Tables 4.9 and 4.10 respectively).

In Figure 4.32(b) the relationship between the ultimate normalized displacement (registered when the maximum load is reached for each specimen) and number of freezing-thawing cycles is plotted. As in the previous graph, for un-cracked specimens a trend of decreasing ultimate normalized displacement with increasing number of cycles can be identified, while for pre-cracked specimens this parameter seems not to be affected by the exposure to freezing and thawing cycles. However, in both cases all the values are closed to the normalized displacement measured in case of zero cycles (maximum average difference equal to 17%) also taking into account the scattering of the results that, for this parameter, can reach 11%.

Figure 4.32(c) shows the results in terms of first cracking strength versus number of cycles. Obviously these results are available only for un-cracked specimens, because the first cracking strength of pre-cracked specimens (collected in Table 4.10 - column 10^{th}) was reached before the exposure of specimens to thermal cycles. For low number of cycles, up to 100, the first cracking strength seems not to be affected by freezing-thawing phenomenon (an enhancement of the strength is even registered with respect to the 0 cycles condition), while the exposure to a higher number of cycles causes a clear decrease of this property, as a damage of the matrix is developing. It is important to point out that this parameter is characterized by a larger scattering than the ultimate strength. This is due in part to the larger variability of the mortar mechanical properties but, in particular, to the small eccentricities that may arise during the first phase of the test due to the mortar shrinkage, that causes a small curvature of the specimen. This curvature causes a misalignment of the load applied at the two ends of the specimen, generating a bending moment on the specimen. The misalignment registered in all the experimental campaign is smaller than 3 mm and, for this reason, affects only the

first cracking strength without any significant contribution on the cracked phase, also because of the formation of cracks that work as hinges at the specimen ends.

Considering the specimen mass variation, literature results state that, for conventional concrete, specimens exhibit a mass reduction due to the surface scaling, even if air entraining agent is added to the mix: considering a concrete characterized by a mean compressive strength of 40 MPa and a water to cement ratio equal to 0.45, Marzouk and Jiang (1994) measured a mass loss, increasing with the number of cycles, up to 2.2% (700 cycles) for 75x75x350 mm^3 specimens and up to 5.5% (700 cycles) for thin specimens with dimension of 20x75x300 mm^3; also Shang and Yi (2013) registered a mass loss increasing with the number of cycles and with the decreasing of the class of concrete. Considering a High Strength Concrete characterized by a water to binder ratio equal to 0.3 and a mean compressive strength equal to 70 MPa, Marzouk and Jiang (1994) found a smaller mass variation with respect to the normal strength concrete (-0.6% for 75x75x350 mm^3 specimens and -0.5% for 20x75x300 mm^3 specimens, considering 700 cycles in both cases). For lower value of water to binder ratio, some cementitious particles in the hardened state of concrete remain un-hydrated. Hence, the mass loss due to scaling is balanced by the water absorption, that leads to the hydration of un-hydrated cementitious particles and to the development of hydration products, resulting in a mass gain. Graybeal and Tanesi (2007) observed this phenomenon investigating the freezing-thawing durability of a Ultra High Performance Concrete, characterized by a water to cement ratio equal to 0.15. The phenomenon is enhanced in case of specimens cured in air (as those considered in this Section), because they exhibit lower levels of hydration if compared to UHPC cured in wet environment. The later hydration can affect the mechanical properties of the material, limiting the strength reduction due to freezing-thawing exposure.

Figure 4.32(d) shows the percentage mass variation of the specimens with the

increasing number of cycles. It is worth noting that all the specimens exhibit a mass increase due to the exposure to freezing-thawing cycles. Considering un-cracked specimens, the amount of this enhancement increases with the increasing number of cycles up to a percentage of about 3.5% (registered for 150 and 500 cycles). In case of pre-cracked specimens, the percentage variation of mass is higher than 5% for low number of cycles (25, 50, 75 and 100), while decreases for 150 and 500 cycles.

Comparing the results here discussed with those presented in the literature that exhibit a mass loss, it is important to point out that, differently from literature, the specimens here investigated were not fully saturated when the cycles started. Even if the selected matrix is characterized by a very low water absorption (less than 1%), the water absorption measured on a TRC specimen (not thermally treated) 100 mm long, 70 mm wide and 6 mm thick reached an asymptote of about 5% after less than one week. This result indicates that fabric represents a channel that favours water penetration inside the specimen since the fabric cross section is flush with the specimen short edges.

In the case of un-cracked specimen, the fabric is directly in contact with water only on the short sides of the specimen, thus leading to a very slow water penetration and, consequently, a very slow increase of the mass with time for a cycle number smaller than 100. For higher number of cycles, micro-cracking due to the freezing-thawing cycles accelerates the water penetration, as can be observed by the increase of the curve slope between 100 and 150 cycles. The final plateau can be related to the fully saturation of the specimen; the lower value of this plateau with respect the 5% asymptote previously discussed can be due to the scaling phenomenon observed in the case of 150 and 500 cycles, that caused a mass loss.

On the contrary, in pre-cracked specimens, the initial cracks increase the fabric surface directly in contact with water, thus leading to a very fast increase

of the mass (about 5.5%) since the 25 cycles situation, that means a 5 days permanence into the water. It is worth to note that the crack spacing due to pre-cracking is comparable with the length of the specimen used for water absorption measurements, thus confirming the speed of the water penetration process. The sudden decrease of the mass observed from 150 cycles has to be related to the previously discussed scaling phenomenon. The final increase of the mass can be driven, as already discussed by Graybeal and Tanesi (2007), by a later hydration.

Figure 4.32(e) shows the trend of the Effectiveness Factor with the cycle number growth. This factor is a measure of the effectiveness of the fabric-matrix bond: a value larger than one indicates a positive interaction between the mortar and its reinforcement, while values lower than the unit mean a bond weakness: the lower the value the higher this weakness. Looking at the graph, it is clear that, even if for a low number of cycles the un-cracked specimens behave better than pre-cracked ones, for a high number of cycles the EF tends to converge to the value of 0.8.

In Figure 4.32(f) the evolution, with the number of cycles, of three stiffness coefficients (k_1, k_2 and k_3) is plotted. These coefficients are defined in Figure 4.16(a) and (b) and the values they assume are collected in Table 4.11. k_1 represents the initial stiffness of the composite material in the un-cracked condition (hence specimens are tested from the beginning with the rigid clamping system) and it is computed as the slope of the nominal stress vs. normalized displacement curve between zero and $0.1\sigma_{max}$; this parameter is just a measure of the initial stiffness of the composite computed to compare specimens treated with a different number of cycles, but does not correspond to the Young Modulus of the cementitious matrix as the normalized displacement is taken into account instead of the strain (hence the sliding between the specimen and the clamping devices is accounted). Considering un-cracked condition, also parameter k_2 is computed. This coefficient is obtained as the slope of the final branch of the nominal stress

vs. normalized displacement curve of TRC in tension, in which only the contribution of the fabric is noticeable and no further cracks appear in the matrix. In this case 0.7 σ_{max} and 0.8 σ_{max} are assumed as limit values. Finally, k_3 is computed as k_2, but referring to pre-cracked specimens.

The evolution of the initial stiffness (k_1) is mainly related to the damage induced by the thermal cycles to the mortar matrix and it is possible to observe that it is similar to that experienced by the first cracking strength. This is due to the fact that both parameters are governed by the same damage of the matrix, but also that they have the same sensitivity to the test scheme eccentricity. In any case, it is clear from the results that very small damage (stiffness reduction lower than 20%) is available in the mortar matrix.

Regarding the post-cracking stiffness (k_2 and k_3), the evolution of these parameters represents the damage achieved both into the fabric itself and into the mortar-fabric interface. It is worth noting that, in the case of pristine material (0 cycles), the stiffness in the cracked phase (k_2 and k_3) is scantly affected by the test modalities, showing a maximum average difference lower than 5%. Also these parameters confirm the low sensitivity of the TRC to freezing-thawing cycles.

Table 4.11: Test results - values of k_1, k_2 and k_3

Spec.	k_1 $[MPa]$	k_2 $[MPa]$	*Spec.*	k_3 $[MPa]$
U0_1	7254.3	1081.08	C0_1	863.42
U0_2	6009.74	1012.2	C0_2	956.25
U0_3	5598.6	906.75	C0_3	1039.46
Average	6287.55	1000.01	Average	953.04
U25_1	6403.71	889.68	C25_1	649.62
U25_2	7467.13	1020.65	C25_2	747.63
U25_3	5589.34	958.7	C25_3	948.68
Average	6486.73	956.34	Average	781.98
U50_1	5478.66	775.01	C50_1	869.11
U50_2	6868.3	892.53	C50_2	646.21
U50_3	5555.35	956.78	C50_3	883.51
Average	5967.44	874.77	Average	799.61
U75_1	6481.21	704.08	C75_1	890.84
U75_2	6643.82	925.72	C75_2	810.2
U75_3	6054.21	971.94	C75_3	778.8
Average	6393.08	867.25	Average	826.61
U100_1	7011.5	845.81	C100_1	774.05
U100_2	8168.9	794.49	C100_2	1010.1
U100_3	7146.75	835.15	C100_3	988.58
Average	7442.38	825.15	Average	924.24
U150_1	4142.88	938.82	C150_1	1002.4
U150_2	4592.96	909.86	C150_2	1008.96
U150_3	5426.36	831.85	C150_3	1099.21
Average	4720.73	893.51	Average	1036.86
U500_1	5401.61	628.15	C500_1	759.45
U500_2	5174.05	748.38	C500_2	779.74
U500_3	5902.93	991.99	C500_3	959.13
Average	5492.86	789.51	Average	832.77

5

Experimental investigation on sandwich solution

The experimental campaign presented in this chapter concerns the investigation of failure mechanisms of a sandwich solution characterized by two external layers 10 mm thick made of Textile Reinforced Concrete (TRC) connected by an insulation layer of expanded polystyrene foam (EPS 250) 100 mm thick (Figure 5.1).

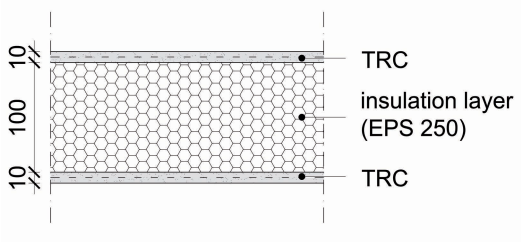

Figure 5.1: Sandwich cross-section (measures in mm).

5.1 Materials

The expanded polystyrene foam used is commercially known as EPS250 and is characterized by a compressive strength of 0.25 MPa at a strain equal to 10% and by a low thermal conductivity (0.034 W/mK according to European Standard EN 13163 "Thermal insulation products for buildings - Factory made products of expanded polystyrene (EPS)", 2008). The elastic modulus is equal to 13.7 MPa: it was measured performing compressive tests on three 100x100x150 mm^3 nominally identical specimens (Figure 5.2). According to uni-axial tensile tests performed on a similar EPS [Colombo et al. (2008)], the tensile behaviour is expected to be elastic-brittle; the value of tensile strength specified in the European Standard EN 13163 for EPS250 is larger than the compressive strength and is equal to 0.35 MPa. The shear modulus can vary between 4.14 and 4.41 MPa for this class of expanded polystyrene foam according to ASTM C 578-92 "Standard Specification for Rigid, Cellular Polystyrene Thermal Insulation".

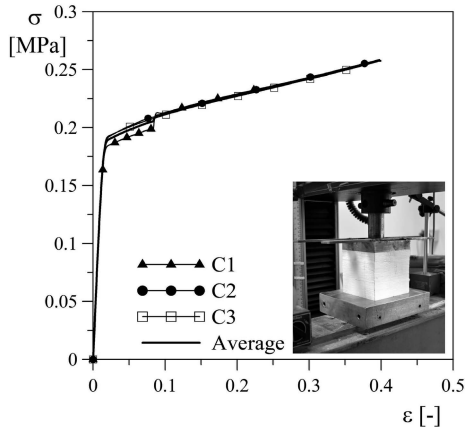

Figure 5.2: EPS behaviour in compression.

The TRC layers are obtained reinforcing a high strength fine grain mortar

with one layer of fabric "F3" (whose characteristics are shown in Table 4.5 and Figure 4.1).

The matrix used to cast the sandwich specimens is the same described in Table 4.1 (considering an amount of superplasticizer equal to 56 kg/m^3) at which two changes were made. First of all, the maximum aggregate size is enhanced from 600 μm to 1 mm in order to optimize the production process at a larger scale. Secondly, the amount of water is increased in order to obtain a higher water to binder ratio (0.225) and, hence, a more workable matrix that guarantees the possibility to cast the mortar in pressure.

The in pressure casting technique (Figure 5.3) is adopted in order to minimize the voids (defects) in the mortar and to enhance the bond between TRC layers and EPS, also because just the insulating material is used to transfer the shear between the external TRC layers. A proper formwork characterized by transparent walls was built in order to check by visual inspection the injection of the mortar (Figure 5.3(a)). An EPS layer with an AR-glass fabric fixed on each side is first placed into the formwork. After mixing, the fresh mortar is allowed to flow into a tank (Figure 5.3(b)), that, once filled, is closed (Figure 5.3(c)) and then pressurized. In this way the mortar can be injected in the formwork from the bottom through a spherical valve (Figure 5.3(d)). 48 hours after casting, specimens are demoulded and then cured in air at least for 28 days before testing.

At 28 days, the mortar is characterized by a bending tensile strength (f_{ctf}) equal to 13.5 MPa and by a cubic compressive strength (f_{cc}) equal to 73 MPa; these mechanical properties are determined according to the European Standard for cement testing (UNI EN 196 - part 1, 2005) considering two and four nominally identical specimens respectively for bending and compression. At about 150 days, the cubic compressive strength measured testing 32 specimens is found to be 95.1 MPa ($STD = 5.82\%$); this enhancement in the mortar mechanical properties was also found by Brameshuber et al. (2006), that measured an increase in the

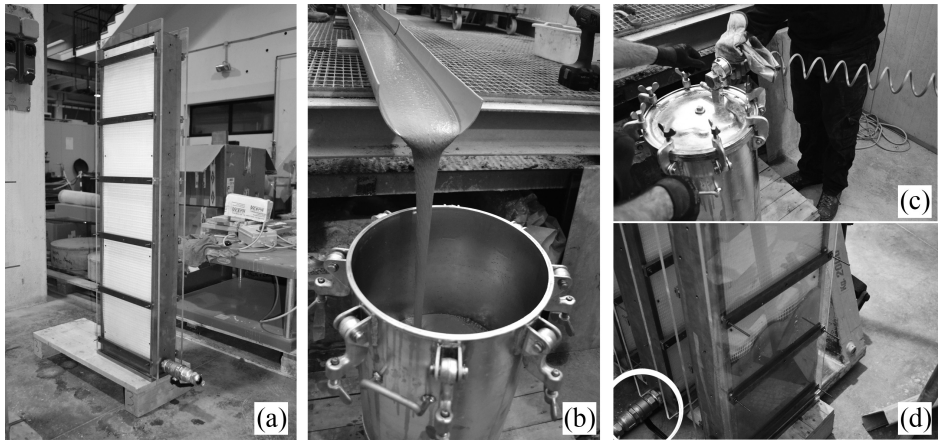

Figure 5.3: Casting of the sandwich beams: formwork with the EPS panel and the fabrics placed inside (a), tank filling (b), tank closure (c) and in-pressure injection of the mortar inside the framework (d).

compressive strength passing from 74 MPa at 28 days to 89 MPa at 90 days and 92 Mpa at 360 days, considering a matrix characterized by the same maximum aggregate size and cement type.

5.2 Four point load tests on small and big sandwich specimens

5.2.1 Geometry and test set-up

Four point bending tests are performed on sandwich beams using an electromechanical press INSTRON 5867 with a maximum load capacity of 30 kN. Two specimen geometries are taken into account: a small beam (550x150x120 mm^3; identified by "S" letter) and a larger one (1200x300x120 mm^3; identified by "B" letter). In all cases the fabric warp is aligned with the beam longitudinal direction. The specimen geometries and the test set-ups are shown both for small and

big specimens respectively in Figure 5.4(a) and 5.4(b); the measured cross-section sizes of each specimen are summarized in Table 5.1, in which specimen width (b) and height (h) as well as the thickness of the two TRC layers (h_{TRC}^{sup} and h_{TRC}^{inf}) are collected. Metallic plates 50 and 80 mm wide are glued on each specimen over the supports and under the knives through which the load is applied in order to reduce stress concentration. The loading and the supporting cylinders have a diameter equal to 40 mm and are free to rotate on their axis and around the plane perpendicularly to the longitudinal axis of the specimen.

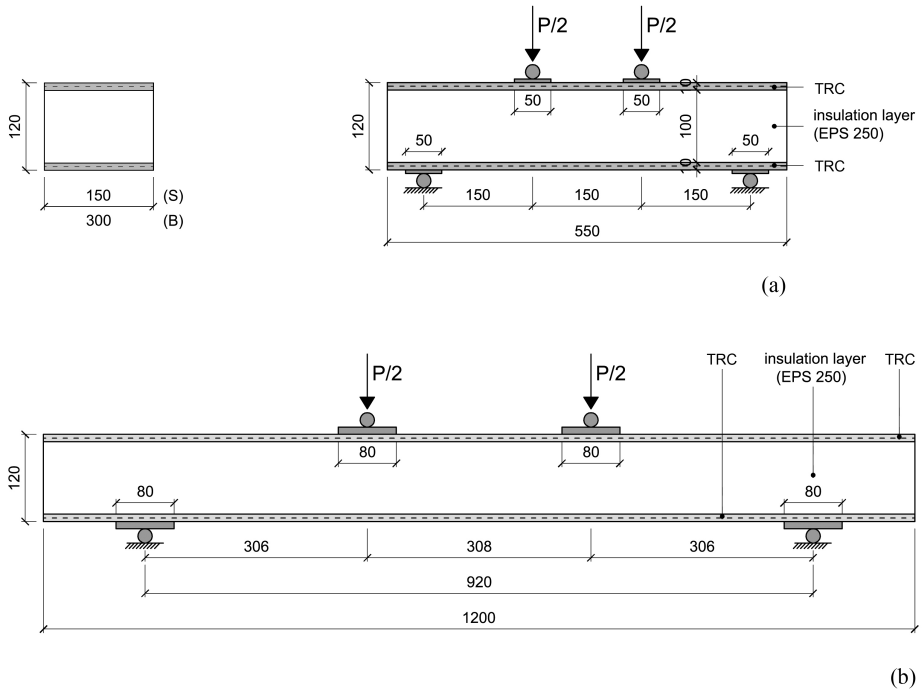

Figure 5.4: Sandwich beam geometry and test set-up (measures in mm): small "S" (a) and big "B" (b) specimen.

As shown in Figure 5.5, each specimen is instrumented with the following displacement transducers:

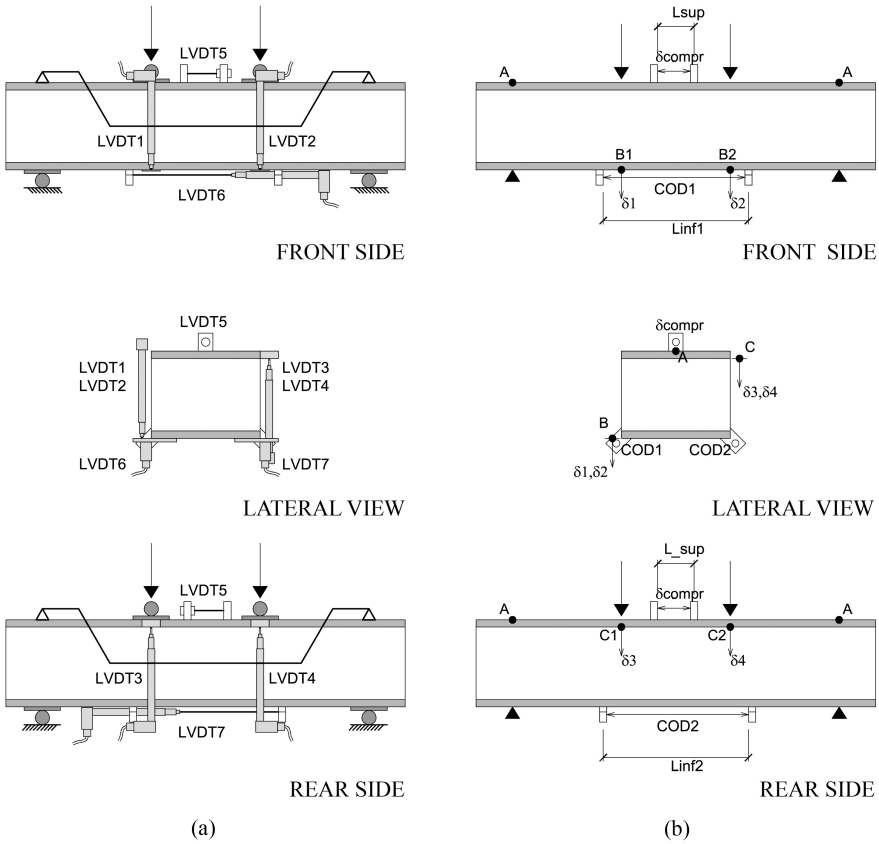

Figure 5.5: Geometry of the instrumented sandwich beam (a) and measures read by the instruments (b).

Table 5.1: Sandwich beams: sizes, peak load and corresponding vertical stroke, lengths of the gauges

Spec.	b $[mm]$	h $[mm]$	h_{TRC}^{sup} $[mm]$	h_{TRC}^{inf} $[mm]$	P_{max} $[kN]$	$stroke_{max}$ $[mm]$	L_{sup} $[mm]$	L_{inf1} $[mm]$	L_{inf2} $[mm]$
S1	147.5	122	11.8	9.7	7.66	30.31	51	195	195
S2	150.5	121.4	10.5	11.4	9.01	58.33	51	202	200
S3	150.2	122.2	9.7	12	9.19	79.85	53	201.5	201
S4	147.8	121.5	11.5	9.5	8.68	76.82	49	199	201
B1	302.5	121.8	9.9	11.7	16.31	41.91	100	399	395
B2	304.5	121.8	10.8	10.6	10.27	7.99	102	399.5	400.5
B3	300.5	121.2	11.7	8.4	16.38	52.99	103	399	402
B4	302	121.1	8.7	11.6	15.74	42.97	103	403.5	403

- LVDT1 and LVDT2 are placed in vertical position on the front side of the specimen and are aimed at measuring the specimen deflection under the loading knives (δ_1 and δ_2). The measured values δ_1 and δ_2 are the relative displacements of points B1 and B2 with reference to point A (Figure 5.5(b)). δ_{inf} is obtained as the mean value of δ_1 and δ_2.

- LVDT3 and LVDT4 are placed in vertical position on the rear side of the specimen and are aimed at measuring the deflection of the upper TRC layer under the loading knives (δ_3 and δ_4). δ_3 and δ_4 represent the relative displacement of points C1 and C2 with reference to point A. δ_{sup} is obtained as the mean value of δ_3 and δ_4.

- LVDT5 is placed on the upper TRC layer with a gauge length defined as L_{sup} (Table 5.1) in order to measure the superior longitudinal displacement (δ_{compr}) on the compressed side in the constant bending moment region.

- LVDT6 and LVDT7 are placed on each side of the lower TRC layer astride the constant bending moment region with a gauge length defined respectively as L_{inf1} and L_{inf2} (Table 5.1) for LVDT6 and LVDT7. These trans-

ducers are instrumental to measure the crack opening displacement (COD) on both the front (COD1) and the rear (COD2) side.

In order to not affect the deflection measures δ_{inf} and δ_{sup} by the crushing of the material at the supports, a proper frame is used. Two C profiles are placed on the upper surface of the specimen over the supports; on these profiles, two aluminium bars, carrying the transducers LVDT1, LVDT2, LVDT3 and LVDT4, are placed. All the transducers used are inductive full bridge type, with a nominal displacement equal to 10 mm, with the exception of the LVDT5 employed in the case of small specimens, that is an inductive half bridge with a nominal displacement of $+/-\ 1mm$. The data acquisition is performed by using the electronic measurement system SPIDER8 by HBM.

Four nominally identical tests were performed for both small and big specimens. Figure 5.6 shows a small and a big specimen during a test. The tests are displacement-controlled, considering the machine cross-head displacement (stroke) as feedback parameter and are performed by imposing an initial stroke rate of $1E-3\,mm/s$. After crack formation, in the second phase of the test, the rate is increased up to $4E-3\,mm/sec$.

(a) 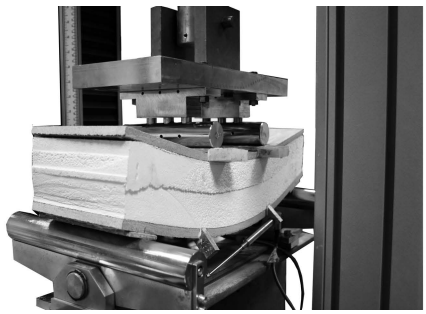 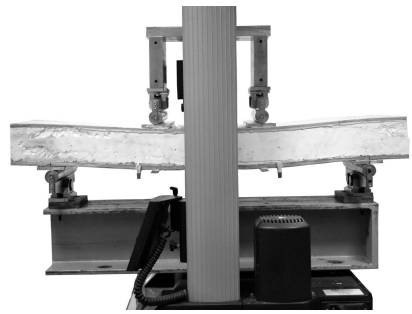 (b)

Figure 5.6: Specimens during testing: small "S" sandwich beam (a) and big "B" sandwich beam (b).

5.2.2 Experimental results

The results are shown in Figures 5.7 and 5.8 respectively for small and big specimens in terms of load vs. stroke and bending moment vs. nominal curvature curves. The bending moments are obtained by multiplying the load acting on one knife for the lever arm, while the nominal curvature is defined as:

$$\theta = \frac{\varepsilon_{inf} + \varepsilon_{sup}}{h} \tag{5.1}$$

with:

$$\varepsilon_{inf} = (\frac{COD1}{L_{inf1}} + \frac{COD2}{L_{inf2}}) \tag{5.2}$$

and:

$$\varepsilon_{sup} = \frac{\delta_{compr}}{L_{sup}} \tag{5.3}$$

The values of δ_{compr}, COD1 and COD 2 measured through the displacement transducers LVDT5, LVDT6 and LVDT7 are corrected before computing the curvature by taking into account that each instrument is not placed exactly on the specimen surface, but it is located at a certain distance. To correct these measures a rigid rotation assumption is considered.

Figures 5.9, 5.10 and 5.11 show the pictures of the specimens after test both for small and big specimens.

Looking both the load-stroke curves and the pictures, it is worth noting that the test on specimen S1 was stopped due to external causes before reaching the failure, while specimen B2 presented an early shear failure due to the presence of a small connector used to fix the fabric to the insulation material, that acted as a local defect in the EPS. Besides, in the case of specimen B1, a knife release

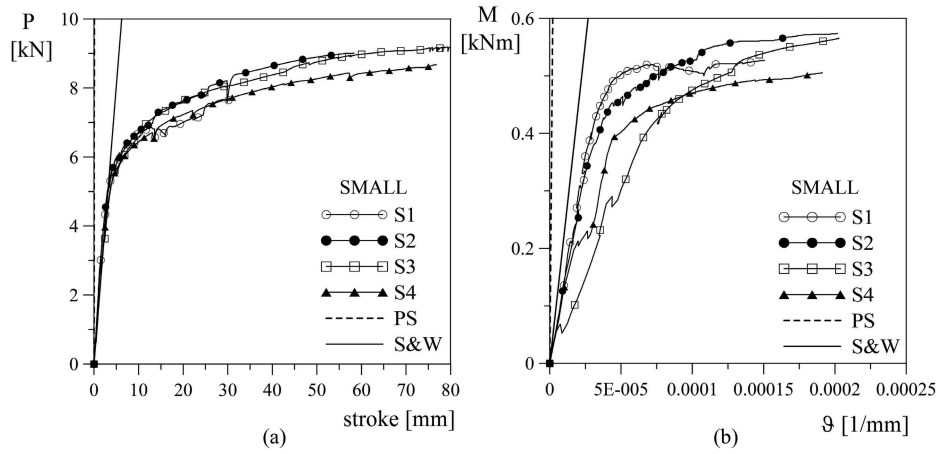

Figure 5.7: Test results: load vs. stroke (a) and bending moment vs. nominal curvature (b) curves for small "S" specimens.

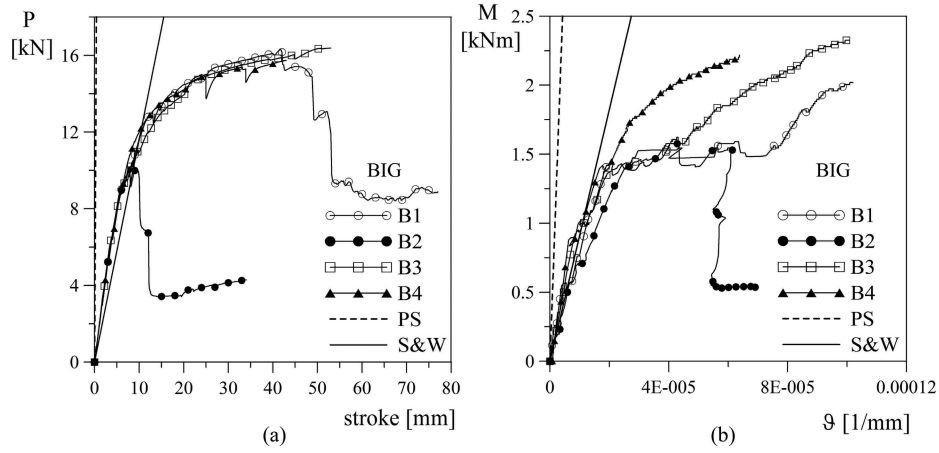

Figure 5.8: Test results: load vs. stroke (a) and bending moment vs. nominal curvature (b) curves for big "B" specimens.

occurred, causing the upper TRC punching.

Considering the load-stroke graphs, in both cases the results are characterized by a good repeatability, especially in the initial phase; the scatter remains very limited also in the second branch of the curve (st. dev. less than 5%). The maximum load (P_{max}) reached by each specimen, together with the corresponding displacement ($stroke_{max}$), is summarized in Table 5.1.

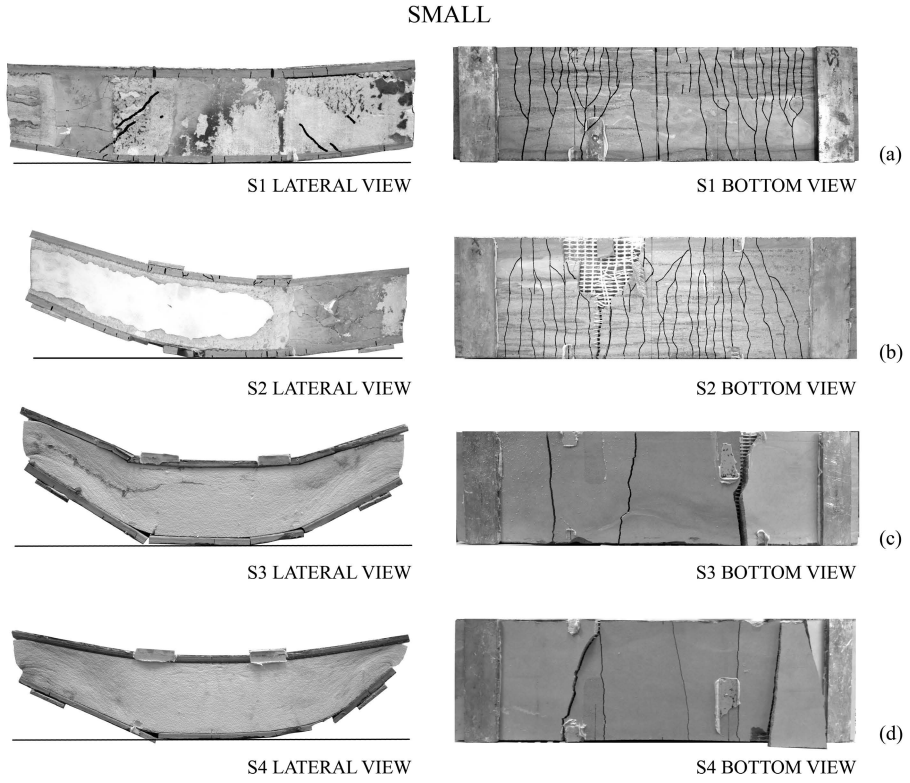

Figure 5.9: Lateral and bottom view of small "S" specimens after test: S1 (a), S2 (b), S3(c) and S4 (d).

Considering small specimens (Figure 5.9), it is possible to observe that multi-cracks occurred in both the upper and the lower TRC layers, hence each specimen

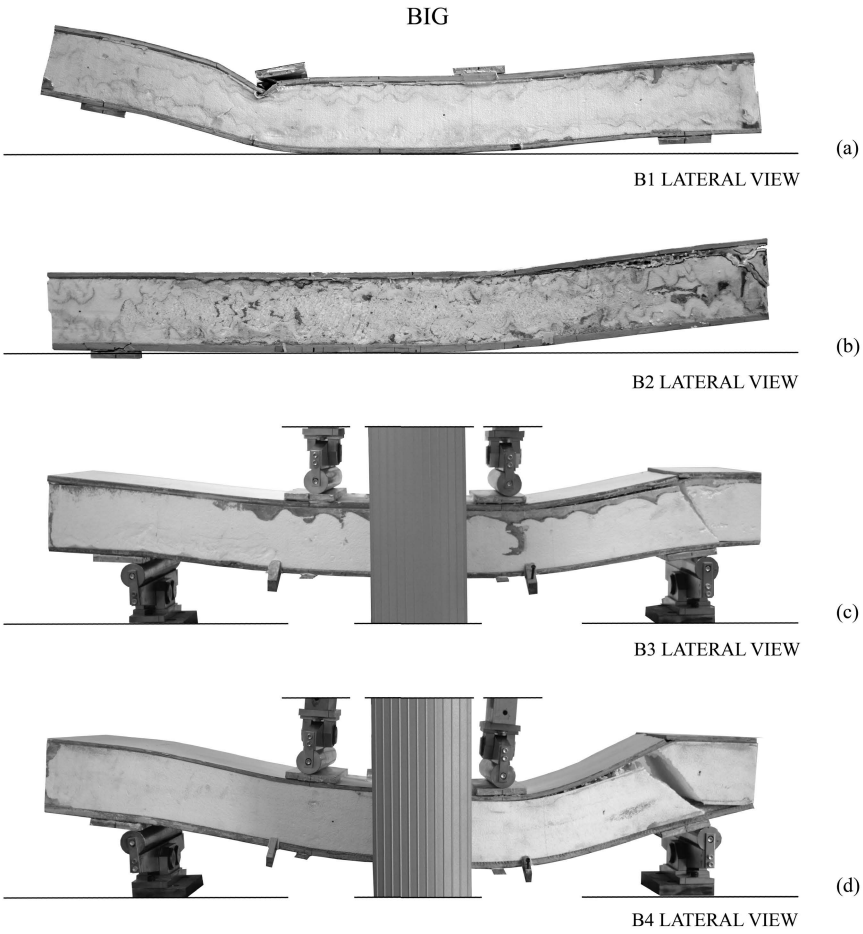

Figure 5.10: Failure mode of big "B" specimens: B1 (a), B2 (b), B3(c) and B4 (d).

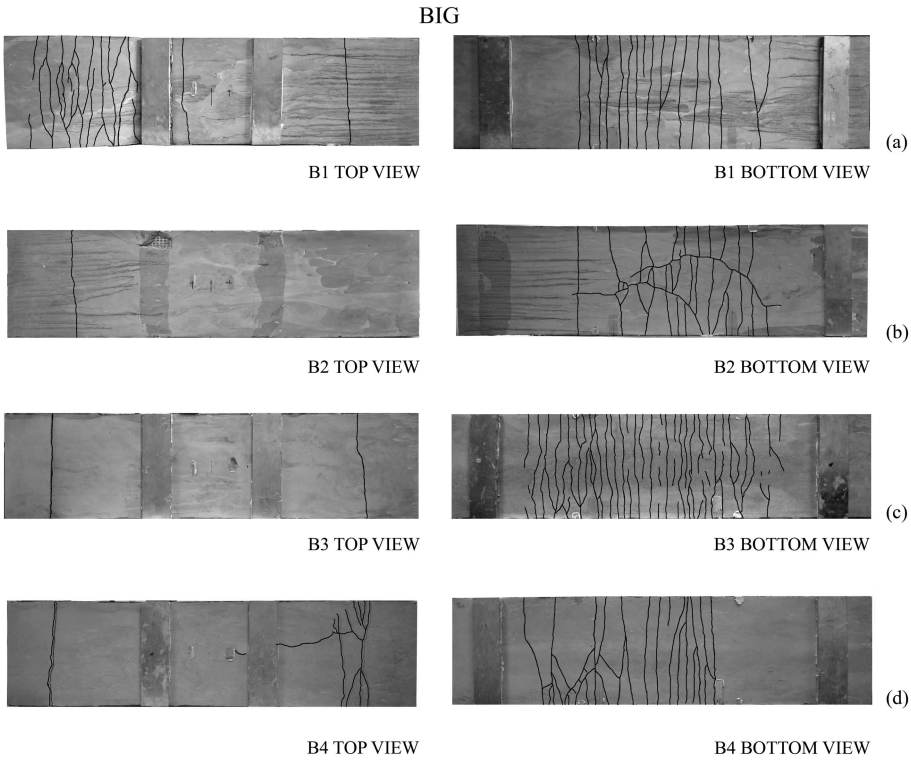

Figure 5.11: Crack pattern of big "B" specimens on the top and bottom sides: B1 (a), B2 (b), B3(c) and B4 (d).

behaves as a partially composite panel [Einea et al. (1991)]: the insulation layer can transfer just a percentage of the longitudinal shear required for a fully composite panel. In the upper TRC face the multi-cracking took place under the plates used to distribute the load and to reduce stress concentration. Looking at the lower TRC face, it is possible to note that, even if the multi-cracking phenomenon occurred in all the specimens, in cases S1 and S2 cracks are quite close (cracking space equal to about 15 mm), while in cases S3 and S4 only few larger cracks developed. The difference in the crack pattern may be related to the fabric position inside the lower TRC layer. As a matter of fact, specimens that experienced a more dense crack pattern (S1 and S2) are characterized by the fabric placed in the middle of the layer or closer to the external surface. For the situations in which the fabric remained close to the EPS (S3 and S4), a larger crack distance is observed (Figure 5.9(c) and (d)).

However, the ultimate failure mechanism is the same in all the cases and the global response is characterized by a good repeatability. Taking a careful look to the crack pattern of specimens S1 and S2, it is possible to observe that cracks are not symmetric with respect to the longitudinal axis: this lack of symmetry may be due to a small penetration of mortar on just one of the lateral side of the specimen, thus creating a very thin (less than 1 mm) lateral layer of mortar on just a portion of the side itself. This thin layer causes a difference in the stiffness between rear and front side, thus compromising the symmetry of the crack pattern. The ultimate failure of the small specimens (specimens S2, S3 and S4) occurred when the tensile failure of the lower face is achieved, even if the mechanism that mainly contributes to the non-linear behaviour of the response is the plastic shear deformation of the core.

Looking at crack patterns in Figure 5.11 , also big specimens behave as partially composite panels since they present the multi-cracking phenomenon on both the TRC layers; some differences can be identified if the behaviour is compared

with the small specimen one. First of all, even if the shear band formation in EPS is noticeable and contribute to the non-linearity of the response, the bending behaviour is more important if compared with the small specimens. Some cracks appear also on the upper surface of the specimens (Figure 5.11, top view), thus indicating that tensile stresses arise on the extrados of the upper TRC layer close to the supports. These tensile stresses can be justified considering the upper TRC layer as a thin beam laying on a continuous deformable support that experiences a negative (upper surface in tension) bending moment close to the supporting cylinders. The number of cracks on the upper TRC layer is related to the mortar thickness. In both the big specimens that reached the ultimate failure (B3 and B4), this failure is governed by the development of a shear crack in the EPS layer over one support (Figure 5.10). The main shear crack also propagates longitudinally along the specimen, leading to the debonding between TRC and EPS.

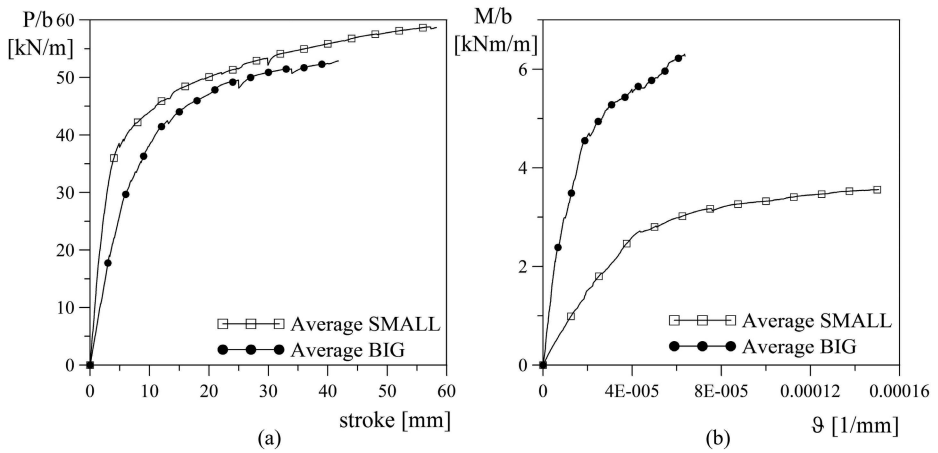

Figure 5.12: Test results: specific load vs. stroke (a) and specific bending moment vs. nominal curvature (b) average curves.

The load vs. crosshead displacement behaviour of the two different solutions

is compared in Figure 5.12(a) by normalizing the applied load with the specimen width. The average curves of nominally identical tests for each solution are reported in this figure. It is worth noting that both the solutions are characterized by a comparable behaviour and, in particular, the final plastic branch is very similar, thus indicating that the shear behaviour of both the solutions plays a key role in the overall response of the specimens.

Concerning the moment vs. nominal curvature behaviour of the two solutions investigated (Figures 5.7(b) and 5.8(b)), it is important to underline that each curve is stopped when one of the displacement transducers involved in the computation of the curvature (LVDT5, LVDT6 or LVDT7) reached its maximum displacement, that always happened before the ultimate failure of the specimens.

The two solutions are compared in Figure 5.12(b) in terms of specific moment vs. nominal curvature, where the specific moment is computed dividing the bending moment by the specimen width. The curves plotted are the average curves of nominally identical specimens. It is worth to remind that the nominal curvature is computed in the constant bending moment region between the loading knives. Large differences between the two solutions can be observed: the final plastic branch is characterized by a larger specific moment value in the case of big specimens, thus indicating a more significant contribution of bending. Even the initial stiffness of the two average curves is quite different. In order to better discuss this difference, two analytical solutions for the elastic behaviour of sandwich beam are adopted to predict the elastic stiffness of the two specimen geometries: the plane section (PS) approach and the Stamm & Witte (S&W) model [Stamm and Witte (1974)]. Both of them were discussed in Subsection 2.7. In both cases linear elastic materials, perfect bond between the EPS and the TRC layers, no compressibility of the sandwich beam and small displacement and strain are considered.

The first model is based on the assumption that the section remains plane and,

hence, there is a linear strain distribution over the cross section ($\vartheta_{EPS} = \vartheta_{TRC}$, Figure 5.13); the shear deformations (γ_{xz}, considering x as the longitudinal axis and z the vertical one) of both TRC and EPS layers are assumed to be negligible. The elastic stress distribution over the cross-section is reported in Figure 5.13.

The second model, proposed by Stamm and Witte (1974), is based on the following assumptions (Figure 5.13):

- the EPS core is soft if compared with the outer TRC layers, hence σ_x^{EPS} can be taken equal to zero while τ_{xz}^{EPS} is constant;
- the bending stiffness of the outer TRC layers is not negligible if compared to the one of the whole sandwich beam, hence the membrane state of stress of these outer layers due to sandwich global behaviour has to be superimposed on the local bending state of each external layer;
- the shear stiffness of the outer TRC layers is large, hence TRC shear deformations γ_{xz}^{TRC} can be neglected; the cross sections of the outer layers thus remain planar and perpendicular to the axis even after the deformation (Bernoulli hypothesis);
- due to the shear deformation of the EPS core, the total cross section of the sandwich beam is not flat, but it deforms to a broken line.

The results obtained for the two different models are plotted in Figures 5.7 and 5.8 respectively for small and big specimen solutions. An elastic behaviour is considered in both the models: an elastic modulus of 13.7 MPa is adopted for EPS according to experimental results, while a value of 30 GPa is considered for the TRC according to literature results on cement matrix characterized by similar compressive strength and maximum aggregate size [Brameshuber et al. (2006)]. Just in the case of S&W model, a EPS shear modulus equal to 4.14 MPa

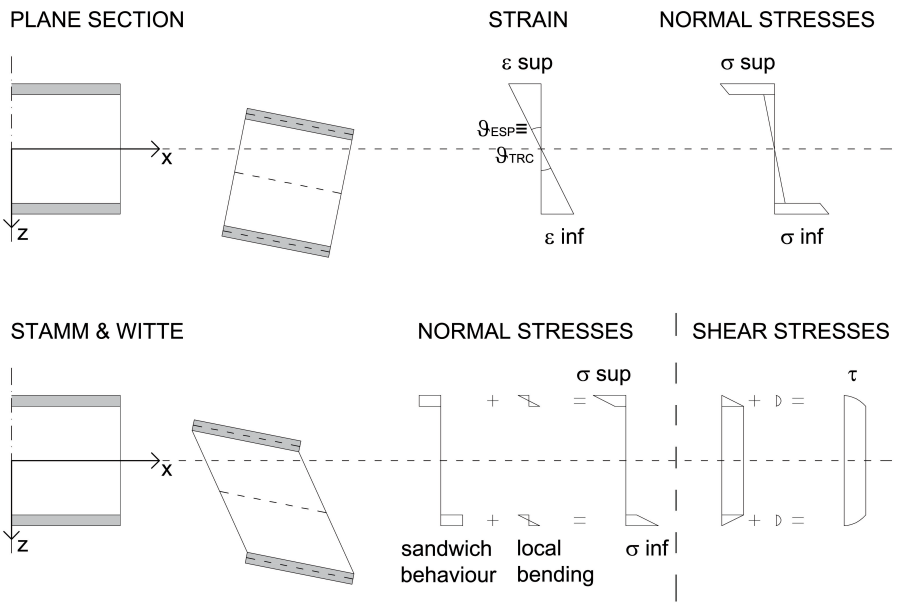

Figure 5.13: Assumptions of the analytical solutions adopted to predict the elastic behaviour of the sandwich beams: Plane Section (PS) and Stamm & Witte (S&W) models.

is assumed (lower value proposed by ASTM C 578-92 - "Standard Specification for Rigid, Cellular Polystyrene Thermal Insulation" - for this class of EPS).

Looking at the results, it is clear that the plane section assumption, that neglects the EPS shear deformability, is not able to provide a reliable prediction of the sandwich stiffness. Only considering the behaviour of a partially composite beam, as suggested by Stamm and Witte (1974), it is possible to predict the initial linear global response of the composite both in terms of vertical displacement and nominal curvature. It is worth to note that the nominal curvature of the models was computed in the same way used for experimental results (Eq. 5.1) once the strain of TRC at the extrados and at the intrados of the specimen is known. The reliability of the S&W approach allows to conclude that the difference observed

in Figure 5.12(b) is mainly related the EPS shear deformability. Furthermore, the large difference between PS and S&W approaches is more pronounced in the case of small specimens, thus confirming the most important shear deformation contribution in this case.

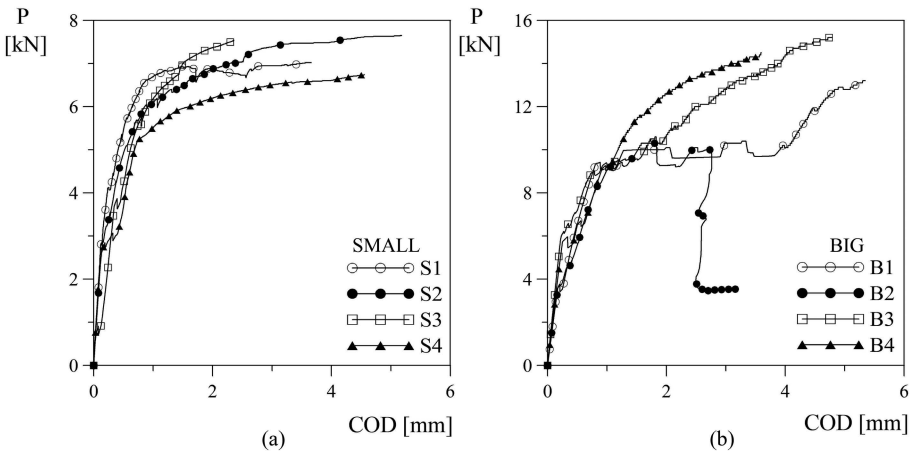

Figure 5.14: Test results: load vs. Crack Opening Displacement curves for small "S" (a) and big "B" (b) specimens.

The behaviour of the two different geometries tested is represented in Figure 5.14 by means of the load vs. crack opening displacement (COD) curves; the large COD measured are representative of the multicracking pattern experienced by the lower TRC layer. It is important to note that the cracking of the lower TRC layer does not clearly correspond to a significant non-linearity in the global response of both the specimen geometries considered; as a matter of fact, when a COD measure of 0.5 mm is read, the TRC is clearly cracked, but the global load vs. COD curve is still linear. It is also worth to note that typical multi-crack formation branch available in the classical uniaxial tensile response of a TRC (Figure 3.5) is not observable in the global response of the specimens, maybe due to a stabilization effect given by both the EPS and the sandwich behaviour.

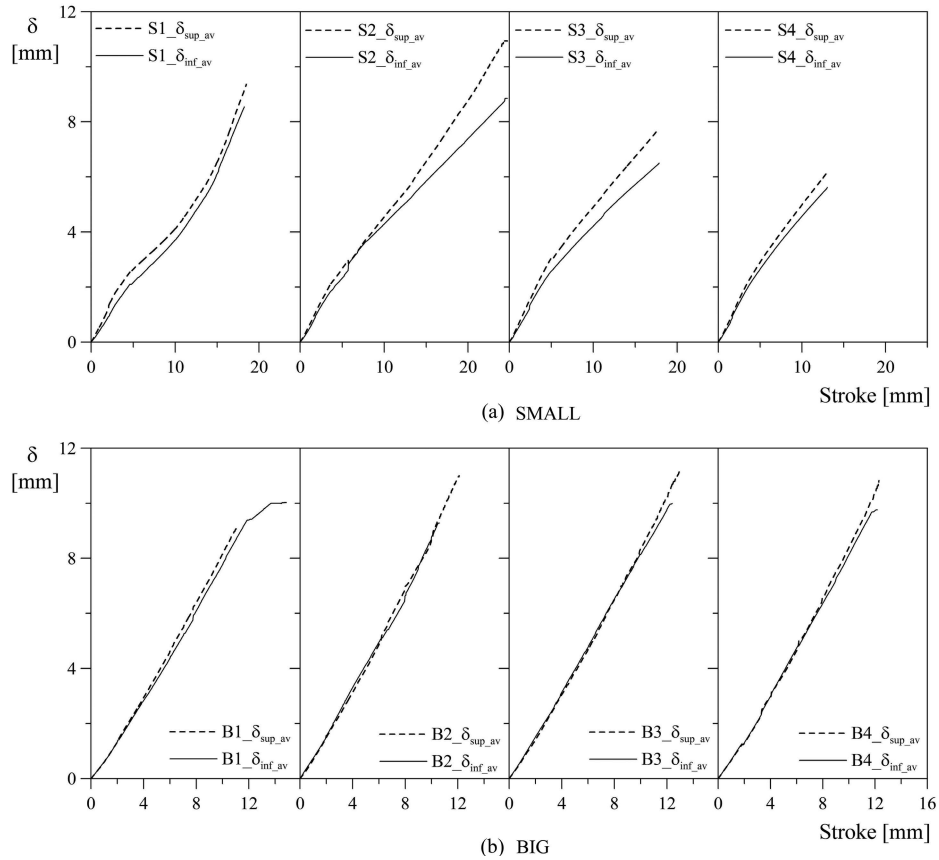

Figure 5.15: Test results: superior and inferior displacement vs. stroke curves for small "S" (a) and big "B" (b) specimens.

Finally, Figure 5.15 presents the measurements of the different vertical displacements under the loading knives for each test. δ_{sup_av} represents the average between the top layer displacements (δ_3 and δ_4), while δ_{inf_av} is the mean value of the bottom layer displacements (δ_1 and δ_2). It is clear that, since the beginning, small specimen experiences a larger transverse compression (ε_z) of the EPS, thus indicating that this specimen mainly behaves as a 2D body and that the 1D beam assumption ($\varepsilon_z = 0$) is not reliable for this geometry. This transverse compression can be also clearly observed in the deformed shape at failure (Figure 5.9), especially on the lateral part of the specimen.

On the contrary, negligible transverse strain (ε_z) can be observed for big specimens, indicating that two dimensional effect disappears for larger span and the sandwich solution respects the 1D beam assumption.

5.3 Concentrated load tests on sandwich specimens

5.3.1 Geometry and test set-up

Square sandwich plates 300x300x120 mm^3 are tested with a proper set-up in order to verify their resistance when loaded with a concentrated load. The same electromechanical press adopted in bending tests is used. During the test the specimen is simply supported on all the four edges of the bottom face (free length equal to 190 mm in both the directions) and is loaded in the center of the upper face by means of a steel cylinder punch with a diameter of 19 mm (Figure 5.16). A LVDT displacement transducer, with the same characteristics of those used for sandwich beams, is placed in contact with the bottom surface of the specimen in order to measure the vertical displacement δ_2 shown in Figure 5.16(a). The tests are displacement-controlled, considering the machine cross-head displacement (stroke) as feedback parameter, and are performed by imposing an initial

stroke rate of $1E-3\,mm/s$.

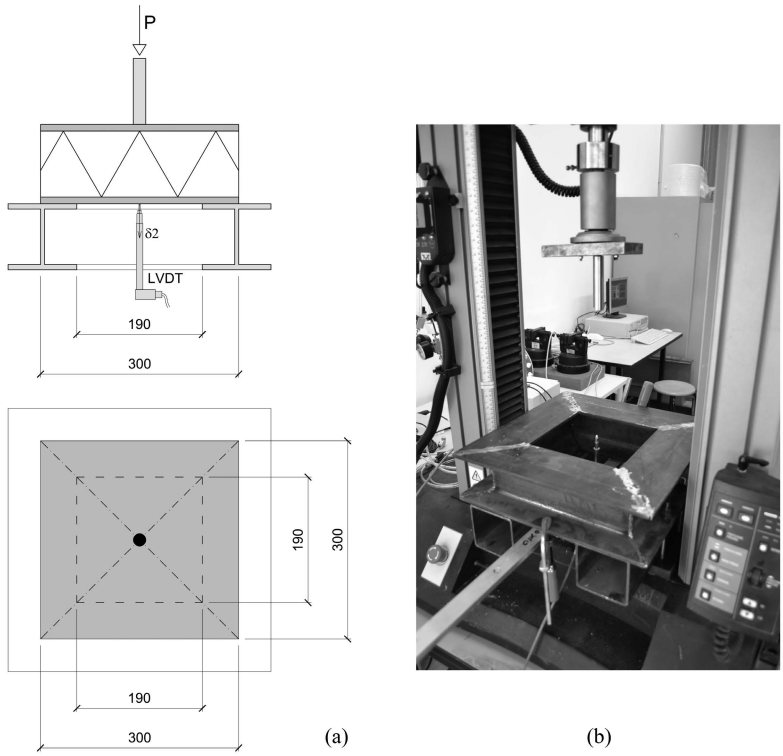

Figure 5.16: Concentrated load test set-up: geometry (a) and picture (b).

The geometrical characteristics of each specimen are collected in Table 5.2; in particular the following measures are shown: the thickness of the upper TRC layer (h_{TRC_sup}), the thickness of the lower TRC layer (h_{TRC_inf}), the thickness of the EPS layer (h_{EPS}) and the length in both directions (b_1 and b_2). The thickness of each layer is obtained as the mean value of several measures done in different points.

Looking at the upper surface of specimen P4 before performing the test, it

Table 5.2: Geometrical characteristics of the specimens and experimental results

	$P1$	$P2$	$P3$	$P4$
$h_{TRC\_sup}[mm]$	11.1	10.4	11.0	10.0
$h_{TRC\_inf}[mm]$	9.7	10.5	10.2	10.7
$h_{EPS}[mm]$	100.0	99.9	99.5	99.5
$b_1[mm]$	302.0	300.5	301.5	300.8
$b_2[mm]$	295.0	296.8	296.8	299.0
$P_{max}[kN]$	5.60	4.45	5.20	4.60
$\delta_u[mm]$	2.69	2.33	3.05	3.32
$\delta 2_u[mm]$	0.35	0.25	0.47	0.23

was possible to observe some cracks (crack pattern visible in Figure 5.17). These cracks could be seen by visual inspection; in fact, the crack width measured was equal to 125 μm.

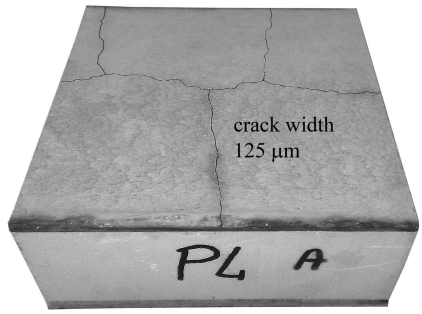

Figure 5.17: Crack pattern of the upper surface of specimen P4 before testing.

In Figure 5.18 two pictures of a specimen during a test are displayed: sub-figure (a) shows the specimen in the initial phase of the test, while sub-figure (b) shows the specimen at failure.

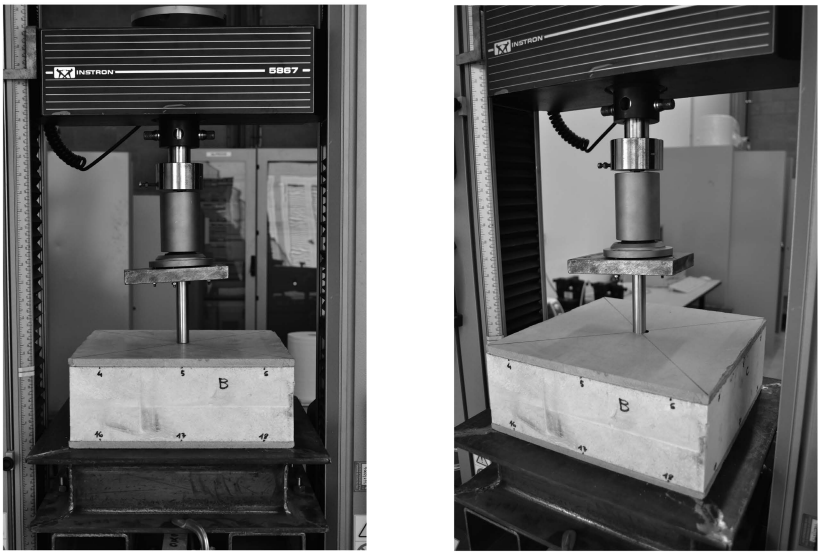

(a) (b)

Figure 5.18: Specimen during the concentrated load test: in the initial phase (a) and at failure (b).

5.3.2 Experimental results

The experimental curves obtained for each specimen are collected in Figures 5.19 and 5.20 in terms of load vs. stroke and load vs. $\delta 2$ vertical displacement curves respectively. A superposition of the load vs. stroke curves is presented in Figure 5.21. The maximum load measured for each specimen (P_{max}), together with the corresponding stroke (δ) and bottom displacement ($\delta 2$), is collected in Table 5.2. In Figure 5.22 the crack pattern of each specimen after test is shown.

Looking both at the experimental curves and at the crack patterns, it is possible to identify two main failure mechanisms governing the behaviour of the sandwich solution when subjected to a concentrated load:

- the formation of a circular crack (diameter of about 150 mm) in the upper

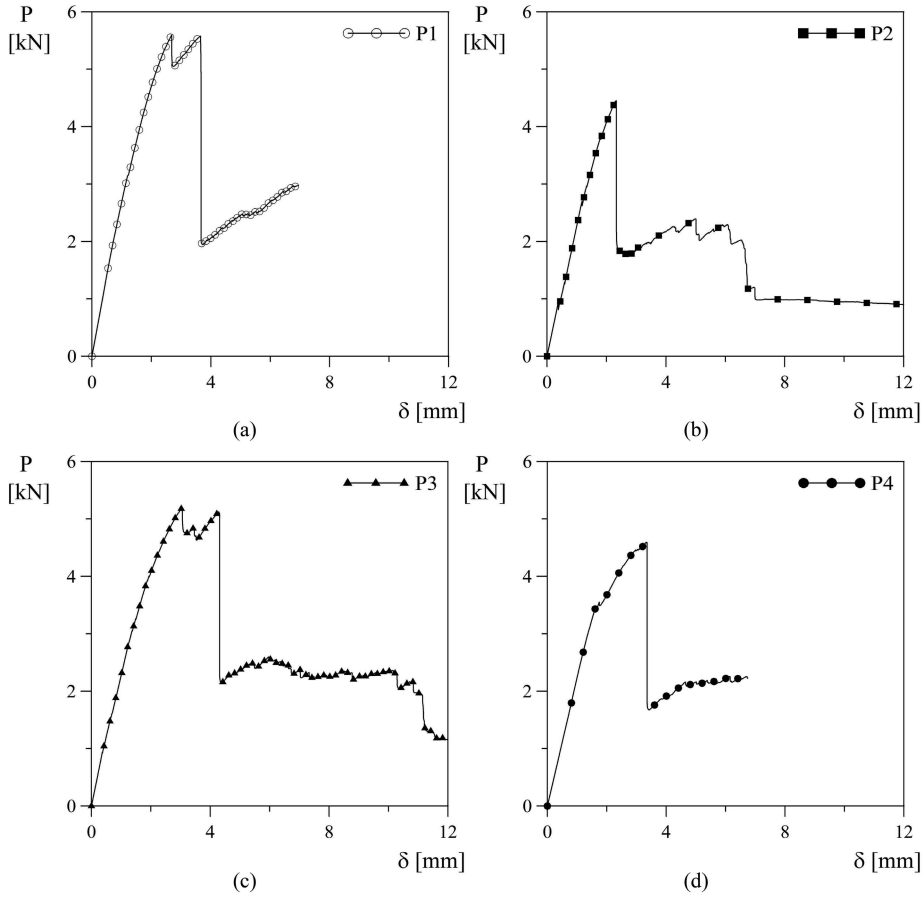

Figure 5.19: Concentrated load test results: load vs. stroke curves for specimen P1 (a), P2 (b), P3 (c) and P4 (d).

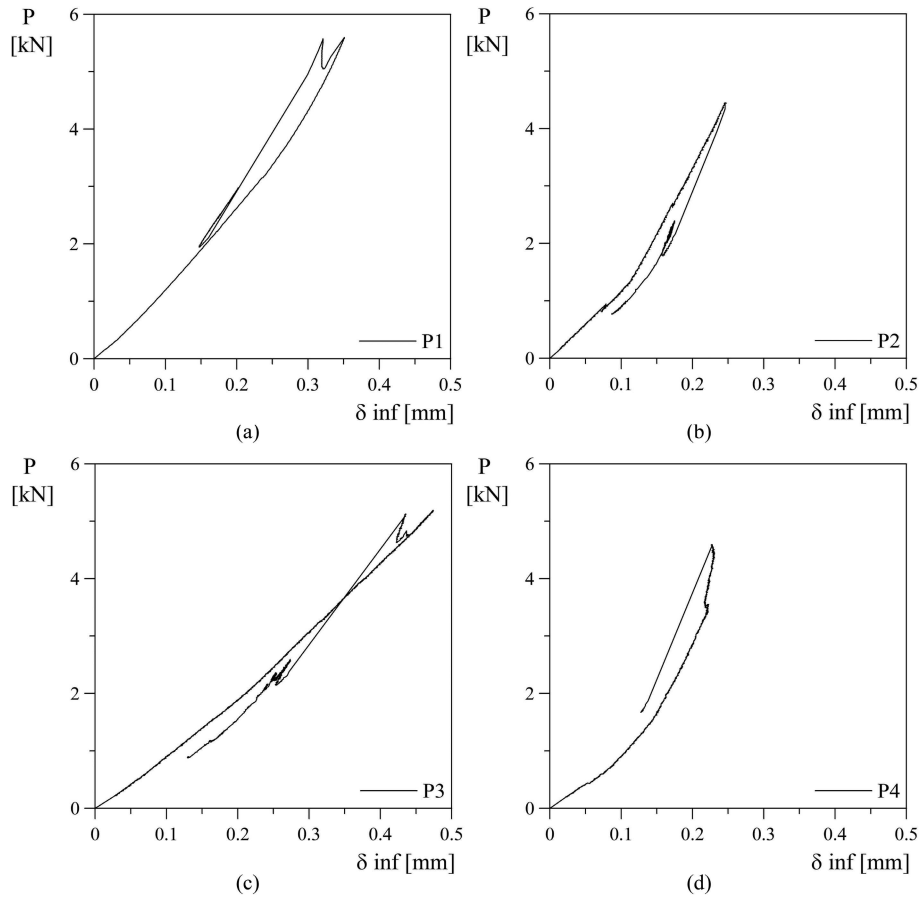

Figure 5.20: Concentrated load test results: load vs. vertical displacement $\delta 2$ (δ_{inf}) for specimen P1 (a), P2 (b), P3 (c) and P4 (d).

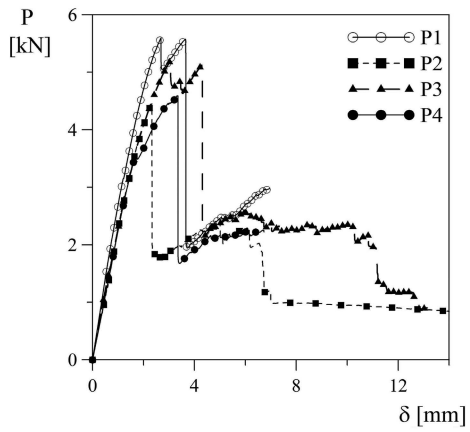

Figure 5.21: Concentrated load test results: superposition of the load vs. stroke curves.

TRC layer;

- the development of a diagonal crack following the surface of a truncated cone (punching shear failure) where the load is applied.

In particular, the former occurs in specimens P1, P3 and P4, while the latter occurs in all the cases and it is responsible for the sudden and pronounced load decrease, after which the upper TRC layer is completely failed. A residual load is still carried by the EPS layer, that is crushing, and by the lower TRC layer.

A common behaviour characterizes specimens P1 and P3:

- initial bending of both the TRC layers up to the peak load ($\delta 2$ lower than δ because of the EPS crushing);
- development of the circular crack with diameter of about 150 mm in the upper TRC layer: during the load decrease due to cracking, an elastic recovery of the vertical displacement $\delta 2$ occurs;
- going on with the test and imposing an increasing stoke to the upper TRC

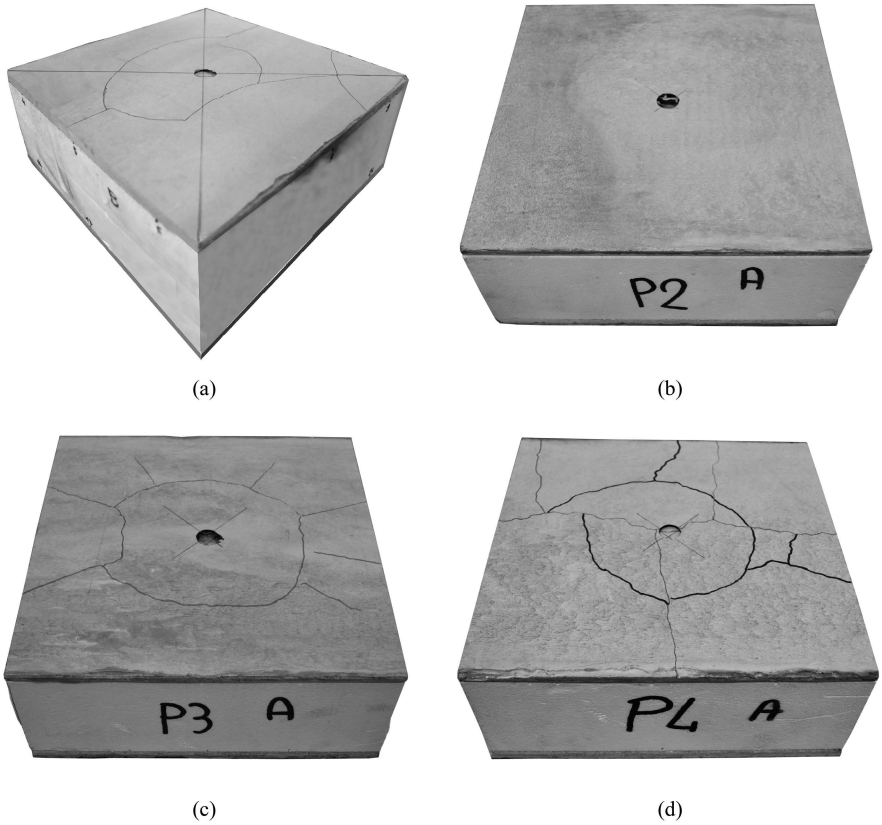

(a) (b) (c) (d)

Figure 5.22: Crack pattern after test: specimen P1 (a), P2 (b), P3 (c) and P4 (d).

layer, no further increase of the bottom TRC layer displacement is registered (the circular crack on the upper TRC layer works as a plastic hinge and the EPS works as an elastic soil);

- when the peak load is reached again, a circular crack (with a diameter equal to that of the loading cylinder) forms on the upper TRC layer, it propagates along the surface of a truncated cone and the failure of this TRC layer occurs. The bottom TRC layer elastically recovers another part of the displacement $\delta 2$ previously registered;
- imposing an increasing stroke, the crushing of the EPS under the failure cone causes an increase of both the load and the displacement $\delta 2$.

In specimen P4 the load at which the large circular crack develops (around 3.5 kN) is lower than the peak load measured in the test (4.6 kN), at which the punching shear failure occurs. Furthermore, no load decrease due to cracking is observed, but just a change in the slope of the global response is visible. A possible reason is the presence of pre-existing cracks on the upper TRC layer before performing the test (as shown in Figure 5.17).

Looking at the behaviour of specimen P2, it is possible to note that just one mechanism (the development of the diagonal crack along the cone surface) takes place and, in fact, just one peak is visible both in Figure 5.19(b) and in Figure 5.20(b). After the punching shear failure the upper TRC layer is completely failed, hence the other mechanism (the formation of the circular crack) can not take place. This fact can be explained considering that the activation of the two mechanisms probably occurs at the same stress level reached in the concrete. This is also reflected by the fact that, for specimen P1 and P3, the two failure modes occur at the same peak load.

To evaluate this possibility, the state of stress for a certain load value is estimated in the upper TRC layer following two approaches, in order to un-couple

the two phenomena. The value assumed for the concentrated load is equal to 5.4 kN; considering the two specimens that showed the common behaviour described above (P1 and P3), 5.4 kN represents the load at which both the circular crack formation and the punching shear failure occur.

The solution proposed by Westergaard (1926) concerning a rectangular plate laying on an elastic foundation is used to estimate the negative bending moment acting on the upper surface of the TRC layer. The peak of this negative moment is equal to about 108 Nmm/mm ($M/P \simeq 0.02$, Figure 5.23). According to Westergaard, the negative moment peak takes place at a distance from the load application point equal to $2l$, where l is computed according to the following formula:

$$l = \sqrt[4]{\frac{E \cdot h^3}{12(1-\nu^2)k}} \tag{5.4}$$

in which

- E represents the Young modulus of the concrete and it is assumed equal to 30000 MPa;
- h is the TRC layer nominal thickness, equal to 10 mm;
- ν is the Poisson's coefficient, assumed equal to 0.2;
- k represents the modulus of subgrade reaction; it is computed dividing the EPS elastic modulus (13.7 MPa) by the EPS thickness (100 mm) and it results equal to 0.137 N/mm^3.

Hence, according to Westergaard, the circular crack due to negative bending

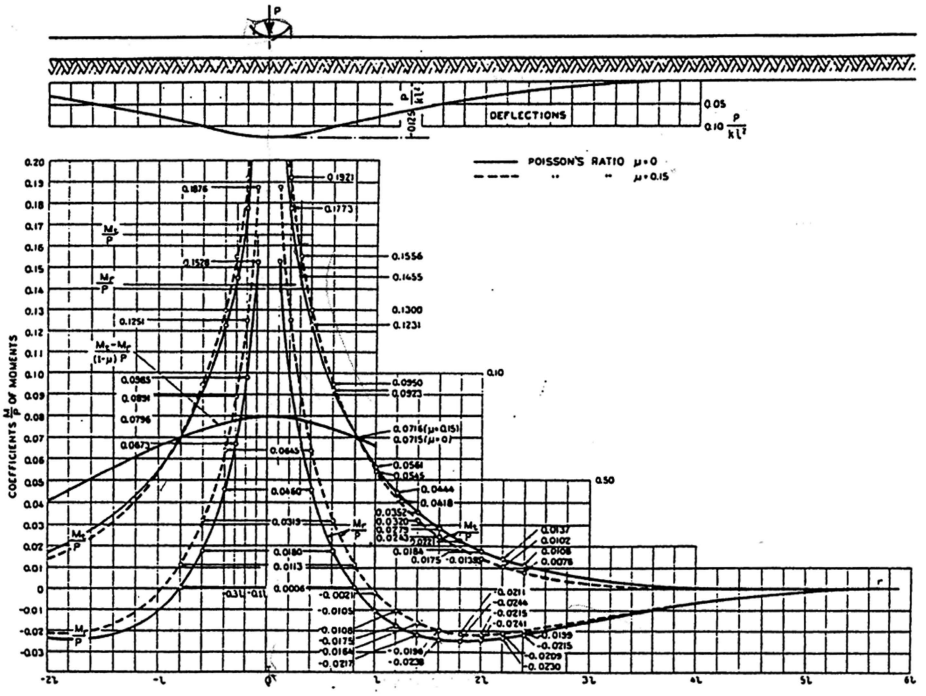

Figure 5.23: Tangential and radial bending moment produced by a concentrated load which acts at a point of the interior at a considerable distance from the edges [Westergaard (1926)].

moment results located at 132 mm from the load application point. The level of stress corresponding to the specific bending moment is equal to about 6.5 MPa.

In order to estimate the state of stress available in the concrete when the punching shear failure occurs, the upper TRC layer is modeled in Abaqus FEA software considering just the central portion of the concrete slab (100x100x10 mm^3). The material is assumed elastic, with an elastic modulus equal to 30000 MPa and a Poisson's coefficient equal to 0.2. The modeled part of the plate is assumed to be simply supported on all the lower surface, with exception of a central portion with diameter equal to 39 mm (assuming a slope of the truncated

cone surface of 45 degrees), and it is loaded with a distributed load over the area corresponding to the loading cylinder. The loading condition with constrains and the mesh adopted are shown in Figure 5.24.

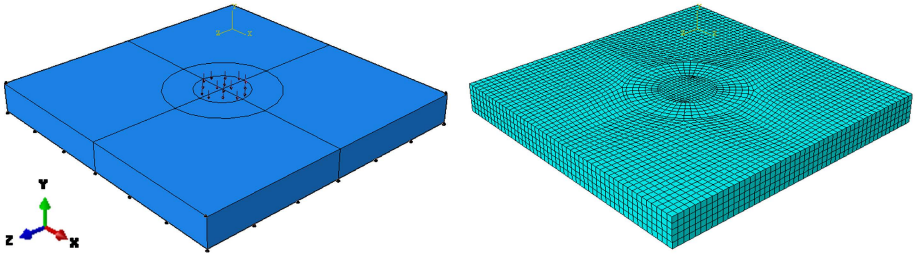

(a) (b)

Figure 5.24: Portion of the plate modeled in Abaqus: geometry with loads and constrains (a) and mesh (b).

The development of the crack along the surface of a truncated cone is clearly visible in Figure 5.25, in which the minimum principal stresses are plotted. The value of stress leading to this failure is equal to about 7.5 MPa.

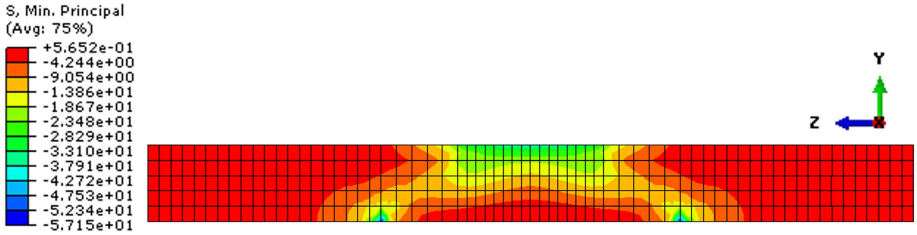

Figure 5.25: Minimum principal stresses in the mid-section of the plate, central portion.

Summing up, the level of stress in the upper TRC layer is estimated to be equal to 6.5 MPa for the circular crack formation and to 7.5 MPa for the punching shear failure. Considering that the bending tensile strength f_{ctf} experimentally measured for the matrix is equal to 13.5 MPa, both these values are close to

the tensile strength of the cementitious matrix, that can be assumed equal to 4.7 MPa (Equations 4.1 and 4.2, considering α_{fl} equal to 0.04 as discussed in Section 4.1.1). Therefore, it can be assumed that the activation of one mechanism rather than that of the other mainly depends on the presence of local defects in the concrete matrix.

page intentionally left blank

6

Environmental effect

In this Section the influence of freezing-thawing phenomenon on the behaviour of sandwich beams is investigated. The specimens considered are small "S" sandwich beams, nominally identical to those presented in Section 5.

48 hours after the in-pressure casting, specimens are demoulded and then cured in air for at least 28 days. The air condition is that of a laboratory with temperature ranging between 18 and 22 ℃ during winter and between 22 and 27 ℃ during summer; the related relative humidity ranges respectively between 40-60% and 50-80%. Table 6.1 summarizes all the dates related to the specimen history (the specimen identification is explained in the following).

Afterwards, the specimens are treated in a climatic chamber following the same procedure A of ASTM International C666/C 666M - 03 "Standard Test Method for Resistance of Concrete to Rapid Freezing and Thawing" used for TRC specimens (Section 4.2). The range of temperature varies between +4 ℃ and -18 ℃ with both cooling and heating rate equal to 11 ℃/h and a 30 minutes rest phase both at +4 ℃ and at -18 ℃ (Figure 4.12). Just one TRC layer of each specimen is immersed in water, icing and de-icing during thermal cycles (Figure

Table 6.1: Specimen history: dates of casting, pre-cracking, beginning and end of cycles and performing of the test

Spec.	*Casting*	*Pre cracking*	*Beginning of cycles*	*End of cycles*	*4PL− test*
S_U150_1	18/12/2012	-	09/01/2013	09/02/2013	14/02/2013
S_U150_2	18/12/2012	-	09/01/2013	09/02/2013	19/02/2013
S_U500_1	21/03/2013	-	14/02/2014	25/06/2014	30/06/2014
S_U500_2	21/03/2013	-	14/02/2014	25/06/2014	08/07/2014
S_U500_3	21/03/2013	-	14/02/2014	25/06/2014	02/07/2014
S_C500_1	21/03/2013	05/02/2014	14/02/2014	25/06/2014	04/07/2014
S_C500_2	21/03/2013	05/02/2014	14/02/2014	25/06/2014	09/07/2014
S_C500_3	21/03/2013	05/02/2014	14/02/2014	25/06/2014	01/07/2014

6.1 (a)); this choice is due to the fact that, in a real panel applied on a façade, just the external TRC layer is exposed to rain. Specimens exposed to 150 and 500 cycles are considered; in particular the following scenarios are taken into account:

- un-cracked specimens subjected to 150 cycles;
- un-cracked specimens subjected to 500 cycles;
- pre-cracked specimens subjected to 500 cycles (pre-cracking phase performed before the exposure to freezing-thawing cycles).

Figure 6.1 (b) shows the distribution of the specimens in the climatic chamber both in section and plan view.

Each specimen is identified trough the following notation: letter "S", that indicates that small sandwich beams are involved; a letter, that specifies if the specimen was un-cracked (U) or pre-cracked (C) when thermally treated; a number, that stands for the number of cycles the specimen was exposed and another number that denotes the nominally identical specimens (e.g. S_U500_2 stands for small sandwich beam, un-cracked specimen treated trough 500 cycles, specimen number 2).

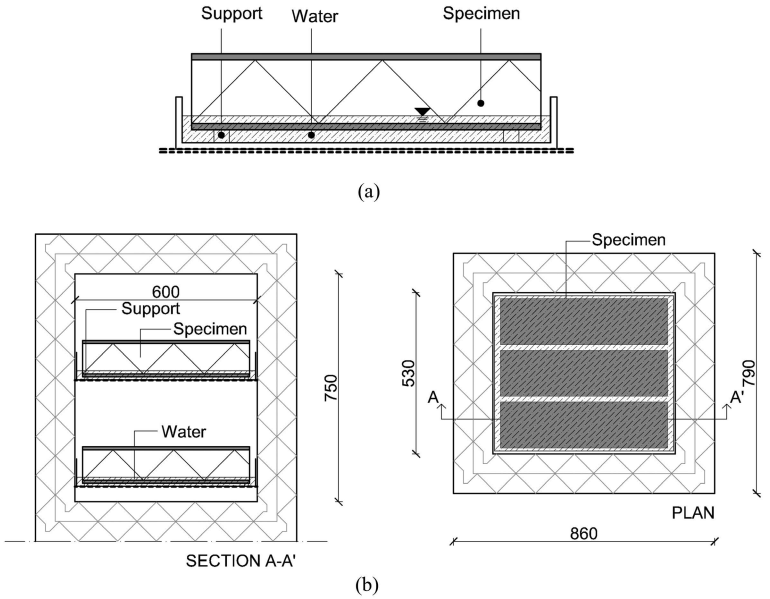

Figure 6.1: Sandwich beam immersed in water while performing the cycles (a) and distribution of the specimens in the climatic chamber (b).

Once performed the thermal cycles, specimens are tested according to a four point loading scheme considering the test set-up shown in Figure 5.4 (a). During the test, each specimen is instrumented as shown in Figure 5.5. The sandwich beams are loaded keeping face down the TRC layer previously immersed in water. In the case of pre-cracked specimens, this TRC layer is also the one that presented cracks due to pre-cracking. Hence, this loading condition is the most critical as the most damaged TRC layer (immersed in water during cycles and also pre-cracked in "C" specimens) is loaded in tension.

The tests are displacement controlled and are performed, as those presented in Section 5, by imposing a stroke rate that is initially equal to $1E-3\ mm/s$ and then, after cracking, is increased up to $4E-3\ mm/s$.

6.1 Small sandwich beams after 150 cycles

Two nominally identical un-cracked small sandwich beams subjected to 150 cycles were tested. The geometrical characteristics of the specimens, together with the maximum load and corresponding displacement registered during test and the lengths of the gauges, are collected in Table 6.2.

Table 6.2: Sandwich beams subjected to 150 freezing-thawing cycles: sizes, peak load and corresponding vertical stroke, lengths of the gauges

Spec.	b $[mm]$	h $[mm]$	h_{TRC}^{sup} $[mm]$	h_{TRC}^{inf} $[mm]$	P_{max} $[kN]$	$stroke_u$ $[mm]$	L_{sup} $[mm]$	L_{inf1} $[mm]$	L_{inf2} $[mm]$
S_U150_1	145.0	121.5	10.0	9.5	7.75	42.64	50.0	200.0	203.0
S_U150_2	151.9	122.0	10.7	10.2	9.84	55.08	52.0	203.0	203.0

Figure 6.2 shows the results in terms of load vs. stroke and bending moment vs. nominal curvature curves. The bending moments are obtained by multiplying the load acting on one knife for the lever arm, while the nominal curvature is defined in Equation 5.1.

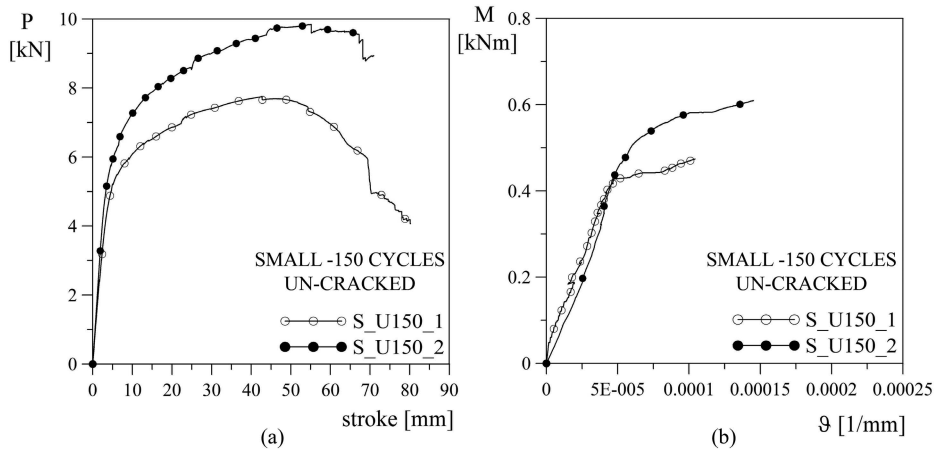

Figure 6.2: Test results: load vs. stroke (a) and bending moment vs. nominal curvature (b) curves for un-cracked small "S" specimens subjected to 150 cycles.

Figure 6.3 shows the pictures of the specimens after test (lateral and bottom view). Looking at the crack pattern, it is possible to observe that the cracks are not symmetric with respect to the longitudinal axis. The same phenomenon was observed in specimens S1 and S2 (Section 5) and the reason was found in the presence of a thin layer of mortar on one side of each specimen, that causes a difference in the stiffness between rear and front side.

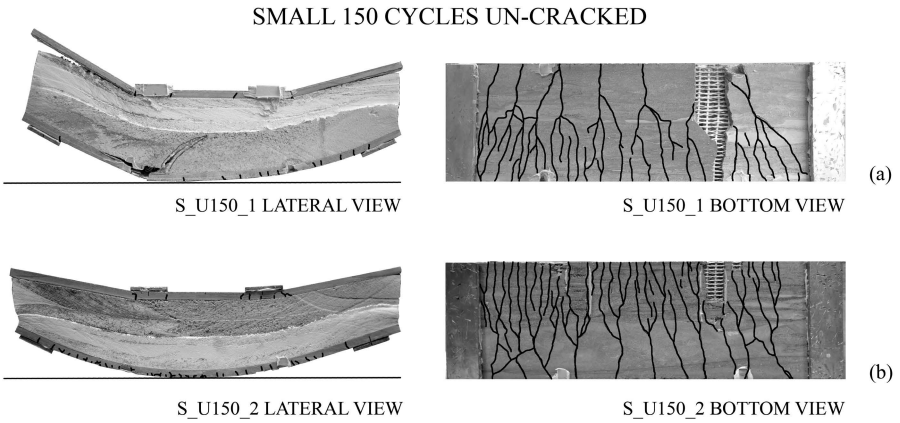

Figure 6.3: Lateral and bottom view of un-cracked small "S" specimens exposed to 150 cycles after test: S_U150_1 (a) and S_U150_2 (b).

Looking both at the curves shown in Figure 6.2 and at the crack patterns, it is possible to note that both the global behaviour and the failure mechanisms involved are comparable with those of specimens not subjected to freezing-thawing cycles (Figures 5.7 and 5.9 - see also the description of these figures in the text). It is worth noting that a huge scatter is registered between specimen S_U150_1 and S_U150_2. However, as the average behaviour can be superimposed to the curves of un-treated specimens (Figure 5.7), it is deduced that the variability of the S_U150 specimen response falls within a typical dispersion of the results.

Figures 6.4 and 6.5 respectively show the load vs. crack opening displacement (COD) and the vertical displacement vs. stroke curves for un-cracked specimens

treated with 150 cycles.

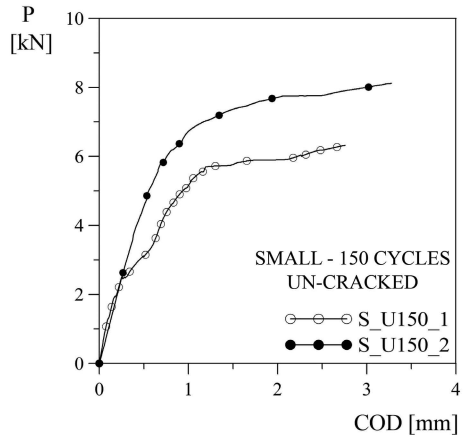

Figure 6.4: Test results: load vs. Crack Opening Displacement curves for un-cracked small "S" specimens exposed to 150 cycles.

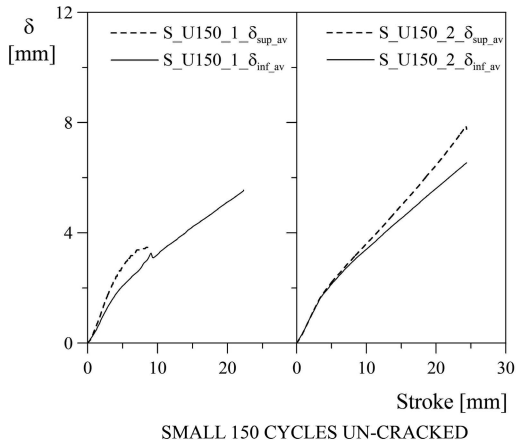

Figure 6.5: Test results: superior and inferior displacement vs. stroke curves for un-cracked small "S" specimens exposed to 150 cycles.

As happened for un-treated small sandwich beams, also for "S_U150" samples a large COD is measured, evidence of the multi-cracking experienced by the lower

TRC layer. It is worth noting that specimen S_U150_1 leaves early the linear branch of the P-COD curve if compared with other small specimens, both un-treated and treated with freezing-thawing cycles.

Concerning Figure 6.5, a transverse compression of the EPS layer comparable with that shown in Figure 5.15 (a) for un-treated specimens is registered.

6.2 Small sandwich beams after 500 cycles

In the case of 500 cycles, both un-cracked (U) and pre-cracked (C) specimens are taken into account to understand the effect of a large number of cycles on the behaviour of the sandwich beams. In both cases three nominally identical specimens were tested. The geometrical characteristics of the specimens, together with the maximum load and corresponding displacement registered during test and the lengths of the gauges, are collected in Table 6.3.

Table 6.3: Sandwich beams subjected to 500 freezing-thawing cycles: sizes, peak load and corresponding vertical stroke, lengths of the gauges

Spec.	b $[mm]$	h $[mm]$	h_{TRC}^{sup} $[mm]$	h_{TRC}^{inf} $[mm]$	P_{max} $[kN]$	$stroke_u$ $[mm]$	L_{sup} $[mm]$	L_{inf1} $[mm]$	L_{inf2} $[mm]$
S_U500_1	150.5	121.2	7.0	14.1	8.36	45.91	54.3	199.0	201.0
S_U500_2	151.0	121.0	8.3	12.7	7.89	33.03	55.5	203.0	206.0
S_U500_3	146.7	120.6	7.1	12.9	8.26	62.11	52.3	201.0	208.0
S_C500_1	147.0	121.1	11.0	9.9	8.33	41.44	52.3	197.0	201.0
S_C500_2	148.8	121.9	8.6	12.6	8.57	36.76	52.2	201.0	199.5
S_C500_3	148.1	121.4	9.5	11.8	9.44	40.57	47.0	199.0	199.0

"C" specimens are cured in air and then pre-cracked before the exposure to thermal cycles. The pre-cracking phase is performed using the same test set-up adopted for the four point loading tests (Figure 5.4 (a)) and loading the beams up to a load equal to 3.5 kN.

This load was selected considering that, at the Serviceability Limit State, a

maximum wind pressure equal to 1.50 kN/m^2 could act on the panel (according to the Italian Standard "Norme Tecniche delle Costruzioni", 2008, assuming a building 30 m tall, placed in an area characterized by unfavourable wind condition - zone 7). Assuming a panel 1.5 m wide and 3 m high and considering the elastic solution proposed by Bares [Gambarova et al. (2007)] for a plate supported on four points at the corners, the maximum acting specific moment is equal to:

$$m_{max\,SLS} = 0.1300 \cdot p_{SLS} \cdot b^2 = 1.76\,kNm/m \tag{6.1}$$

at the corner, with b corresponding to the height of the panel. Considering the specimen width (0.15 m) and the lever arm (0.15 m), the pre-cracking load equal to 3.5 kN is computed.

The pre-cracking curves are plotted in Figure 6.6 in terms of load versus stroke. Looking at the graph, it is possible to observe the formation of one crack in each specimen; a sharp sound was also heard when each crack developed, however the cracks were not visible by visual inspection, thus indicating that their width is lower than 50 μm.

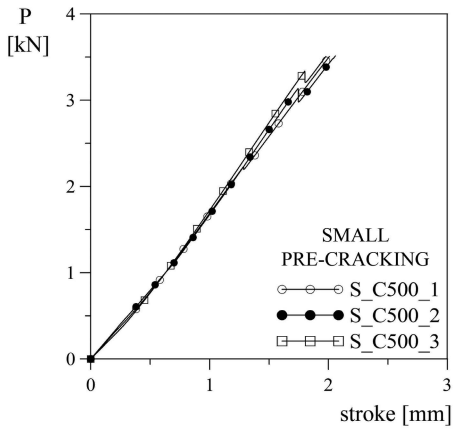

Figure 6.6: Pre-cracking - Load vs. stroke curves.

The experimental results are shown in Figures 6.7 and 6.8 in terms of load vs. stroke and bending moment vs. nominal curvature respectively for un-cracked and pre-cracked specimens.

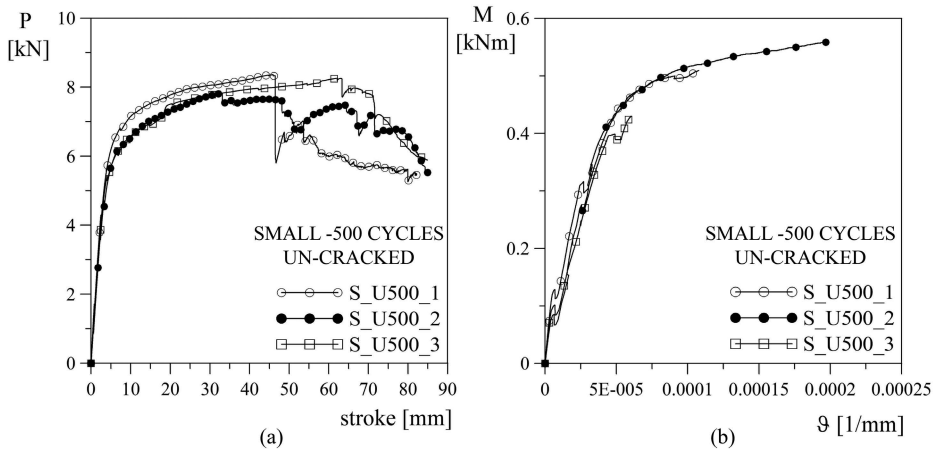

Figure 6.7: Test results: load vs. stroke (a) and bending moment vs. nominal curvature (b) curves for un-cracked small "S" specimens subjected to 500 cycles.

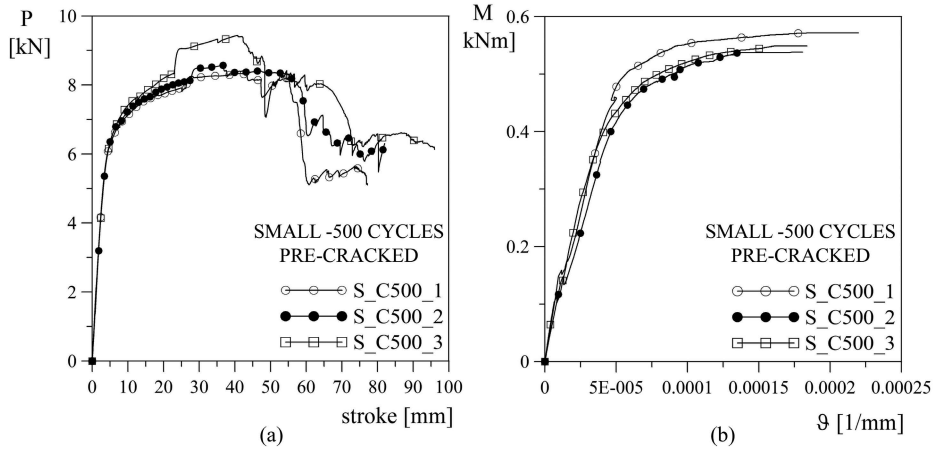

Figure 6.8: Test results: load vs. stroke (a) and bending moment vs. nominal curvature (b) curves for pre-cracked small "S" specimens subjected to 500 cycles.

A good repeatability is obtained as the curves are characterized by a low scatter. Comparing the load-stroke response of specimens subjected to 500 cycles (Figures 6.7 (a) and 6.8 (a)) with the behaviour of un-treated specimens (Figure 5.7 (a)), it is clear that the exposure to freezing and thawing phenomenon affects mainly the ductility of the beams rather than the performances in terms of initial elastic global response and maximum load reached. This observation is also confirmed by the bending moment - nominal curvature curves, that are comparable for un-treated specimens (Figure 5.7 (b)), un-cracked specimens treated with 500 cycles (Figures 6.7 (b)) and pre-cracked specimens treated with 500 cycles (Figure 6.8 (b)). It is recalled that, in subfigures (b), each curve is stopped when one of the displacement transducers involved in the computation of the curvature (LVDT5, LVDT6 or LVDT7) reached its maximum displacement, that always happened before the achievement of the maximum load. The pre-cracking seems not to affect the sandwich beam behaviour.

Pictures of specimens after tests are available in Figures 6.9 and 6.10. Subfigures (a) show a lateral view of each sample, while subfigures (b) show the multi-cracking patterns. As explained in Section 5, the number of cracks is related to the position of the fabric in the lower TRC layer thickness: more the fabric is close to the external surface, the higher is the number of cracks.

After test, specimens S_U500_1, S_U500_2 and S_C500_2 are characterized by a deformed shape as that shown in Figure 6.11: the upper TRC layer is so thin (especially on one side in the second and the latter cases) that it behaves as a thin beam laying on an elastic foundation, with a negative bending moment causing the cracking of the upper surface of the specimen.

Figures 6.12 and 6.13 respectively show the load vs. crack opening displacement (COD) and the vertical displacement vs. stroke curves for un-cracked and pre-cracked specimens treated with 500 cycles.

As happened for un-treated small sandwich beams and for specimens exposed

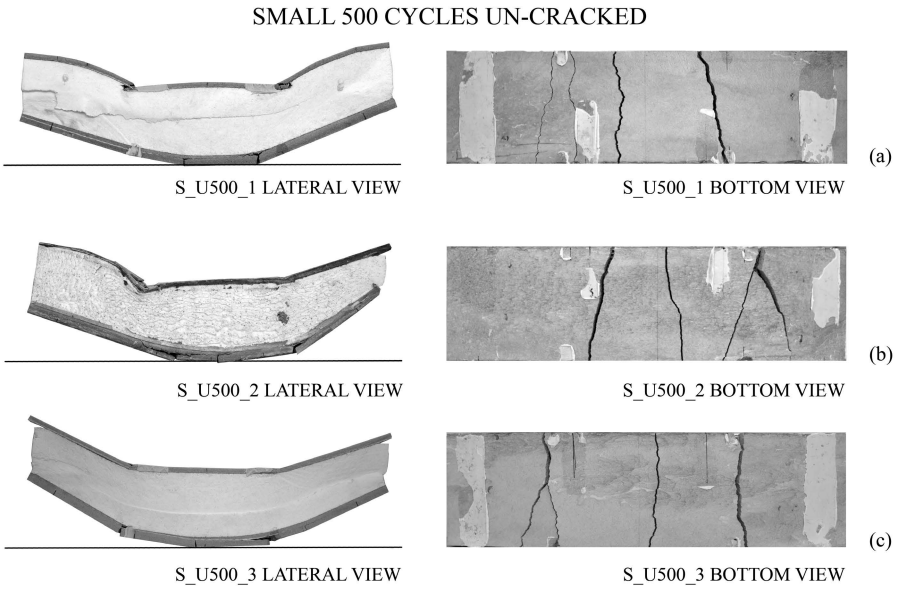

Figure 6.9: Lateral and bottom view of un-cracked small "S" specimens exposed to 500 cycles after test: S_U500_1 (a), S_U500_2 (b)and S_U500_3(c).

to 150 cycles, the multi-cracking experienced by the lower TRC layer is evidenced by the high Crack Opening Displacement measured.

Also in the case of 500 cycles, as seen for 150 cycles, the transverse compression of the EPS layer is comparable with that shown in Figure 5.15 (a) for un-treated specimens.

6.3 Comparison of results

In order to compare the behaviour of un-treated and treated small sandwich beams, Figure 6.14 collects the average load-stroke curves for:

- small sandwich beams (S);
- un-cracked small sandwich beams exposed to 150 freezing-thawing cycles

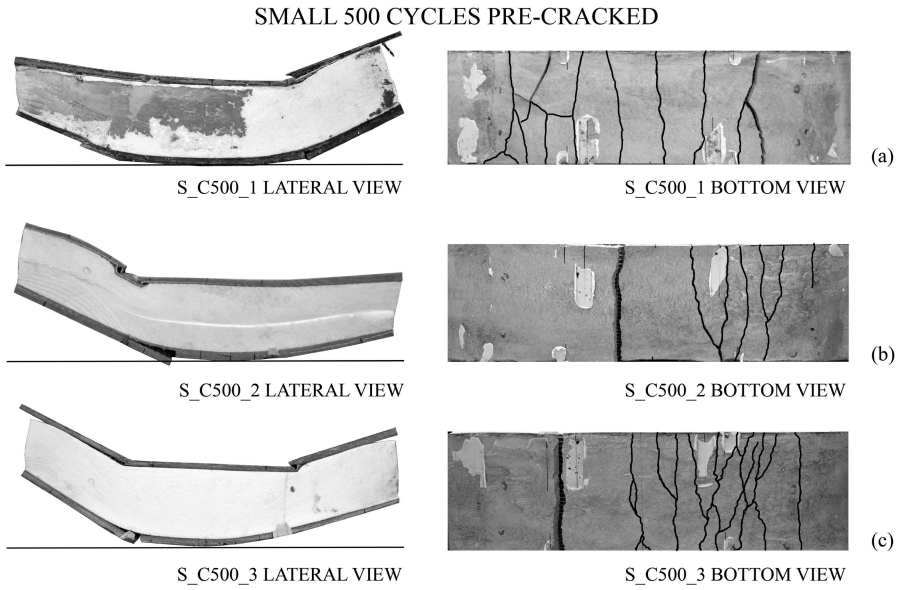

Figure 6.10: Lateral and bottom view of pre-cracked small "S" specimens exposed to 500 cycles after test: S_C500_1 (a), S_C500_2 (b)and S_C500_3(c).

(S_U150);

- un-cracked small sandwich beams exposed to 500 freezing-thawing cycles (S_U500);

- pre-cracked small sandwich beams exposed to 500 freezing-thawing cycles (S_C500).

Looking at this graph, it is clear that, up to a stroke of 45 mm, the behaviour is not affected by the freezing-thawing phenomenon. As a matter of fact, up to this stroke value, the curve "S_C500_av" is even higher than the others. These results are extremely important as they demonstrate that the panel is not expected to show a loss of performance due to freeze-thaw attack at Serviceability Limit State.

Figure 6.11: View of specimen S_U500_1 exposed to 500 cycles after test.

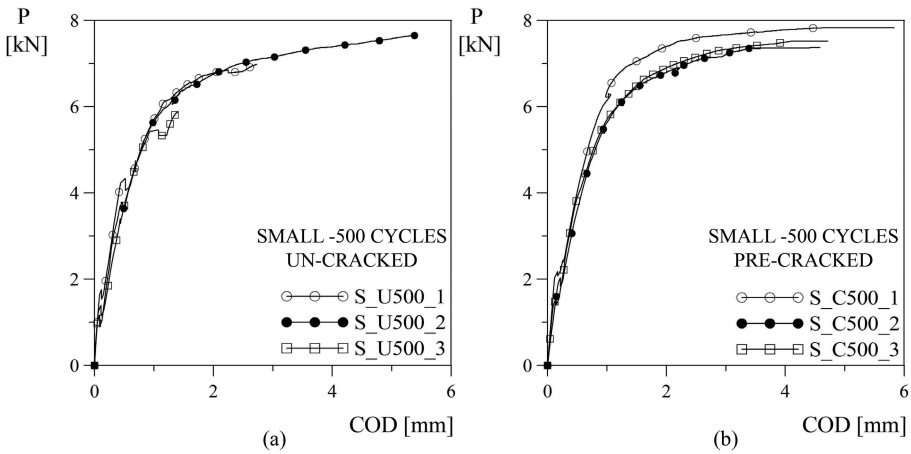

Figure 6.12: Test results: load vs. Crack Opening Displacement curves for small "S" specimens exposed to 500 cycles.

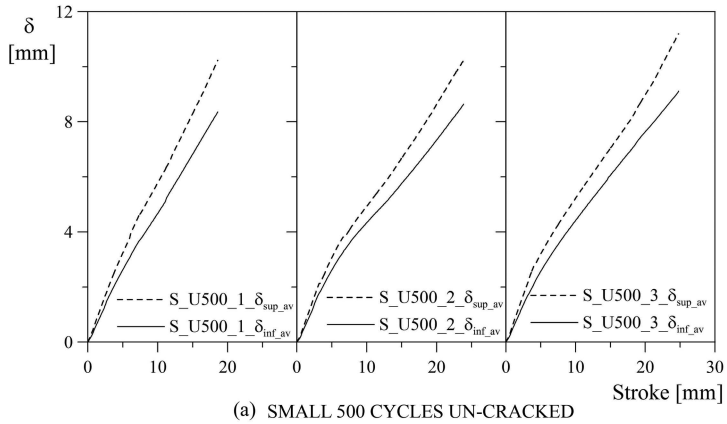

(a) SMALL 500 CYCLES UN-CRACKED

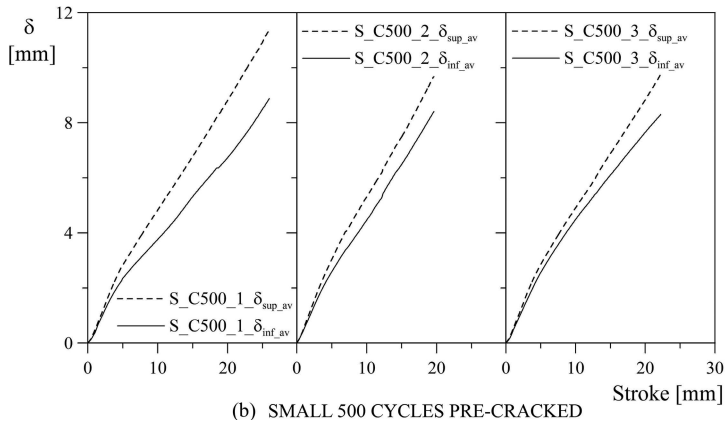

(b) SMALL 500 CYCLES PRE-CRACKED

Figure 6.13: Test results: superior and inferior displacement vs. stroke curves for small "S" specimens exposed to 500 cycles.

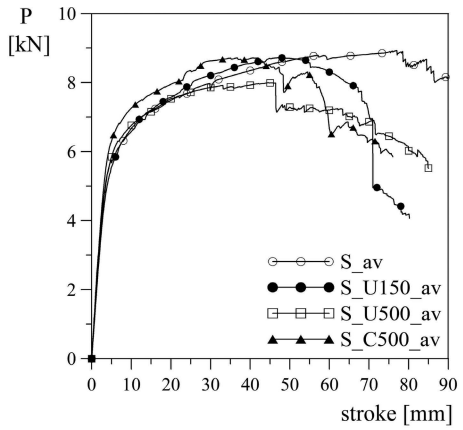

Figure 6.14: Test results: comparison between load vs. stroke curves for small "S" specimens -un-treated and treated beams.

To investigate the influence of thermal cycles on the sandwich beam response, the variation with cycle number of the main parameters that characterize the behaviour is shown in Figure 6.15. In all the graphs, each un-filled marker represents the value assumed by the considered parameter for each specimen, normalized by the average value registered in the zero cycles case; the average of these points is represented by filled markers. Circular markers refer to un-cracked specimens, while rhomboid markers refer to pre-cracked specimen. The parameter considered are:

- the maximum load achieved (P_{max});
- the corresponding displacement (δ_u);
- the secant bending stiffness (EI) defined as the slope of the bending moment vs. nominal curvature curves at a moment level equal to 0.3 kNm;
- the percentage variation of the mass after the exposure to the thermal cycles ($\Delta m/m_i$; Δm = difference between the final and the initial mass,

m_i = initial mass).

The latter data is available only in the case of 500 cycles. It is worth noting that the mass variation is measured by weighing the specimens after cycles, but the water absorption occurred just from the lower TRC layer, that was immersed in water during the thermal treatment.

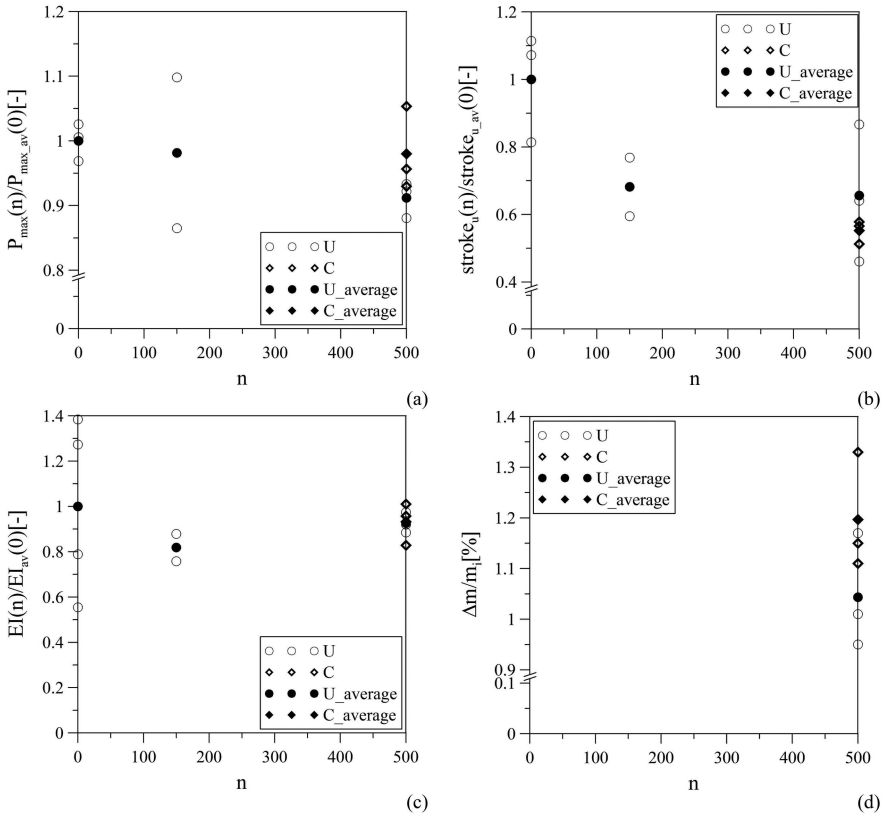

Figure 6.15: Test results: (a) normalized peak load vs. number of cycles, (b) normalized ultimate displacement vs. number of cycles, (c) bending stiffness vs. number of cycles and (d) mass variation vs. number of cycles.

Looking at subfigure (b) it is confirmed that the exposure to freezing-thawing cycles affects mainly the ductility of the specimens: in fact, a reduction of the

normalized ultimate displacement down to 0.5 is registered when the thermal treatments are performed.

On the other hand, other parameters such as the maximum load achieved (subfigure (a)) and the bending stiffness measured (subfigure (c)) are scantily affected by freezing-thawing phenomenon: minimum normalized value registered equal to 0.86 and 0.76 respectively.

It is interesting to observe a stiffness recovery passing from 150 to 500 cycles, thus indicating a possible activation of the self-healing and late hydration phenomena due to a longer permanence in water. This bond strength recovery was also observed in TRC specimens treated with freezing-thawing cycles and tested in tension (Figure 4.32 - see the explanation of the figure in the text).

It is also interesting to note that, in the case of 500 cycles, the bending stiffness of pre-cracked (C) specimens is even slightly higher than the bending stiffness of un-cracked (U) specimens, thus confirming the activation of the self-healing and late hydration phenomena, made easier by the presence of cracks during the thermal cycles, that facilitated the penetration of water. The larger water absorption of pre-cracked specimens, that is directly related to the self-healing, is also clearly visible in the mass growth shown in Figure 6.15 (d).

page intentionally left blank

7

Full-scale panel

In this Section the experimental results concerning tests performed on a real scale panel are shown. The panel has a dimension of 3300 x 1500 mm^2; its cross-section is shown in Figure 7.1. As it can be noted, the section was slightly modified passing from the lab scale (Figure 5.1) to the real scale production. In particular, the nominal thickness of the TRC layers was enhanced to 12 mm in order to guarantee a minimum thickness of these layers of 7 mm, considering the fact that the EPS layer has a planarity tolerance of $\pm 5mm/m$.

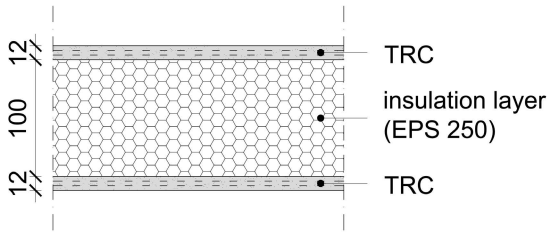

Figure 7.1: Full scale panel cross-section (measures in mm).

Besides, each TRC layer is reinforced with two "F3" fabrics (Table 4.5 and

Figure 4.1) rather than one: one fabric has the warp aligned with the longitudinal axis of the panel, while the other has the warp oriented perpendicularly to this axis. This choice guarantees a bi-directional behaviour of the sandwich panel.

The matrix used is the same presented is Section 5.1, but, as the panel was cast in a precast production plant where high power mixer and not completely dry sand are used, some changes were introduced. In particular, the maximum aggregate size used is equal to 2 mm and the amount of water was adjusted in order to obtain a proper workability of fresh concrete. The updated mix design can be found in Table 7.1. The grain size distribution curve of the sand is shown in Figure 7.2. The compressive strength f_{cc}, measured testing cubic specimens cast together with the panel, is equal to 71.9 MPa at 7 days and to 93.4 MPa at 28 days (both values are the average of two specimens). Considering a larger number of samples (including other 12 specimens at 7 days and 8 at 28 days cast in different dates using the same mix), these values of strength become respectively 78.9 MPa ($STD = 12.2\%$) and 87.7 MPa ($STD = 15.6\%$).

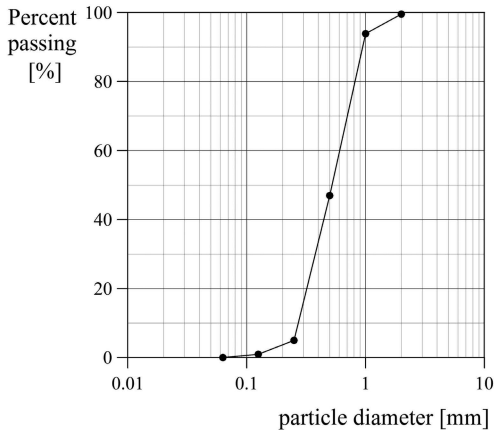

Figure 7.2: Grain size distribution curve of sand.

The expanded polystyrene foam used (EPS250) is also the same presented in

Table 7.1: Mix design $w/(c+s) = 0.19$

Component	Content
Cement I 52.5	600 kg/m^3
Quartz sand 0-2 mm	847 kg/m^3
Water	207 l/m^3
Superplasticizer	33 kg/m^3
Slag	500 kg/m^3

Section 5.1.

The detail of the edges of the real scale panel is shown in Figure 7.3.

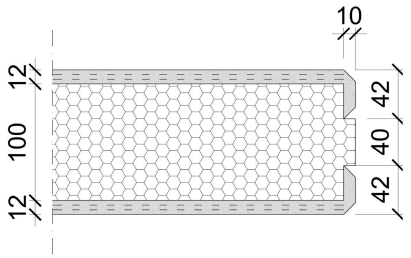

Figure 7.3: Detail of the full scale panel edges (measures in mm).

The panel was cast on August 29, 2014 by means of an in-pressure casting technique using a proper steel formwork (Figure 7.4(a)); the injection of the mortar from the bottom is carried out through two valves, one for each TRC layer, connected to a screw pump. The following day, the panel was demoulded (Figure 7.4(b)) and stored in the open air, in a storage area, keeping it upright (Figure 7.4(c)). After 10 days it was tested. Initially, a Serviceability Limit State test is performed on the panel; then, after un-loading, the panel is loaded again up to failure in order to verify its behaviour at Ultimate Limit State. The two tests and the corresponding results are described in the following.

(a) (b) (c)

Figure 7.4: Formwork for the in-pressure casting (a), panel handling (b) and storage of the panel in the open air (c).

7.1 SLS test

In this section the test performed on the panel at Serviceability Limit State is described. The test set-up together with the loading scheme adopted is shown in Figures 7.5 and 7.6.

The panel is simply supported on four points (150 x 150 mm^2 elastomeric bearings) placed on the short sides. In these points the panel will be anchored to the façade through a proper anchoring system, that has been studied in the European EASEE project [EASEE (2016)]. As the wind is the main load the panel has to bring, a distributed load is applied on the upper surface by filling a pool with water. A picture of the test set-up is shown in Figure 7.7. The load is measured by the flow-meter shown in Figure 7.8.

As it can be seen in Figures 7.5 and 7.6, during SLS test the panel is instrumented with the following displacement transducers:

- four LVDTs are placed in vertical position on the bottom surface of the

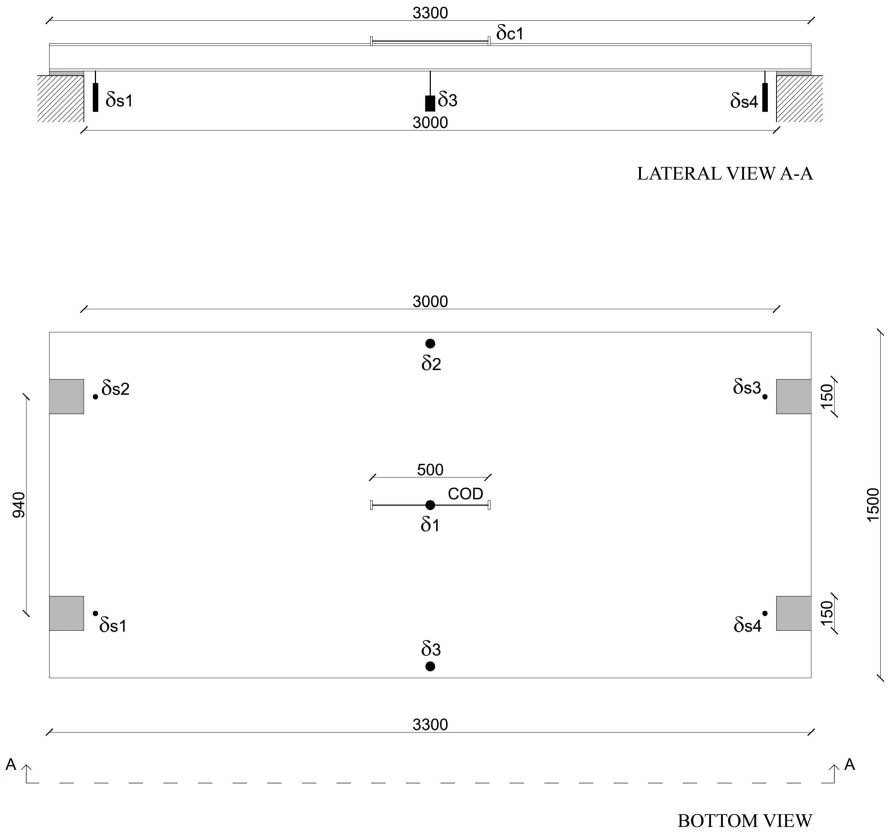

Figure 7.5: Full scale panel test set-up (measures in mm).

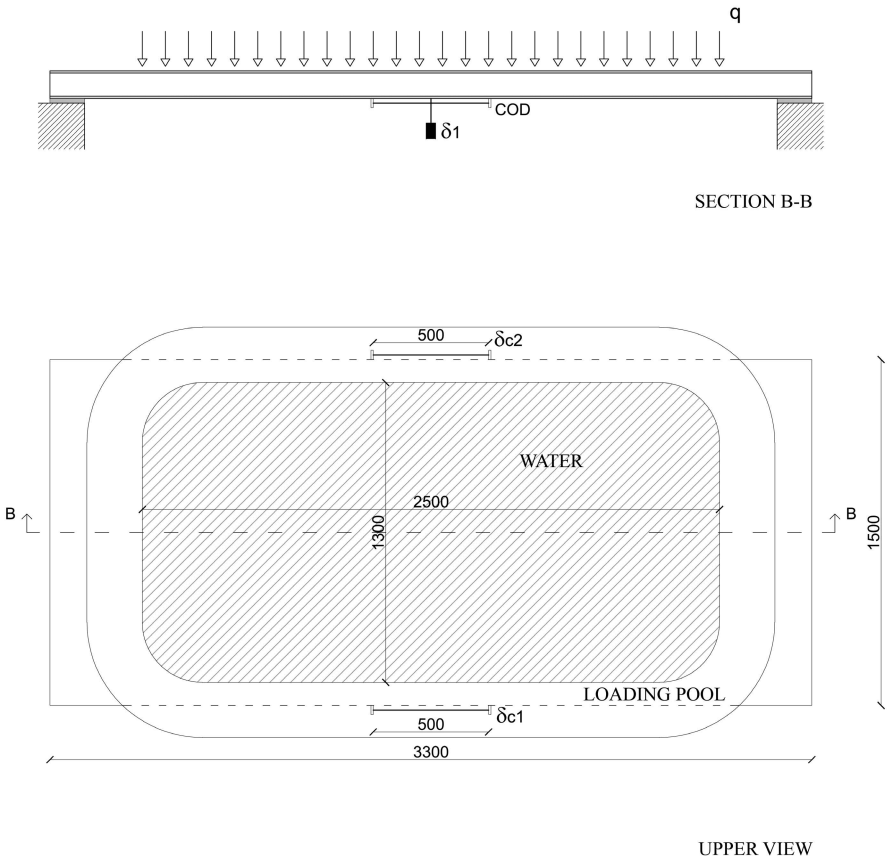

Figure 7.6: Full scale panel: loading scheme at SLS test (measures in mm).

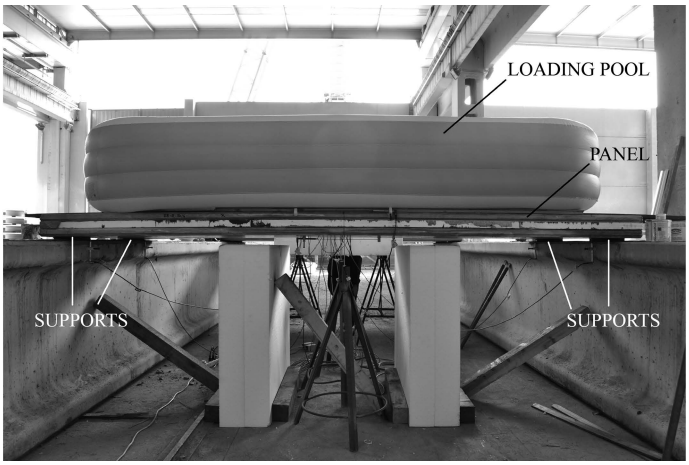

Figure 7.7: SLS full scale panel test.

Figure 7.8: Full scale panel instrumentation: flow-meter used to measure the distributed load applied on the panel.

panel and are aimed at measuring the specimen vertical displacement next to the supports (δ_{S1}, δ_{S2}, δ_{S3} and δ_{S4} - Figures 7.5 and 7.9);

Figure 7.9: Full scale panel instrumentation: LVDTs used to measure the vertical displacement next to the supports.

- three potentiometer transducers are placed in vertical position on the bottom surface of the panel and are aimed at measuring the specimen vertical displacement at mid-span (δ_1, δ_2 and δ_3 - Figures 7.5 and 7.10);

- a displacement transducer is placed on the bottom surface of the panel astride the mid-span with a gauge length equal to 500 mm and is instrumental to measure the Crack Opening Displacement (COD - Figures 7.5 and 7.10);

- two LVDTs are placed on each side of the upper TRC layer astride the mid-span with a gauge length equal to 500 mm in order to measure the superior longitudinal displacements on the compressed side (δ_{c1} and δ_{c2} - Figures 7.6 and 7.11).

Displacements $\delta_{S1,S2,S3,S4}$, COD and $\delta_{c1,c2}$ are measured through inductive full bridge type transducers, with a nominal displacement equal to 10 mm, while $\delta_{1,2,3}$ are measured using potentiometer transducers, with a nominal displacement

Figure 7.10: Full scale panel instrumentation: LVDTs used to measure the vertical displacement at mid-span.

Figure 7.11: Full scale panel instrumentation: LVDT used to measure the superior longitudinal displacement of the upper TRC layer.

equal to 150 mm. The data acquisition is performed by using the electronic measurement system SPIDER8 by HBM.

A picture of the panel during the test is shown in Figure 7.12, while the panel after test is shown in Figure 7.13.

Figure 7.12: Full scale panel subjected to a distributed load equal to 2.66 kN/m^2.

In Figure 7.14 the distributed load vs. mid-span vertical displacement curves are plotted. The mid-span displacements measured (δ_1, δ_2 and δ_3) are adjusted by deducting the average value of the displacements measured next to the supports (δ_{S1}, δ_{S2}, δ_{S3} and δ_{S4}).

The test results are also shown in Figure 7.15 in terms of distributed load vs. relative displacements measured at the extrados (Figure 7.15(a)) and distributed load vs. Crack Opening Displacement (Figure 7.15(b)).

Taking into account that the load is applied in steps, in both Figures 7.14 and 7.15 it is possible to observe the effect of the permanence of a certain load for some minutes (increment of the measured displacements for a constant applied load). This is related to the applied test rate and to the consequent time of crack propagation. It is important to remind that the main load acting on the façade

Figure 7.13: Full scale panel after the SLS test.

panel is the wind, whose gusts last seconds and not minutes.

This permanence of load leads to a final Crack Opening Displacement equal to about 1 mm; the corresponding crack pattern, clearly visible by visual inspection, is show in Figure 7.16. At Serviceability Limit State, a maximum wind pressure equal to 1.50 kN/m^2 could act on the panel (according to the Italian Standard "Norme Tecniche delle Costruzioni", 2008, assuming a building 30 m tall, placed in an area characterized by unfavourable wind condition - zone 7); for this level of pressure, the measured COD (over the mid-span with a gauge length of 500 mm) is equal to 68 μm. Considering that multi-cracking occurs in this region, it can be assumed that cracks are not visible to the naked-eye (crack width lower than 50 μm), thus satisfying an important requirement for a façade panel.

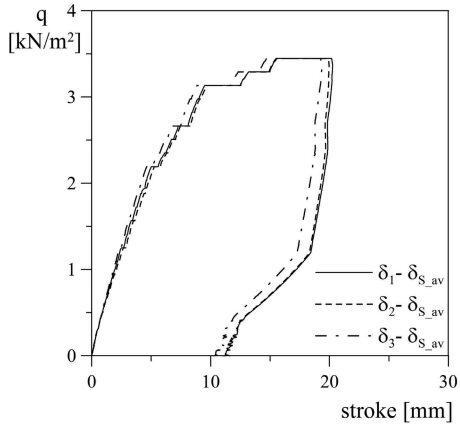

Figure 7.14: SLS full scale panel test results: distributed load vs. mid-span vertical displacement curves.

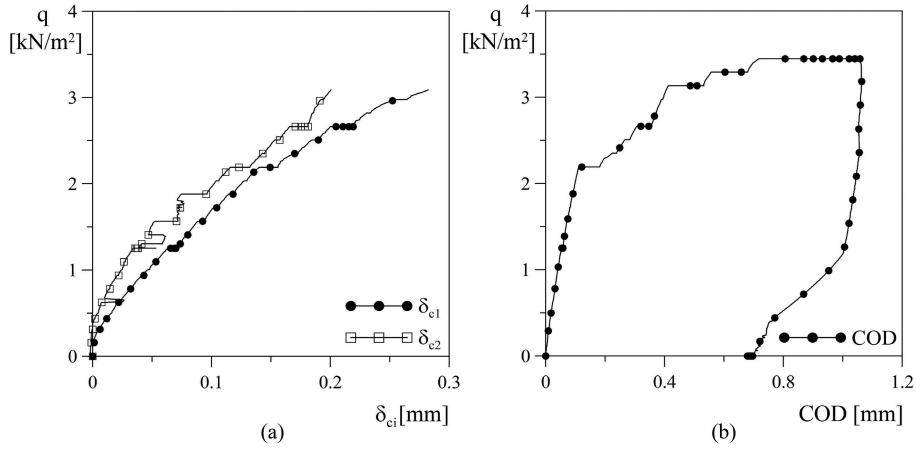

Figure 7.15: SLS full scale panel test results: load vs. relative displacement in compression δ_{ci} $(i = 1, 2)$ (a) and load vs. Crack Opening Displacement (b) curves.

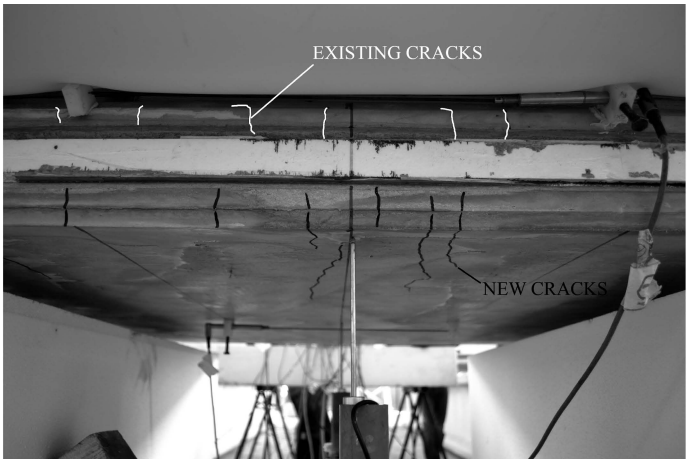

Figure 7.16: SLS full scale panel test: multi-cracking of the lower TRC face after test.

7.2 ULS test

In this section the test performed on the panel up to failure (Ultimate Limit State) is described. The test was carried out by loading the panel with concrete blocks with a nominal size equal to 500 x 500 x 1600 mm^3. Overall, four blocks were applied to bring the panel to failure. In Table 7.2 the weight of each block is collected. The blocks were put on some EPS lumps in order to allow the operator to remove the belts, hooked into the overhead travelling crane, once placed each block.

Table 7.2: ULS full scale panel test: weight of the concrete blocks

Concrete block	*Weight* $[kg]$
1	1000
2	1060
3	1020
4	1000

The first concrete block was placed on one side of the panel, at the inner edge

of the supporting beam (Figure 7.17(a)).

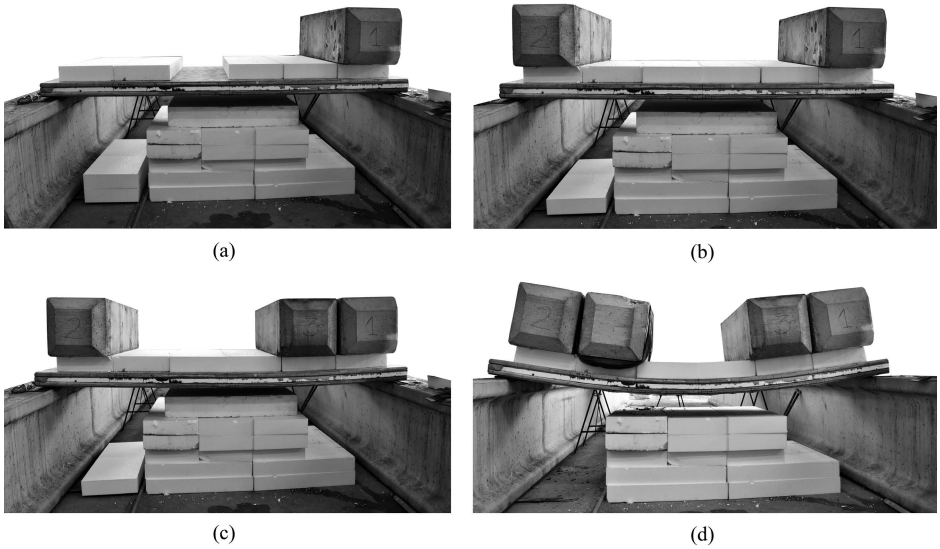

Figure 7.17: ULS full scale panel test: application of the first (a), second (b), third (c) and fourth (d) concrete block.

The second block was placed at the opposite side of the specimen, always in correspondence with the inner edge of the supporting beam (Figure 7.17(b)). The vertical displacement measured at mid-span was equal to 8 mm on both the panel sides.

The third concrete block was placed at 35 mm from the first block (Figure 7.17(c)), leading to a vertical displacement at mid-span of 32 mm on one side and 33 mm on the other side.

The fourth block was placed at 35 mm from the second block (Figure 7.17(d)) and led to failure (Figure 7.18).

The cracking of the bottom surface, indicating the incipient panel failure, is visible in Figure 7.19, while two pictures representing failure details are shown in Figures 7.20 and 7.21.

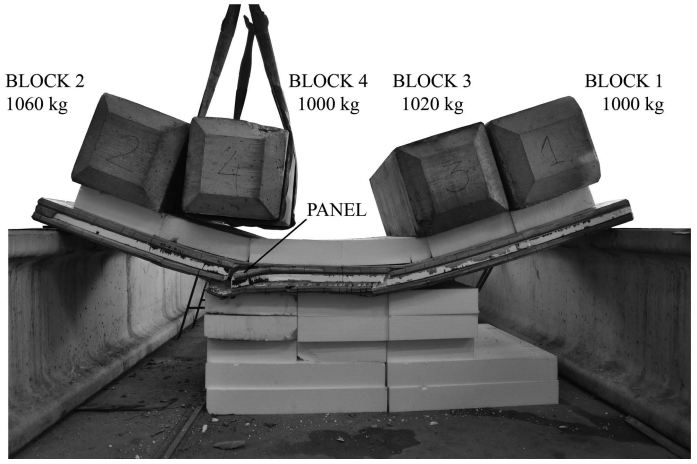

Figure 7.18: ULS full scale panel test: panel failure.

Figure 7.19: ULS full scale panel test: incipient panel failure.

Although the procedure followed for the load application is critical for the panel shear resistance, no shear failure was observed. The failure is due to the achievement of the tensile strength of the lower TRC layer (failure of the fabric reinforcement), that led to the propagation of a tensile crack in the polystyrene layer and to the failure of the EPS at the EPS/lower TRC layer interface.

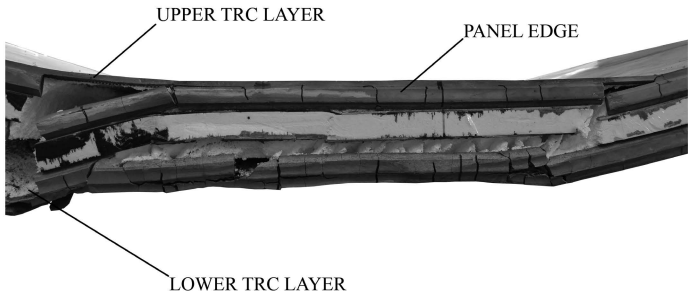

Figure 7.20: ULS full scale panel test: panel failure detail.

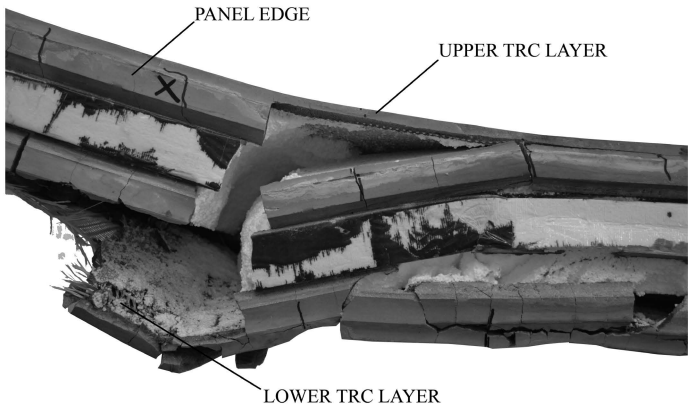

Figure 7.21: ULS full scale panel test: panel failure detail.

8

Numerical prediction

The results of the experimental tests performed on small and big sandwich beams (Subsection 5.2) have been predicted by means of both a finite element model and an analytical model based on the Stamm and Witte Theory (Subsection 2.7.2). The finite element model was also applied to simulate the tests performed on the full-scale panel both at Serviceability and Ultimate Limit State, explained in Section 7.

The results obtained with the analytical and the finite element models are collected in this Chapter.

8.1 Stamm & Witte model modified with stiffness reduction

An analytical model has been implemented following the same approach proposed by Shams et al. (2014a) in order to account the non-linear material behaviour in the Stamm and Witte model (Section 2.7.3). The beam is divided into a finite number of elements with equal length and axial and bending stiffness are assigned to each element accounting non-linearity according to a secant stiffness

approach. The differential equations of the Stamm and Witte model (Stamm and Witte (1974), Section 2.7.2) are solved by using constant equivalent stiffness properly defined for the whole beam.

At the beginning, the initial stiffness EA_{sup}, EA_{inf}, EI_{sup} and EI_{inf} and the core initial shear modulus G are imposed. The load, initially null, is incremented by ΔP and the values of the vertical displacement w, the rotation γ, the bending moments M_s, M_o and M_u are computed according to the Stamm and Witte classical model (Section 2.7.2) as a function of the coordinate x along the beam length.

Once the material behaviour becomes non-linear, the stiffness of each element are computed by means of a secant approach referring to generalized constitutive models ($M-\theta$ and $N-\varepsilon$) for the TRC layers and to a shear $\tau-\gamma$ constitutive relationship for the EPS. A proper description of these constitutive relationships is provided in Section 8.1.1. Referring to a generic i-th step, for TRC layers, the stiffness at position x is defined starting from M and N evaluated at the previous $(i-1)$ step for that position. Generalized constitutive laws allow to define the corresponding θ and ε respectively and, therefore, axial ($EA = N/\varepsilon$) and bending ($EI = M/\theta$) stiffness (Figure 8.1(a) and (b)). A similar approach is adopted for EPS: γ is computed from the model at step $(i-1)$, the $\tau-\gamma$ constitutive law allows to define the corresponding value of τ and, therefore, secant shear modulus at i-th step is defined as $G = \tau/\gamma$ (Figure 8.1(c)). It is worth noting that, in the model, axial and bending actions acting on the external faces are uncoupled.

In order to define equivalent stiffness to be used in the Stamm and Witte differential equations, the local stiffness evaluated for each element are weighted according to different response parameters. In particular, equivalent values of EA and EI of TRC are evaluated by using the displacement w as weighting function, while equivalent shear modulus G of EPS considers shear deformation γ as weighting function.

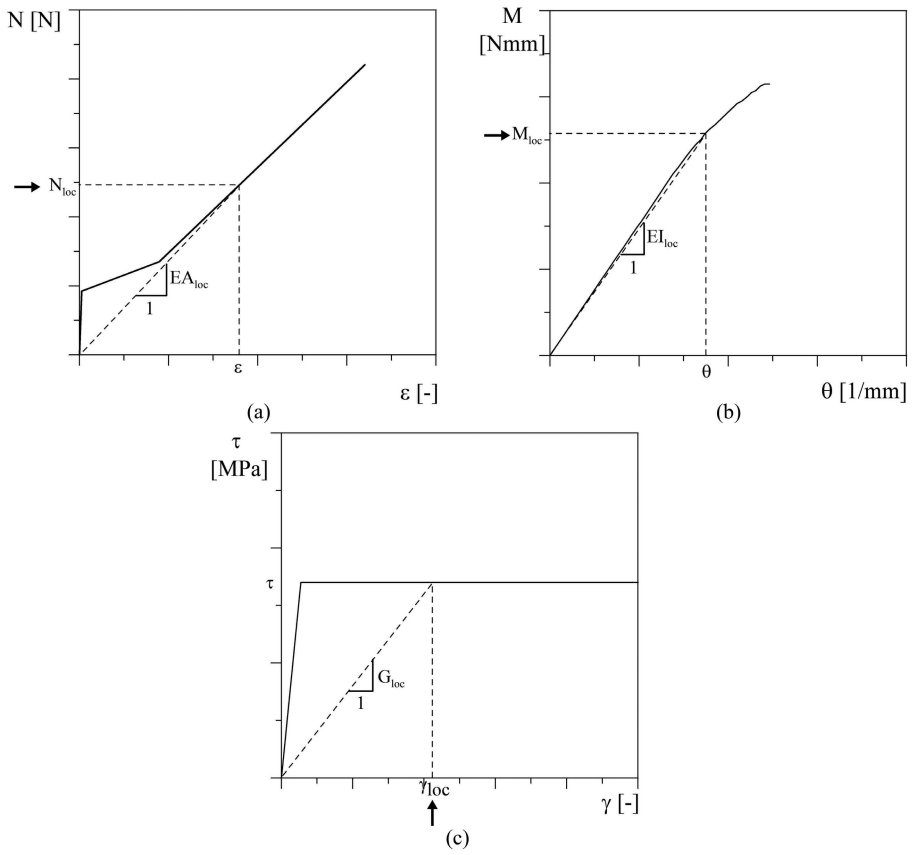

Figure 8.1: Analytical model: $N - \varepsilon$ (a), $M - \theta$ (b) and $\tau - \gamma$ (c) relationships.

For convenience, the stress distribution and the deformed configuration assumed by Stamm and Witte (1974) for the sandwich beam with no negligible face bending stiffness, previously shown in Section 2.7.2, are displayed again in Figure 8.2.

A flow chart representing the steps of the analytical model is proposed in Figure 8.3. In the figure the axial stiffness of the upper and the lower layer, previously called D_o and D_u according to Stamm and Witte (1974), are respectively named EA_{sup} and EA_{inf}, while the bending stiffness, previously called B_o and

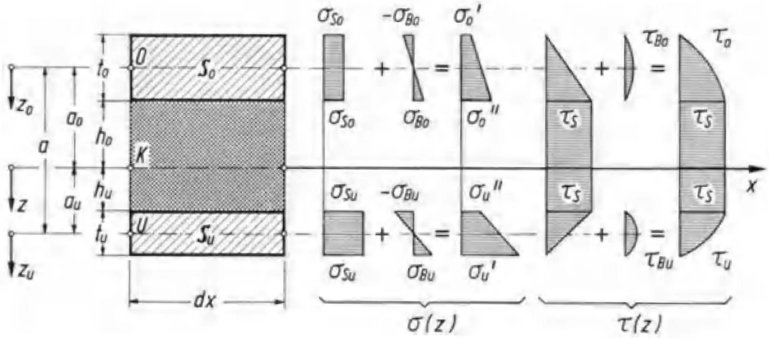

(a)

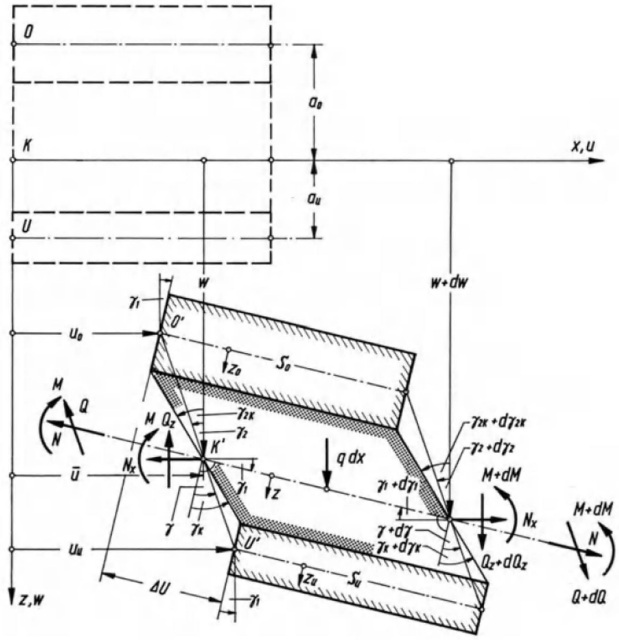

(b)

Figure 8.2: Stress distribution (a) and deformed configuration (b) for a sandwich beam characterized by no negligible face bending stiffness [Stamm and Witte (1974)].

B_u, are named EI_{sup} and EI_{inf}.

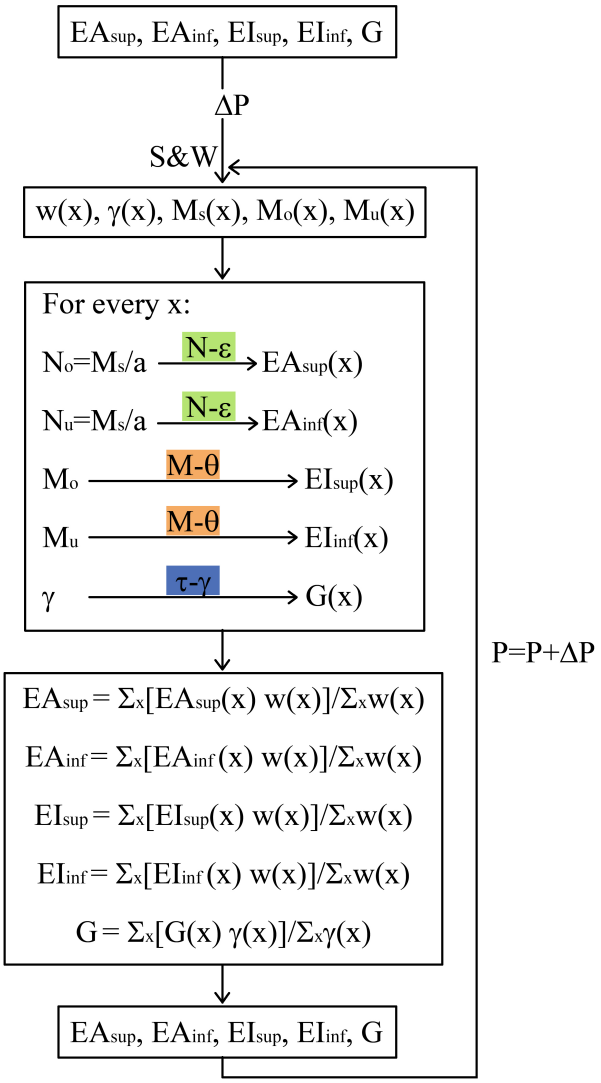

Figure 8.3: Analytical model: flow chart.

It is worth to underline that a strong assumption of the Stamm and Witte

model is that they consider the same rotation, and hence the same curvature, for the upper and the lower TRC layers (see Figure 8.2).

Moreover, in the implemented model, the global stiffness of each layer derive from an average process, along the beam axis, of local stiffness defined according to constitutive models. This process leads to global stiffness that do not directly respect the generalized constitutive laws at each point.

8.1.1 $N-\varepsilon$, $M-\theta$ and $\tau-\gamma$ relationships

The constitutive relationships introduced in the analytical model are shown in Figure 8.4.

In subfigure (a) the tensile stress-strain relationship of Textile Reinforced Concrete reinforced with one fabric "F3" is plotted. The behaviour was deduced from the experimental results of tensile tests performed on 400x70x9 mm^3 TRC specimens; displacement transducers were applied on each specimen in order to measure a strain which was not affected by the relative sliding between the specimen and the clamping devices. The axial force N, computed in order to obtain the $N-\varepsilon$ graph, is obtained by multiplying the stress σ for the TRC layer cross-section area ($b \cdot t$, where b is the specimen width, equal to 150 or 300 mm, and t is the TRC layer thickness, equal to 10 mm).

In subfigure (b) the $M-\theta$ relationships related to the bending behaviour of external layers are shown for both the small and big sandwich beam (in subfigure (c) a zoom is provided). For each specimen size, two relationships representing extreme situations are proposed: a lower limit situation in which the fabric contribution is neglected ("plain concrete"), and a situation in which the contribution of the fabric is accounted and spread all over the thickness of the layer ("TRC"), thus providing an upper limit of the bending behaviour of the faces. In both cases the compressive behaviour shown in Figure 8.5(a) is assumed: a parabolic-

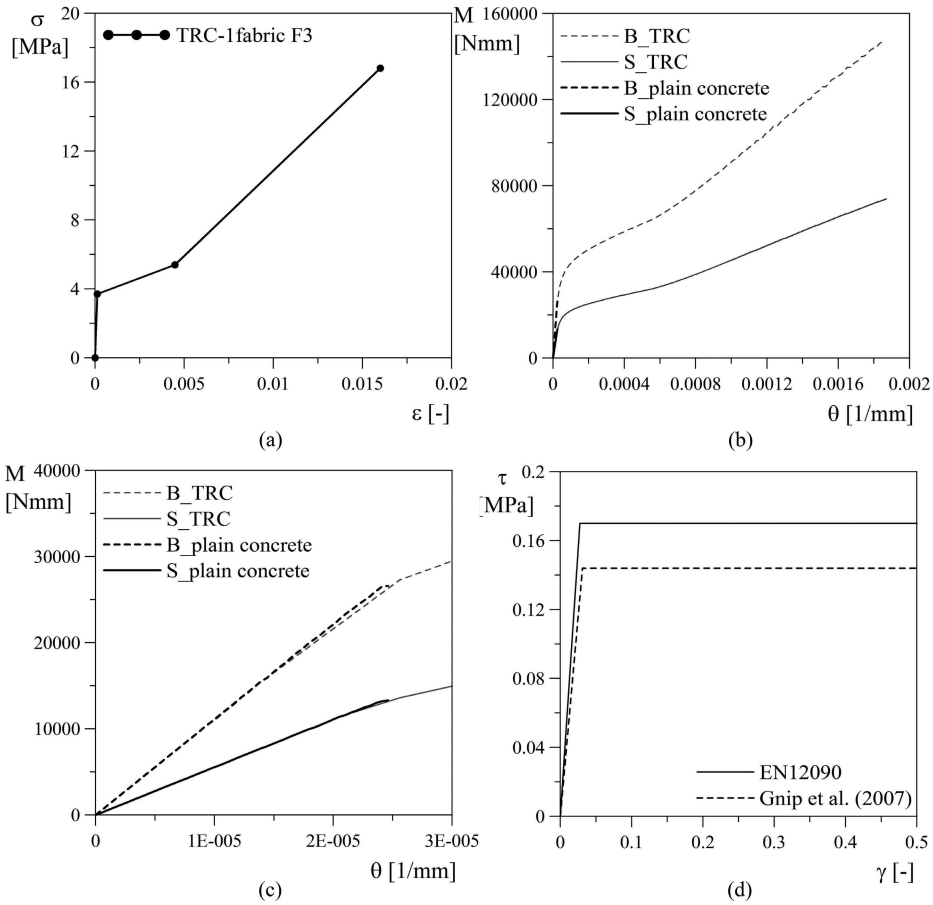

Figure 8.4: Analytical model: $\sigma - \varepsilon$ (a), $M - \theta$ (b), zoom on the $M - \theta$ initial phase (c) and $\tau - \gamma$ (d) relationships.

rectangular stress-strain relationship is adopted [Toniolo and di Prisco (2001)], considering a maximum strength f_{cm} equal to 73 MPa (average cubic compressive strength experimentally measured); this strength is reached at a strain equal to 0.002, while the failure takes place at a strain equal to 0.0035. In tension, in the case of neglecting the fabric contribution, the formulation proposed by Model Code 2010 is adopted (Figure 8.5(b)), considering an average tensile strength of 4.2 MPa (C55 class of concrete) and an elastic modulus of 30 GPa (according to literature results on cement matrix characterized by similar compressive strength and maximum aggregate size [Brameshuber et al. (2006)]). When accounting the fabric contribution, the tensile constitutive law shown in Figure 8.4(a) is adopted to built the $M-\theta$ diagram. The $M-\theta$ relationships are obtained by means of a plane-section approach.

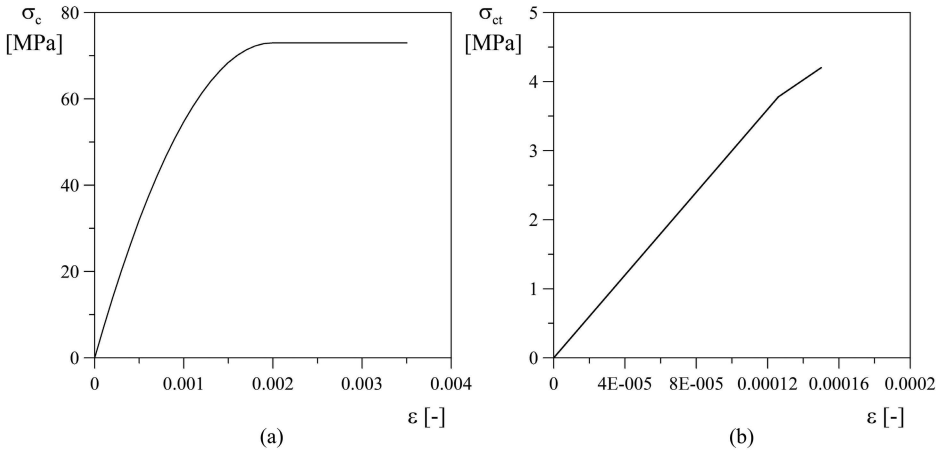

Figure 8.5: Compressive (a) and tensile (b) constitutive behaviour of plain concrete.

Two $\tau-\gamma$ relationships, shown in Figure 8.4(c), are taken into account; both of them are supposed to be elastic-perfectly plastic. The first, named "EN12090", considers the yielding shear strength τ equal to 0.17 MPa; this value is proposed for EPS250 by the European Standard EN 13163 "Thermal insulation products

for buildings - Factory made products of expanded polystyrene (EPS)" and has to be defined according to the European Standard EN 12090 "Thermal insulating products for building applications - Determination of shear behaviour". The initial shear modulus G is computed as:

$$G = \frac{E}{2(1+\nu)} = 6.23\ MPa \tag{8.1}$$

considering an elastic modulus of 13.7 MPa (Section 5.1) and a Poisson's coefficient equal to 0.1. The second relationship, named "Gnip et al. (2007)", assumes a shear modulus G equal to 4.64 MPa and a maximum shear stress τ equal to 0.144 MPa. These values are deduced from the empirical correlations found by Gnip et al. (2007) respectively between the shear modulus and the density of EPS and between the ultimate strength of EPS and its density and thickness.

8.1.2 Analytical results

The analytical model results are shown in Figure 8.6 in terms of load (P) versus displacement (δ) curves for both the small and big sandwich beams.

For each beam size, four numerical curves are proposed, depending on the $\tau - \gamma$ ("EN12090" or "Gnip et al. (2007)") and $M - \theta$ ("Plain Concrete" or "Textile Reinforced Concrete") relationships used in the model. In the case of small sandwich beams, the prediction according to EN12090 overestimates the specimen behaviour, while the prediction which refers to Gnip et al. (2007) is closer to the experimental results. For big sandwich beams, the experimental curves lie in between the numerical predictions. Even if the contribution of the fabric on the bending behaviour of TRC faces is relevant, as it significantly affects the $M-\theta$ diagram (see Figure 8.4(b)), the difference between the global response neglecting or considering the fabric is limited, thus indicating the limited effect of

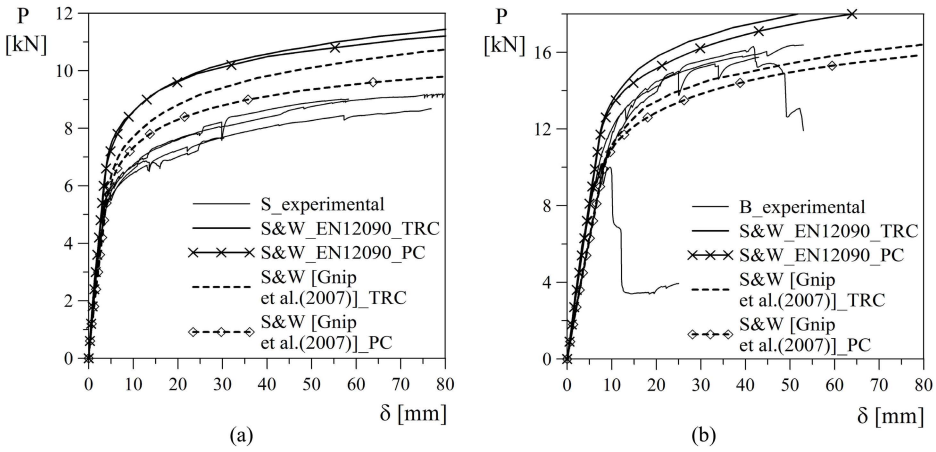

Figure 8.6: Load vs. displacement curves obtained through the analytical model for small (a) and big (b) sandwich beam compared with the experimental results.

the bending of each face with respect to the sandwich action. It is worth noting that the model is not able to catch the specimen failure as no failure criterion is introduced.

8.2 Finite Element numerical model

3D numerical models have been developed in the finite element program ABAQUS/Standard 6.12. The validation of these models has been performed by means of the experimental results presented in Chapters 5 and 7. In order to use these models in design, their prediction capability is evaluated in this Section.

8.2.1 Constitutive laws

The constitutive laws used in the Abaqus finite element models for Textile Reinforced Concrete, expanded polystyrene and steel are here summarized.

Textile Reinforced Concrete

The elastic phase is defined through two parameters:

- the Young's modulus, assumed equal to 30 GPa according to literature results on cement matrix characterized by similar compressive strength and maximum aggregate size [Brameshuber et al. (2006)];
- the Poisson's ratio, assumed equal to 0.2.

Plasticity is introduced through Concrete Damage Plasticity model [Lee and Fenves (1998)], which is implemented in Abaqus. The model is a continuum, plasticity-based, damage model for concrete. It assumes that the main two failure mechanisms are tensile cracking and compressive crushing of the concrete material. The evolution of the yield (or failure) surface is controlled by two hardening variables, $\tilde{\varepsilon}_t^{pl}$ (tensile equivalent plastic strain) and $\tilde{\varepsilon}_c^{pl}$ (compressive equivalent plastic strain), linked to failure mechanisms under tension and compression loading, respectively [Simulia (2011)].

Two damage variables (d_t and d_c) are defined in the model in order to account the degradation of the elastic stiffness observable when the concrete specimen is unloaded. These variables are functions of the plastic strains.

Considering E_0 as the initial elastic modulus of the material, the stress-strain relations are:

$$\sigma_t = (1 - d_t)E_0(\varepsilon_t - \tilde{\varepsilon}_t^{pl}) \tag{8.2}$$

$$\sigma_c = (1 - d_c)E_0(\varepsilon_c - \tilde{\varepsilon}_c^{pl}) \tag{8.3}$$

The definition of the damage variables becomes crucial if cyclic tests are modeled. In the simulation here considered d_t and d_c are assumed equal to zero (no damage is accounted) as monotonic tests are taken into account. This means that the model behaves simply as a plasticity model.

In Figure 8.7 the behaviour of concrete in tension and in compression is shown; the equivalent plastic strains and the damage variables are shown in the figure.

In the model, the "effective" tensile and compressive cohesion stresses are also defined:

$$\bar{\sigma}_t = \frac{\sigma_t}{(1 - d_t)} = E_0(\varepsilon_t - \tilde{\varepsilon}_t^{pl}) \tag{8.4}$$

$$\bar{\sigma}_c = \frac{\sigma_c}{(1 - d_c)} = E_0(\varepsilon_c - \tilde{\varepsilon}_c^{pl}) \tag{8.5}$$

For $d_t = d_c = 0$ they correspond to the stresses defined above.

Considering a multi-axial behaviour, the effective stress is defined as:

$$\bar{\boldsymbol{\sigma}} = \mathbf{D}_0^{el} : (\varepsilon - \varepsilon^{pl}) \tag{8.6}$$

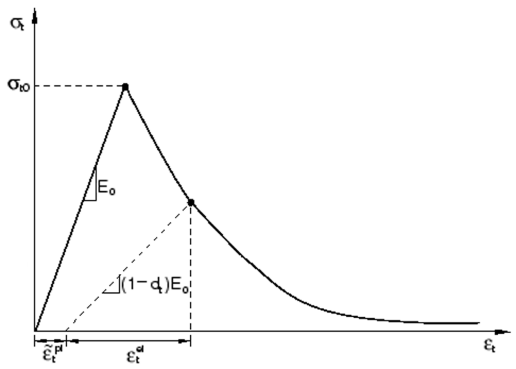

(a)

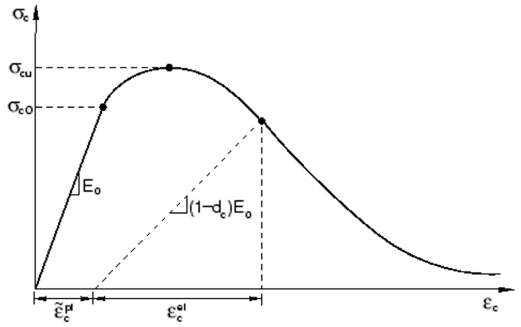

(b)

Figure 8.7: Response of concrete to uniaxial loading in tension (a) and compression (b). [Simulia (2011)]

Two stress invariants of the effective stress tensor ($\bar{\boldsymbol{\sigma}}$) are used when the plastic flow potential function and the yield surface are defined:

- the hydrostatic pressure stress

$$\bar{p} = -\frac{1}{3} trace(\bar{\boldsymbol{\sigma}}) \tag{8.7}$$

- the Mises equivalent effective stress

$$\bar{q} = \sqrt{\frac{3}{2}(\bar{\mathbf{S}} : \bar{\mathbf{S}})} \tag{8.8}$$

with

$$\bar{\mathbf{S}} = \bar{\boldsymbol{\sigma}} - \bar{p}\mathbf{I} \tag{8.9}$$

The non-associated potential plastic flow used in Concrete Damage Plasticity is the Drucker-Prager hyperbolic function:

$$G = \sqrt{(\epsilon\sigma_{t0} + tan\psi)^2 + \bar{q}^2} - \bar{p}{\cdot}tan\psi \tag{8.10}$$

in which ψ is the dilation angle measured in $p-q$ plane at high confining pressure, σ_{t0} is the uniaxial tensile stress at failure and ϵ is a parameter referred to the eccentricity.

The yield function used by the model is that proposed by Lubliner et al. (1989), with the modifications carried by Lee and Fenves (1998) to account for different evolution of strength under tension and compression. The evolution of the yield surface is controlled by the hardening variables $\tilde{\varepsilon}_t^{pl}$ and $\tilde{\varepsilon}_c^{pl}$. In this function the following ratio are included: the ratio between the initial equi-biaxial compressive yield stress and the initial uni-axial compressive yield stress (σ_{b0}/σ_{c0}) and the ratio of the second stress invariant on the tensile meridian, to that on the compressive meridian (K_c).

Default plasticity parameters are used in the finite element analysis (Table 8.1).

Table 8.1: Plasticity parameters for Concrete Damage Plastcity model

Dilation angle	*Eccentricity*	σ_{b0}/σ_{c0}	K_c	*Viscosity parameter*
38	0.1	1.16	0.67	0

The compressive behaviour is assumed to be elastic-perfectly plastic, with a yield stress equal to 73 Mpa. This value corresponds to the average cubic compressive strength obtained for both the matrices used to cast the sandwich

beams and the full-scale panel. Concerning the full-scale panel, a value of 71.9 MPa was measured on cubic specimens tested at 7 days; it is worth noting that the SLS and ULS tests were performed ten days after the panel casting.

The plastic tensile behaviour is defined introducing a stress-strain relationship, which has been deduced from the experimental results of tensile tests performed on 400x70x9 mm^3 TRC specimens. In Figure 8.8 the nominal stress vs. normalized displacement experimental curves are shown. Subfigures (a) and (b) refer to TRC specimens respectively reinforced with one fabric "F3", warp aligned with the longitudinal direction, and two fabrics "F3", one perpendicular to the other. Displacement transducers were applied on each specimen in order to measure a strain which differs from the normalized displacement and is not affected by the relative sliding between the specimen and the clamping devices.

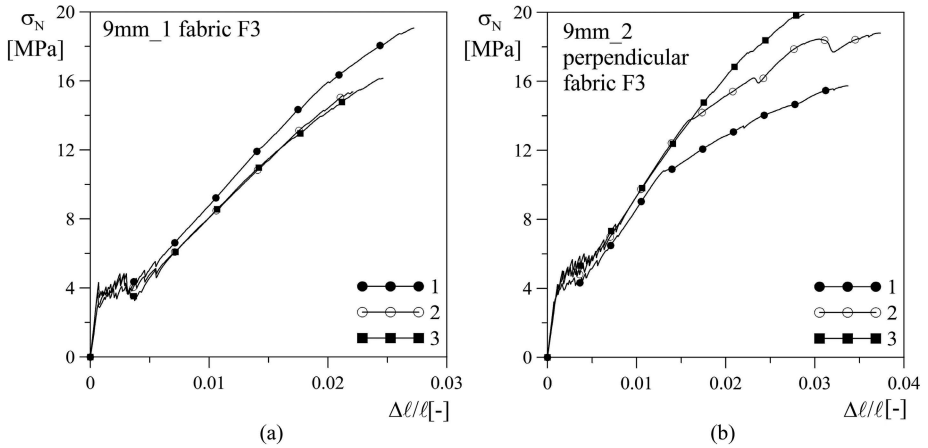

Figure 8.8: Experimental tensile test results: nominal stress vs. normalized displacement curves for 400x70x9 mm^3 TRC specimens reinforced with one (a) and two perpendicular (b) "F3" fabrics.

The plastic stress-strain relationships introduced respectively in the sandwich beam and in the full-scale panel model, deduced considering displacement transducer measurements, are shown in Figure 8.9.

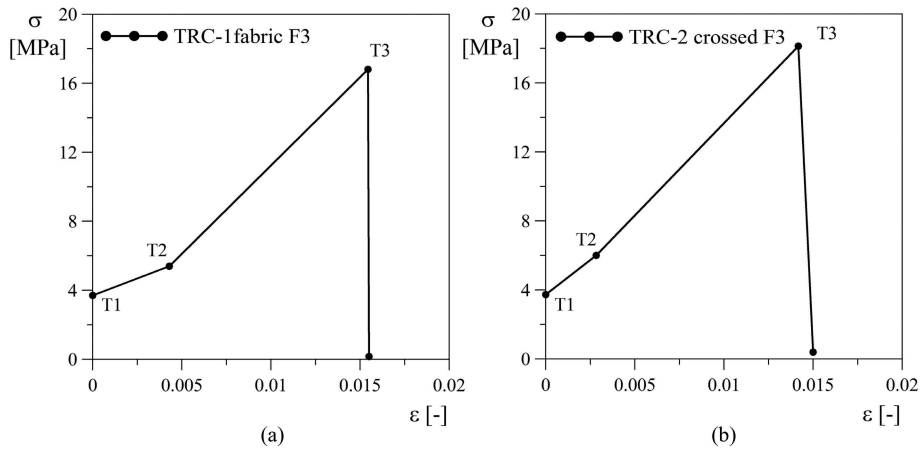

Figure 8.9: TRC tensile stress-strain relationships introduced in Concrete Damage Plasticity model respectively for sandwich beams (a) and full-scale panel (b).

Some relevant points typical of the TRC tensile behaviour (see Figure 3.5) are highlighted in the figure: $T1$, which corresponds to the beginning of the multi-cracking branch; $T2$, after which the contribution of the fabric only is acting; and $T3$, at which the brittle failure of the fabric occurs.

Expanded Polystyrene

The elastic phase of EPS is defined by introducing a Young's modulus equal to 13.7 MPa and a Poisson's ratio equal to 0.1. The elastic modulus was measured performing compressive tests on three 100x100x150 mm^3 nominally identical specimens; these results were shown in Figure 5.2.

To consider plasticity, Crushable Foam model with volumetric hardening implemented in Abaqus is used [Simulia (2011)]. The phenomenological isotropic model was originally developed, for metallic foams, by Deshpande and Flek (2000). The model assumes that the evolution of the yield surface is controlled by the volumetric compacting plastic strain experienced by the material.

Considering the pressure stress (p), the Mises stress (q) and the deviatoric stress ($\mathbf{S}$) as defined above, the yield surface (Figure 8.10) is defined as:

$$F = \sqrt{q^2 + \alpha^2 (p - p_0)^2} - B = 0 \tag{8.11}$$

with:

- p_c, yield stress in hydrostatic compression;
- p_t, strength of the material in hydrostatic tension;
- $p_0 = (p_c - p_t)/2$, centre of the yield ellipse on the p-axis;
- $A = (p_c + p_t)/2$, size of the (horizontal) $p-$axis of the yield ellipse;
- $B = \alpha A$, size of the (vertical) $q-$axis of the yield ellipse;
- α, a constant which constitutes the shape factor of the yield ellipse and defines the relative magnitude of the axes.

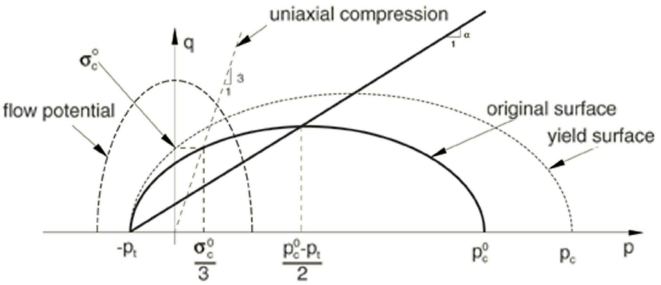

Figure 8.10: Crushable foam model with volumetric hardening: yield surface and flow potential in the $p - q$ stress plane.

The shape factor can be computed using the initial yield stress in uniaxial compression, σ_c^0, the initial yield stress in hydrostatic compression, p_c^0, and the yield strength in hydrostatic tension, p_t:

$$\alpha = \frac{3k}{\sqrt{(3k_t + k)(3 - k)}} \tag{8.12}$$

with the compression yield stress ratio k ($0 \leq k \leq 3$) equal to:

$$k = \frac{\sigma_c^0}{p_c^0} \tag{8.13}$$

and the hydrostatic yield stress ratio k_t ($k_t \geq 0$) equal to:

$$k_t = \frac{p_t}{p_c^0} \tag{8.14}$$

The flow potential chosen in the Crushable Foam model (also visible in Figure 8.10) is defined as:

$$G = \sqrt{q^2 + \frac{9}{2}p^2} \tag{8.15}$$

and the equivalent plastic strain rate is defined as:

$$\dot{\bar{\varepsilon}}_{pl} = \frac{\sigma : \dot{\varepsilon}_{pl}}{G} \tag{8.16}$$

The model assumes that p_t remains fixed throughout any plastic deformation process. By contrast, the compressive strength, p_c, evolves as a result of compaction (increase in density) or dilation (reduction in density) of the material.

To calibrate the parameters, the procedure proposed by Gilchrist and Mills (2001) was followed, using the experimental compressive test results (Section 5.1).

The model parameters were set in order to impose the initial yielding surface to satisfy the following conditions:

- the uni-axial compressive yielding stress (σ_{c0}) is equal to that obtained from the experimental tests in uni-axial compression at the end of the initial

linear branch ($\sigma_{c0} = 0.192MPa$). This condition means that the initial yield surface passes through the point ($p = \sigma_{c0}/3$; $q = \sigma_{c0}$);

- the uni-axial tensile strength (σ_{t0}) is that defined by UNI EN 13163, "Thermal insulation products for buildings - Factory made products of expanded polystyrene (EPS)- Specification", for EPS250 ($\sigma_{t0} = 0.35MPa$). This condition means that the initial yield surface passes through the point ($p = -\sigma_{t0}/3$; $q = \sigma_{t0}$)).

The resulting initial yield surface is represented in Figure 8.11 and the related parameters are summarized in Table 8.2. In the same table also the uni-axial compression hardening curve is reported. This curve is directly taken from the experimental results.

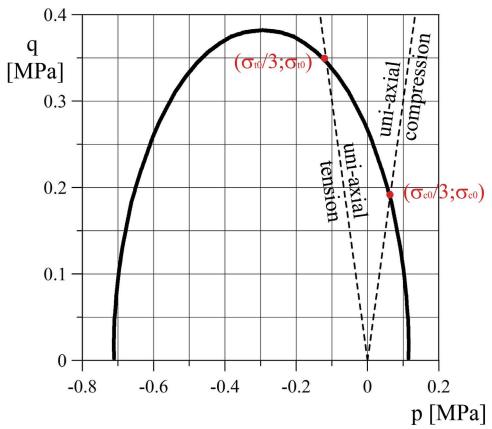

Figure 8.11: Crushable foam model with volumetric hardening: yield surface in the $p-q$ stress plane for $k = 1.6$ and $k_t = 6.0$.

In order to assess the reliability of the adopted parameters, a numerical model of the uni-axial compressive tests was performed. 8-node linear brick elements with a dimension of 3.03 x 3.03 x 3 mm^3 were used; a sketch of the mesh and of the boundary conditions is represented in Figure 8.12. In Figure 8.13 the numerical

Table 8.2: Definition of the parameters in Crushable Foam and Crushable Foam Hardening Matrix

		HARDENING	
k	k_t	σ_c	*Uniaxial plastic strain*
1.6	6.0	0.192	0
		0.265	0.285

results in terms of nominal stress ($\sigma = P/A$; $P = load$; $A = cross-section\ area$) versus nominal strain ($\varepsilon = \delta/h$; $\delta = top\ displacement$; $h = specimen\ heigth$) are compared with the average experimental results. A good agreement with the experimental data was achieved. In the figure, point $E1$ is highlighted: once this point is reached, a significant change in the slope of the response is registered.

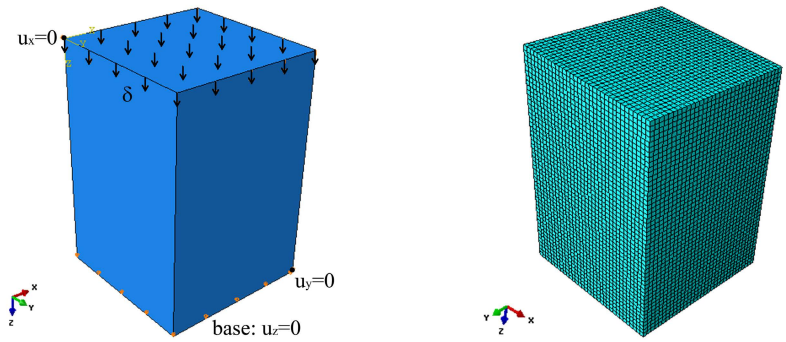

(a) (b)

Figure 8.12: EPS specimen: geometry with constraints (a) and mesh (b) in Abaqus.

It is worth to note that, even if the yield surface passes through the correct value of the uni-axial tensile strength, the numerical model assumes a uni-axial tensile elastic-plastic hardening behaviour, while the material is elastic-brittle. Hence, it is necessary to verify if the EPS tensile strength is exceeded or not, in order to check if a tensile failure of the core is occurred.

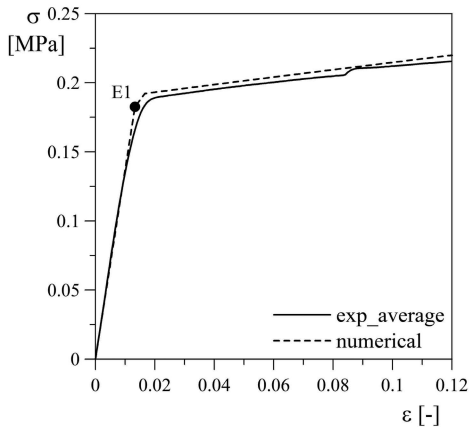

Figure 8.13: EPS 250 stress-strain relationship in compression: comparison between experimental results and numerical curve obtained through Crushable Foam model.

Steel

Steel plates used to reduce stress concentration in sandwich beam tests are assumed to be elastic, with a Young's modulus equal to 210 GPa and a Poisson's ratio equal to 0.3.

8.2.2 Four point load tests on sandwich beams

Both small and big sandwich beams, having the size of 550x150x120 mm^3 and 1200x300x120 mm^3 respectively, are modeled.

The TRC layers, the EPS layer and the steel plates are all modeled as solid homogeneous sections, assuming perfect bond at interfaces. The perfect bond assumed at the TRC/EPS interface, with no interface elements introduced, constitutes a strong assumption of the model, but, as no detachment was observed during experimental tests, this assumption is expected to be reliable. TRC layers, EPS layer and steel plates are discretized with 8-node linear brick elements (C3D8R). The characteristics of the finite element mesh are reported in Tables

8.3 and 8.4 respectively for small and big sandwich beam models; in particular, the number of nodes, the number of elements, the number of elements over the thickness and the maximum aspect ratio (ratio between the longest and shortest edge of an element) are specified.

Table 8.3: Small sandwich beam model: mesh characteristics.

Small sandwich beam	TRC_{sup}	EPS	TRC_{inf}	*Entire model*
Nodes	10400	28600	10400	44200
Elements	7425	24750	7425	39600
Elements over the thickness	3	10	3	-
Max. aspect ratio	1.9	1.9	2.3	2.3

Table 8.4: Big sandwich beam model: mesh characteristics.

Big sandwich beam	TRC_{sup}	EPS	TRC_{inf}	*Entire model*
Nodes	15128	41602	15128	64294
Elements	10890	36300	10890	58080
Elements over the thickness	3	10	3	-
Max. aspect ratio	3.1	1.1	3.1	3.1

Small sandwich beams

The model geometry together with the constraints and the mesh is shown in Figure 8.14.

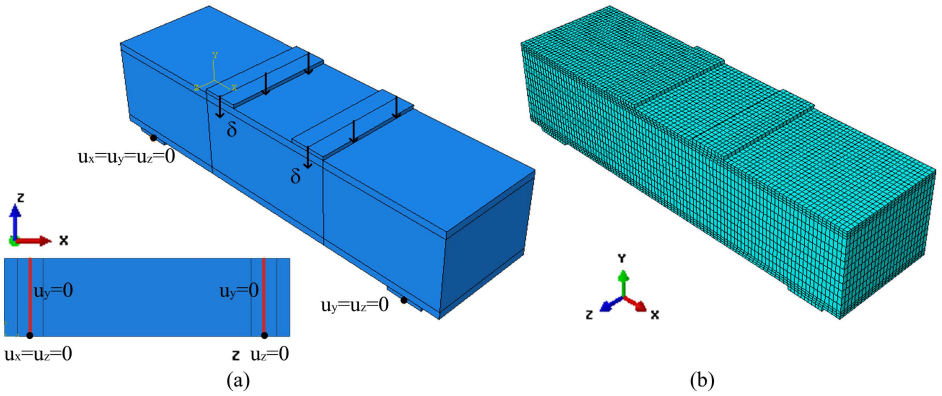

Figure 8.14: Small specimen: geometry with constraints (a) and mesh (b) in Abaqus.

The numerical results obtained for a small sandwich beam are shown in Figure 8.15 in terms of load (P) versus displacement (δ) curve. δ represents the machine cross-head displacement.

In subfigure (a) this curve is compared with the experimental results already presented in Chapter 5: a superposition between the experimental and the numerical curves is achieved. The numerical curve does not show the same ductility exhibited by the specimens tested; it is worth to note, however, that the numerical analysis stopped due to convergence problem when the materials were still able to carry the load.

In subfigure (b) just the numerical load versus vertical displacement curve is plotted. Some relevant points are highlighted; in particular, points $T1(sup)$ and $T1(inf)$ indicate that the upper and the lower TRC layers start to crack, and points $T2(sup)$ and $T2(inf)$ indicate the end of the multi-cracking phase respectively for the upper and the lower TRC layer. As observed during the

experimental tests, both the TRC layers are cracked, thus confirming that the small beam acts as a partially composite sandwich. It is worth noting that, even if the TRC is cracking, the global response remains linear up to point $E1$.

The multi-cracking phenomenon, observable in both the TRC layers, is shown in Figure 8.16 by displaying the maximum principal plastic strains; in the same figure, the crack pattern of specimen S1 is shown (lateral and bottom view). Comparing the pictures related to numerical and experimental test, it is possible to state that the numerical analysis well represents the regions involved in multi-cracking: in the upper TRC layer the cracks form under the loading knives, while the lower TRC layer is cracked along the entire length.

The significant change in the slope of the composite global response is related to the development of a compressive strut in the EPS layer when point $E1$ is reached. This compressive strut is well visible in Figure 8.17. As shown in subfigure (c), the numerical analysis is also able to catch the plastic strain concentration at the upper edges of EPS, that caused the debonding of the upper TRC face in the experimental tests.

It is possible to state that the numerical solution well represents the behaviour of the composite sandwich beam, not only in terms of load versus displacement curve, but also in terms of failure mode identification.

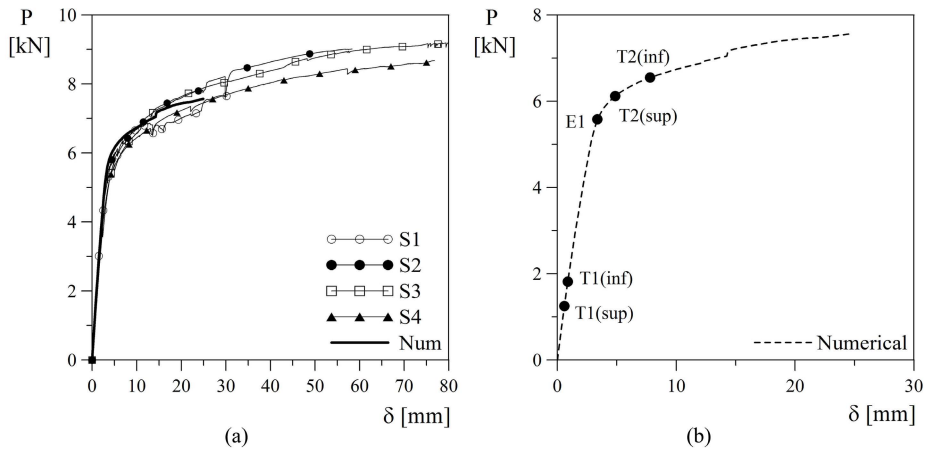

Figure 8.15: Small sandwich beams - vertical load vs. displacement curves: comparison between experimental and numerical results (a) and numerical response with the identification of relevant points (b).

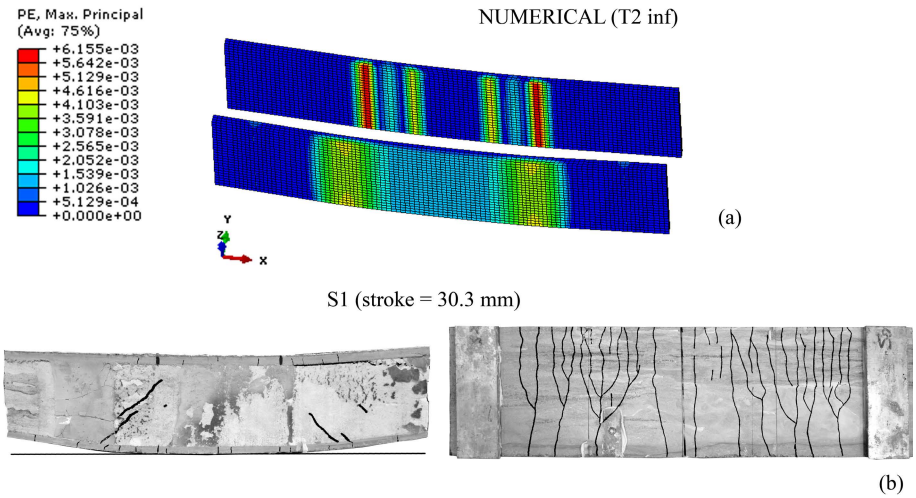

Figure 8.16: Small sandwich beams - multi-cracking of both the TRC layers: maximum principal plastic strain at point $T2_{inf}$ (a) and pictures of specimen S1 at the end of the test (b).

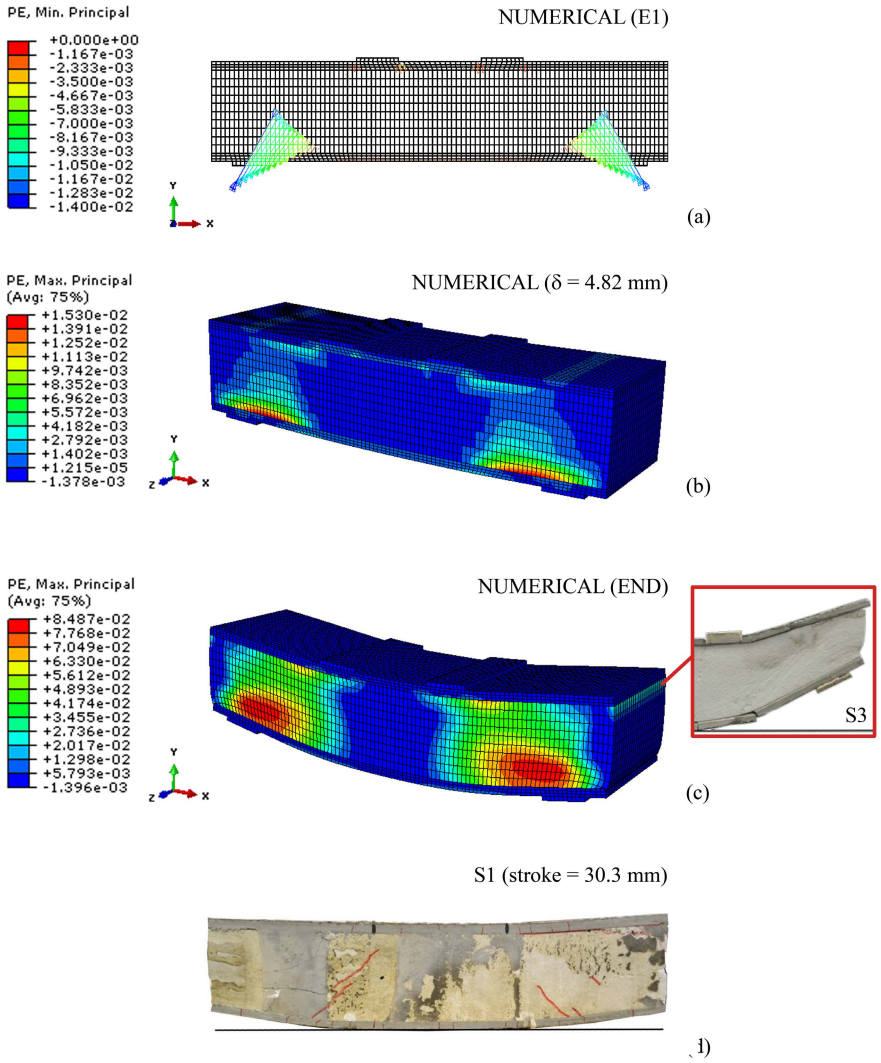

Figure 8.17: Small sandwich beams - development of a compressive strut in the EPS layer: minimum principal plastic strain at point $E1$ (a), maximum principal plastic strain at $\delta = 4.82\,mm$ (b), maximum principal plastic strain at the end of the analysis with a picture of specimen S3 (c) and picture of specimen S1 after test (d).

Big sandwich beams

The model geometry together with the constraints and the mesh is shown in Figure 8.18.

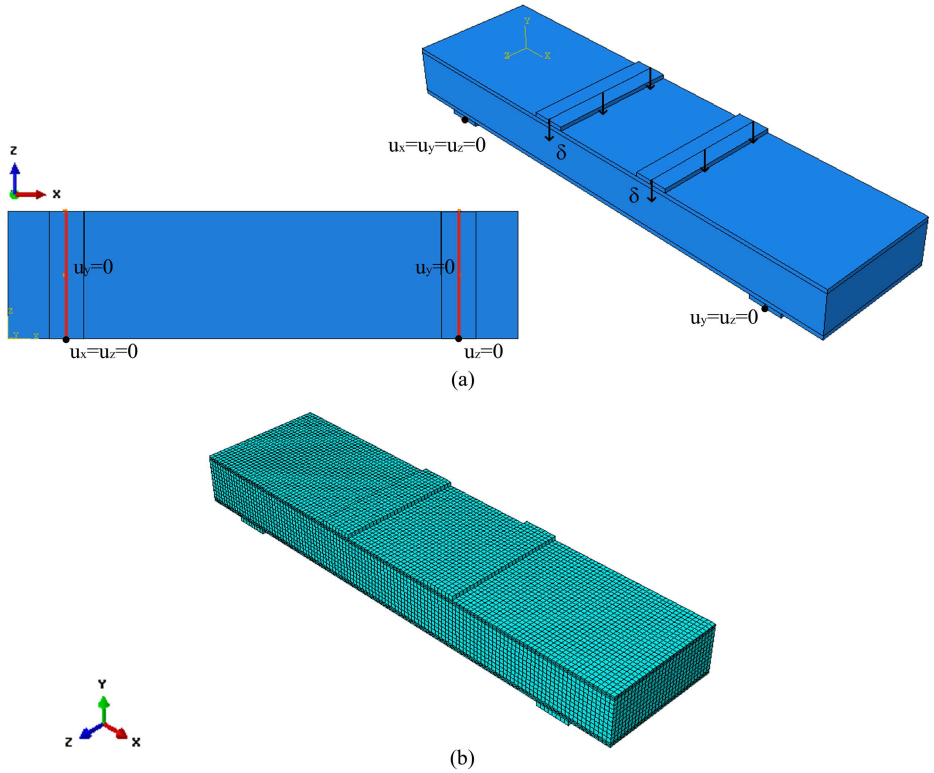

Figure 8.18: Big specimen: geometry with constraints (a) and mesh (b) in Abaqus.

The results of the numerical analysis performed for the big sandwich beam are shown in Figures 8.19, 8.20 and 8.21.

As done for small sandwich beam, the load versus displacement numerical curve is compared with the experimental results, achieving quite a good agreement in terms of global response (Figure 8.19(a)). The relevant points related to the material constitutive laws are highlighted on the numerical response in Figure

8.19(b); in this case the large displacements measured during experimental tests are reached (no convergence problems) and the failure of the upper TRC layer takes place, as point $T3$ in the TRC tensile constitutive law is achieved. This failure observed in the numerical solution is not in agreement with the experimental evidences: in big specimens tested, the upper TRC layer was cracked, but did not exhibit the failure of the fabric; conversely, the development of a tensile crack in the EPS took place, causing a sudden failure of the specimens. As explained above, the Crushable Foam model is not able to predict a tensile failure of the EPS, as it assumes an hardening behaviour in uni-axial tension for the material. However, the strain concentration leading the tensile crack formation in the EPS is clearly visible in the numerical model, as shown in Figure 8.21.

Conversely to what happened in the case of small sandwich beam, in big sandwich beam the strain concentration at the upper edges of the EPS does not take place; in fact, looking at the tested specimens, no debonding was observed at the upper TRC/EPS interface in these points. The debonding visible in Figure 8.21(c) occurred at failure and was only due to the EPS tensile crack propagation.

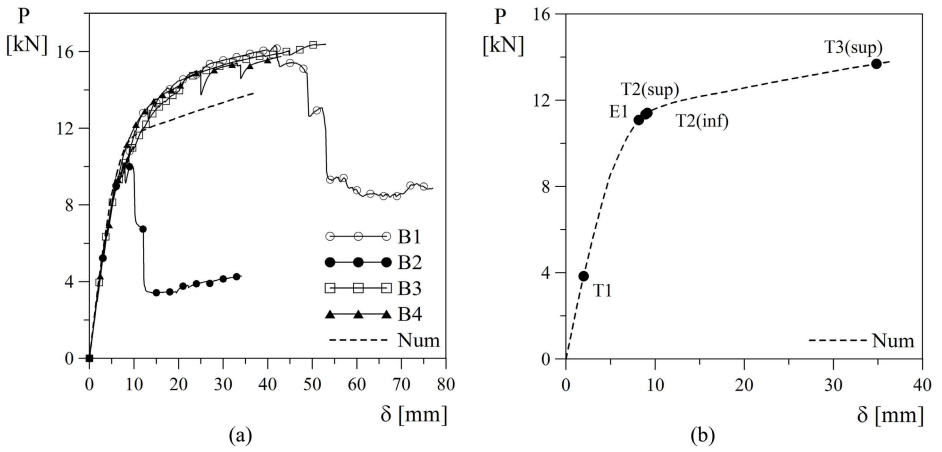

Figure 8.19: Big sandwich beam - vertical load vs. displacement curves: comparison between experimental and numerical results (a) and numerical response with the identification of relevant points (b).

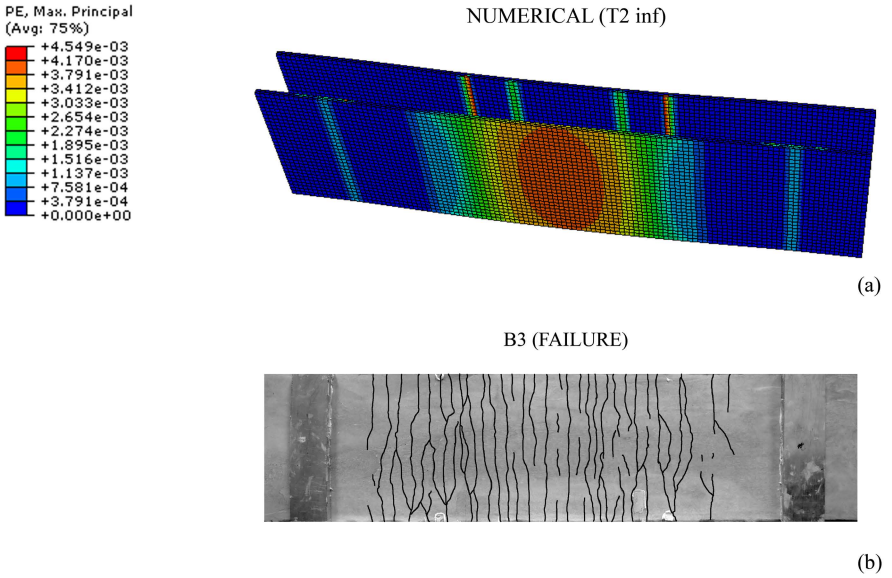

Figure 8.20: Big sandwich beam - multi-cracking of both the TRC layers: maximum principal plastic strain at point $T2_{inf}$ (a) and a picture of specimen B3 at the end of the test (b).

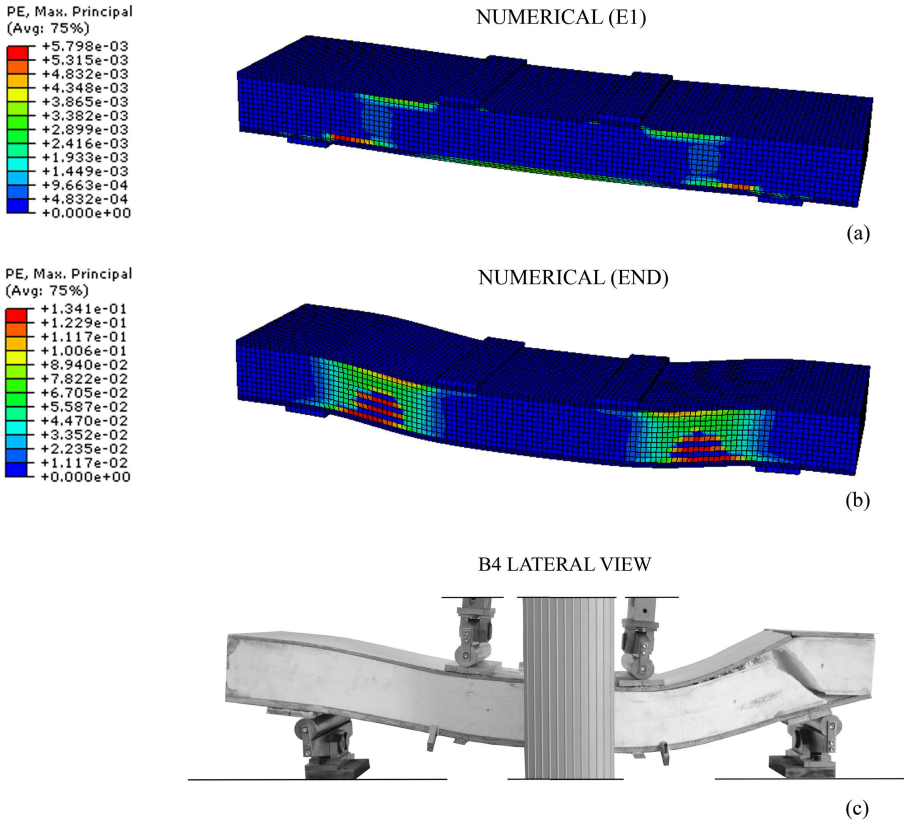

Figure 8.21: Big sandwich beam - development of a compressive strut in the EPS layer: maximum principal plastic strain at point $E1$ (a), maximum principal plastic strain at the end of the analysis (b) and picture of specimen B4 at failure (c).

8.2.3 Full-scale panel tests

The tests performed on the full-scale panel, whose results are shown in Chapter 7, have been modeled in Abaqus FEA software. Two configurations have been developed: one for the test at Serviceability Limit State and one for the test at Ultimte Limit State. In the following subsections the two configurations and the corresponding results are described. It is worth to remember that, in the full-scale panel, each layer of Textile Reinforced Concrete was characterized by two perpendicular fabric "F3"; hence, the tensile stress-strain relationship introduced in Concrete Damage Plasticity model is the one shown in Figure 8.9(b).

SLS

Just one quarter of the panel is modeled, exploiting both the $x-y$ and the $z-y$ symmetries. The 150 x 150 mm^2 elastomeric bearing plate is modeled through vertical linear springs characterized by a proper stiffness in y direction. This stiffness is computed considering the height of the bearing plate (25 mm), the area of the mesh elements on the support (15x15 mm^2) and assuming an elastic modulus of the elastomer equal to 2.5 MPa. An increasing distributed load is applied on the area corresponding about to that occupied by the water pool shown in Figure 7.6.

As done for the sandwich beams, both the TRC layers and the EPS layer are modeled as solid homogeneous sections, assuming perfect bond at the TRC/EPS interfaces (no interface elements introduced). Both TRC and EPS layers are discretized with 8-node linear brick elements (C3D8R). The characteristics of the finite element mesh are reported in Table 8.5, in which the number of nodes, the number of elements, the number of elements over the thickness and the maximum aspect ratio are specified. The model geometry together with the constraints and the mesh is shown in Figure 8.22.

Table 8.5: Full-scale panel model at SLS: mesh characteristics.

Full scale panel – SLS	TRC_{sup}	*EPS*	TRC_{inf}	*Entire model*
Nodes	22644	62271	22644	96237
Elements	16500	55000	16500	88000
Elements over the thickness	3	10	3	-
Max. aspect ratio	4.6	1.6	4.6	4.6

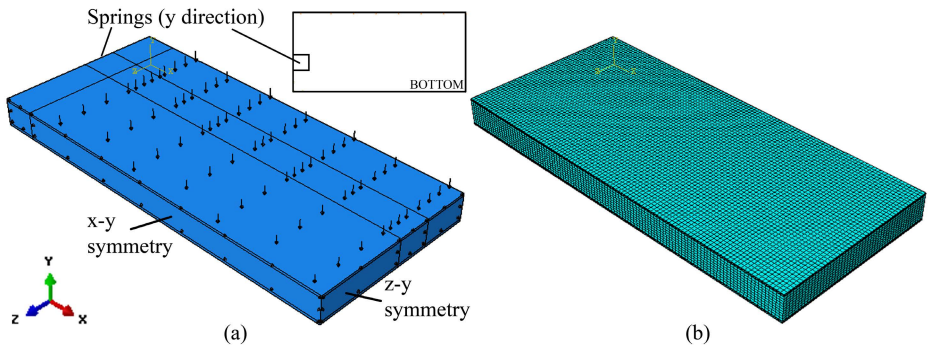

Figure 8.22: Full-scale panel tested at SLS: geometry of a quarter of the panel with loads and constraints (a) and mesh (b).

The numerical results and the comparison with the experimental response are shown in Figure 8.23 in terms of distributed load versus displacement. δ_1, δ_2 and δ_3 represent the specimen vertical displacements at mid-span; in particular δ_1 is the central one, and δ_2 and δ_3 are the lateral (Figure 7.5). For comparison purposes, the experimental curves previously shown in Chapter 7 are in this section cleaned from the horizontal branches related to the time needed by the cracks to propagate. Considering the wind, which is the main out-of-plane load acting on the panel, the cracks do not have the time to propagate as the load is cyclic, with a period in the order of seconds.

In Figure 8.23(a) some relevant points in the TRC tensile constitutive law are highlighted; $T1\ inf$ and $T2\ inf$ refer respectively to the beginning and the end of the multi-cracking phase at mid-span in the lower TRC layer. Conversely to what

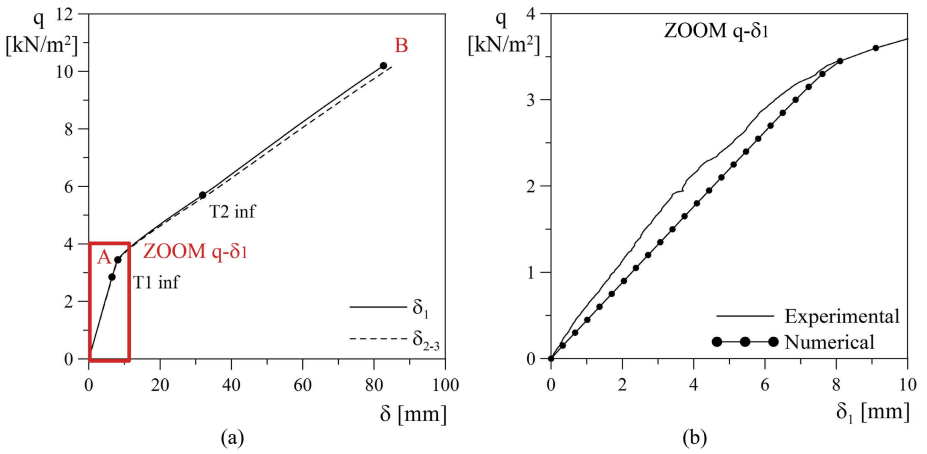

Figure 8.23: Full-scale panel tested at SLS: numerical response in terms of distributed load vs. displacement curve (a) and comparison between numerical and experimental results in terms of distributed load vs. central vertical displacement δ_1 (b).

was observed in the case of sandwich beams, in the full-scale panel at SLS the upper TRC layer remains un-cracked up to point B (at which the simulation was stopped), thus indicating that the panel acts more as a fully-composite structure thanks to its higher slenderness and the loading scheme considered. The global response is affected by the multi-cracking of the lower TRC layer once point A is reached, resulting in a significant change in the slope. In Figure 8.24, the multi-cracking of the lower TRC layer at points A and B is shown by plotting the maximum principal plastic strains.

As the experimental test was stopped at a load equal to 3.5 kN/m^2, a zoom on the numerical curve up to this value is shown in Figure 8.23(b) in order to compare the results. As it can be seen, a good agreement is obtained.

As it could be expected, a local stress concentration is registered over the bearing plate both in EPS and TRC materials, leading to the development of plastic strains localized in this region.

The experimental and numerical responses are also compared in terms of

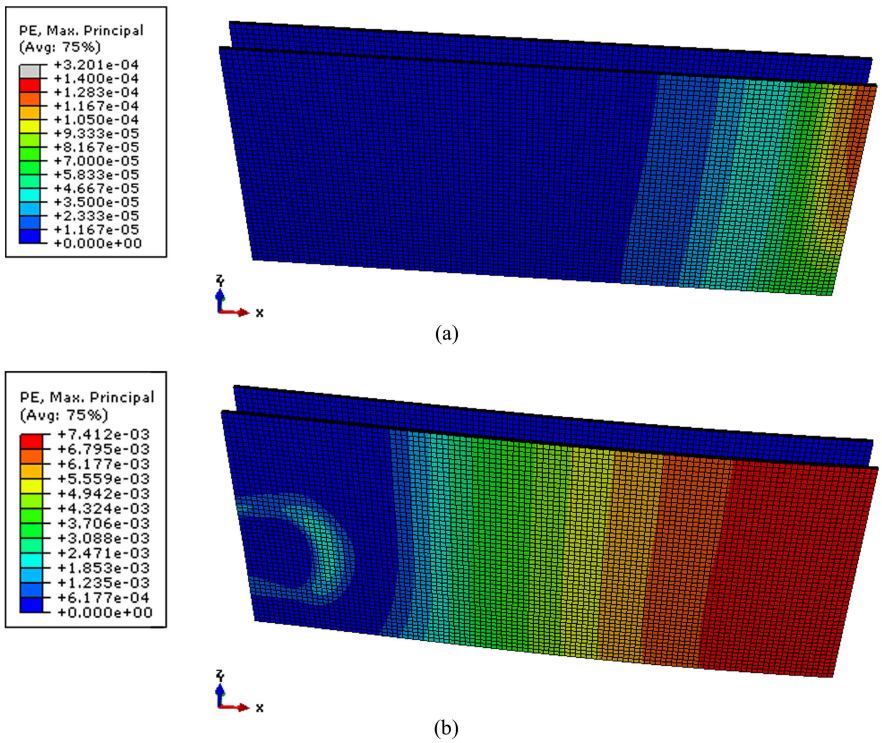

Figure 8.24: Full-scale panel tested at SLS: maximum principal plastic strains in TRC layers at point A (a) and B (b).

distributed load vs. crack opening displacement (COD) in Figure 8.25. Also in this case a good agreement is obtained.

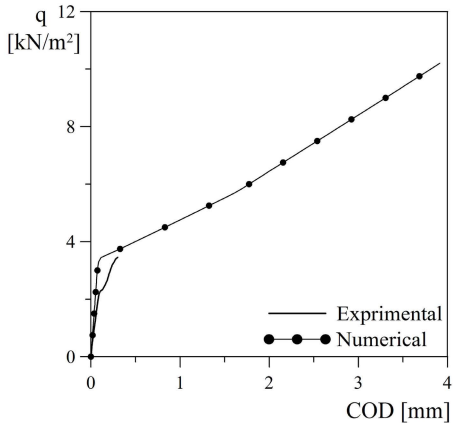

Figure 8.25: Full-scale panel tested at SLS: comparison between numerical and experimental results in terms of distributed load vs. crack opening displacement COD.

ULS

As seen in Section 7, the ULS test was performed by applying concrete blocks over the multilayer panel. The application of loads was not symmetric with respect to the $y-z$ plane, hence an half of the panel is modeled, exploiting just the $x-y$ symmetry.

Again, the 150 x 150 mm^2 elastomeric bearing plates are modeled through springs characterized by a proper stiffness in y direction. The load is applied, according to the experimental test, as a distributed load over the area occupied by each concrete block. Four distributed loads, corresponding to the four concrete blocks, are applied one by one over the panel and each load, once applied, persists up to the end of the numerical analysis (Figure 8.26).

As done for SLS, both the TRC layers and the EPS layer are modeled as solid homogeneous sections, assuming perfect bond at the TRC/EPS interfaces (no

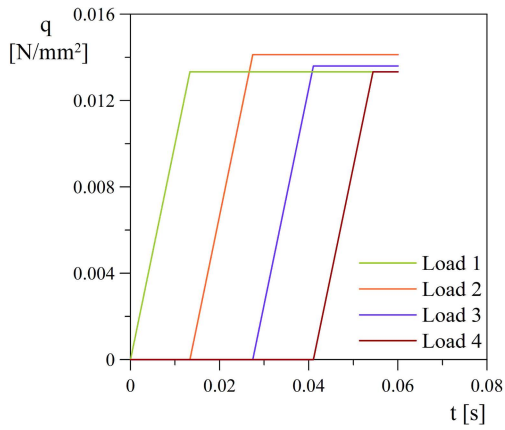

Figure 8.26: Full-scale panel tested at ULS: application of loads over time.

interface elements introduced). Both TRC and EPS layers are discretized with 8-node linear brick elements (C3D8R). The characteristics of the finite element mesh are reported in Table 8.6, in which the number of nodes, the number of elements, the number of elements over the thickness and the maximum aspect ratio are specified. The model geometry together with the constraints and the mesh is shown in Figure 8.27.

Table 8.6: Full-scale panel model at ULS: mesh characteristics.

Full scale panel − ULS	TRC_{sup}	*EPS*	TRC_{inf}	*Entire model*
Nodes	44676	122859	44676	189873
Elements	32700	109000	32700	174400
Elements over the thickness	3	10	3	-
Max. aspect ratio	4.6	1.6	4.6	4.6

The numerical results in terms of total load versus lateral vertical displacement at mid-span are plotted in Figure 8.28. In the same figure, the experimental results are shown through dots: each dot refers to the displacement measured after the application of a concrete block; the application of the fourth block (*Load*4)

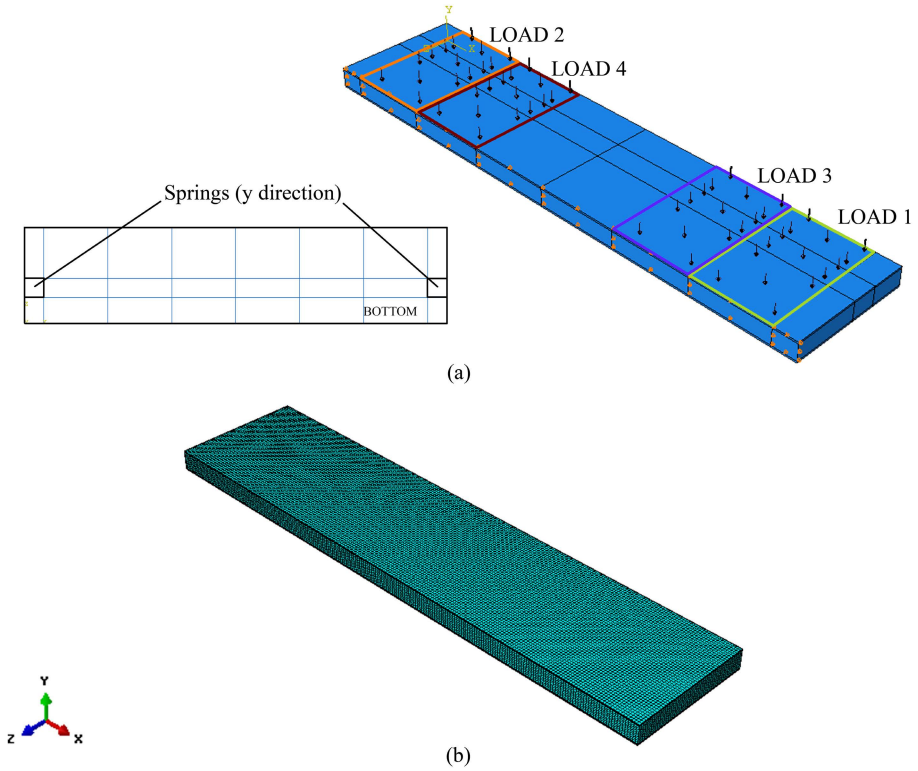

Figure 8.27: Full-scale panel tested at ULS: geometry of an half of the panel with loads and constraints (a) and mesh (b).

led to the panel failure and made the measure of the vertical displacement not possible, hence there is not a point on the graph referring to *Load* 4.

Also this numerical analysis well catch the real behaviour of the sandwich panel if *Load* 1, *Load* 2 and *Load* 3 are taken into account. Point $T1_{inf}$ in the figure indicates that the lower TRC layer starts to crack. Once this point is reached, a change in the slope of the global response is registered. The upper TRC layer remains elastic during the whole analysis.

In the experimental test *Load* 4 led to the tensile failure of the lower TRC

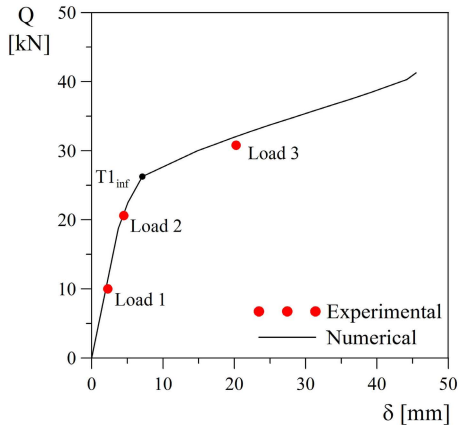

Figure 8.28: Full-scale panel tested at ULS: numerical curve of total load vs. lateral vertical displacement at mid-span.

layer and the consequent propagation of a crack in the EPS material; conversely, in the numerical analysis, the lower TRC layer is still multi-cracking after the application of this load and its tensile failure is not registered.

8.2.4 Consideration on the tensile behaviour of TRC in the finite element model

In the Concrete Damage Plasticity model the tensile behaviour of TRC layers is assumed homogeneous over the layer thickness. The constitutive laws adopted, shown in Figure 8.9, have been deduced from the results of tensile tests performed on 400x70x9 mm^3 TRC specimens.

Finite element analysis revealed that both the TRC layers are not simply subjected to axial stresses (due to sandwich action), but are bended (partially-composite sandwich action, see Figure 2.5). This evidence is in agreement with experimental results.

Even if the TRC layers are bended, good predictions of experimental results

are obtained through finite element analysis considering an homogeneous tensile behaviour for the whole TRC thickness. As demonstrated in the following, the choice of deducing the TRC tensile constitutive law testing in tension 9 mm thick specimens allows to well predict also the bending behaviour. In fact 9 mm results an effective thickness, in which the interaction between the fabric and the matrix exists.

TRC plates with size of 400x70x12 mm^3 and reinforced with one fabric "F3", with the warp oriented in the longitudinal direction, were tested in bending according to the test set-up shown in Figure 8.29. The same test is modeled in Abaqus, assigning TRC Concrete Damage Plasticity material presented in Subsection 8.2.1 to the whole plate. Hence, the tensile constitutive law deduced from 9 mm thick TRC specimen has been spread over a thickness of 12 mm.

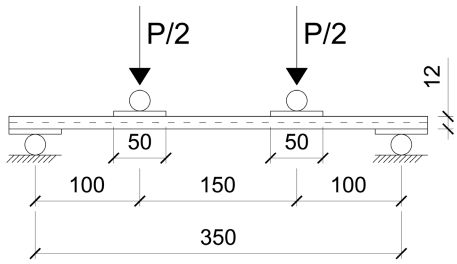

Figure 8.29: 12 mm thick TRC plate: test set-up.

The Abaqus model is shown in Figure 8.30, and the comparison between experimental results and numerical response is shown in Figure 8.31.

The overestimation of the numerical response can be considered acceptable also considering that, in the model of sandwich beams and real scale sandwich panel, the tensile constitutive law deduced from 9 mm thick TRC specimens has been spread over a thickness of 10 mm, instead of 12, thus leading to a lower

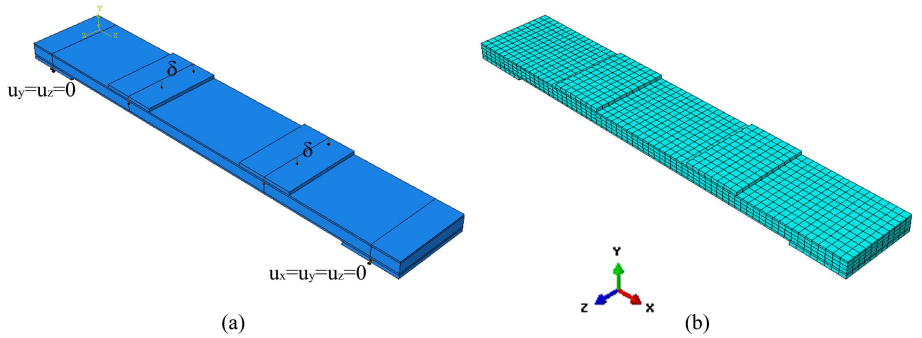

Figure 8.30: TRC plate: geometry with constraints (a) and mesh (b) in Abaqus.

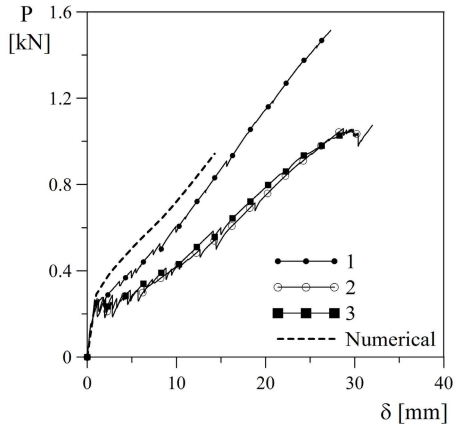

Figure 8.31: TRC plate in bending: comparison between numerical and experimental results in terms of load vs. displacement.

error in the estimation of the bending response of the faces.

9

Concluding remarks and further developments

A multi-layer precast façade panel is proposed as a durable alternative to the exterior insulation and finishing system, usually adopted in the energy retrofitting of existing building. The work presented in this thesis is aimed at demonstrating the capabilities of this panel with respect to its mechanical behaviour.

An extensive experimental campaign has been developed in order to investigate the mechanical behaviour of the panel, operating at three levels: material, lab-scale and full-structure level. The experimental results have been presented in Chapters 4, 5, 6 and 7, and the numerical predictions in Chapter 8. Basing on what obtained, some significant conclusions can be drawn.

The investigation reveals the need to treat Textile Reinforced Concrete as an homogeneous material constituted by fabrics embedded in the matrix, and not - as reinforced concrete - as the union of two materials with distinct constitutive laws; this is due to the fact that the reinforcement exhibits a brittle failure and it is constituted by several filaments, characterized by a negligible bending stiffness;

the telescopic failure of the yarn is strictly related to the interaction with the matrix. The fabric/matrix bond is the key point in the TRC behaviour.

Considering the use of TRC in a composite structure (e.g. the façade sandwich panel subject of this thesis), the main question is how to characterize it for the structural design of the element.

In uniaxial compression, the contribution of the fabric does not play a key role, hence its presence can be neglected and the mortar can be characterized by following standard procedures.

In uniaxial tension, the influence of different factors on the TRC behaviour was deeply investigated and the results are collected in Chapter 4. In the following the main aspects are summarized:

- the behaviour of TRC is strongly influenced by the reinforcement amount, with both the equivalent cross-section and the bond surface of the warp roving playing an important role. In contrast, the weft roving seems to mainly control cracking distance and therefore the overall ductility. As a result, with reference to a single fabric, a limit reinforcement ratio can be detected via the computation of an Effectiveness Factor (EF), based on the ratio between the peak loads of the TRC composite and the AR-glass fabric. When the value of EF is less than 1, a progressive reduction in effectiveness is experienced. The smallest value of EF measured in the present experimental investigation was 0.67 for a reinforcement ratio of about 3.20%. The EF value can be increased by boosting the number of fabric layers; in this case the layers should be separated, as full overlap can significantly reduce EF due to the loss of bond surface. An analysis of the employed leno weave assembling technique resulted in the identification of a minimum weft spacing able to prevent fabric sliding, with a value detected for the TRC used in the present study close to 30 mm. Smaller values may

favour delamination effects;

- since curing conditions can affect matrix shrinkage, they are also associated with the bond phenomenon in the composite material. The greater the shrinkage, the greater the bond strength that develops; consequently both the first cracking and peak strength increase. Curing in air at environmental temperature is found to be the best solution if compared to curing at 60 ℃ or in water;

- as with other cement-based materials, TRC behaviour depends on strain rate. In the present study, a loss in strength and ductility with decreasing displacement rate was also associated with a coarser cracking pattern. Further research regarding this phenomenon is required;

- no significant peak strength reduction was observed in terms of the size effect. Specimen size partially affected the post cracking branch, with a reduction in ductility observed with increasing specimen size. For specimen lengths larger than twice specimen width, negligible variation in the first cracking strength was observed.

The approach here proposed for design is based on the identification of a tensile behaviour starting from tensile tests. At Serviceability Limit State, test results allow to define the constitutive law; at Ultimate Limit State, the Effectiveness Factor (EF) is proposed to be used in order to account for the fabric-matrix interaction. This ULS mechanical interpretation represents a practical design alternative to the approach suggested by Hegger et al. (2006), which considers two distinct phases (concrete matrix and fabric reinforcement) interacting by means of experimentally calibrated coefficients.

Concerning bending, the use of a tensile constitutive law determined from tensile tests allows to properly predict bending behaviour of TRC specimens

reinforced in the same way up to a certain thickness (in the case study one fabric "F3" is used as reinforcement and 9 mm is found to be a well representative thickness).

The behaviour of sandwich panels characterized by two TRC faces and an internal polystyrene layer has been investigated at different scales.

In coupling TRC with polystyrene in order to obtain sandwich structures, no interface surface treatment was adopted with the aim of improving the bond between subsequent layers. However, no delamination occurred during testing, since a good bond is guaranteed by the innovative in-pressure technique used in casting.

Small and big multi-layered sandwich beams were tested considering a four point bending scheme (Chapter 5). Considering both the geometries investigated, a large ductility was experienced in either case (big: $\delta_u/\delta_I = 10$; small: $\delta_u/\delta_I = 20$); this ductility was achieved as effect of both large compressive plastic strain in the EPS core and multi-cracking pattern in the TRC outer layers. The multi-cracking pattern seems to be affected, especially in the small geometry, by the fabric position in the TRC layer thickness; nevertheless the different crack pattern did not affect the global response of the specimen. This consideration may lead to conclude that fabric position is more important at Serviciability Limit State (SLS), when crack opening displacements are regarded, rather than at the Ultimate Limit State (ULS), when the maximum bearing capacity is considered.

Comparing the initial response of the two different geometries with two elastic analytical solutions for sandwich, it clearly appears that an important contribution to the global response is given by the large shear deformability of the EPS, that also causes the solution to behave as a partially composite sandwich. Even if the non-linear global response is strongly driven by the EPS plastic compressive strains, the specimen failures are respectively related to the tensile failure of TRC for small specimens and to the EPS brittle cracking in the case of bigger

geometry.

Furthermore, increasing the specimen size, the transverse behaviour of the sandwich becomes less important, thus moving from a geometry (the small one) in which the two-dimensional contribution is underlined by the not negligible transverse strain, to the case in which the larger slenderness makes more reliable the mono-dimensional beam assumption.

A good correlation with the results proposed by Hegger and Horstmann (2009) (Figure 2.7) has been found considering TRC sandwich panels characterized by a core in similar polystyrene.

The sandwich solution was also investigated considering a concentrated load (Chapter 5). Two failure modes were identified: the formation of a crack in the upper TRC layer due to negative bending moment and the punching shear failure under the loading area. However, further investigations are needed in order to account impact phenomena and the effect of the boundary conditions on the response.

A real scale panel with size of 3.3 x 1.5 m^2 was tested considering both Serviceability and Ultimate Limit State (Chapter 7). The SLS test allows to state that, even if the panel multi-cracks under service condition, these cracks are not visible to the naked-eye (crack width lower than 50 μm), thus satisfying an important requirement for a façade panel. Concerning ULS, no shear failure was observed in the core; the failure took place when 41 kN were applied on the panel and it was due to the achievement of the tensile strngth of the lower TRC layer.

An important topic investigated in the thesis is the durability of TRC structures when exposed to freezing-thawing cycles. This aspect is crucial especially considering that the panel is cracked during its service life. Both TRC specimens and sandwich beams characterized by TRC faces are considered (in Chapter 4 and 6 respectively). Two different phenomena seem to govern the behaviour of

the material: the damage due to thermal cycles and the matrix self-healing and late hydration due to the permanence in water of the material. Thanks to the presence of cracks during the thermal cycles, and therefore an easier penetration of water, self-healing and late hydration effect mainly appears in pre-cracked (C) situation. The larger water absorption of pre-cracked specimens, that is directly related to the self-healing, is also clearly visible in the specimen mass growth. In the case of sandwich beams, the exposure to freezing-thawing cycles mainly affects the ductility of the specimens, while the maximum load achieved and the bending stiffness result scantly affected by this environmental condition.

A standard modeling of sandwich structures is proposed in the thesis (Chapter 8): a literature analytical model, which was implemented in order to take into account material non linearities, and a finite element model in Abaqus FEA software, making use of default material models. A good agreement between experimental results and analytical-numerical global responses has been found in all the simulations. The assumption of perfect bond between TRC and EPS used in both the models can be considered reliable before failure. The numerical solution also allows to identify failure modes. However, when failure is reached, the finite element model is not able to catch the debonding between EPS and TRC as no interface elements are used. The Crushable Foam model implemented in the software has been used for the EPS material: even though it is not able to catch the tensile failure of the foam, EPS never reached its maximum tensile strength.

9.1 Further development

Three main further developments are crucial for the application of the panel on real buildings:

- the investigation on the cyclic mechanical behaviour of the sandwich solution, as the panel is mainly loaded by wind action;
- the investigation on the panel behaviour when exposed to thermal cycles, thinking in particular at the sun radiation;
- the identification of proper connection to fix the panel at the existing façade, taking into account the small thickness of mortar involved.

Currently, all these topics are the main focus of the EASEE European project, now at the end of its third year.

page intentionally left blank

References

Aitcin, P. (2003). The durability characteristics of High Performance Concrete: A review. *Cement and Concrete Composites*, 25(4-5 SPEC):409–420. 3.3

Banholzer, B. (2004). *Bond Behaviour of Multifilament Yarn Embedded in Cementitious Matrix*. PhD thesis, RWTH Aachen. 3.1

Benayoune, A., Samad, A., Trikha, D., Ali, A., and Ellinna, S. (2008). Flexural behaviour of pre-cast concrete sandwich composite panel - Experimental and theoretical investigations. *Construction and Building Materials*, 22(4):580–592. 2.5

Brameshuber, W., Brockmann, T., Curbach, M., Meyer, C., Vilkner, G., Mobasher, B., Peled, A., Reinhardt, H., Kruger, M., and Wastiels, J. (2006). *Textile Reinforced Concrete - State-of-the-art Report of RILEM Technical Committee 201-TRC: Textile Reinforced Concrete*, volume Report 36, chapter Concrete/Matrix, pages 29–56. RILEM Publications S.A.R.L. 5.1, 5.2.2, 8.1.1, 8.2.1

Butler, M., Hempel, S., and Mechtcherine, V. (2011). Modelling of ageing effects on crack-bridging behaviour of AR-glass multifilament yarns embedded in cement-based matrix. *Cement and Concrete Research*, 41:403–411. 3.1

Butler, M., Mechtcherine, V., and Hempel, S. (2010). Durability of Textile Reinforced Concrete made with AR glass fibre: Effect of the matrix composition. *Materials and Structures/Materiaux et Constructions*, 43(10):1351–1368. 3.3

Cavdar, A. (2014). Investigation of freeze-thaw effects on mechanical properties

of Fiber Reinforced Cement mortars. *Composites Part B: Engineering*, 58:463–472. 3.3

Cohen, Z. and Peled, A. (2010). Controlled telescopic reinforcement system of Fabric-Cement Composites - Durability concerns. *Cement and Concrete Research*, 40:1495–1506. (document), 3.3

Colombo, I. G., Magri, A., Zani, G., Colombo, M., and di Prisco, M. (2013). Erratum to: Textile Reinforced Concrete: experimental investigation on design parameters. *Materials and Structures*, pages 1–19. 4.1.3

Colombo, M., di Prisco, M., and Zecca, C. (2008). On the couplig of soft materials with thin layers of Glass Fibre Reinforced mortar. In *CCC 2008 - Challenges for Civil Construction*. 2.6, 5.1

Curbach, M. and Jesse, F. (1999). Lecture No. 513: Basic tensile tests on strain specimens of Textile-Reinforced Concrete. In *Techtextil Symposium*. 4.1.1

Curbach, M. and Sheerer, S. (2011). Concrete light - Possibilities and Visions. In *Proceedings of the fib Symposium Prague 2011 - Concrete Engineering for Excellence and Efficiency*, pages 29–44. (document), 3.1, 3, 3.6, 3.2, 3.14

Davies, J. (2001). *Lightweight Sandwich Construction*. Wiley-Blackwell. (document), 2.2, 2.2, 2.3, 2.4, 2.3, 2.4, 2.4

de Andrade Silva, F., Butler, M., Mechtcherine, V., Zhu, D., and Mobasher, B. (2011). Strain rate effect on the tensile behaviour of Textile-Reinforced Concrete under static and dynamic loading. *Materials Science and Engineering A*, 528(3):1727–1734. (document), 3.2, 4.1.3

Deshpande, V. S. and Flek, N. (2000). Isotropic Constitutive Model for Metallic Foams. *Journal of the Mechanics and Physics of Solids*, 48:1253–1276. 8.2.1

di Prisco, M., Cadoni, E., Colombo, M., Bonalumi, P., Caverzan, A., and Martinelli, P. (2013). On the Mitigation of the Risk of prefabricated Tunnel Linings: the ACCIDENT Project. In *Proceedings of "Protect 2013 - Performance, Protection and Strengthening of Structures under Extreme Loading - Mysore, India"*. (document), 3.2, 3.13

di Prisco, M., Ferrara, L., Lamperti, M., Lapolla, S., Magri, A., and Zani, G. (2012). Sustainable Roof Elements: A Proposal Offered by Cementitious Composites Technology. In Fardis, M. N., editor, *Innovative Materials and Techniques in Concrete Construction*, pages 167–181. Springer Netherlands. (document), 2.6, 2.8

di Prisco, M. and Zani, G. (2012). Experimental and numerical analysis of advanced cementitious composites for sustainable roof elements. In *Proceedings of the "Numerical modeling - Strategies for Sustainable Concrete Structures - Aix-en-Provance, France"*. 2.6, 3.2

EASEE (2012-2016). European Project: Envelope Approach to improve Sustainability and Energy efficiency in Existing multi-storey multi-owner residential buildings (www.easee-project.eu). 1, 2.6, 7.1

Einea, A., Salmon, D. C., Fogarasi, G. J., Culp, T. D., and Tadros, M. K. (1991). State-of-the-art of Precast Concrete Sandwich Panels. *PCI Journal*, 36(6):78–92. 2.5, 2.5, 5.2.2

Ferrara, L., Colombo, M., di Prisco, M., and Zecca, C. (2008). Sandwich panels with Glass Fiber Reinforced surfaces for affordable housing. In *CCC 2008 - Challenges for Civil Construction*. 2.6

Gambarova, P. G., Coronelli, D., and Bamonte, P. (2007). *Linee guida per la progettazione delle piastre in c.a.* Pàtron Editore Bologna. 6.2

Gara, F., Ragni, L., Roia, D., and Dezi, L. (2012). Experimental behaviour and numerical analysis of floor sandwich panels. *Engineering Structures*, 36:258–269. 2.5

Gilchrist, A. and Mills, N. (2001). Impact deformation of rigid polymeric foams: experiments and FEA modelling. *International Journal of Impact Engineering*, 25:767–786. 8.2.1

Gnip, I., Veyelis, S., Kersulis, V., and Vaitkus, S. (2007). Deformability and Strength of Expanded Polystyrene (EPS) under Short-term Shear Loading. *Mechanics of Composite Materials*, 43:85–94. 8.1.1, 8.1.2

Graybeal, B. and Tanesi, J. (2007). Durability of an Ultrahigh-Performance Concrete. *Journal of Materials in Civil Engineering*, 19(10):848–854. 3.3, 4.2.3

Gries, T., Roye, A., Offermann, P., Engler, T., and Peled, A. (2006). *Textile Reinforced Concrete - State-of-the-art Report of RILEM Technical Committee 201-TRC: Textile Reinforced Concrete*, chapter Textiles, pages 11–27. RILEM Publications S.A.R.L. (document), 3, 3.2

Hartig, J., Jesse, F., Schicktanz, K., and Haussler-Combe, U. (2012). Influence of experimental setups on the apparent uniaxial tensile load-bearing capacity of Textile Reinforced Concrete specimens. *Materials and Structures/Materiaux et Constructions*, 45(3):433–446. 4.1.2, 4.2.2

Hegger, J. and Horstmann, M. (2009). Light-weight TRC sandwich building envelopes. In *Excellence in Concrete Construction through Innovation*, pages 187–194. (document), 2.5, 2.6, 2.6, 2.7, 3.12, 9

Hegger, J., Horstmann, M., and Shams, A. (2011). Load-Carrying Behaviour of Sandwich Panels at Ultimate Limit State. In *Proceedings of the fib Symposium Prague 2011 - Concrete Engineering for Excellence and Efficiency*. 2.7.3

Hegger, J. and Voss, S. (2008). Investigations on the bearing behaviour and application potential of Textile Reinforced Concrete. *Engineering Structures*, 30:2050–2056. (document), 3, 3.11

Hegger, J., Will, N., Bentur, A., Curbach, M., Jesse, F., Mobasher, B., Peled, A., and Wastiels, J. (2006). *Textile Reinforced Concrete - State-of-the-art Report of RILEM Technical Committee 201-TRC: Textile Reinforced Concrete*, chapter Composite materials, pages 133–186. RILEM Publications S.A.R.L. 9

Hegger, J., Will, N., Curbach, M., and Jesse, F. (2004). Tragverhalten von textilbewehrtem Beton. *Beton-und Stahlbetonbau*, 99:452–455. (document), 3.1, 3.5

Horstmann, M., Hegger, J., Zell, M., and Kulas, C. (2008). Large-sized building envelopes and slender shell structures made of TRC. In *Proceedings of the 8th International Symposium on Utilization of High-Strength and High-Performance Concrete (Tokyo)*, pages 1183–1190. 3

Lee, J. and Fenves, G. (1998). Plastic-Damage Model for Cyclic Loading of Concrete Structures. *Journal of Engineering Mechanics*, 124(8):892–900. 8.2.1, 8.2.1

Lomboy, G. and Wang, K. (2009). Effects of strength, permeability, and air void parameters on freezing-thawing resistance of concrete with and without air entrainment. *Journal of ASTM International*, 6(10). (document), 3.3, 3.15

Lubliner, J., Oliver, J., Oller, S., and Onate, E. (1989). A Plastic-Damage Model for Concrete. *International Journal of Solids and Structures*, 25:299–329. 8.2.1

Magri, A. (2012). *Advanced Cementitious Composites for Structural Retroftting*. PhD thesis, Doctoral School in Structural, Seismic and Geotechnical Engineering. (document), 3.2, 3.9, 3.10

Marzouk, H. and Jiang, D. (1994). Effects of Freezing and Thawing on the Tension Properties of High-Strength Concrete. *ACI Materials Journal*, 91:577–586. 3.3, 4.2.3

Mechtcherine, V. (2013). Novel cement-based composites for the strengthening and repair of concrete structures. *Construction and Building Materials*, 41:365–373. 3.2

Mechtcherine, V. and Leboldt, M. (2011). Permeation of water and gases through cracked Textile Reinforced Concrete. *Cement and Concrete Composites*, 33:725–734. 4.2.2

Metelli, G., Bettini, N., and Plizzari, G. (2011). Experimental and numerical studies on the behaviour of concrete sandwich panels. *European Journal of Environmental and Civil Engineering*, 15(10):1465–1481. 2.5

Müller, F., Kohlmeyer, C., and Schnell, J. (2012). Load-Bearing Behaviour of Sandwich Strips with XPS-Core and Reinforced HPC-Facings. In *Ultra-High Performance Concrete and Nanotechnology in Construction, Proceedings of Hipermat 2012 - 3rd International Symposium on UHPC and Nanotechnology for High Performance Construction Materials*, pages 781–788. Kassel University Press. 2.6

Müller, H. S., Mechtcherine, V., and et al (2008). *Constitutive modelling of High Strength / High Performance Concrete - State-of-the-art report. fib bulletin 42.* International Federation for Structural Concrete (fib). 4.1.1

Mobasher, B., Peled, A., and Pahilajani, J. (2006). Distributed cracking and stiffness degradation in fabric-cement composites. *Materials and Structures*, 39:317–331. 3.1

Muhaxheri, M. (2014). *Behaviour of coupling beams retrofitted with advanced cementitious composites : experiments and modelling.* PhD thesis, Doctoral School in Structural, Seismic and Geotechnical Engineering. (document), 3.2, 3.7

Naito, C., Hoemann, J., Beacraft, M., and Bewick, B. (2011). Performance and characterization of shear ties for use in insulated precast concrete sandwich wall panels. *Journal of Structural Engineering*, 138(1):52–61. 2.5

Neville, A. (1996). *Properties of Concrete.* Wiley, New York. 3.3, 4.1.3

ODYSSEE_MURE (2012). Report: Energy Efficiency Trends in Buildings in EU - Lessons from the ODYSSEE MURE project (www.odyssee-indicators.org). 1

Ohno, S. Hannant, D. (1994). Modelling the stress-strain response of continuous Fiber Reinforced Cement Composites. *ACI Mater Journal*, 91:306–312. 3.1

Orlowsky, J. and Raupach, M. (2008). Durability model for AR-glass fibres in Textile Reinforced Concrete. *Materials and Structures/Materiaux et Constructions*, 41(7):1225–1233. 3.3

Peled, A. (2013). Lecture: Textile (fabric) Reinforced Concrete - TRC, Summer School: Textile Reinforced Concrete design - material and structural behaviour, Politecnico di Milano - Lecco Campus. (document), 3.2

Peled, A., Sueki, S., and Mobasher, B. (2006). Bonding in fabric-cement systems: Effects of fabrication methods. *Cement and Concrete Research*, 36:1661–1671. 3.1

Peled, A., Zaguri, E., and Marom, G. (2008). Bonding characteristics of multifilament polymer yarns and cement matrices. *Composites: Part A*, 39:930–939. (document), 3.1, 3.1, 3.4

Plantema, F. J. (1966). *Sandwich construction: the bending and buckling of sandwich beams, plates and shells.* Wiley. 2.7.2, 2.7.2

Purnell, P. and Beddows, J. (2005). Durability and simulated ageing of new matrix Glass Fibre Reinforced Concrete. *Cement and Concrete Composites*, 27(9-10):875–884. 3.3

Salmon, D., Einea, A., Tadros, M., and Culp, T. (1997). Full scale testing of precast concrete sandwich panels. *ACI Structural Journal*, 94(4):354–362. (document), 2.5, 2.5

Setzer, M. (1997). *Freeze-Thaw Durability of Concrete (rilem Proceeings 30)*, chapter Action of frost and deicing chemicals - basic phenomena and testing, pages 3–23. E & FN Spn. 3.3

Shams, A., Hegger, J., and Horstmann, M. (2014a). An analytical model for sandwich panels made of Textile-Reinforced Concrete. *Construction and Building Materials*, 64:451–459. (document), 2.7.3, 2.13, 2.7.3, 8.1

Shams, A., Horstmann, M., and Hegger, J. (2014b). Experimental investigations on Textile-Reinforced Concrete (TRC) sandwich sections. *Composite Structures*, 118:643–653. 2.6

Shang, H. and Yi, T. (2013). Freeze-thaw durability of air-entrained concrete. *The Scientific World Journal*, 2013. 4.2.3

Sharaf, T., Shawkat, W., and Fam, A. (2010). Structural performance of sandwich wall panels with different foam core densities in one-way bending. *Journal of Composite Materials*, 44(19):2249–2263. 2.6

Simulia (2011). *Abaqus Analysis User's Manual.* (document), 8.2.1, 8.7, 8.2.1

Soranakom, C. and Mobasher, B. (2009). Geometrical and mechanical aspects of fabric bonding and pullout in cement composites. *Materials and Structures*, 42:765–777. 3.1

Stamm, K. and Witte, H. (1974). *Sandwichkonstruktionen: Berechnung, Fertigung, Ausfiihrung*. Springer -Verlag, Wien New York. (document), 2.7.2, 2.10, 2.11, 2.7.2, 2.7.2, 2.7.3, 5.2.2, 5.2.2, 8.1, 8.1, 8.1, 8.2

Sueki, S., Soranakom, C., Mobasher, B., and Peled, A. (2007). Pullout-slip response of fabrics embedded in a cement paste matrix. *J Mater Civ Eng*, 19:718–727. 3.1

Sun, W., Zhang, Y., Yan, H., and Mu, R. (1999). Damage and damage resistance of High Strength Concrete under the action of load and freeze-thaw cycles. *Cement and Concrete Research*, 29(9):1519–1523. (document), 3.3, 3.3, 3.17, 3.18

Toniolo, G. and di Prisco, M. (2001). *Cemento Armato - Calcolo agli Stati Limite - volume 2A*. Zanichelli editore. 8.1.1

Vinson, J. (1999). *The Behavior of Sandwich Structures of Isotropic and Composite Materials*. Technomic Publishing Company. (document), 2.2, 2.2, 2.3

Vinson, J. (2005). *Sandwich Structures 7: Advancing with Sandwich Structures and Materials*, chapter Sandwich Structures: Past, Present and Future, pages 3–12. Springer Netherlands. 2.1, 2.3

Wang, K., Lomboy, G., and Steffes, R. (2009). Investigation into Freezing-Thawing Durability of Low-Permeability Concrete with and without Air Entraining Agent. Technical report, National Concrete Pavement Technology Center - Institute for Transportation - Iowa State University. (document), 3.3, 3.16

Westergaard, H. (1926). Stresses in Concrete Pavements Computed by Theoretical Analysis. *Public Roads*, 7(2):25–35. (document), 5.3.2, 5.23

Zani, G. (2013). *High Performance Cementitious Composites for Sustainable Roofing Panels*. PhD thesis, Doctoral School in Structural, Seismic and Geotechnical Engineering. 3.2

Zastrau, B., Richter, M., and Lepenies, I. (2003). On the analytical solution of pullout phenomena in Textile Reinforced Concrete. *J Eng Mater Technol*, 125:38–43. 3.1